Theses and Dissertations

May 2015

Chiral Modification of the Pd(111) Surface By Small Organic Molecules

Mausumi Mahapatra
University of Wisconsin-Milwaukee

CHIRAL MODIFICATION OF THE Pd(111) SURFACE BY SMALL

ORGANIC MOLECULES

by

Mausumi Mahapatra

A Dissertation Submitted in

Partial Fulfillment of the

Requirement for the Degree of

Doctor of Philosophy

In Chemistry

At

The University of Wisconsin-Milwaukee

May 2015

ABSTRACT

CHIRAL MODIFICATION OF THE Pd(111) SURFACE BY SMALL ORGANIC MOLECULES

by

Mausumi Mahapatra

The University of Wisconsin Milwaukee, 2015
Under the Supervision of Distinguished Professor Wilfred T. Tysoe

Chiral modification of a metal surface is one of the most successful approaches of achieving enantioselective catalysis in heterogeneous phase. In this approach, an active metal surface is directly modified by adsorption of a chiral molecule (chiral modifier), the metal is responsible for catalytic activity while the adsorbed modifier controls the stereochemistry of adsorption and subsequent reactions through substrate interactions. So far, there are three types of widely recognized metal/modifier catalytic systems: tartaric acid modified Ni catalysts for the hydrogenation of β-ketoesters, cinchona modified Pt catalysts for hydrogenation of α-ketoesters and Pd catalysts modified with cinchona for selective activated alkene hydrogenation, where high activity and enantiomeric excess is gained in comparison to the unmodified surfaces. However, the exact manner in which chirality is bestowed to a metal surface and how that affects a chiral reaction is not well understood and warrants the development of model studies (surface science analysis on well-defined single crystal surfaces under ultrahigh vacuum conditions). These model studies and surface science analysis are necessary to promote the fundamental

understanding and to facilitate the rational design of a suitable metal/modifier system, which is the principal focus of this dissertation.

This dissertation is primarily focused on two aspects. First, a number of complementary surface science studies have been performed to characterize four different chiral modifiers: D-alanine, (S,S) tartaric acid, L-aspartic acid and α-(1-naphthyl) ethylamine on a Pd(111) surface to gain insight into the way in which they impart chirality to the surface. Second, the enantioselectivity of the chirally modified surfaces has been measured in ultrahigh vacuum. This has been achieved by exposing the modified surface to both enantiomers of another chiral molecule (the probe), to observe if there is any enantiospecific interaction between the modifier and the probe. The enantioselectivity is measured from the enantioselectivity ratio which is the ratio of relative coverages of two enantiomers of the probe on a surface modified with a single enantiomer of the modifier.

Combined experimental results and theoretical density functional theory calculations suggest that the amino acid modifiers impart chirality to the Pd(111) surface by an ensemble mechanism, where they work collectively to form discrete *chiral templates,* which interact with the chiral probe propylene oxide and glycidol enantiospecifically whereas, tartaric acid and naphthylethylamine provide individual chiral *motifs* which interact with the probes in a *one to one* fashion.

To my parents Mr. Krishna Prasad Mahapatra and Usha Mahapatra

TABLE OF CONTENTS

LIST OF FIGURES

Figure A-13 Structures of the most stable docking complexes from the keto tautomer of MP (A and B) and from the enol tautomer (C through G). The interaction energies calculated including van der Waals' interactions are shown below each structure, as well as the expected equilibrium proportions. The STM images simulated by the Tersoff-Hamman method are shown adjacent to each structure. The angles between the axis in the simulated images of the *enol* tautomer of MP, indicated by a blue line, and the long axis of the naphthyl group of R-NEA, indicated by a red line, are also indicated. 334

LISTS OF TABLES

ACKNOWLEDGMENTS

I am indebted to many people who guided me, helped me in my research and supported throughout my graduate studies. I would first thank to my advisor Professor Wilfred Tysoe for taking me under his wings as a PhD student. I will be always grateful to him for his faith in me when things did not go as planned in my research. Prof. Tysoe was always available to clarify my doubts and it was a great opportunity to learn from his vast research expertise. The joy and enthusiasm he has for his research been very motivational during though times in my PhD pursuit. I appreciate all his contributions of time, idea and funding to make my PhD an enjoyable and productive experience. I had no previous experience prior to joining his research group. I learned everything about my research from Prof. Tysoe and the past and present group members that I have had the pleasure to work with as a graduate student.

My utmost thanks to Dr. Luke Burkholder who taught me basic vacuum techniques and TPD. I would like to thank Dr. Octavio Furlong, Dr. Brendan Miller and Dr. Anibal Boscoboinik for all their help during initial stage of my PhD. These four always encouraged me, taught me how to fix instruments, helped me in my presentations and trained me for the rest of my graduate studies. A good support system is essential for surviving and staying calm in grad school. I was lucky to have a group of friends in Dr. Michael Garvey, Dr. John Kestell and Heather Adams to be that support system. They have contributed immensely to my professional and personal time at UWM. Dr. Garvey taught me all about DFT and was kind enough to carry out many calculations for my research. Though he was a senior member in the group I knew that I could always ask

him for advice and opinions in lab related issues. He always helped me with a smile in his face. John is a dear friend and I can't thank him enough for all his help in teaching me STM and many other excellent techniques. I find a true scientist in him. His knowledge in a vast range of subject inspired me. A special thanks to Heather Adams who became one of my very first friends in grad school. She is a wonderful human being and very generous friend. On numerous times she helped me with her excellent problem solving techniques, fixing instruments and DFT calculations. I will never forget the coffee breaks, walks around campus and the camping trip together. Rasha is a dear friend and we learned from each other while working together. She is motivated and curious to learn new things in research. It was a pleasure working alongside Ted Thuening. He is a nice, smart, happy guy, always curious to learn and ready to help. Dustin Olson is very hard working, motivated, humble person and I am excited to work with him in the LEED and STM chambers in future. I thank all the past members that I had the pleasure to work with: Dr. Yun Bai, Dr. Sunil Devarajan, Josh Walker and Shaimaa Alghareeb.

I sincerely thank the members of my doctoral committee Professor Dennis Bennett, Professor Jorg Woehl, Professor Peter Geissenger, Professor Alan Schwabacher and Professor Wilfred Tysoe. My entire committee members have been very gracious and generous with their time, sharing ideas and providing valuable inputs. I would like to thank the wonderful staff Kevin Blackburn, Shelley Hagen, Megan Garrett, Wendy Grober and Elise Nicks in the Chemistry and Biochemistry department. A special thanks to Daniel Shurilla and Neal Korfhage for helping me in my research with their expertise and hard work.

Finally, I would like to thank my family members for all their love and support. My father Krishna Prasad Mahapatra has been my idol from my childhood. Being a college professor himself, he always encouraged me to go for higher studies. His innocence, simplicity and desire to learn always impressed me. My mother Usha Mahapatra is my source of inspiration and I call her almost every day to get that extra boost of energy. Her unconditional love and support gives me strength to chase my dreams. Thank you both for guiding me as a person, teaching me that my goal in life is to learn and to be happy. My brother Chandan (Sikun) deserves my wholehearted thanks as well for his support. I thank my in-laws (Gangadhar Rath and Sudhamayee Rath) for encouraging me to study further and follow my dreams. I will mention Situ, Mona, my gradparents, uncles, aunts, cousin brothers and sisters for their unconditional love and support. Finally, I would like to thank my husband Sabysachi Rath. He was always there cheering me up and stood by me through the good times and bad. He was instrumental in pushing me to apply for grad school when I did not have faith in myself. He had confidence in me and always told me that I had the right attitude, temperament and patience in me to succeed in grad school and ultimately in my pursuit for research in surface science. Thank You!

Chapter 1

Introduction

1.1   Asymmetric Catalysis in Heterogeneous Phase

The increasing demand for enantiomerically pure compounds has spurred the development of efficient methods in the field of enantioselective catalysis. Over the past few decades, intense research has been carried out in this field to expand the scope of catalytic reactions that can be performed with high enantioselectivity and efficiency, [1-2] and the use of chiral ligands in combination with transition metals has proven to be the most efficient catalytic strategy for achieving this.[3-7] Accordingly, many chiral ligands and their transition-metal complexes have been developed for the homogeneous-phase chiral catalysis. Despite this remarkable success, there are only few examples of asymmetric catalysts which can be used for the large-scale production in the industrial processes. The main concern in this field is the need of a reusable catalyst. Due to the high cost of both the metal and chiral ligands, systems that allow straightforward separation of catalyst from the reaction mixture is highly desirable, which is usually very difficult to achieve in the homogeneous phase. Another major drawback in homogeneous phase catalysis is product contamination by metal leaching,[8-10] which is unacceptable for the production of fine chemicals and pharmaceuticals. Therefore, the use of heterogeneous-phase asymmetric catalysis is beneficial which provides a good strategy to resolve such problems associated with homogeneous-phase chiral catalysis.

Heterogeneous asymmetric catalysis [11-19] has gained a large amount of attention

over the past few decades, but is still lagging behind due to concerns with performance, mechanistic insights, and the range of reactions that can be addressed.

Various strategies have been applied in the development of heterogeneous chiral catalysts, which can be broadly classified into three categories. One strategy for transformation of a homogeneous catalysts into a heterogeneous one, is the immobilization of a homogeneous catalyst, [3, 20] where the catalyst is anchored to a stationary support, which allows the easy separation of the catalyst from the reaction mixture and potentially can be reused multiple times. The main goal for the development of an immobilized chiral catalyst is to combine the positive aspects of a homogeneous catalyst (e.g. high activity, high enantioselectivity, reproducibility) with those of heterogeneous catalyst (ease of catalyst separation, stability and reusability). However, the choice of support material is crucial and there are examples where supported catalysts suffer from lower catalytic activity and are less stable than their homogeneous counterpart.

Using an intrinsically chiral solid surface is another way of achieving heterogeneous asymmetric catalysis. Chiral bulk materials such as quartz or calcite inherently exposes chiral surfaces, but achiral structures can also expose chiral surfaces, for example, a metal may contain defects such as kinks which are chiral. Such intrinsically chiral sites can be created deliberately by cutting a single crystal metal along certain high-Miller-index planes. Such chiral metal surfaces have been studied extensively to explore the catalytic activity by Gellman *et al.*[21-27]

An alternate, and, perhaps the most promising strategy for achieving heterogeneous chiral catalysis is to directly modify the catalyst surface by using a chiral

ligand, which is analogous to that exploited in homogeneous phase. The modification of an active metal surface by an adsorbed chiral modifier has been shown to be very successful for heterogeneous asymmetric catalysis. In this approach, a metal surface is used in combination with a suitable chiral ligand (chiral modifier) as an inherently heterogeneous asymmetric catalyst. While the metal is responsible for catalytic activity, the surface adsorbed modifier controls the stereochemistry of the reaction through substrate interactions. This strategy has met with some success, predominately in the enantioselective hydrogenation of several prochiral reactants, and high substrate specificity is observed when using chirally modified metal surfaces as heterogeneous catalysts. So far, there are three types of widely recognized efficient catalyst systems: tartaric-acid modified Ni catalysts for the hydrogenation of β-ketoesters, cinchona modified Pt catalysts for the hydrogenation of α-ketoesters[17, 28-38] and Pd catalysts modified with cinchona alkaloids for selective activated alkene hydrogenation. The mechanisms involved in the reactions have also received some attention and model studies have been performed by using single crystal surfaces under ultrahigh vacuum (UHV) conditions, the aim being to understand the adsorption of the modifier onto the metal surface to identify nature of the active site and its interaction with the reactant. An important advantage of surface studies under UHV is that the surface can be studied over a wide range of coverages and temperatures. This allows chiral properties to be studied as a function of coverage, starting from nucleation to saturation coverage. Those model studies are absolute necessary to interpret and predict the catalytic behavior of the systems, as well as to facilitate the rational design of suitable modifiers which still remains as a challenging goal. The main concern related with the model studies under

UHV environment is the pressure gap, because the real catalysts operate under ambient condition.

This dissertation is focused on the later strategy, which is the chiral modification of a Pd(111) metal surface. Four different classes of chiral modifiers: amino acids, tartaric acid, aspartic acid and naphthylethylamine (NEA) are characterized on a Pd(111) surface under UHV environment. The principal aim is to fundamentally understand the nature of chiral modification which is of prime importance in the field of heterogeneous asymmetric catalysis. We have measured the enantioselective chemisorption of chiral probe molecules on chirally modified Pd(111) surface in UHV which will be described in section 1.4 of this chapter.

1.2 Chirality on a Surface

The understanding of surface chirality has become a strong focus of surface-science studies. Surface chirality is relevant to applications ranging from biocompatibility, enantioselective catalysis, nonlinear optical devices, chiral separation, etc. There are two broad ways in which chirality is imparted to the surface: via adsorption of a suitable organic molecule or by carefully cutting the crystal to expose the chiral kinked or stepped surface. The latter approach is not within the scope of this dissertation, which is primarily focused on adsorption of chiral molecules (chiral modifiers) on an achiral Pd(111) surface.

A surface contains a plane of inherent asymmetry, because it is the interface where the bulk material meets the surroundings. Thus, at a surface only those symmetry elements that are perpendicular to it can exist, e.g. rotation axes and reflection planes normal to the surface, [39] which lead to a substantial reduction in symmetry of the surface

compared to the bulk material. According to the Cahn-Ingold-Prelog rule, the creation of surface chirality requires destruction of all the symmetry elements which can be met by adsorption of a chiral molecule. One of the interesting issues in this field is how the organic molecules bestow chirality to a non-chiral surface. A number of review papers have been recently published to address this issue.[39-43] Surface chirality can be recognized in many ways. Broadly speaking, either the chiral molecules create local "chiral motifs" by individual adsorption event (point chirality) or the individual motifs self-organize to form one-dimensional or two-dimensional chiral domains on the surface (organizational chirality or space group chirality).

When chiral molecules adsorb on the surface with the chiral center intact, that will inevitably lead to a local chiral motif. It is impossible to create any mirror chiral motif by just translation and rotational symmetry elements present on the surface. Thus a globally chiral system is produced.

Chiral motifs can also be created by the adsorption of achiral molecules, where the presence of surface induces the loss of both molecular and surface reflection symmetry elements. However, the non-chiral molecules only form local chiral motifs, due to the presence of both the enantiomers; chirality disappears at a global level.[44]

One-dimensional surface chirality is exhibited in systems where intermolecular interactions are constrained to a specific direction leading to the formation of simple structures such as chains of molecules that either have an intrinsic lack of mirror symmetry and/or run in a non-symmetric direction across the metal surface, thus breaking the existing mirror symmetry. Two-dimensional surface chirality is exhibited when the molecules self-organize to form complex chiral two-dimensional structures on the

surface. In some cases the surface consists of discrete, chiral two-dimensional clusters, which possess no mirror symmetry elements and thus forming a "chirally templated surface" or the molecules self-organize to form extended ordered arrays of long range periodicity, which breaks the underlying symmetry element of the surface.

Over the last few decades, extensive research has been carried out in this field to gain insight about the nature of chiral modification which leads to the origin of surface chirality. Tartaric acid, amino acids and cinchonidine and other analog molecules are heavily studied as chiral modifiers on transition metal surfaces. The Raval and Ernst groups have extensively studied the formation of chiral surfaces on Cu.[45-54] The Tysoe,[55-63] Zaera[64-69] and Baddeley[45-46, 48, 50-51, 70-72] groups have studied the modification of reactive surfaces; Pd, Pt and Ni respectively. The main focus has been a fundamental characterization of the organic molecules on the surface, which can be used in catalysis-related phenomena.

A large focus of this dissertation is characterizing the modifier molecules on a Pd(111) surface, which has been achieved by using a number of complementary surface science spectroscopies. Temperature programmed desorption (TPD) experiments provide information of the thermal stability and desorption kinetics of the adsorbate, while the structural details such as chemical bonding and the orientation of the molecules is largely determined by surface infrared absorption Spectroscopy (RAIRS). X-ray photoelectron spectroscopy (XPS) provides information on the chemical state of the adsorbed species and compositional analysis. Scanning tunneling microscopy (STM) yields spatial information about the surface structure and the nature of ordering on the surface at a molecular level. However, even the use of all these powerful techniques has not been able

to provide many of the nano scale details required for fundamental understanding. Therefore, density functional theory (DFT) calculations have been carried out which allows good models to be developed for interpreting the complex surface interactions. The experimental results are taken as the robust starting point for the DFT calculations, which provide insights on the bonding, intermolecular interaction, and detailed adsorption geometry of the adsorbates on surface.

1.3   Enantioselectivity of the Chirally Modified Pd(111) Surfaces

Enantioselective catalysis arises from enantiospecific interaction of prochiral and chiral species (adsorbed reactants) with a chiral catalytic surface. These interactions manifest themselves as differences in energies between R- and S- chiral adsorbates on the R- (or –S) enantiomorphs of the catalyst. The mechanism by which these interactions are affected on a chirally modified surface is highly dependent on the nature of chiral modification and is broadly classified into two categories.

1: *Chirally templated surfaces*, where chiral modifiers adsorbed on a achiral surface self-assemble into discrete chiral templates or extended ordered structures which provide the chiral site for the enantiospecific adsorption of chiral adsorbates (chiral probe)

2: *One to one chiral modifiers*, where an isolated chiral modifier (chiral motifs) on an achiral metal surface interacts enantiospecifically with a chiral probe or a prochiral adsorbate to form a one to one complex. Such a *one to one* interaction does not require long range ordering of the modifiers on surface. The Orito reaction, the enantioselective hydrogenation of methyl pyruvate (prochiral reactant) to R-methyl lactate on chinchonidine-modified Pt catalysts was originally proposed to occur by chiral template mechanism but later on the experimental results indicated that the reaction occur due to

one to one docking interaction between methyl pyruvate and cinchonidine.
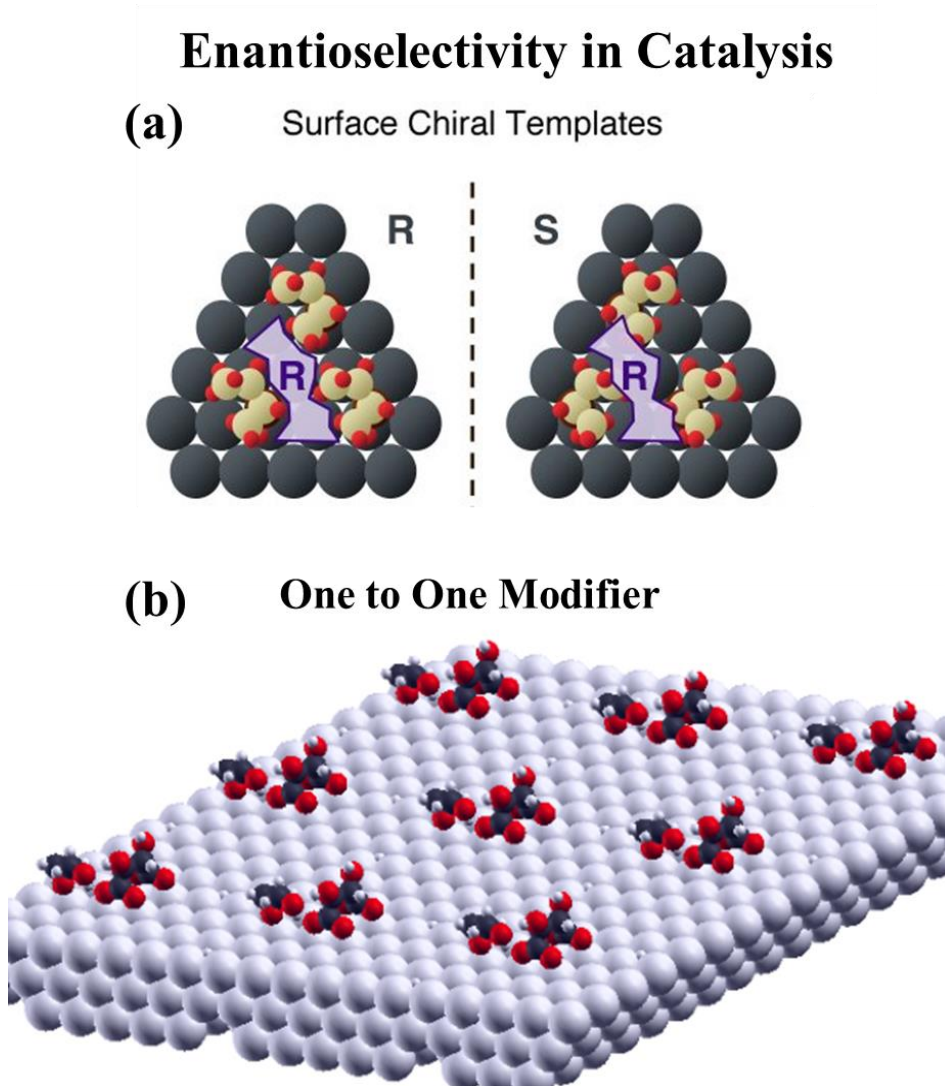
Figure 1-1 Schematic illustrations of the models by which chiral molecules (chiral modifiers) are proposed to bestow enantioselectivity to heterogeneous catalysts. (a) Shows the formation of supramolecular surface chiral templates, where three molecules of the enantiopure templating agents (2-butoxide adsorbates), either the (R) (left panel) or the (S) (right panel) form a pocket of specific chirality on the surface. The (R) purple structure fits nicely in the chiral site by the(R) butoxides but not on that defined by the (S) enantiomers. (Part of the image reproduced with permission [73]) (b) Illustration of one to one chiral interaction on the surface. The chiral modifier (tartaric acid) provides individual chiral motifs, which interact enantiospecifically with a chiral probe in one to one fashion.

To directly identify the nature of chiral modification and the interaction between

the modifier and probe we have used scanning tunneling microscopy (STM). The results of this dissertation show direct evidence for the observation of both template and one to one mechanisms which will be presented in the following chapters.

1.4 Measurement of Chemisorptive Enantioselectivity in UHV

Most of the surface science techniques (except STM) are not sensitive to the chirality of molecules on the surface. Enantiomers have the same mass and molecular composition and therefore give rise to the same mass spectra and same vibrational modes. Therefore, a method was developed by the Tysoe group to measure the chemisorptive enantioselectivity of chirally modified surfaces by using a chiral probe molecule in ultrahigh vacuum. This is been achieved by means of chiral titration TPDS, where the modified surface is exposed to a suitable enantiopure probe molecule of both chiralities and the relative coverages of the probe molecules is measured. The enantioselectivity is measured from enantioselective ratio, which is the ratio of the coverages of the two probe enantiomers for the same coverage of the modifier. The enantioselective ratio is calculated from the equation: $R_e = \Theta_D^R/\Theta_D^S = \Theta_L^S/\Theta_L^R$

where, Θ is the probe molecule saturation coverage and the superscripts (*S* or *R*) are the chiralities of the probe and the subscripts (*D* or *L*) are those of the modifier. Using this idea the chemisorptive enantioselectivity of amino acid and tartaric acid modified surfaces is measured by chiral probe molecules: propylene oxide and glycidol which is described in Chapters 5 and 8.

1.5 Organization of the Manuscript

This section briefly introduces the contents of the dissertation in the context of

surface chirality and measurement of enantioselectivity of chirally modified surfaces.

Chapter 2 describes the experimental methods and equipment used to perform the experiments described in the later chapters. A brief overview of the principle underlying each technique is also given.

Chapter 3 presents the surface characterization of the α-amino acids (chiral modifier molecules) on Pd(111) surface by means of both experimental techniques and DFT calculations, which reveals that they provide organizational chirality to the surface by forming a "*templated* " surface.

Chapter 4 presents surface studies of the chiral molecule glycidol on Pd(111) surface, which is used as a chiral probe to measure the enantioselectivity of the chirally modified surfaces in Chapters 5 and 8. The results are compared to propylene oxide which has been used as a chiral probe in the past by the Tysoe group.

In Chapter 5 the enantioselectivity of the amino-acid modified Pd(111) surfaces is measured by chiral titration experiments, where both propylene oxide and glycidol are used as chiral probes. By correlating measured enantioselectivity with the amino acid surface structure on Pd(111) (Chapter 3), it was concluded that the amino acid chiral templates provide enantiospecific adsorption sites for the chemisorption of chiral probe propylene oxide and glycidol.

In Chapter 6 another modifier molecule D-(-)-tartaric acid is spectroscopically characterized on a Pd(111) surface and the results are compared with similar studies carried out on other transition metal surfaces, e.g. Cu and Ni. The results reveal that tartaric acid molecules on the surface are dynamic and evolve entities in response to adsorption temperature and adlayer coverage.

Chapter 7 presents STM and DFT study of D-(-)-tartaric acid on Pd(111). STM experiments are carried out to examine the surface structure of different tartaric acid derived species as a function of adsorption temperature and coverage as a basis for correlating the surface structure with the spectroscopic results (Chapter 6). STM results show that tartaric acid imparts chirality to the surface by both forming chiral motifs and organizational chirality which is highly dependent on the adsorption temperature and coverage. DFT calculations are carried out to interpret the STM results.

Chapter 8 presents the enantioselectivity measurements of D-(-)-tartaric acid by using both propylene oxide and glycidol as chiral probe molecules. The results show that propylene oxide does not show any enantioselectivity while glycidol does, and that is ascribed its ability to form hydrogen bonds to tartaric acid. By correlating the STM structures and enantioselectivity conditions, it is proposed that enantioselectivity is imparted by a *one-to-one* interaction between the chiral modifier, bitartrate and the probe, glycidol.

Chapter 9 presents some preliminary results of the surface characterization of aspartic acid on a Pd(111) surface, the motivation being to test if this can be used as a chiral modifier. The results are compared to the surface structures of alanine and tartaric acid. Ongoing DFT calculations are also discussed.

In Chapter 10, a transition is made towards understanding the chemical interactions between the chiral modifier R-1-(1-Naphthylethylamine) (NEA) and a prochiral reactant methyl pyruvate on a Pd(111) surface. STM was performed by coadsorbing NEA and MP to directly identify the nature of interaction. The results show a *one-to-one* docking interaction between the modifier and prochiral reactant which leads

to enhanced hydrogenation of methyl pyruvate on a NEA modified Pd(111) surface.

Chapter 11 presents an STM study of four C_3 hydrocarbons: propylene oxide, glycidol, propene and 3,3,3 trifluoropropene with the principal aim being to characterize the surface structures. The first part of this chapter focusses on characterization of propylene oxide and glycidol as a comparative study between Pd and Pt surfaces. The second part of the chapter is focused on surface characterization of propene and its fluorinated analog. 3,3,3 trifluoropropene is studied to explore whether replacing the –CH_3 group in propene by a –CF_3 group has any effect on the surface ordering due to the stronger dipole-dipole interaction of the fluorinated groups.

Chapter 12 summarizes the main conclusions presented in this dissertation.

1.6   References

1.   Collins, A. N.; Sheldrake, G.; Crosby, J., *Chirality in industry II: Developments in the commercial manufacture and applications of optically active compounds*. John Wiley & Sons: 1997; Vol. 2.

2.   Crosby, J., Chirality in industry—an overview. *Chirality in Industry* 1992, 1-66.

3.   Wang, Z.; Ding, K.; Uozumi, Y., An Overview of Heterogeneous Asymmetric Catalysis. *Handbook of Asymmetric Heterogeneous Catalysis* 2008.

4.   Kolb, H. C.; Sharpless, K. B., Asymmetric aminohydroxylation. In *Transition Metals for Organic Synthesis*, Beller, M.; Bolm, C., Eds. Wiley-VCH: Weinheim, Germany, 1998; Vol. 2, pp 243-260.

5.   Knowles, W. S., Asymmetric Hydrogenations (Nobel Lecture). *Angewandte Chemie International Edition* 2002, *41* (12), 1998-2007.

6.   Noyori, R., Asymmetric Catalysis: Science and Opportunities (Nobel Lecture). *Angewandte Chemie International Edition* 2002, *41* (12), 2008-2022.

7.   Sharpless, K. B., Searching for New Reactivity (Nobel Lecture). *Angewandte Chemie International Edition* 2002, *41* (12), 2024-2032.

8.   Song, C. E.; Lee, S.-g., Supported Chiral Catalysts on Inorganic Materials. *Chemical Reviews* 2002, *102* (10), 3495-3524.

9.   McMorn, P.; Hutchings, G. J., Heterogeneous enantioselective catalysts: strategies for the immobilisation of homogeneous catalysts. *Chemical Society Reviews* 2004, *33* (2), 108-122.

10.   Corma, A.; Garcia, H., Crossing the Borders Between Homogeneous and Heterogeneous Catalysis: Developing Recoverable and Reusable Catalytic Systems. *Top Catal* 2008, *48* (1-4), 8-31.

11.   Baiker, A., Progress in asymmetric heterogeneous catalysis: Design of novel chirally modified platinum metal catalysts. *Journal of Molecular Catalysis A: Chemical* 1997, *115* (3), 473-493.

12.   Baiker, A., Chiral catalysis on solids. *Current Opinion in Solid State and Materials Science* 1998, *3* (1), 86-93.

13.   Baiker, A., Transition state analogues—a guide for the rational design of enantioselective heterogeneous hydrogenation catalysts. *Journal of Molecular Catalysis A: Chemical* 2000, *163* (1), 205-220.

14.   Bein, T., Asymmetric catalysis on solids. *Current Opinion in Solid State and Materials Science* 1999, *4* (1), 85-96.

15.   Blaser, H.; Jalett, H.; Monti, D.; Baiker, A.; Wehrli, J., Enantioselective hydrogenation of ethyl pyruvate: effect of catalyst and modifier structure. *Studies in Surface Science and Catalysis* 1991, *67*, 147-155.

16.   Blaser, H.-U.; Jalett, H.-P.; Müller, M.; Studer, M., Enantioselective hydrogenation of α-ketoesters using cinchona modified platinum catalysts and related systems: A review. *Catalysis today* 1997, *37* (4), 441-463.

17.   Bürgi, T.; Baiker, A., Heterogeneous enantioselective hydrogenation over cinchona alkaloid modified platinum: mechanistic insights into a complex reaction. *Accounts of chemical research* 2004, *37* (11), 909-917.

18.   McIntosh, A. I.; Watson, D. J.; Burton, J. W.; Lambert, R. M., Heterogeneously Catalyzed Asymmetric CC Hydrogenation: Origin of Enantioselectivity in the Proline-Directed Pd/Isophorone System. *Journal of the American Chemical Society* 2006, *128* (22), 7329-7334.

19.   Murzin, D. Y.; Mäki-Arvela, P.; Salmi, T., Mechanisms of Asymmetric Heterogeneous Catalysis1. *Kinetics and catalysis* 2003, *44* (3), 323-333.

20.   De Vos, D.; Vankelecom, I. F.; Jacobs, P. A., *Chiral catalyst immobilization and recycling*. John Wiley & Sons: 2008.

21.   Gellman, A. J.; Tysoe, W. T.; Zaera, F., Surface Chemistry for Enantioselective Catalysis. *Catalysis Letters*, 1-13.

22.   Horvath, J. D.; Baker, L.; Gellman, A. J., Enantiospecific orientation of R–3-methylcyclohexanone on the chiral Cu (643) R/S surfaces. *The Journal of Physical Chemistry C* 2008, *112* (20), 7637-7643.

23.   Kamakoti, P.; Horvath, J.; Gellman, A. J.; Sholl, D. S., Titration of chiral kink sites on Cu (643) using iodine adsorption. *Surface science* 2004, *563* (1), 206-216.

24.   Yun, Y.; Gellman, A. J., Enantioselective Separation on Naturally Chiral Metal Surfaces: d, l-Aspartic Acid on Cu (3, 1, 17) R&S Surfaces. *Angewandte Chemie International Edition* 2013, *52* (12), 3394-3397.

25.   Rampulla, D.; Gellman, A., Enantioselective decomposition of chiral alkyl bromides on Cu (643) R&S: Effects of moving the chiral center. *Surface science* 2006, *600* (14), 2823-2829.

26.   Rampulla, D.; Francis, A.; Knight, K.; Gellman, A., Enantioselective surface chemistry of R-2-bromobutane on Cu (643) R&S and Cu (531) R&S. *The Journal of Physical Chemistry B* 2006, *110* (21), 10411-10420.

27.   Baber, A. E.; Gellman, A. J.; Sholl, D. S.; Sykes, E. C. H., The real structure of naturally chiral Cu {643}. *The Journal of Physical Chemistry C* 2008, *112* (30), 11086-11089.

28.   Orito, Y.; Imai, S.; Niwa, S., Asymmetric hydrogenation of a-keto esters using a platinum-alumina catalyst modified with cinchona alkaloid. *J. Chem. Soc. Jpn.* 1980, (4), 670-2.

29.   Meheux, P. A.; Ibbotson, A.; Wells, P. B., Enantioselective hydrogenation. II. Variation of activity and optical yield with experimental variables in methyl pyruvate hydrogenation catalyzed by cinchona-modified platinum/silica (EUROPT-1). *J. Catal.* 1991, *128* (2), 387-96.

30.   Blaser, H. U.; Jalett, H. P.; Muller, M.; Studer, M., Enantioselective hydrogenation of alpha-ketoesters using cinchona modified platinum catalysts and related systems: A review. *Catalysis Today* 1997, *37* (4), 441-463.

31.   Pfaltz, A.; Heinz, T., Enantioselective Hydrogenation of Ethyl Pyruvate over Pt/Alumina - Systematic Variation of the Modifier Structure. *Top Catal* 1997, *4* (3), 229-239.

32.   Kacprzak, K.; Gawroński, J., Cinchona Alkaloids and Their Derivatives: Versatile Catalysts and Ligands in Asymmetric Synthesis. *Synthesis* 2001, (07), 0961-0998.

33.   Bürgi, T.; Baiker, A., Heterogeneous Enantioselective Hydrogenation over Cinchona Alkaloid Modified Platinum: Mechanistic Insights into a Complex Reaction. *Accounts of chemical research* 2004, *37* (11), 909-917.

34.   Diezi, S.; Hess, M.; Orglmeister, E.; Mallat, T.; Baiker, A., Chemo and enantioselective hydrogenation of fluorinated ketones on platinum modified with (R)-1-(1-naphthyl)ethylamine derivatives. *Journal of Molecular Catalysis A-Chemical* 2005, *239* (1-2), 49-56.

35.   Blaser, H.-U.; Studer, M., Cinchona-Modified Platinum Catalysts: From Ligand Acceleration to Technical Processes. *Accounts of chemical research* 2007, *40* (12), 1348-1356.

36.   Demers-Carpentier, V.; Laliberté, M.-A.; Lavoie, S. p.; Mahieu, G.; McBreen, P. H., Two-Dimensional Self-Assembly and Catalytic Function: Conversion of Chiral Alcohols into Self-Assembled Enols on Pt(111)†. *The Journal of Physical Chemistry C* 2009, *114* (16), 7291-7298.

37.   Demers-Carpentier, V.; Goubert, G.; Masini, F.; Lafleur-Lambert, R.; Dong, Y.; Lavoie, S.; Mahieu, G.; Boukouvalas, J.; Gao, H.; Rasmussen, A. M. H.; Ferrighi, L.; Pan, Y.; Hammer, B.; McBreen, P. H., Direct Observation of Molecular Preorganization for Chirality Transfer on a Catalyst Surface. *Science* 2011, *334* (6057), 776-780.

38.   Demers-Carpentier, V.; Rasmussen, A. M. H.; Goubert, G.; Ferrighi, L.; Dong, Y.; Lemay, J.-C.; Masini, F.; Zeng, Y.; Hammer, B.; McBreen, P. H., Stereodirection of an α-Ketoester at Sub-molecular Sites on Chirally Modified Pt(111): Heterogeneous Asymmetric Catalysis. *Journal of the American Chemical Society* 2013, *135* (27), 9999-10002.

39.	Raval, R., Chiral expression from molecular assemblies at metal surfaces: insights from surface science techniques. *Chemical Society Reviews* 2009, *38* (3), 707-721.

40.	Ernst, K.-H., Supramolecular surface chirality. In *Supramolecular chirality*, Springer: 2006; pp 209-252.

41.	Gellman, A. J., Chiral surfaces: accomplishments and challenges. *ACS nano* 2010, *4* (1), 5-10.

42.	Gellman, A. J.; Tysoe, W. T.; Zaera, F., Surface Chemistry for Enantioselective Catalysis. *Catalysis Letters* 2015, *145* (1), 220-232.

43.	Barlow, S. M.; Raval, R., Complex organic molecules at metal surfaces: bonding, organisation and chirality. *Surface Science Reports* 2003, *50* (6), 201-341.

44.	Ernst, K.-H., Molecular chirality in surface science. *Surface science* 2013, *613*, 1-5.

45.	Lorenzo, M. O.; Haq, S.; Bertrams, T.; Murray, P.; Raval, R.; Baddeley, C. J., Creating chiral surfaces for enantioselective heterogeneous catalysis: R,R-Tartaric acid on Cu(110). *Journal of Physical Chemistry B* 1999, *103* (48), 10661-10669.

46.	Lorenzo, M. O.; Baddeley, C. J.; Muryn, C.; Raval, R., Extended surface chirality from supramolecular assemblies of adsorbed chiral molecules. *Nature* 2000, *404*, 376-378.

47.	Humblot, V.; Haq, S.; Muryn, C.; Hofer, W. A.; Raval, R., From local adsorption stresses to chiral surfaces: (R,R)-tartaric acid on Ni(110). *Journal of the American Chemical Society* 2002, *124* (3), 503-510.

48.	Lorenzo, M. O.; Humblot, V.; Murray, P.; Baddeley, C. J.; Haq, S.; Raval, R., Chemical transformations, molecular transport, and kinetic barriers in creating the chiral phase of (R,R)-tartaric acid on Cu(110). *Journal of Catalysis* 2002, *205* (1), 123-134.

49.	Raval, R., Chiral expressions at metal surfaces. *Current Opinion in Solid State & Materials Science* 2003, *7* (1), 67-74.

50.	Humblot, V.; Lorenzo, M. O.; Baddeley, C. J.; Haq, S.; Raval, R., Local and global chirality at surfaces: Succinic acid versus tartaric acid on Cu(110). *Journal of the American Chemical Society* 2004, *126* (20), 6460-6469.

51.	Humblot, V.; Haq, S.; Muryn, C.; Raval, R., (R,R)-tartaric acid on Ni(110): the dynamic nature of chiral adsorption motifs. *Journal of Catalysis* 2004, *228* (1), 130-140.

52.   Behzadi, B.; Romer, S.; Fasel, R.; Ernst, K.-H., Chiral recognition in surface explosion. *Journal of the American Chemical Society* 2004, *126* (30), 9176-9177.

53.   Romer, S.; Behzadi, B.; Fasel, R.; Ernst, K. H., Homochiral conglomerates and racemic crystals in two dimensions: tartaric acid on Cu (110). *Chemistry-A European Journal* 2005, *11* (14), 4149-4154.

54.   Lawton, T. J.; Pushkarev, V.; Wei, D.; Lucci, F. R.; Sholl, D. S.; Gellman, A. J.; Sykes, E. C. H., Long Range Chiral Imprinting of Cu (110) by Tartaric Acid. *The Journal of Physical Chemistry C* 2013, *117* (43), 22290-22297.

55.   Stacchiola, D.; Burkholder, L.; Tysoe, W. T., Enantioselective chemisorption on a chirally modified surface in ultrahigh vacuum: Adsorption of propylene oxide on 2-butoxide covered Pd(111). *Journal of the American Ceramic Society* 2002, *124*, 8984-8989.

56.   Stacchiola, D.; Burkholder, L.; Tysoe, W. T., Probing enantio selective chemisorption in ultrahigh vacuum. *Journal of Molecular Catalysis A-Chemical* 2004, *216* (2), 215-221.

57.   Stacchiola, D.; Burkholder, L.; Zheng, T.; Weinert, M.; Tysoe, W. T., Requirements for the formation of a chiral template. *Journal of Physical Chemistry B* 2005, *109* (2), 851-856.

58.   Gao, F.; Wang, Y. L.; Burkholder, L.; Tysoe, W. T., Enantioselective chemisorption of propylene oxide on a 2-butanol modified Pd(111) surface: The role of hydrogen-bonding interactions. *Journal of the American Chemical Society* 2007, *129* (49), 15240-15249.

59.   Gao, F.; Wang, Y.; Tysoe, W. T., Enantioselective Chemisorption and Reactions on Model Chirally Modified Surfaces: 2-Butanol on l-Proline Templated Pd (111) Surfaces. *The Journal of Physical Chemistry C* 2008, *112* (15), 6145-6150.

60.   Gao, F.; Wang, Y. L.; Tysoe, W. T., Enantioselective chemisorption and reactions on model chirally modified surfaces: 2-butanol on L-proline templated Pd(111) surfaces. *Journal of Physical Chemistry C* 2008, *112* (15), 6145-6150.

61.   Gao, F.; Wang, Y. L.; Li, Z. J.; Furlong, O.; Tysoe, W. T., Enantioselective reactions on a Au/Pd(111) surface alloy with coadsorbed chiral 2-butanol and propylene oxide. *Journal of Physical Chemistry C* 2008, *112* (9), 3362-3372.

62.   Burkholder, L.; Stacchiola, D.; Boscoboinik, J. A.; Tysoe, W. T., Enantioselective Chemisorption on Model Chirally Modified Surfaces: 2-Butanol on α-(1-Naphthyl) ethylamine/Pd (111). *The Journal of Physical Chemistry C* 2009, *113* (31), 13877-13885.

63.   Mahapatra, M.; Tysoe, W. T., Structure and decomposition pathways of D-(−)-tartaric acid on Pd (111). *Surface Science* 2014.

64.   Kubota, J.; Zaera, F., Adsorption geometry of modifiers as key in imparting chirality to platinum catalysts. *Journal of the American Chemical Society* 2001, *123* (44), 11115-11116.

65.   Chu, W.; LeBlanc, R. J.; Williams, C. T.; Kubota, J.; Zaera, F., Vibrational band assignments for the chiral modifier cinchonidine: Implications for surface studies. *The Journal of Physical Chemistry B* 2003, *107* (51), 14365-14373.

66.   Ma, Z.; Kubota, J.; Zaera, F., The influence of dissolved gases on the adsorption of cinchonidine from solution onto Pt surfaces: an in situ infrared study. *Journal of Catalysis* 2003, *219* (2), 404-416.

67.   Lee, I.; Zaera, F., Enantioselectivity of adsorption sites created by chiral 2-butanol adsorbed on Pt (111) single-crystal surfaces. *The Journal of Physical Chemistry B* 2005, *109* (26), 12920-12926.

68.   Lee, I.; Zaera, F., Chiral templating of surfaces: Adsorption of (S)-2-methylbutanoic acid on Pt (111) single-crystal surfaces. *Journal of the American Chemical Society* 2006, *128* (27), 8890-8898.

69.   Lee, I.; Ma, Z.; Kaneko, S.; Zaera, F., 1-(1-Naphthyl) ethylamine adsorption on platinum surfaces: On the mechanism of chiral modification in catalysis. *Journal of the American Chemical Society* 2008, *130* (44), 14597-14604.

70.   Jones, T. E.; Baddeley, C. J., A RAIRS, STM and TPD study of the Ni{111}/R,R-tartaric acid system: Modelling the chiral modification of Ni nanoparticles. *Surface Science* 2002, *513* (3), 453-467.

71.   Jones, T. E.; Baddeley, C. J., Direct STM evidence of a surface interaction between chiral modifier and pro-chiral reagent: Methylacetoacetate on R,R-tartaric acid modified Ni{111}. *Surface Science* 2002, *519* (3), 237-249.

72.   Jones, T. E.; Noakes, T. C. Q.; Bailey, P.; Baddeley, C. J., Adsorbate-induced segregation in the Ni{111}/Au/(R,R)-tartaric acid system. *J. Phys. Chem. B* 2004, *108* (15), 4759-4766.

73.   research.chem.ucr.edu

Chapter 2
Experimental Methods

2.1 Introduction

All the experiments described in this thesis are carried on a Pd(111) single crystal surface under ultrahigh vacuum (UHV) conditions by using a number of different surface science techniques. This chapter briefly describes the instrumentation and experimental details of the present work. The main body of this chapter consists of four different sections which are organized as follow. The chapter starts with a brief description of the necessity of UHV for surface science experiments, followed by a section to describe typical UHV chambers and components for achieving UHV. The next section includes the design of the essential components of a UHV chamber and sample cleaning procedure. The final section describes the experimental techniques, UHV chambers and instrumentation associated with each experimental technique.

2.2 Necessity of Ultra-high vacuum

Surface science is the study of the nature of the surface and its interaction with the surrounding atoms and molecules. The physical and chemical nature of a surface depends on its electronic structure, which is a function of the nature of the surface atoms and their distribution. Real surfaces consist of a mixture of flat places and defects such as steps, kinks and point defects. Therefore the spatial distribution and the electronic properties are not uniform throughout the surface. Each surface site has its own physical and chemical properties. Therefore the reactions that occur on the real surfaces are diverse and complex. The complexity can be simplified by using a well-defined single crystal surface,

where the defects sites concentrations are very low in comparison to the flat part of the surface (terraces). Another requirement for surface science experiment is a clean environment during the time lapse of the experiment, which can be achieved if the experiments are carried out under ultrahigh vacuum conditions. There are two principal reasons why most of the surface science techniques are performed in UHV conditions and they are described below.

(1) To Maintain Sample Cleanliness

The surface cleanliness is very important during the time required to carry out an experiment. This can be achieved by maintaining the pressure surrounding the sample sufficiently low such that it is not contaminated by the background gas molecules. At any pressure, the incident flux of molecules onto any surface is given by the Hertz- Knudsen equation:

$$F = \frac{p}{\sqrt{2\pi m k_B T}} \tag{2.1}$$

Where, p is the pressure, m is the mass of a molecule in the gas phase, k_B is the Boltzmann constant, and T is the temperature. From the above equation, it is clear that for a fixed mass and temperature; the lower the pressure (p), the lower the flux (F). Therefore in UHV (with pressures in the range of 10^{-10} Torr), this flux is very low in comparison to atmospheric pressure. The time required to form a monolayer is that for a surface to be covered by a layer of the gas of one molecule thickness. This time is given by the ratio between the number of molecules required to form a compact monolayer and the incident flux. Hence in UHV, where the incident flux is very low because of extreme low pressure, it takes longer time (hours) to form a monolayer. All of the work of this dissertation consists of the adsorption of different organic molecules on a Pd(111) single

crystal surface. Carbon monoxide (CO) is a primary contaminant in a UHV chamber. At a background pressure of 10^{-6} Torr, assuming that it contains only CO, the flux is 10^{15} molecules/cm^{2}s. Given that a typical surface has about 10^{15} atoms/cm^2, and assuming a sticking coefficient of unity (every molecule which impinges on the surface will stick to it), it takes about a second for the Pd surface to be completely covered by CO. Lowering the background pressure to 10^{-10} Torr increases the monolayer formation time to 10000s (2.75hour). Typical surface science experiments take about an hour or more to complete, so experiments can be performed with a very low percent of surface contamination under UHV conditions.

(2) To Minimize Gas-phase Collisions

An additional reason for carrying out experiments in UHV is to minimize the number of gas phase collisions. The mean free path (λ) of molecules in the gas phase is given by the equation:

$$\lambda = \frac{k_B T}{\sqrt{2\pi d^2 p}} \tag{2.2}$$

Where d is the effective diameter of a molecule, p is the pressure k_B is the Boltzmann constant and T is the temperature. Many of the techniques used in surface science require molecules, ions, or electrons to physically move through space, either from source to sample or from sample to detector, or both.[1] This distance is usually in the order of few centimeters, but at atmospheric pressure, the mean free path of a molecule is ~ 70 nm, making these techniques impossible without vacuum. Decreasing the pressure to UHV range dramatically increases the mean free path to the order of meters. So the gas-phase collision becomes extremely rare.

2.3 Typical UHV chambers and Components for Achieving UHV

2.3.1 Schematic of a Typical UHV Chamber
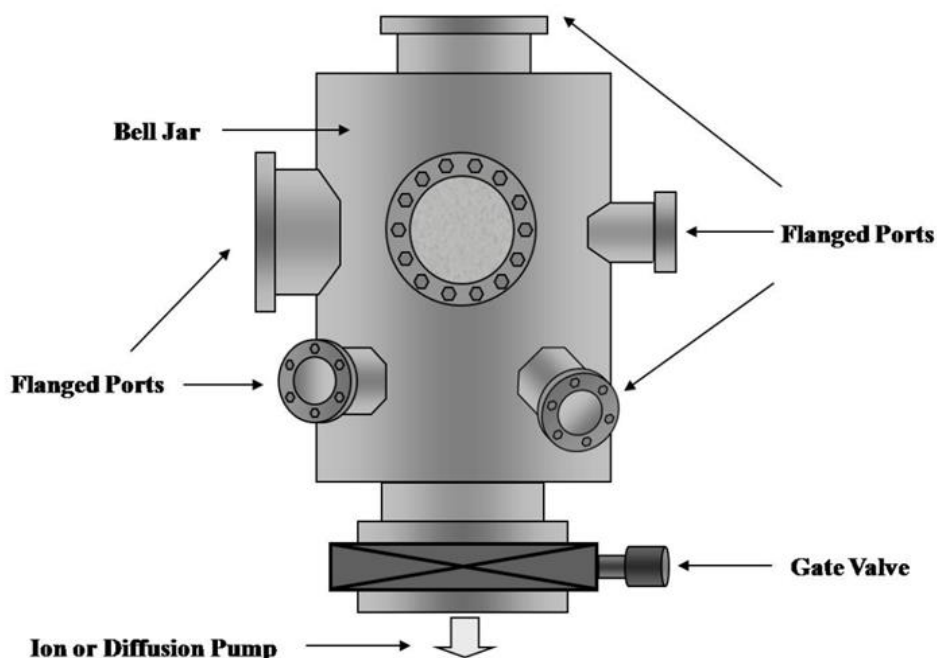
Figure 2-1 Schematic diagram of a typical UHV chamber [2]

The UHV chambers are usually cylindrical or spherical in shape (Figure 2-1).[2] Most surface science techniques require the movement of charged particles like electrons, ions etc. inside the UHV chamber. To avoid any magnetic or electrical interference to these movements, the outer body is typically made up of a non-magnetic material, 304 stainless series. This material has low outgassing rate and has a sufficient mechanical strength to withstand the pressure difference and therefore widely used for building UHV chambers. Various ports of different standard sizes are attached to the main body of the chamber which allows the installation of different dosing sources, experimental hardware, sample manipulator, view port windows, pressure measurement gauge, vacuum pumps etc. The ports are sealed with knife-edged flanges cut into copper gaskets,

known as Conflat flanges to make a UHV compatible seal. All the electrical connections to the chamber are applied by high vacuum feed through.

Once the system is leak tight, it is pumped down by vacuum pumps to attain low pressures. The pump down sequence from atmosphere to UHV is carried out in three stages of pumping. First, mechanical pumping is required for bringing down the pressure to the range of 10^{-3} Torr. In the second step, a turbomolecular pump is used to further lower the pressure to $\sim 10^{-5}$ Torr or lower, and this can be easily achieved within an hour of pumping. The final stage of pumping is done by using either an ion pump or a diffusion pump to achieve UHV. The ultimate pressure achieved after the pump down sequence is usually in the range of $\sim 5 \times 10^{-8}$ Torr even after ~ 12 hours of continuous pumping and continues to decrease at a very slow rate. This relatively high pressure is mostly due to slow desorption of water from the inner walls of the chamber. In order to accelerate the process of water desorption from the inner walls, the whole system is baked to $\sim 130^{\circ}$C for ~ 48 hours with continuous pumping by all the pumps. The bake-out is achieved by placing resistive heating tapes around the chamber and covering the chamber with two layers of aluminum foil. The first layer of foil is wrapped tightly around the chamber to help distribute the heat (aluminum is a much better thermal conductor than stainless still) and the second layer of foil is wrapped loosely over the entire chamber to insulate the chamber during bake-out, and for homogeneous heating. As a good vacuum practice, the filaments and the sample inside the chamber are degassed after the bake-out is turned off and while the chamber is still warm. The sample is degassed by heating to high temperature and the filaments are degassed by simply running a higher than normal current through the filaments for a short period of time.

During bake-out while the contaminants can easily desorb from the inner volume of the chamber, it is difficult to desorb those from the filaments which can remains quite gassy. Therefore, degassing while the chamber is warm helps to desorb the contaminants without contaminating the inner walls of the chamber and helps to achieve a good background pressure. After the bake out procedure the chamber is allowed to cool to room temperature and the background pressure reaches a value of $\sim 2 \times 10^{-10}$ Torr.

The choice of vacuum pumps and their required pumping speed depends on the desired background pressure and the gas load of the chamber. The gas load of the chamber is the sum of the residual gas remaining from the initial atmosphere, the vapor pressure of the materials present in the chamber and the virtual leakage, out gassing and permeation through the outer wall of the chamber. Therefore it is necessary to install the pumps which have a pumping speed higher that the total gas load of the chamber and continuous pumping is required even after achieving UHV.

2.3.2   Vacuum Pumps

Vacuum pumps are the most indispensable part of any vacuum system which is required to attain and maintain a low pressure inside the vacuum systems. The principle of operation of different pumps is described in the following.

2.3.2.1   Mechanical (Rotary) Pump

Mechanical pumps work by the process of positive gas displacement.[3-4] During their operation, the pump (Figure 2-2) periodically creates increasing and decreasing volumes to remove the gases from the system, and exhaust them to the atmosphere. A rotating vane traps the gas on the suction side of the pump forcing it towards the discharge side. The moving parts are submerged in pump oil, which serves as lubricant

and sealant. The ultimate pressure achieved by a mechanical pump is in the range of few millitorrs. Although UHV cannot be achieved by using a mechanical pump, it is an indispensable component of a UHV system. It is used as a roughing pump for the initial pump down of the chamber from atmosphere, and also as a backing pump for the turbomolecular and oil diffusion pumps.
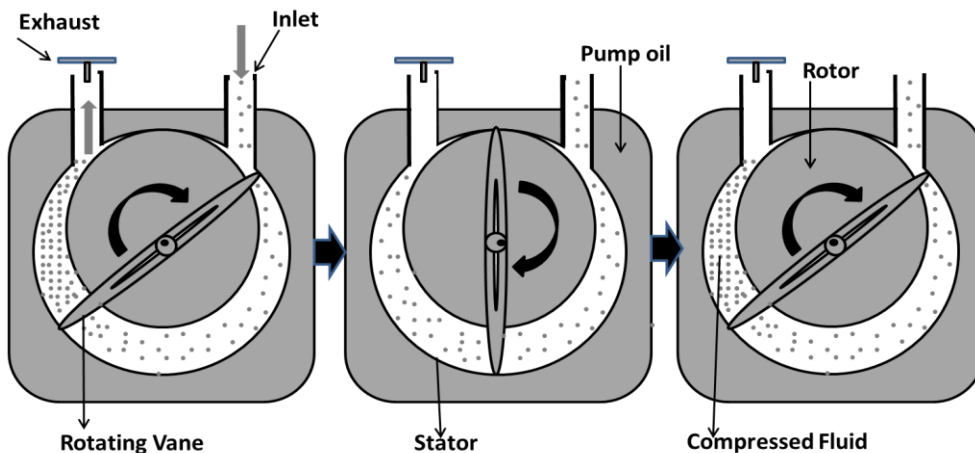
Figure 2-2 Mechanical pump schematics and operation

They can run for years with very little maintenance and are cheaper in comparison to other pumps. However there is a major disadvantage due to the use of oil which sometimes back stream and contaminates the chamber and they are very noisy and provide mechanical vibration to the system.

2.3.2.2 Turbomolecular Pump

The turbo molecular pumps operate by the principle of momentum transfer [5] similar to that of a jet engine. They consist of multiple stages of rotor-stator pairs organized in series. The rotor blades spin at a very high speed (typically 75 KRPM). As the gas molecules enter the inlet, the rotor blades collide with the molecules. Thus the mechanical energy of the blades is transferred to the gas molecules. With this newly

acquired momentum, the gas molecules enter the gas transfer holes in the stator. This leads them to the next stage where they again collide with the rotor surface, and this process is continued, finally leading the molecules outwards through the exhaust. The relationship of orientation between blades of the rotor/stator pair is such that it increases the probability of molecules going towards the outlet, generating a pressure difference with respect to the inlet. The pump requires a backing pump during the operation.

The pump operates over a wide variety of pressure range starting from 10^{-4} to 10^{-10} Torr and it works extremely well to pump heavier gases. They are clean because they do not use any oil for the operation. However, they are noisy, provide vibration to the system and are expensive.

2.3.2.3 Diffusion Pump

Diffusion pumps are another variety of momentum transfer pumps.[6,7] They are widely used in vacuum systems to achieve a base pressure of ~1×10^{-10} Torr or lower after the system is initially pump down by the mechanical pump. The diffusion pump comprises of a stainless steel cylinder containing a vertically stacked, cone-shaped jet assembly. There is a heater on the bottom of the pump which heats the oil to its boiling point. This step is done after the system is rough pumped to the range of militorrs, otherwise there will be no pumping action occurs by the pump due to oxidation of the pump oil. Once the oil starts to boil, the vapor is forced up through the central column of the jet assembly and then expelled downwards through a downward directed jet assembly, displacing molecules on its way and forcing them to leave the chamber. As the molecules from the system enter the pump they encounter the top jet and are gradually forced to move downwards until they reach the foreline and pumped away by the backing

pump. Since backstreaming of the oil can be a serious problem, diffusion pumps use specialized oil with a low vapor pressure and a high molecular weight. For the same reason, UHV systems have a cryotrap located between the pump and the chamber. This minimizes the back-streaming of oil molecules, preventing them from entering the UHV system. Some advantages of diffusion pumps are: they are noise free, reliable, have a simple design, relatively inexpensive and have high pumping speeds. On the other hand, the major disadvantage of these pumps is that they can back stream some oil vapor.
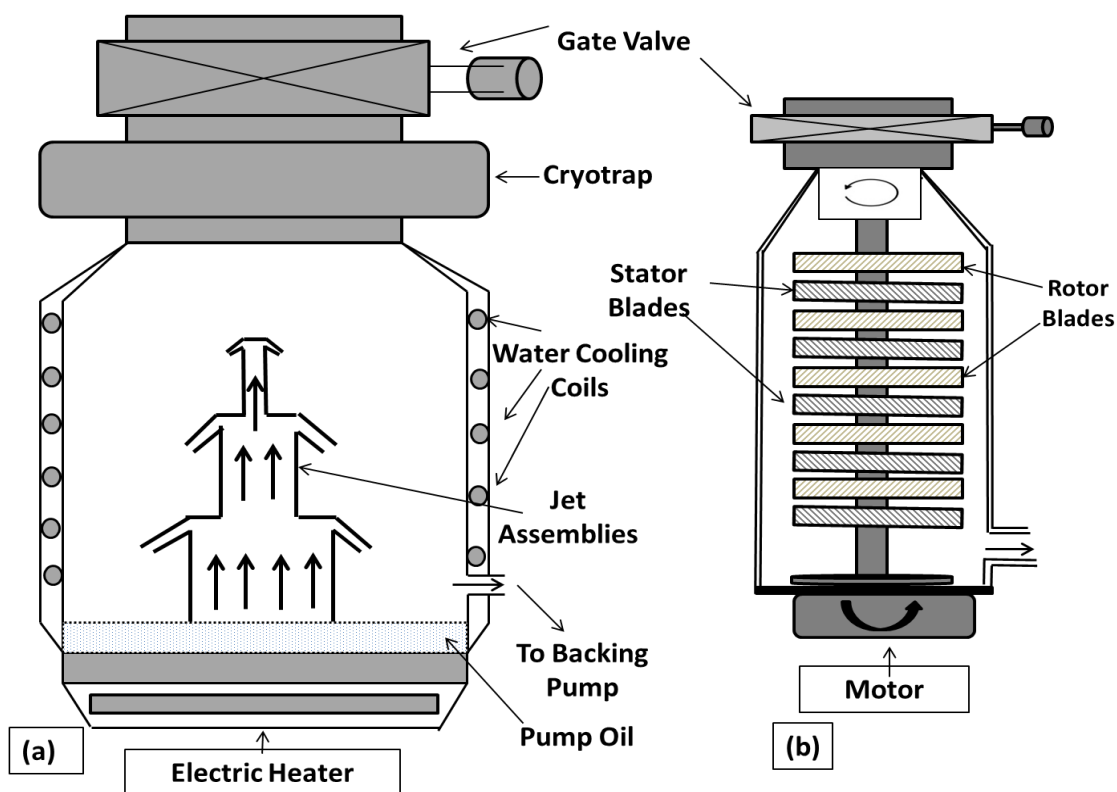
Figure 2-3 Schematics of (a) Diffusion pump (b) Turbomolecular pump

2.3.2.4 Ion Pump

Ion pumps are the primary choice in UHV systems. They are clean, vibration free, can operate over a relatively wide range of pressures (10^{-6} to 10^{-11} Torr). The basic

components of an ion pump are: a parallel array of short stainless-steel tubes (anode), two titanium plates (cathode) and a magnet (Figure 2-4). The cathode plates are positioned on both sides of the anode tubes. A strong magnetic field is oriented along the axis of the anode, which is generated by permanent magnets located outside the vacuum. Electrons are emitted from the cathode due to the action of an electric field and due to the presence of magnetic field they move in a long helical trajectory (a penning trap). This trajectory enhances the collision of the electrons with the incoming gas molecules. The result of this collision creates a positive ion which accelerates towards the cathode with sufficiently high kinetic energy to be buried in the cathode. When heavier gases and molecules are pumped they often have high enough kinetic energy to sputter some of the cathode material away and deposit them on the other parts of the pump providing a continuous supply of gettering material and thus increasing the pump efficiency. Reactive molecules like CO, O_2, N_2 etc. form stable complexes with titanium[8] and thus are permanently removed from the system. When pumping inert gases for example Ar, the molecules are buried deep inside the cathode by a sorption process. Since Ti does not form a stable complex with Ar, this pumping effect is not permanent since, because of the erosion of the cathode material, previously implanted molecules can be released which is often referred to as "argon instability". Therefore ion pumps are not ideal for pumping inert gases.

Since ion pump works by either chemisorbing or physiosorbing ions into the electrodes, it does not require a backing pump. Ion pumps require very low maintenance and form a closed vacuum system with the vacuum chamber. It is also clean and vibration free.
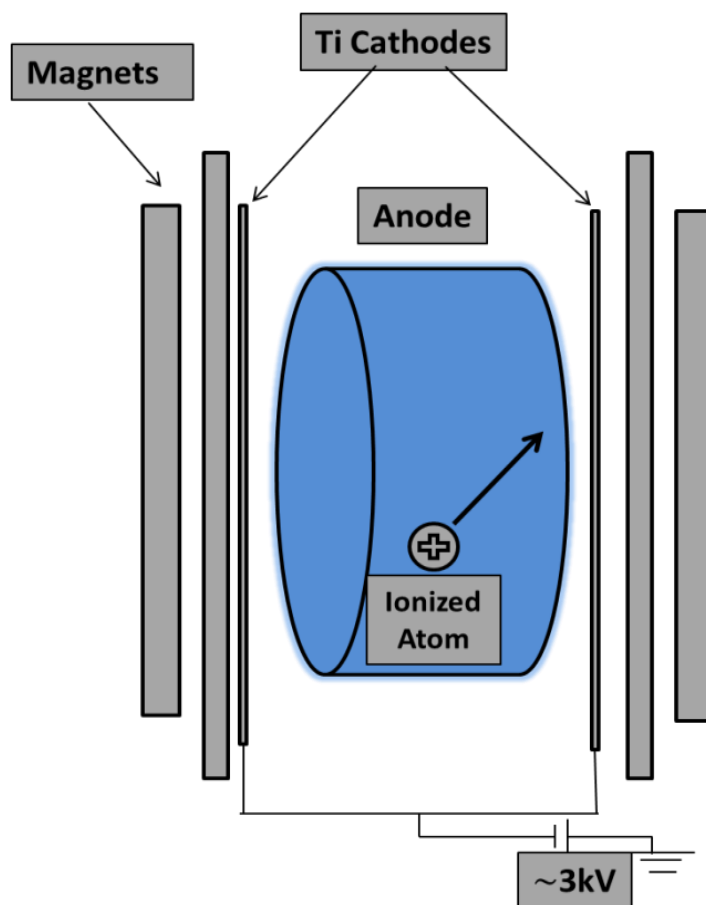
Figure 2-4 Schematic diagram of an ion pump

2.4   Common Procedures and UHV Components

2.4.1   Introducing Gases into UHV Chamber

Reactant gases are introduced into the UHV chamber in a controlled manner through leak valves attached to gas-handling lines (for introducing gases or liquids of moderate to high vapor pressure) and/or a Knudsen source (for introducing solids or liquids of very low or very high vapor pressure). The following section presents a typical design of a gas line and a Knudsen source used frequently in the laboratory.

2.4.1.1   Gas-handling Line

A gas-handling manifold is attached to each chamber for introducing gases. A typical diagram for a gas line is given in Figure 2-5. The gas line is constructed from Pyrex glass. The low reactivity of Pyrex glass minimizes the decomposition of introduced gases in the gas line and reduces the risk of contamination and adhesion into the walls of the glass material. The gas lines are usually pumped by a combination of mechanical pump and diffusion pump. The pressure is measured by a diaphragm monometer attached to it. The gas line can reach a pressure of 10^{-7} Torr without baking. Gases are introduced into the gas line directly from a gas cylinder which is connected to the gas line by a flexible hose and 1/4" Swagelok fitting. If the sample to be introduced is in the liquid form then the sample is transferred to a glass vial and stored in the gas line by Swagelok fittings and purified by several freeze-pump-thaw cycles before introduction to the UHV chamber. The gas line is connected to leak valves (which are attached to the UHV chamber) by glass-to-metal seals. The gas line is usually divided into two or three separate sections. Each section is isolated from others by gas valves with Teflon stopcocks. Each arm connects to a leak valve which is attached to the vacuum chamber. This allows the gas line to be filled with multiple gases at the same time to be introduced into the vacuum system when doing co-adsorption experiments.
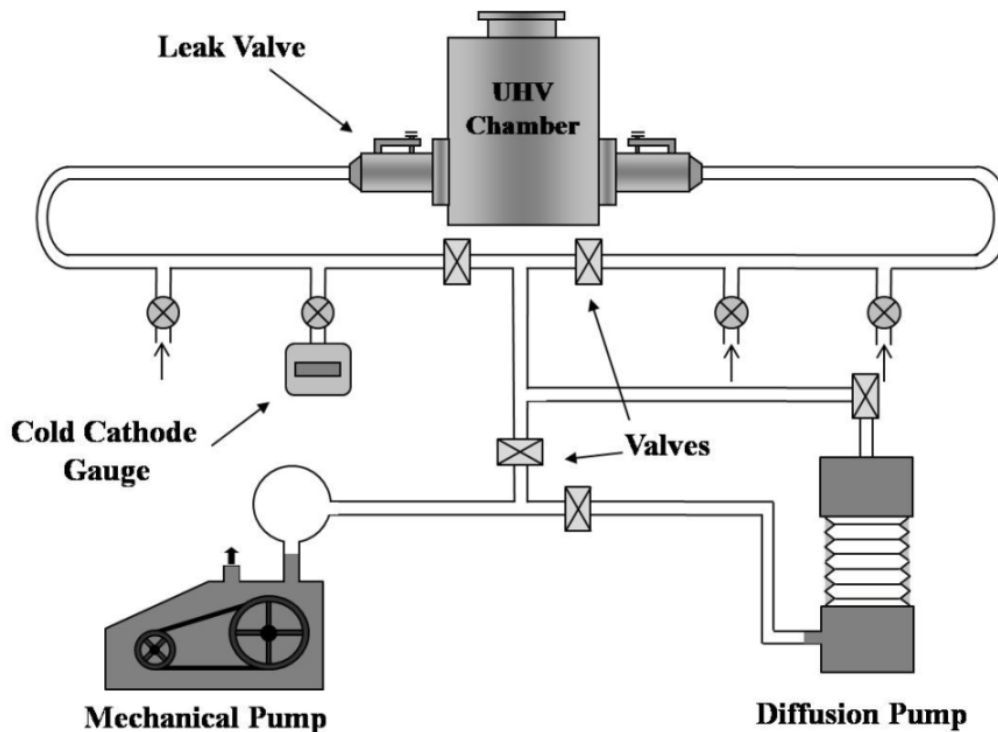
Figure 2-5 Schematic diagram of a typical diffusion pumped gas line [2]

2.4.1.2 Knudsen source

There are some compounds used in this study which are either solids or liquids having very low vapor pressures and cannot be introduced from the gas line or are very reactive and require differential pumping while dosing. For these molecules a homebuilt Knudsen source is used. The Knudsen source is made up of two 2 ¾" Conflat flanges welded to the ends of a ¼" stainless-steel tubing. A "T" is introduced in the middle to accommodate the sample to be introduced either by a blank Swagelok fitting or a glass vial. A turbo molecular pump is mounted at one end of the Knudsen source on a Conflat flange for differential pumping and a dosing tube is welded on the chamber side to the flange for direct dosing into the sample. The dosing tube is either made of stainless steel or glass tubing. For dosing compounds with very high vapor pressure, the compound is attached to the source by a glass vial. Depending on the desired dosing rate and the vapor

pressure of the sample, the compound is either dosed for a short period of time at room temperature or the compound is immersed in a cryostatic bath such as ethylene glycol-dry ice mixture or ice water - salt etc. while dosing. For compounds with very low vapor pressure and require heat for dosing, a small amount was placed in the source by a 1/4" blank stainless steel Swagelok fitting. The whole source was uniformly wrapped with resistive heating tapes and connected to a variable transformer. The whole Knudsen source assembly is wrapped up uniformly with two layers of aluminum foil for uniform heat distribution. If the temperature is not even throughout the source, then the vapor will condense on the cold spots and problems will arise when dosing the sample. A thermocouple junction is spot welded to the Swagelok fitting of the Knudsen source assembly to monitor the temperature of the source.

2.4.2   Sample cleaning

The Pd(111) crystal was initially bulk cleaned by several cycles of argon ion bombardment at an energy of 2 kV with a background argon pressure of ~3×10^{-5} Torr measuring a sample current of ~2 microamps, and then annealing to ~1100 K in vacuum after each bombardment cycle. The next cleaning steps consisted of one cycle of argon ion bombardment, annealing to ~1100 K in vacuum, followed by heating the sample to ~800 K in ~4×10^{-8} Torr of oxygen for ~15 minutes (oxygen roasting) and then briefly annealing to ~1100 K in vacuum. These steps are repeated several times and then the sample cleanliness is checked by Auger spectroscopy. The primary contaminants were found to be sulfur and carbon. While the amount of sulfur on the surface can be easily seen by Auger spectroscopy, it is difficult to gauge the amount of carbon because one of the Pd peaks overlap with the carbon peak. However, to estimate the amount of carbon

present on the surface using Auger spectroscopy, a ratio of height of carbon peak to the most intense palladium peak was measured. A ratio of C: Pd peak of 1:5 indicates that the sample is almost free of carbon contamination. Sulfur contamination can be removed easily by a few cycles of Ar sputtering. Finally Temperature-Programmed desorption spectroscopy (TPD) was carried out to check the cleanliness of the sample, where the sample is dosed with molecular oxygen at room temperature and then heated to high temperature while monitoring desorption products, mostly molecular oxygen and carbon monoxide in the mass spectrometer. If the sample is contaminated with carbon, it will react with atomic oxygen and desorb form the surface as CO at ~800 K. However, if the surface is clean, the atomic oxygen will recombine and desorb as molecular oxygen without any CO desorption. The sample is usually briefly argon ion bombarded and cleaned with oxygen as a part of normal cleaning procedure before carrying out any experiments. Periodically the sample cleanliness is checked by Auger spectroscopy and by oxygen TPD.

2.5 Experimental Techniques, UHV Chambers and Instrumentation

All the surface science experimental techniques are complementary to each other. No single technique can give all the relevant information about a system. Therefore, a number of different surface science techniques are used in combination to explore the surface related phenomena. The theory and the corresponding instrumentation associated with each experimental technique are described in this section.

2.5.1 Temperature Programmed Desorption (TPD)

2.5.1.1 TPD Theory

Temperature-programmed desorption (TPD), also known as thermal desorption spectroscopy (TDS) is a basic surface science technique that records a thermal desorption spectrum by monitoring the partial pressure of desorbing species as a function of temperature. In this technique, a sample, placed in vacuum, is dosed with reactant molecules and then heated in a controlled manner by using a linear heating rate. Then the desorbing species are detected by a mass spectrometer. The temperature at which molecules desorb from a surface depends on the energy with which they are adsorbed, and the intensity of the signal detected by the mass spectrometer is proportional to the rate of desorption of the adsorbate. Desorption is an activated process that has Arrhenius behavior, where the rate constant(k_{des}) of desorption depends on the temperature and is given by:

$$k_{des} = A \, exp\left(\frac{-E_{des}}{RT}\right) \tag{2.3}$$

Where E_{des} is the activation energy for desorption, R is the gas constant, T is the temperature and A is the pre-exponential factor. During a TPD experiment, as the temperature increases the rate of desorption increases. However, because the coverage starts to decrease at the same time, the net result is the appearance of a peak as shown in Figure 2-6. Typically a linear heating rate is used: $T(t) = T_0 + \beta t$, where T is the final temperature, T_0 is the initial temperature, β is the heating rate, and t is time.
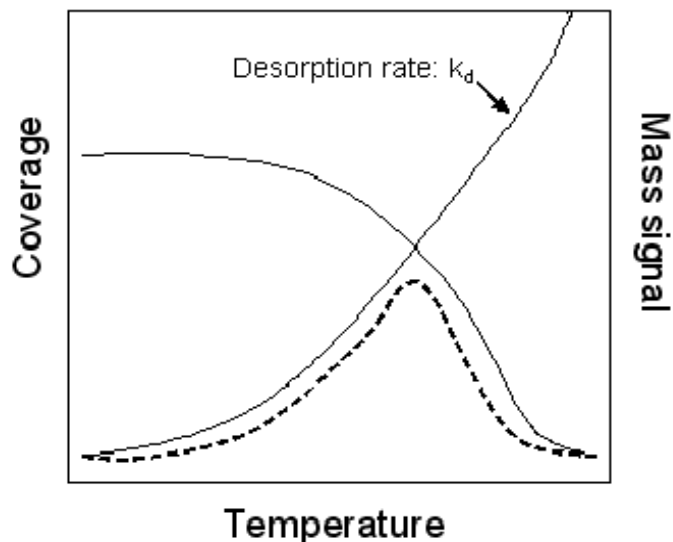
Figure 2-6 Origin of peak features during a TPD experiment

A qualitative TPD profile analysis can be used to gain a lot of information about a surface reaction. For example:

(i)TPD can be used to determine the desorption kinetics of a reaction

The rate of desorption is usually expressed by a rate law of nth order [9]

$$r_{des} = -\frac{d\theta}{dt} = k_{des}\theta^n \tag{2.4}$$

where k_{des} is rate constant for the desorption process, θ is the adsorbate coverage and n is the kinetic order of desorption. By substituting the value of k_{des} from equation 2.3 equation 2.4 becomes:

$$r_{des} = -\frac{d\theta}{dt} = A \exp\left(\frac{-E_{des}}{RT}\right)\theta^n \tag{2.5}$$

which is known as Polanyi-Wigner equation. When the heating rate (β) is constant, a relationship can be derived for the desorption rate as a function of temperature $(\frac{d\theta}{dT})$ which is described in the following. As described above, typically a linear heating rate is used which is given by,

$$T = T_0 + \beta t \tag{2.6}$$

Taking the first derivative we get,

$$\frac{dT}{dt} = \beta \;\Rightarrow\; \frac{dt}{dT} = \frac{1}{\beta} \tag{2.7}$$

The desorption rate as a function of temperature ($\frac{d\theta}{dT}$) be written as,

$$\frac{d\theta}{dT} = \frac{d\theta}{dt}\frac{dt}{dT} \tag{2.8}$$

Substituting the value of $\frac{dt}{dT}$ from equation 2.7 we get,

$$\frac{d\theta}{dT} = \frac{1}{\beta}\frac{d\theta}{dt} \tag{2.9}$$

Using the value of $\frac{d\theta}{dt}$ from equation 2.5 the above expression becomes,

$$\frac{d\theta}{dT} = \frac{1}{\beta}\, A \exp\left(\frac{-E_{des}}{RT}\right)\theta^n \tag{2.10}$$

At the maximum peak temperature (when $T = Tp$) the derivative of the rate of

desorption($\frac{d\theta}{dt}$) becomes zero and the equation 2.10 can be solved assuming that E_{des} is

independent of coverage, i.e.

$$\frac{d^2\theta}{dt^2} = 0 \;\; when \; T = Tp$$

As a result,

$$\frac{d^2\theta}{dT^2} = 0 \; when \; T = Tp$$
$$\Rightarrow \frac{d^2\theta}{dT^2} = n\theta^{n-1}\frac{d\theta}{dT} + \theta^n\frac{E_{des}}{RT_p^2} = 0 \tag{2.11}$$

Inserting the values of $\frac{d\theta}{dT}$ from equation 2.10 the above expression becomes:

$$n\theta^{n-1}\frac{1}{\beta}\, A \exp\left(\frac{-E_{des}}{RT}\right)\theta^n + \theta^n\frac{E_{des}}{RT_p^2} = 0 \tag{2.12}$$

Solving the above equation for $\frac{E_{des}}{RT_p^2}$ we get,

$$\frac{E_{des}}{RT_p^2} = \frac{1}{\beta} A \exp\left(\frac{-E_{des}}{RT}\right) n\theta^{n-1} \tag{2.13}$$

For a first order reaction (n=1) the above equation becomes:

$$\frac{E_{des}}{RT_p^2} = \frac{1}{\beta} A \exp\left(\frac{-E_{des}}{RT}\right) \tag{2.14}$$

which implies that for a first order process, T_p is independent of the coverage, while a second order process depends on coverage and T_p decreases with increase in coverage. If lateral interactions between the adsorbates are ignored, for a second-order desorption process the peak shape is nearly symmetric, while first-order desorption peak shapes are asymmetric. Thus the peak shape gives information about the reaction order of the desorption process. The pre-exponential factor has the units of frequency, and is given by:

$$A = \frac{kT}{\hbar} \left(\frac{Z^t}{Z_{in}}\right) \tag{2.15}$$

where $\hbar$ is plank's constant over 2π, and Z^t and Z_{in} are the partition functions of the initial and transition state respectively. If the two partition functions are equal, for example molecules desorb directly from their adsorption site, then A is in the order of molecular vibrational frequencies, $\sim 10^{13}$ s^{-1}. If the partition functions are different, e.g. mobile adsorbates diffuse on the surface, A can be significantly different, in this example smaller.

Also, the peak temperature gives information about the nature of bonding of the adsorbates to the sample. The peak at lower temperature corresponds to weakly bound species and the peak at higher temperature corresponds to strongly bound species to the surface.

(ii) Calculating Activation Energy of Desorption

In 1962, Redhead derived a relationship between desorption activation energy (E_{des}) and T_p by assuming that A and E_{des} is independent of coverage and the desorption kinetics are first order. The Redhead equation[10] is given by,

$$E_{des} = RT_p \left[ln \left(\frac{AT_p}{\beta} \right) - 3.64 \right]$$

(2.16)

This equation is widely used in surface science to calculate the heat of desorption of the adsorbates by knowing the heating rate, pre-exponential factor and peak temperature. For a given heating rate, the peak temperature can be obtained from a TPD spectrum and it is usually assumed that the magnitude of A is in the order of molecular vibrational frequencies $\sim 10^{13} \text{ s}^{-1}$.

(iii) Relative Coverage Measurement from TPD profile

The integrated area under any desorption profile is proportional to the amount originally adsorbed, thus it can be used to determine relative coverages of an adsorbate.

(iv) Decomposition Mechanism and Reaction products

TPD may also be used to determine the decomposition mechanisms and reaction products, by sequentially monitoring several masses. Since mass spectrometric detection is used, the sensitivity of the technique is good with attainable detection limits below 0.1% of a monolayer of the adsorbate.

2.5.1.2   TPD Chamber

TPD experiments are carried out in the TPD chamber as described below. This system consists of a 12-inch diameter bell jar chamber, pumped by a combination of a mechanical pump, turbomolecular pump and an ion pump (250 L/s). The system achieves a base pressure is $\sim 1 \times 10^{-10}$ Torr following bake out. The chamber is equipped with a

quadruple mass spectrometer for TPD experiments, a double-pass cylindrical mirror analyzer with a built in electron gun for Auger spectroscopy analysis, a X-ray source for X-ray photoelectron spectroscopy, an ion gun for argon sputtering, respective sources for sample dosing (leak valves and Knudsen source) and preparation and an ion gauge for measuring the background pressure of the chamber. Gases are introduced into the chamber by a gas handling line through leak valves. There are three leak valves attached to the chamber, two leak valves are used for backfilling the chamber and the other one has a direct dosing tube attached to it. While dosing reactants through a dosing tube, the sample position is adjusted such that the dosing tube is directly pointed towards it which helps to keep the background pressure low. It has been observed that the dosing tubes enhance the dosing rate by a factor of ~10 or higher in comparison to background dosing. Therefore reactant gases which pump slowly from the UHV chamber are generally introduced through a dosing tube, while for introducing gases such as oxygen and argon for sample cleaning, backfilling is used. A Knudsen source is also attached to the chamber for dosing compounds with very low or high vapor pressure.

A Kurt J. Lesker XYZ precision sample manipulator is used in this system. The manipulator can be moved in X, Y and Z directions and also can be rotated through 360° around the Z axis. A Pd (111) single crystal is mounted on a rotatable feedthrough attached to the manipulator. A cooling system is attached to the manipulator so that the sample can be cooled to ~80 K by contact with a liquid-nitrogen filled reservoir. Sample can be cooled by pumping liquid-nitrogen from a Dewar by a mechanical pump through a capillary tube which is attached to the sample manipulator. The sample is isolated from the ground and can be heated resistively through tantalum mounting wires attached to a

DC power supply. The temperature of the sample is measured by a K-type thermocouple junction spot-welded either to the side or to the back of the sample.

(a)

(b)

(c)
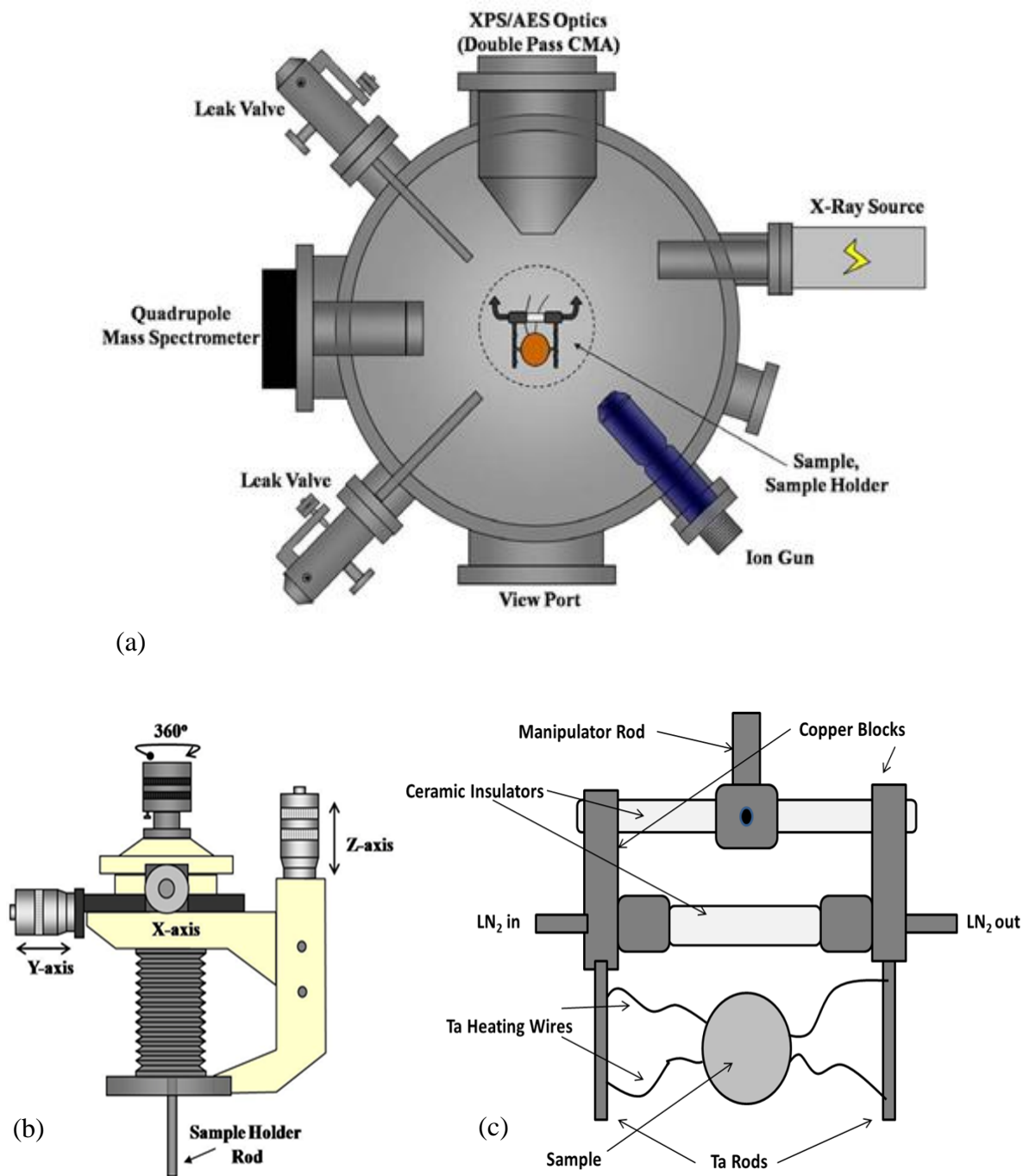
Figure 2-7 (a) Schematics of the TPD-XPS chamber [2] (b) XYZ precision manipulator [2] (c) Sample mounting

2.5.1.3   Instrumentation for the TPD Experiments

A Dycor model M100M is used for the TPD experiments. During TPD data collection the sample (front face) is placed very close to the mass spectrometer. Data collection was controlled by a PC with a data acquisition card by using a Lab View program. The linear heating rate was controlled by using a proportional-integral-derivative (PID) control script in Lab View. The computer collects the temperature readings (in millivolts) from the thermocouple attached to the sample, which passes through a pre-amplifier gain of 100, and collects the intensity of various masses from the control electronics of the mass spectrometer. The Lab View script combines temperature and mass information into one file which can be imported to Origin7 as an ASCII file where the X column is temperature (in millivolts) and the 5 different masses are collected in five different Y columns. The temperature in millivolt is converted to Kelvin by using a script written in Lab View.

2.5.2   X-ray Photoelectron Spectroscopy (XPS)

2.5.2.1   XPS Theory

X-ray photoelectron Spectroscopy (XPS) is a surface sensitive technique developed in the mid-1960s by K. Siegbahn. In 1981 he was awarded the Nobel Prize in Physics for this work. XPS is based on the concept of photoelectric effect which implies that photons can induce electron emission from a solid when their energy (hv) is greater that the work function (φ) of the metal. In XPS a monochromatic beam of X-rays generates photons of energy hv, which are directed towards the solid target. Photons are absorbed by electrons of binding energy E_b below the vacuum level and then emerge from the solid with a kinetic energy(E_k) which is given by:

$$E_k = hv - E_b - \varphi \tag{2.17}$$

MgKα (hv = 1253.6 eV) and AlKα (hv = 1486.6 eV) are usually the X-ray radiation

sources of choice.

Each element has a set of characteristic binding energies associated with each

core atomic orbital; therefore each element has a unique XP spectrum. Therefore XPS is

often used for elemental analysis and is also referred as Electron Spectroscopy for

Chemical Analysis (ESCA). The intensity of the peaks is related to the concentration of

the element in the sampled region. Thus, this technique also provides a quantitative

analysis of the surface composition.
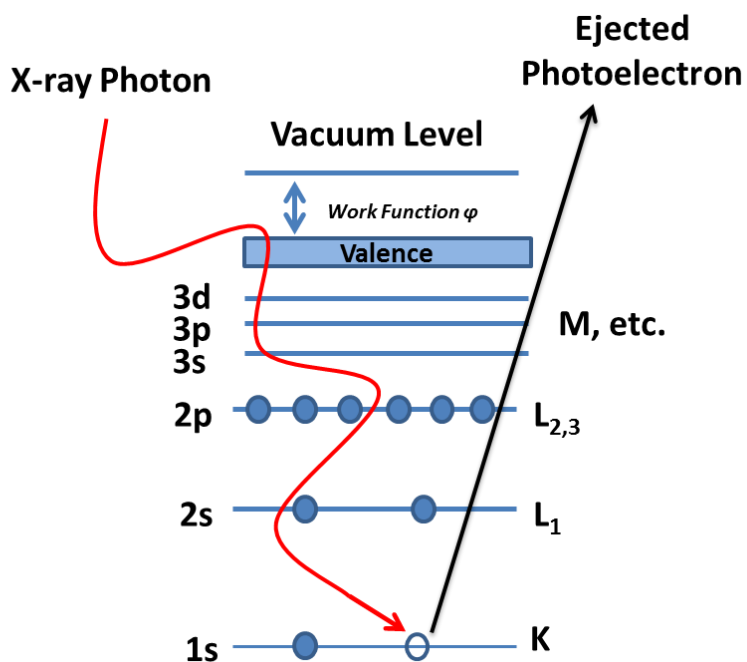
Figure 2-8 X-ray excitation of a 1s core electron

XPS is a very surface sensitive technique since the detected signals are

predominately due to atoms in the surface region. Although XPS is not completely

surface specific but most of the signals detected comes from within a few atomic layers of the surface and a very small part of the signal comes from deeper into the solid because of the short inelastic mean-free path (IMFP) of the electrons in the solid. The IMFP is a measure of the average distance (*d*) travelled by an electron through a solid before it is in elastically scattered.[11] It mostly depends on the initial kinetic energy of the electron and weakly depend on the nature of the solid (Most solids have similar IMFP). IMFP is defined by the following equation which gives the probability of the electron travelling a distance *d* through the solid without undergoing scattering.

$$p(d) = e^{\frac{-d}{\lambda}} \tag{2.18}$$

where λ is the IMFP for the electron of energy E.
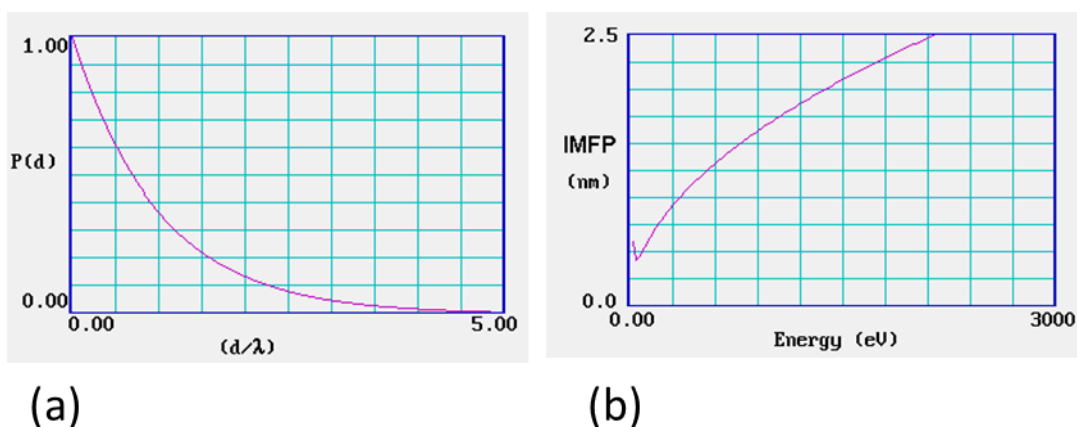
Figure 2-9 (a) the universal plot of *d/λ* vs *P(d)* and (b) the universal curve for the variation of IMFP with the initial electron energy [11]

Figure 2-9 (a) shows the universal plot of *d/λ* vs *P (d)*. From the graph it is clear that the probability of escape of electrons decays rapidly and it is close to zero when d/λ >~3. Therefore the majority of the electrons detected in XPS come from *d=1λ* and 95% of all the signals arises within *d=3λ* and (b) is the universal curve for the variation of IMFP with the initial electron energy. From the graph it is clear that the IMFP (λ) varies

between 1 to 2 nm for AlKα and MgKα radiation. Therefore in XPS signals are detected within 2 to 6 nm below a surface (few atomic layers), thus XPS is considered to be a surface-sensitive technique.

The exact binding energy of a core electron of an atom depends not only on the electronic level from which the photoemission is occurring, but also upon the formal oxidation state of the atom and the local physical and chemical environment. Any changes in these parameters give rise to small shifts in the binding energy in the spectrum which is called "chemical shifts". Atoms of higher oxidation state exhibits higher binding energy due to the extra coulombic interaction between the photo-emitted electron and the nucleus. The ability to discriminate between different oxidation states and chemical environment is one of the major strengths of XPS technique.

2.5.2.2 XPS Chamber

All the XPS spectra were obtained in the TPD chamber (Figure2-7) which is instrumented for both TPD and XPS experiments.

2.5.2.3 Instrumentation for XPS

The chamber is equipped with a Specs XRC 1000 X-ray source. X-rays are generated using an electron impinging on a magnesium anode (MgKα, hν=1253.7 eV) or aluminum anode (AlKα, hν=1486.6 eV), which emits soft X-rays. X-rays are directed at the sample, and the resulting photoelectrons were detected by a PHI15-255G double-pass cylindrical-mirror analyzer (CMA). The X-ray source and the CMA are mounted at an angle of ~ 90° to each other. Therefore during XP spectra acquisition, the sample is positioned such that it is roughly in an angle of 45° to each of them and the final refinement is done by adjusting the sample position to get maximum signal intensity.

Data were collected by a PC with a data acquisition card running Physical Electronics software. XP spectra were processed by XPS peak fit program for background subtraction.

2.5.3 Auger electron Spectroscopy (AES)

2.5.3.1 Auger Theory

Auger electron spectroscopy (AES) is a surface-specific technique which was developed in the late 1960's by Pierre Auger [12] who first observed this effect in 1920's. It is a surface specific technique which utilizes the emission of low energy electrons by the Auger process. The principle of operation of Auger spectroscopy involves three basic steps:

(i) Atomic ionization by removal of a core electron:

The sample is exposed to a beam of high-energy electrons (typically in the range of 2-10 keV), which have sufficient energy to ionize an atom by removing a core-state electron. In the diagram below ionization is shown to occur by removal of a K-shell electron.

(ii) Relaxation and electron emission by Auger process:

The ionized atom after the removal of the core electron remains in a highly excited state. To relax to a lower-energy state, one electron transition occurs from a higher energy state (E_{L_1}) to fill the initial core hole in the K-shell. The transition energy is released either by emitting a photon giving rise to X-ray fluorescence or the energy is simultaneously transferred to a second electron (Auger electron); a fraction of this energy is required to overcome the binding energy of the second electron, the remainder is retained by this emitted Auger electron as kinetic energy which is given by:

$$E_{KIN} = E_k - E_{L_1} - E_{L_{2,3}} - e\varphi \qquad (2.19)$$

The Auger electron kinetic energy is dependent on the binding energy of electrons and not on the incident beam energy. Therefore this technique is very sensitive to chemical composition analysis.

(iii)Analysis of the emitted Auger electrons:

The emitted Auger electrons pass through a CMA and are detected by a channeltron detector. The Auger signals are recorded by a computer as signal intensity *vs* KE. To gain a better sensitivity for detection and to remove the broad background, Auger spectra are also often shown in a differentiated form.
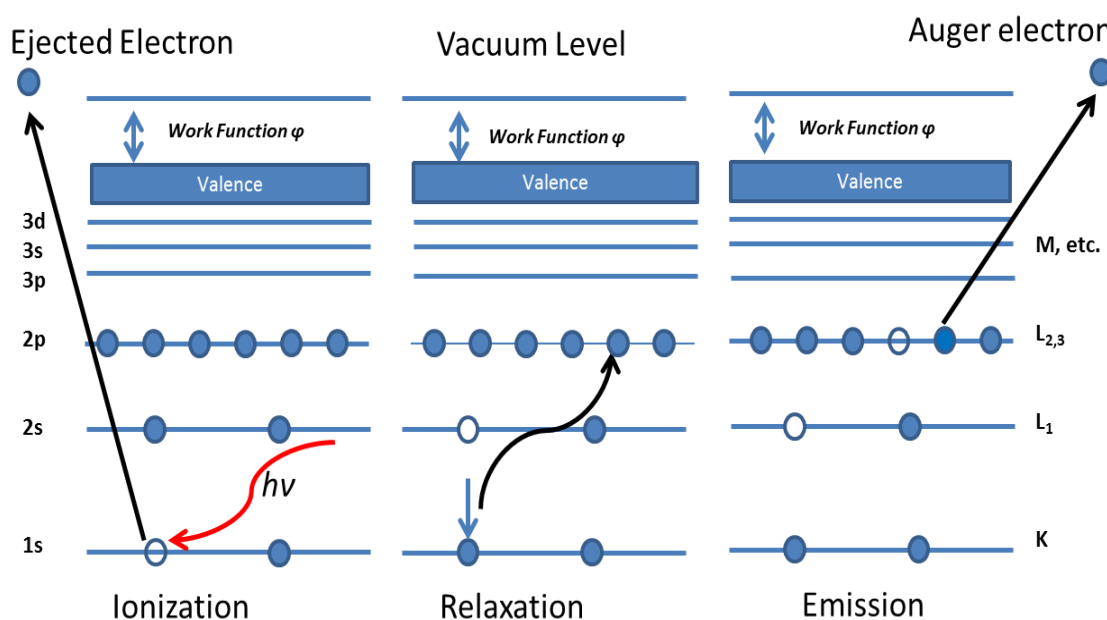
Figure 2-10 Energetics of the Auger process for a $KL_1L_{2,3}$ transition

Auger electron spectroscopy has become a widely used surface spectroscopic technique for elemental analysis of surfaces (within few atomic layers) because of its high sensitivity (typically 1%) for all elements except H and He. Auger spectroscopy is also used to monitor the surface cleanliness of the samples.

2.5.3.2 Auger Instrumentation

All the chambers in our laboratory are equipped with instruments for Auger spectroscopy. The experimental set up consisted of a CMA, either single or double passed, both equipped with a coaxial electron gun. Data acquisition was controlled by a PC running Physical Electronics software and interfaced with a PHI 11-010 electron gun and an 11-500A Auger control, as well as a lock-in amplifier and high voltage power.

2.5.4 Reflection Absorption Infrared Spectroscopy (RAIRS)

2.5.4.1 RAIRS Theory

Vibrational spectroscopy is a very powerful tool for identifying the bonding and orientation of surface species upon molecular adsorption and the species generated during a surface reaction.[13-15] Reflection absorption infrared spectroscopy is widely used for vibrational studies on surfaces having low surface areas (e.g. single crystals). In this technique, an IR beam exits from the IR generating source and is then focused onto a reflective metallic surface. Then the beam reflects off the crystal surface and is collected by a detector. In the gas phase, IR absorption is based on the interaction between the electric field of the incoming IR beam and the dipole moment of the molecules but on metal surfaces the process is dominated by the dielectric behavior of the metal. The theory of reflection at metal surface was developed by Greenler in 1966.[16] In this theory, the importance of surface selection rule is demonstrated and also it has been shown that the best sensitivity for IR measurement on metallic surface is obtained using a grazing-incident reflection of the IR light.

When a molecule with a dynamic dipole moment is adsorbed on a metal surface, it induces an image charge in the metal which is equal in magnitude but opposite in

direction to the real dipole of the metal. If the vibration due to the adsorbed molecule is parallel to the surface then the image dipole and the molecular dipole cancel and there is no net dipole. However, if the vibration is perpendicular to the surface, then the image dipole and the molecular dipole is additive and the net dipole is greater than the molecular dipole which gives rise to infrared absorption.
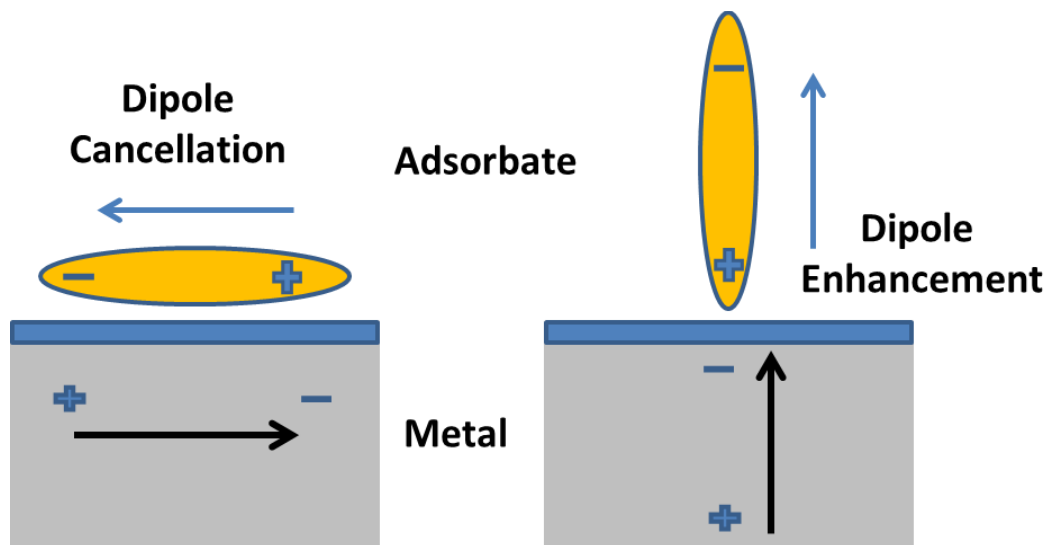
Figure 2-11 The effect of orientation of a dipole on a conducting surface in the creation of an image dipole

The origin of surface selection rule is due to this image-dipole effect. According to the selection rule the vibrations which are perpendicular to the surface (*p*-polarized light) are infrared active while the vibrations which are parallel to the surface (*s*-polarized) are not infrared active.

When an IR beam reflects from a clean metal surface (Figure 2-12), the interaction between the light and the surface is described by the Fresnel equations. The amplitude and phase changes during reflection depend on the direction of the electric field vectors. The electric field vector E is split into two components, one perpendicular to the plane of incidence (*s*-polarized light) and another parallel to the plane of incidence (*p*-polarized light).

Figure 2-12 illustrates the incident and reflected vectors of *s*- and *p*-polarized radiation. The phase between the incident (E_{si}) and reflected (E_{sr}) *s*-polarized light, changes by nearly 180° at all angles of incidence θ, resulting in a destructive interference and a negligible electric field parallel to the surface (E_s). On the other hand, the phase change in the *p*-polarized light generates a constructive interference (E_p) that strongly depends on the incident angle θ. Assuming the absorbance is proportional to the square of the electric field at the surface and to the surface area (number of molecules involved), which increases as $1/\cos\theta$, we can conclude that RAIRS sensitivity is proportional to $E_p^2/\cos\theta$. This function is sharply peaked close to grazing angles, demonstrating the practical requirement of a high angle of incidence.
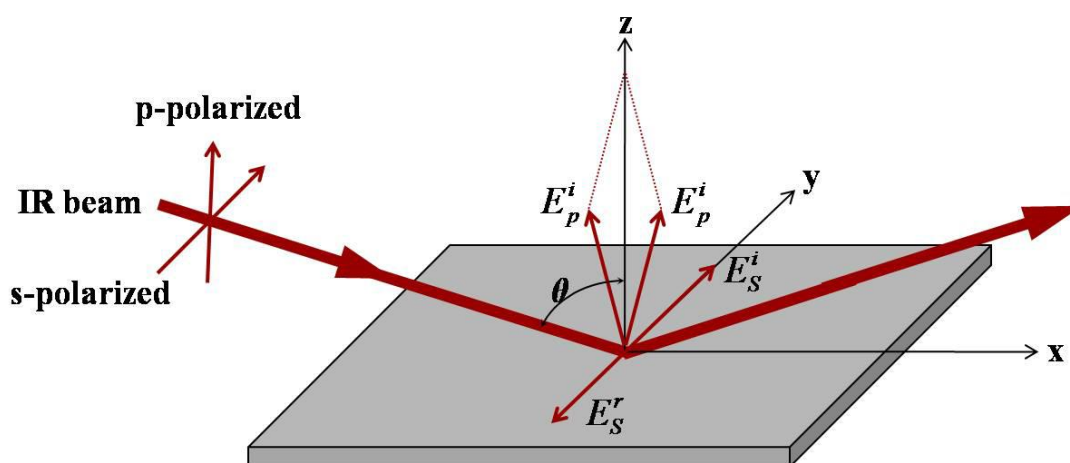
Figure 2-12 The reflection geometry showing the s and p components of the electric fields of incident and reflected radiation

Since this is an optical technique, it can be carried out both in vacuum and ambient conditions. The major problem concerning this spectroscopy is the sensitivity. Typically the sample area is 1cm^2 with less than 10^{15} adsorbed molecules. With modern FT-IR spectrometers, however such small signals (0.01%-2% adsorption) can be recorded at relatively high resolution (1cm^{-1}).

2.5.4.2   RAIRS Chamber

The RAIRS chamber mainly consists of two parts. The main body of the chamber is a 12-inch diameter bell jar, which is pumped by a combination of a mechanical pump, a turbomolecular pump and an ion pump (250 L/s). This part of the chamber is equipped with an ion gun for sample cleaning, a mass spectrometer, and several ports for dosing sources and leak valves, an ion gauge for measuring the background pressure and a single pass CMA. The other part of the chamber mainly consists of an IR cell and a transfer arm which is separated from the main body of the chamber by a gate valve. The IR cell consists of six-way 2 ¾" cube. The sample is mounted on a differentially pumped coaxial manipulator. This manipulator can be moved horizontally and can be rotated 360° along its axis of translation. The sample is usually moved to the main chamber for sample cleaning or performing Auger electron spectroscopy and retracted to the IR cell for infrared analysis. The sample can be cooled to liquid nitrogen temperature in the IR cell. This is achieved by introducing a thin tube into the transfer arm through which liquid nitrogen passes. The sample is connected to the heating wires via insulated feedthroughs. By cooling down the feedthrough (located on the non UHV side) to liquid nitrogen temperatures, the sample can be cooled down. The sample can also be heated resistively to ~1200 K.
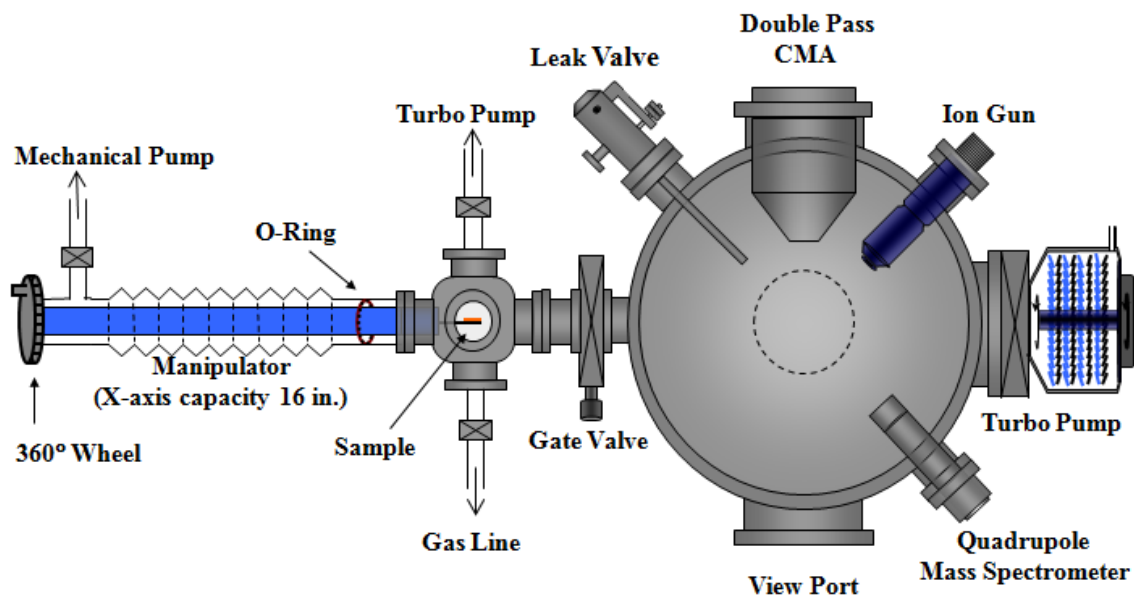
Figure 2-13 Schematic diagram of the RAIRS Chamber [2]

2.5.4.3   RAIRS Instrumentation

The RAIRS chamber is equipped with a commercial Bruker Vertex FT-IR spectrometer. The IR beam exits the spectrometer and is reflected through a series of gold-coated mirrors and then through a polarizer oriented perpendicular to the sample, and finally through a KBr window into the UHV IR cell. The beam is then focused onto the single crystal at a grazing angle and the reflected beam exits the IR cell through a second KBr window. The beam is finally focused onto a liquid-nitrogen cooled mercury-cadmium-telluride (MCT) detector. The entire light path, between the spectrometer and the MCT detector, is enclosed in plexiglass boxes continuously purged with dry air or liquid nitrogen boil off to eliminate the background IR signals due to carbon dioxide and water. Data collection was achieved by a dedicated PC running OPUS software. The same software is used for baseline correction of the original spectra if needed and finally plotted and stacked in Origin 7.0.

2.5.5 Scanning Tunneling Microscopy (STM)

2.5.5.1 STM Theory

Since the invention of Scanning Tunneling Microscopy (STM) by Binning and Rohrer in 1983,[17] it has proved itself as a very powerful imaging technique for surface investigations at atomic scale. STM is based on the concept of quantum tunneling in which an electron can tunnel through a barrier which is classically forbidden. According to classical physics, an electron cannot pass through a barrier if its kinetic energy is smaller than the potential within the barrier, but its quantum nature allows it to be simultaneously on both side of the barrier as a result of the Heisenberg uncertainty principle.
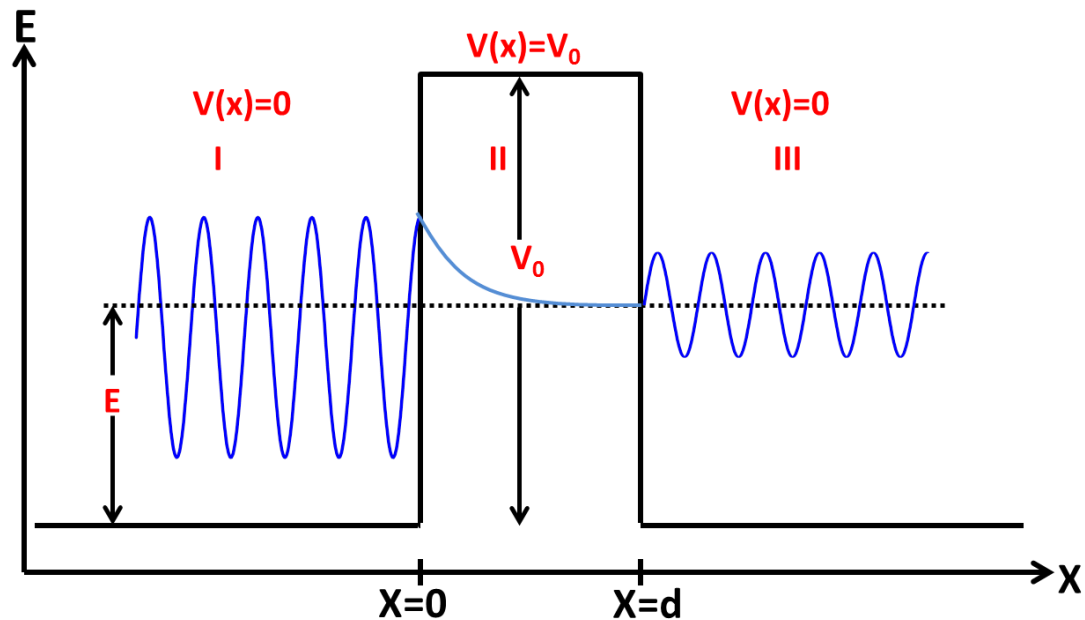
Figure 2-14 Schematic diagram showing tunneling of an electron of energy E through a potential barrier of height V_0 and length d

Figure 2-14 describes the concept for an electron tunneling through a one-dimensional rectangular barrier of width d. If the electron having energy less than the

energy of the potential barrier (V_0) i.e. $E < V_0$, approaches this barrier from left, from classical mechanical point of view, the electron will always be reflected and hence will not penetrate the barrier. However, wave mechanics predicts that the particle has some probability of penetrating through the barrier as shown in the Figure 2-14, $V(x) = 0$ for x < 0 and x > d and $V(x) = V_0$ for 0< x <d.

In quantum mechanics, the electron is described by a wave function ψ(x) that contains all the information of the system and the equation that describes the system is given by Schrodinger's equation:

$$H\psi(x) = E\psi(x) \tag{2.20}$$

where, $H = -\dfrac{h^2}{2m}\dfrac{d^2}{dx^2} + V(x)$. Substituting the value of H, equation 2.20 becomes,

$$\left(-\frac{h^2}{2m}\frac{d^2}{dx^2} + V(x)\right)\psi(x) = E\psi(x) \tag{2.21}$$

$$\Rightarrow \frac{\partial^2\psi(x)}{\partial x^2} + \frac{2m}{\hbar^2}(E - V)\psi(x) = 0 \tag{2.22}$$

The Schrodinger equation for region I (V(x) = 0) is,

$$\frac{\partial^2\psi_1}{\partial x^2} + \frac{2m}{\hbar^2}E(\psi_1) = 0 \tag{2.23}$$

The Schrodinger equation for region II (V(x) = V_0) is

$$\frac{\partial^2\psi_2}{\partial x^2} + \frac{2m}{\hbar^2}(E - V_0)\psi_2 = 0 \tag{2.24}$$

The Schrodinger equation for region III (V(x) = 0) is,

$$\frac{\partial^2\psi_3}{\partial x^2} + \frac{2m}{\hbar^2}E\psi_3 = 0 \tag{2.25}$$

Region I and III are classically allowed region while region II is classically forbidden. The solutions of the Schrodinger's equation in the three regions are given by:

$$\psi_1 = Ae^{ikx} + Be^{-ikx} \tag{2.26}$$

$$\psi_2 = Ce^{Kx} + De^{-Kx} \tag{2.27}$$

$$\psi_3 = Fe^{ikx} + Ge^{-ikx} \tag{2.28}$$

where k is the wave vector for an electron moving in the direction of the vector and its

value is given by $k = \left(\frac{2m(V_0 - E)}{\hbar^2}\right)^{1/2}$ and K is called the decay constant and its value is

given by $K = \left(\frac{2mE}{\hbar^2}\right)^{1/2}$. The coefficients A, B, C, D, F, G are constants and can be

determined from the boundary conditions and the requirements that the wave functions

and its derivative are continuous at x = 0 and x = d. In the classically forbidden region as

given in equation 2.27, if the solution is positive, that would represent an exponential

increase in probability with increase in distance whereas the negative solution represents

an exponential decay of the wave function with distance which makes physical sense and

is an acceptable solution for the classically forbidden region.

$$\psi_2 = De^{-Kx} \tag{2.29}$$

The square of the wave function represents the probability of finding the electron on the

other side of the barrier (x=d) or the probability of tunneling through the barrier and is

given by:

$$P = \psi_2{}^2 = D^2 e^{-2Kd} \tag{2.30}$$

This demonstrates that the probability of tunneling through the barrier decays

exponentially with the width of the barrier.

As shown in Figure 2-14, in STM a similar model can be applied to describe the

STM tunnel junction where electrons flow (tunnel) between two conductive materials (tip

and surface) through a vacuum barrier but in the case of STM, an electric field is applied

(bias voltage) to reduce the barrier.[18] In this technique, a sharp metallic tip is brought

very close (in the order of few Angstroms) to a conductive surface and a small bias is

applied between to the tip sample junction. The overlap of the electron wave functions

permits quantum mechanical tunneling and a current (I) will flow across the gap which is

proportional to the tunneling probability.

$$I \propto |\psi(z)|^2 = [\psi(0)]^2 e^{-2Kd} \qquad (2.31)$$

Here the barrier height is the order of the work function of the tip or the sample

and the barrier width corresponds to the tip-sample distance, Φ is the work function of

the tip material, e is the charge of the electron and V_b is the bias voltage placed between

the tip and the sample. If it is assumed that the work function of the tip and the sample

material are similar and the energy of the electrons are sufficiently small in comparison to

the work function of the tip material ($eV_b < \Phi$), then the above equation is still valid for

the system and a similar model can be applied to describe STM. In this case the value of

decay constant is given by, $K = \left(\frac{2m\Phi}{\hbar^2}\right)^{1/2}$. For a work function of ~5 eV, (a typical

metal) $K = 1.0$ Å^{-1} and the current decreases by an order of magnitude when the gap d

increases by 1Å. This effect provides the basis for the STM and the cause of its

remarkable vertical resolution.

There are two basic modes used in the scanning process, namely constant-current

or constant-height modes. In the constant current mode of operation, first the tip is

brought close to the surface so that at a convenient voltage (between 2 mV to 2 V) the

tunneling current is measurable. The current flow is fixed and a feedback system moves

the tip in Z direction up or down to maintain constant current while the tip is rastered

across the surface. In other words, to maintain a constant current, the feedback system

moves the tip up or down in the Z-direction by keeping the separation between tip and the

sample almost constant and therefore follows the topography of the surface. The applied

bias voltage determines the number of electronic state from which electron can tunnel i.e.

the larger the bias the more number of electrons can tunnel. The polarity of the bias

determines the direction of the flow of electron. When the tip is positively biased with

respect to the sample, electrons tunnel from the occupied states of the sample surface to

the unoccupied states of the tip, and with negative bias the electrons tunnel from the

occupied states of the tip to the unoccupied states of the sample surface. For metallic

systems the polarity of the bias voltage may not have a significant influence on the

resulting image, but for systems that contains organic molecules, a significant

dependence on the bias polarity and magnitude is often observed.[19]

Alternatively, in the constant-height mode of operation, the tip is scanned across

the surface at constant height and voltage while the current is measured. Generally

constant-current mode is highly used for STM data acquisition because with constant

height mode of operation it is possible that, when scanning on an uneven surface, the tip

will be damaged as a result of contact between the tip and sample.

2.5.5.2 STM CHAMBER

STM system mainly consists of a series of four aligned vacuum chambers

connected by two transfer arms. All chambers are separated from each other by gate

valves. In the Figure 2-15 from right to left these are: 1: load lock chamber for the first

entry of sample and tip in and out of the chamber, 2: SPM chamber housing the

microscope, 3: preparation chamber for sample and tip cleaning and also for

characterization of sample surface, 4: high pressure cell for carrying out reactions that

needs high pressure of reactants. The whole system is pumped by two turbomolecular pumps and two ion pumps. The turbomolecular pumps are attached to the high-pressure cell and to the load-lock chamber. The ion pumps are attached to the preparation chamber and the SPM chamber. During the initial pump down from atmosphere, the whole system is pumped by the turbo pumps, followed by ion pumps. During normal operation (while collecting STM images), the turbo pumps are turned off, since they induce vibrations in the system. Ion pumps pump on the main chambers during imaging since they are vibration free.
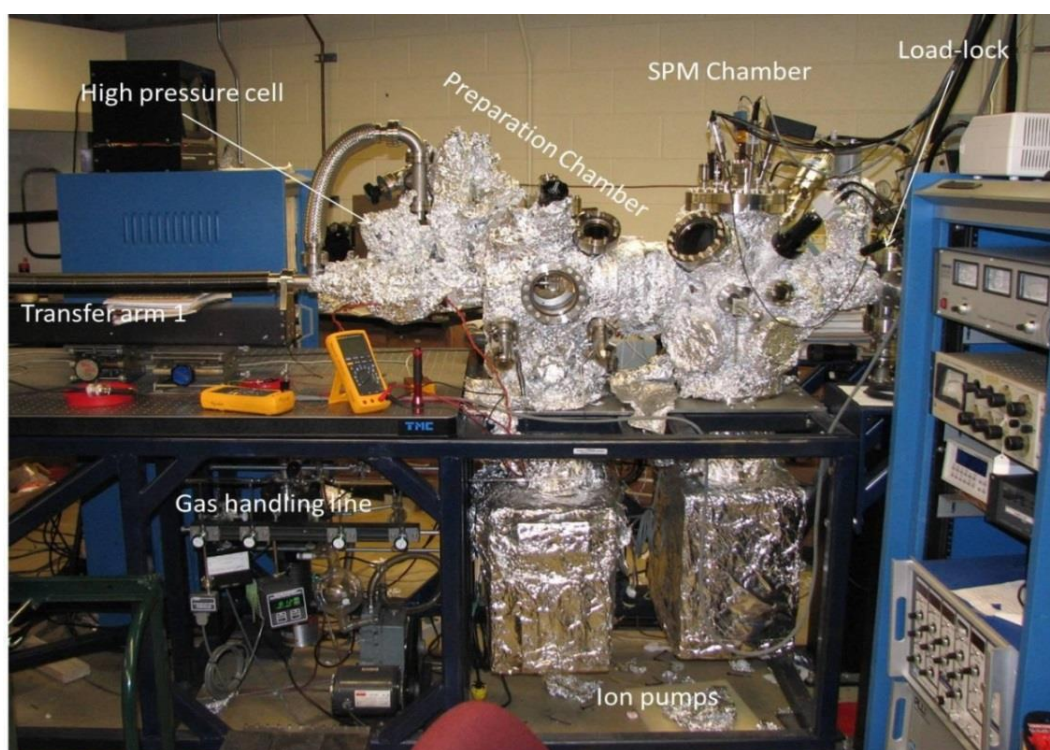
Figure 2-15 Front view Photograph of the vacuum system showing the four aligned chambers in the order: load lock chamber, SPM chamber, preparation chamber and high pressure cell [19]

(1) Load-lock Chamber

The load-lock chamber allows the transfer of samples and tips from and into the SPM chamber without breaking vacuum in other three chambers. The transfer arm

connects the load-lock chamber to the SPM chamber. The load lock chamber has a door

that seals with Viton gasket so can be opened and closed easily. The sample holder or tip

holder is inserted in the fork of the transfer arm and the system is pumped down by the

turbomolecular pump. After this process, the gate valve between the load lock chamber

and the SPM chamber is opened to transfer the sample or tip holder to the SPM chamber.

(2) SPM chamber

The main body of the SPM chamber is a 12-inch-diameter vertical cylinder. This

chamber is fitted with a sample stage, a scanning tunneling microscope aligned vertically

with the sample stage. There are a total number of 6 storage shelves available, 3 of which

are for storing sample holders and the other three are for storing tip exchangers. One of

the ports (from the front side of the chamber) is fitted with a wobble stick, which is used

to move the sample holder or tip exchanger from the sample stage to the shelves or

shelves to the transfer arms, or vice versa. This chamber is also fitted with a leak valve

and a Knudsen source with dosing tubes which are pointed directly towards the sample

stage, so that the sample can be dosed without contaminating the rest of the chamber.

(3) Preparation Chamber

The main body of the preparation chamber is a ~12 inch diameter vertical

cylinder. This part of the system is equipped with a LEED system, an ion gun for sample

and tip cleaning, a mass spectrometer for checking the purity of gases introduced into the

system and two leak valves for introducing gases into the vacuum chamber through a gas

handling manifold. Sample and tip cleaning, annealing etc. are carried out in the

preparation chamber while the gate valve to the SPM chamber is closed so that the SPM

chamber remains clean during the process. The system is pumped by an ion pump during

normal operation and during sample or tip cleaning the chamber is pumped by the turbomolecular pump attached to the high-pressure cell.

(4) High Pressure Cell

The main body of the high-pressure cell is a 2.5 inch diameter stain less still with several ports attached to it. There is a view port and a turbo pump attached to this chamber. One port connects the chamber to the transfer arm which can be rotated 360° and can be moved to the preparation chamber and the SPM chamber for transferring the sample holder and tip holder from one chamber to the other. The end of the transfer arm is designed such that the sample and tip holders can be placed there and it has all the electrical connections for sample heating and temperature measurement.

2.5.5.3 STM Instrumentation

Figure 2-16 presents greatly simplified schematics of the STM instrumentation, where a sharp metallic tip is brought very close a metallic surface and a small bias voltage is placed between them, and a tunneling current is measured. The tip is mounted on the STM scan head which is equipped with piezoelectric material which can either expand or contract upon applying a voltage. The STM tip moves up or down (by help of the piezo electric material) in the response to the feedback electronics to maintain a constant tunneling current. The tunneling current is amplified by a current pre-amp and then recorded by a PC as a STM image which is current *vs* height map of a surface. All the STM images in this thesis are collected by using a RHK STM microscope. The section below presents some of the details of the STM instrumentation associated with the imaging
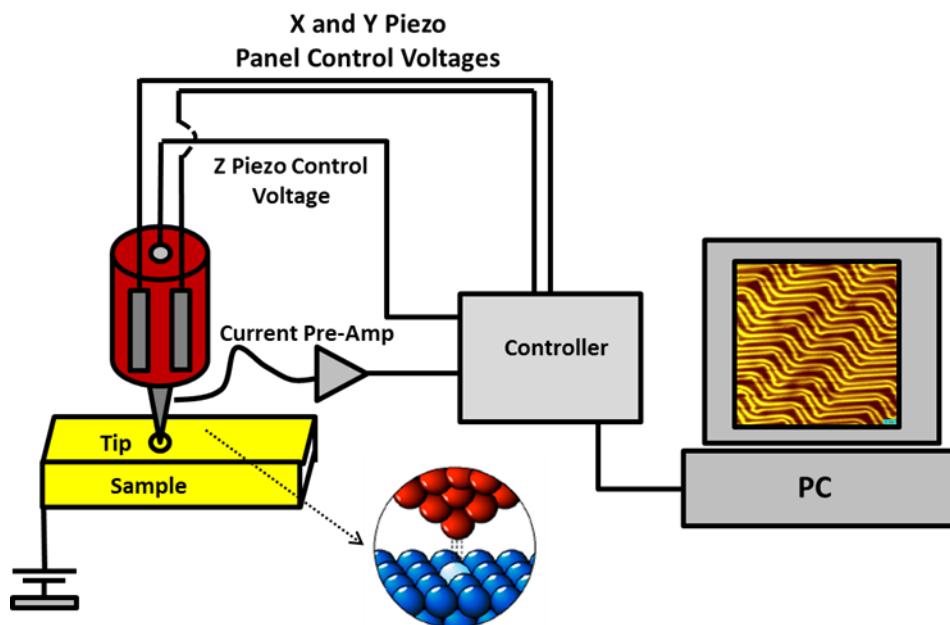
Figure 2-16 A simplified diagram showing instrumentation of STM; a bias voltage is placed between the tip and the sample, a tunneling current is measured, amplified and feedback electronics moves the tip up and down to maintain a constant current

(1) Sample Holder

Figure 2-17 shows the sample holder designed by RHK technology. The sample is mounted at the center of the holder and is sandwiched between two sapphire washers to hold it in place and to keep it isolated from the rest of the assembly so that it can be heated to very high temperature without heating the sample holder. The sample holder has a built in thermocouple to measure the sample temperature and a heating filament. The two leads of the thermocouple and heating filaments protrude from one side of the sample holder. These connections met with a pair of contacts on the sample stage or the transfer arm. The sample can be heated to high temperatures by electron beam heating. If the temperature requirement is low, the sample is heated by just radiative heating from a hot filament without applying any bias voltage. The upper part of the main body of the

holder has three ramps where the piezo legs of the scan head rest and walk down in order

to perform the coarse approach between tip and sample.

ITEM	DESCRIPTION
1	#2-56 x 1/4" SS AU SOCKET HEAD CAP SCREW
2	#2 SS AU BELLEVILLE SPRING WASHER
3	#0-80 X 1/8" SS AU FLAT HEAD SCREW
4	CONTACT (0.020 MOLY WIRE)
5	HEATER ASS'Y
6	0.020" K THERMOCOUPLE
7	0.005" K THERMOCOUPLE
8	SAMPLE HOLDER BODY
9	LEAF SPRING
10	TOP RAMP
11	MOLY WASHER SET
12	HAT SHAPED SAMPLE
13	WASHER
14	CAP
15	INSULATOR
16	COMPRESSION SPRING 0.078x0.14x0.25
17	TC HOLDER PART 2
18	TC HOLDER PART 1
19	SAPPHIRE WASHER

Figure 2-17 Description of the STM sample holder parts (Image reproduced with permission from the RHK Technology Inc ©)

(2) STM Scan Head

Figure 2-18 shows a diagram of RHK STM head. All the necessary electrical

connections are applied to it through flexible wires which are attached to the top portion

of the scan head. There are three piezo legs mounted on the bottom part of the scan head

and the feet of the legs are simple glass balls. There is a fourth piezo tube in the center in

which the STM tip is mounted. The course motions of the tip (during tip approach and

retract and movement in X or Y direction) are controlled by the concerted motions of the

three piezo legs and the actual scanning is performed by the central piezo, which is

controlled independently of the legs. During tip approach to the sample, first the scan

head is lowered such that it rests on top of the ramp of the sample holder. The next

approach step is controlled by the RHK software where it directs the STM control unit to

supply a wave form to the piezo legs which moves the head down the ramp by stick-slip

motion until a tunneling current is measured. Once the tip has approached successfully,

scanning is performed with the central Z piezo while the other three piezo legs are

stationary.
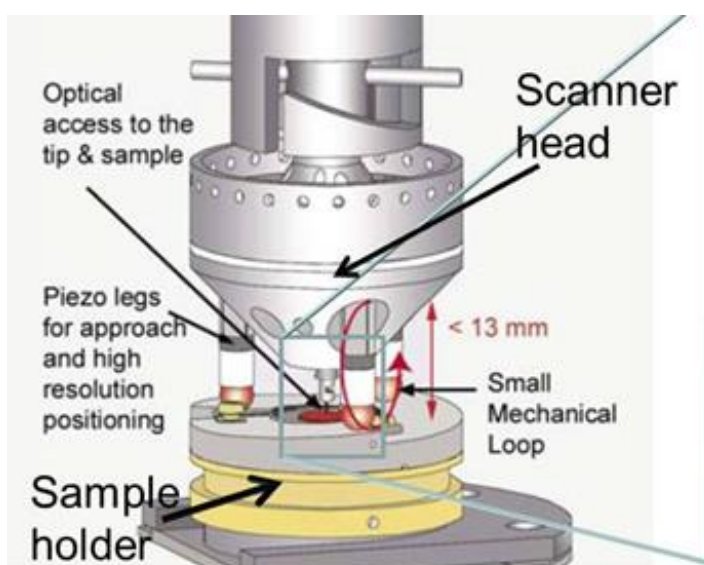
Figure 2-18 STM scan head sitting on top of sample holder, the three Piezo legs sit on the ramps of the sample holder and scanning is performed with the central piezo. (Image reproduced with permission from the RHK Technology Inc.)

Obtaining good quality STM images can be difficult and mainly requires a system

which is free from any external vibrations. The tunneling current measured in STM is

usually in the order of picoamps so that it is very important to reduce all the possible

external vibrations of the system. A noise level of less than 5 pA is required for collecting

STM images. The section below describes the methods we have used for maintaining the STM system relatively vibration free.

(3) Vibration Isolation

The vibration isolation is acquired in three stages. First, the entire frame that supports the vacuum chamber is made from very heavy steel material to provide inertial mass to the system in order to reduce any external vibrations; the frame and the vacuum chambers together weight about half a ton. Second, the frame is suspended on the pneumatic air legs during scanning to get rid of any floor vibrations. The STM chamber is also located in the basement for the same reason. The liquid-nitrogen Dewar which is used during scanning at low temperatures is also mounted to the frame so that every part of the system is isolated during scanning. Finally the sample stage is suspended on springs with an additional Eddy-current damping system, which contributes to the vibration isolation of the sample-head assembly inside the SPM chamber. In addition, all the mechanical pumps and turbo pumps are turned off during imaging and the system is only pumped by the ion pumps which are quiet and vibration free. All the necessary electrical connections are made through flexible wires.

In addition to vibration isolation, another requirement and perhaps the most important need for collecting good quality STM images is a stable and sharp STM tip. The section below describes some of the methods we have used for tip preparation and tip conditioning.

2.6   STM Tip Preparation and Conditioning

One of the outstanding features of STM is its unique spatial resolution at the atomic scale. However, the limiting factor for obtaining good spatial resolution depends

on the dimensions of the probe (tip). Due to the exponential dependence of the tunneling current verses distance, essentially the only electrons at the few topmost atoms of the apex contribute to tunneling; an ideal STM tip has a single atom at the apex. However, it is possible to achieve atomic resolution with tips which have radii of apex curvature of 10 to 20 nm. In this section, a brief overview of the tip preparation and conditioning methods are presented.

All the STM images in this thesis are collected using tungsten tips prepared by etching in our laboratory. Tungsten single crystal wires are ideal for making tips because of its stability, but it is very expensive. The tips made of polycrystalline tungsten wires can work well but often those tips suffer from instability during imaging. Therefore instead of using polycrystalline wires we have used a method by which the polycrystalline wires can be crystallized. The method of making recrystallization of polycrystalline wires are described below.

2.6.1 Tungsten recrystallization process

The concept of recrystallization process used is based on the concept of heating a wire in vacuum under tension, which cause the wire to become more crystalline.[3, 19-20] For the recrystallization process a small vacuum chamber pumped by a turbo molecular pump is used. A high-current feedthrough is mounted to the top flange of the chamber. Polycrystalline tungsten wire of 0.25mm in diameter is looped through a 2 kg weight and the two ends of the wires are wrapped around the ends of the copper feedthroughs. The whole assembly is placed inside the chamber and the resistances between the two leads of the feedthrough, and to the ground were measured to ensure that neither the tungsten wire nor the weights were touching the chamber. The chamber was pumped down to ~10^{-8}

Torr following which the tungsten wire was heated gradually by connecting the leads of the feed through to a variable AC transformer. In first step, heat is applied such that the wire glows a dull red color which is estimated to be 1000 K. This temperature is maintained for 30 to 40 minutes so that the wire is well degassed. Next the temperature is increases such that the wire glows a bright yellow color, estimated to be ~1500 K, at which temperature, recrystallization starts to occur. This is maintained for an hour. Leaving the wire at this temperature for a long period of time, cause it to be brittle, which is not suitable for STM tips. The diameter of the RHK tip holders is 0.3 mm and the tungsten wire has a diameter of 0.25 mm. Therefore a small bent is made in the middle of the tip so that the tip friction fit into the holder. If the wire is very brittle, the tip will break while mounting it into the tip holder. In the final step, the temperature is increased gradually until the wire breaks off under the tension of weight. At this step the crystallization process is completed. The tips made out of tungsten wires recrystallized by this method worked very well and are stable while imaging.

2.6.2   Etching Tungsten Wire to make STM Tips

To obtain a sharp tip, the recrystallized W wire is electrochemically etched. Figure 2-19 describes the apparatus used for tip etching.[3] The tips are prepared by double lamella drop-off technique.[3,21-22] A small piece of recrystallized tungsten wire is placed through a gold wire loop (of inner diameter ~3 mm) with the bottom of the wire slightly immersed in NaCl solution. A drop of 4M NaOH solution is placed inside the gold wire loop which builds a lamella inside the ring. A DC voltage is applied between the gold wire loop and the electrolyte solution which induces the following redox reactions.

$$6H_2O + 6e^- \rightarrow 3H_2 + OH^- \quad (cathode)$$

$$W_{(s)} + 8OH^-_{(aq)} \rightarrow WO^{2-}_{(aq)} + 4H_2O + 6e^- \quad (anode)$$
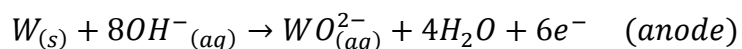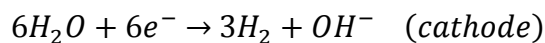
At cathodic side, water molecules are reduced to hydroxide ions and hydrogen gas. At the

anodic side the etching process takes place at the tungsten wire-NaOH solution interface,

where solid W is oxidized and dissolves in water as tungstate anions. As etching

proceeds, the portion of the W wire, which is at the W-NaOH interface becomes thinner

until it is no longer able to hold the weight of the lower part of the wire and finally snaps

under the tension and drops inside the NaCl solution, leaving a very sharp tip.

Simultaneously, as a consequence, the circuit is interrupted and etching stops

immediately and prevents blunting of the tip by further etching.
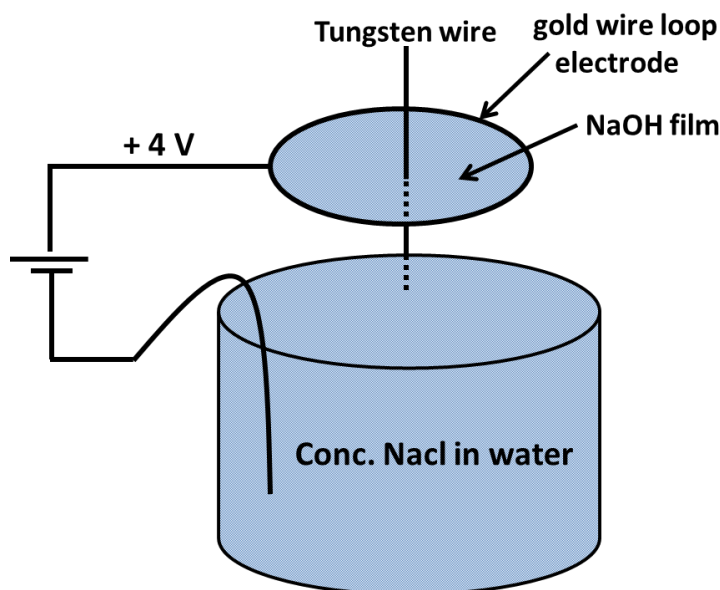
Figure 2-19 Schematic diagram of the apparatus used for etching tungsten wires

However, if the etching process is done in one step, the resulting tips are sharp but

have a long needle like shape. These types of tips are very unstable while scanning and

very prone to mechanical and acoustic vibration. Therefore long and thin tips are

generally less favorable than the ones which have a rather short and thick shank and taper

rapidly towards the apex (as shown in figure 2-20). This problem can be overcome by doing the etching in two steps. In the first step, a rather thick film of NaOH solution is placed in the gold loop and etching is continued until the tungsten wire is thinned down to one third of its original thickness. Then the power supply is turned off and the NaOH film is removed from the Au wire loop. In the second step, a very thin film of NaOH solution is placed inside the loop and W wire is pushed slightly deeper into the film so that the portion of the W wire where it starts to neck down is at the upper meniscus of the lamella. Etching process continues until the lower section drops off leaving a very sharp tip. Finally the tip is cleaned with distilled water followed by an isopropanol rinse and then checked with an optical microscope to get a view of the shape and sharpness of the tip. Although the microscope only resolve down to microns, but it has been observed that the tips which appear reasonable (sharp and symmetric) under the microscope are usually perform well after proper tip conditioning.
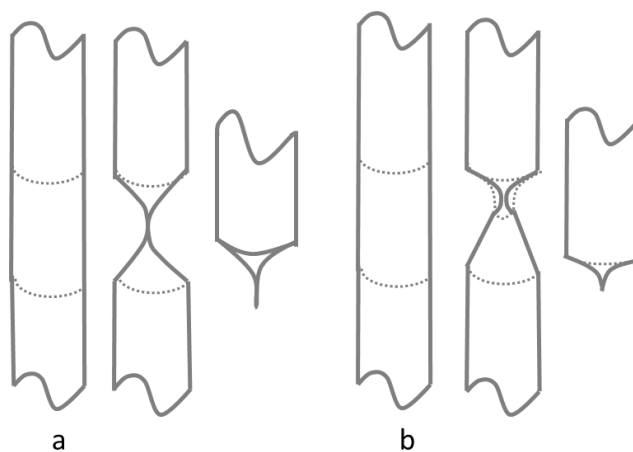
Figure 2-20 Tungsten wire etching (a) in one step, which results in wiry tip apex (b) in two steps, which results in tips that have short shank and taper rapidly towards the apex

2.6.3 Tip Conditioning Methods

The idea behind tip conditioning is to treat the etched tips to make them clean, stable and sharp. It has been achieved in various steps as described in this section.

The first step is to remove the contamination which coats the tip as a result of etching. The etched tips are usually covered by a thick oxide/hydroxide coating. Mineral acids can remove the tungsten dioxide readily but some acids e.g. hydrochloric acid and nitric acids also reacts with metallic tungsten and therefore are not suitable for used in tip cleaning. However, HF (48% in water) reacts with tungsten oxide but not with metallic tungsten,[3] and is suitable to clean the tips. Dipping the tip in HF (10 s) followed by distilled water and an isopropanol rinse results in a very clean tip.

2.6.3.1 Annealing the Tip in Vacuum and Field Emission experiment

Another way of obtaining clean tips is to heat it to ~1100 K in vacuum. At 1075 K, tungsten oxide and tungsten trioxide (major contaminant of tips prepared by etching) sublimes under UHV condition. [23]

$$2WO_3 + W \rightarrow 3WO_2 \uparrow \quad (1075K, UHV)$$
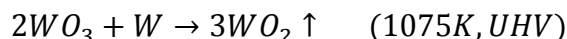
The next step is to carry out field emission experiment to measure the sharpness of the tip and, in some cases also to sharpen it. The section below presents the details of field emission experiments.

In a metal, electrons reside in a potential well mostly due to their interaction with the metal ions and the potential $U(x)$ is given by,

$$U(x) = \Phi - \frac{e^2}{4x} \tag{2.32}$$
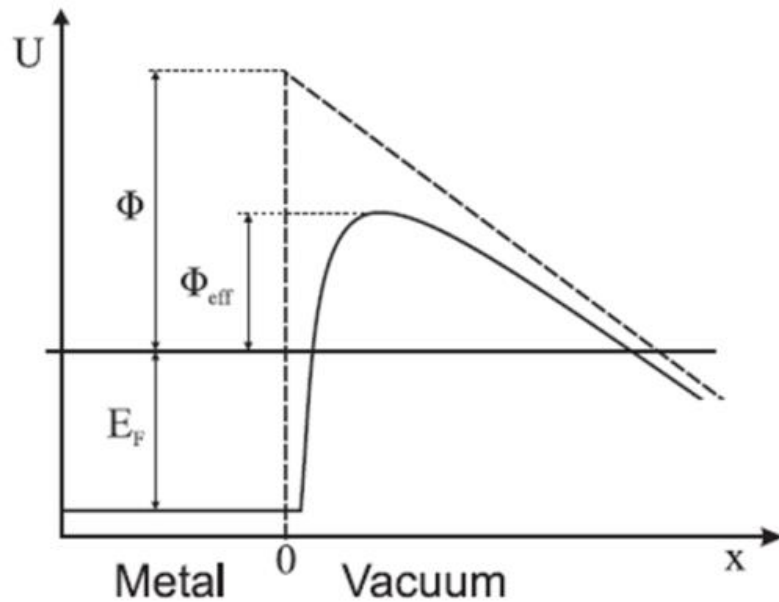
Figure 2-21 The potential experienced by an electron at a metal surface in the presence of an electric field. The dashed line is the potential without the effect of mirror charge [24]

If an electric field F is applied, the potential will be disturbed and is given by,

$$U(x) = \Phi - \frac{e^2}{4x} - F \tag{2.33}$$

so that the electrons close to the Fermi level experience a triangular barrier [24] rather than a rectangular barrier, which it can overcome easily by tunneling. The higher the magnitude of the field, the narrower is the barrier. This pure quantum mechanical effect is called field emission. Using the concept of field emission Fowler and Nordheim derived a mathematical expression for the current density (i) of the emitter in terms of metal's work function (Φ) and the strength of the applied field (F) [3,22] given by:

$$i = 6.2 \times 10^{-6} \left(\frac{\sqrt{\frac{\mu}{\Phi}}}{\alpha^2(\mu + \Phi)} \right) F^2 e^{\left(-6.8 \times 10^7 \frac{\phi^{\frac{3}{2}}\alpha}{F} \right)} \tag{2.34}$$

where i is field emission current density (A/cm^2), Φ is the work function of the metal

and μ is the Fermi level. Both Φ and μ are in eV and the applied field F is in V/cm. α is

the image correction parameter which accounts for the deviation from the simple

triangular potential well. Now we will relate the F-N equation to the geometry (radius) of

the emitter (tip).[24]

If a voltage V is applied to a sphere of radius r, the resulting field experienced by

the sphere is $F=V/r$, although the STM tip can be thought of as a sphere at the end of a

cone-shaped shank which reduces the field to some extent. The electric field at the tip

surface is given by $F=V/kr$ where k is the field reduction term. Substituting the value of F

in equation 2.34, the F-N equation becomes:

$$I = A6.2 \times 10^{-6} \left(\frac{\sqrt{\frac{\mu}{\Phi}}}{\alpha^2(\mu + \Phi)} \right) \left(\frac{V}{kr} \right)^2 e^{\left(-6.8 \times 10^7 \frac{\Phi^{\frac{3}{2}}\alpha kr}{V} \right)} \tag{2.35}$$

Where I is the total field-emitted current (Ampere) and A is the area of the emitter

(cm^2). Taking the natural logarithm of both sides the above equation yields,

$$\ln\left(\frac{I}{V^2}\right) = \ln\left(A \times 6.2 \times 10^{-6} \left(\frac{\sqrt{\frac{\mu}{\Phi}}}{\alpha^2(\mu + \Phi)} \right) \frac{1}{(kr)^2} \right) - 6.8 \tag{2.36}$$

$$\times 10^7 \frac{\Phi^{\frac{3}{2}}\alpha kr}{V}$$

and can be written as,

$$\ln\left(\frac{I}{V^2}\right) = \left(-6.8 \times 10^7 \; \Phi^{\frac{3}{2}}\alpha kr \right)\frac{1}{V} + constant \tag{2.37}$$

Now this is in the form of a linear equation where $\ln\left(\frac{I}{V^2}\right)$ is a linear function of $\frac{1}{V}$. A plot of $\ln\left(\frac{I}{V^2}\right)$ as a function of $\frac{1}{V}$ is called Fowler Nordheim plot and the slope of the line is given by:

$$slope = -6.8 \times 10^7 \; \emptyset^{\frac{3}{2}} \alpha k r \tag{2.38}$$

From the slope of F-N plot, radius of the tip can be calculated. The following section describes the experimental details associated with the annealing and field emission experiments.

The tip prepared by etching is transferred to a vacuum chamber operating at a base pressure of 5×10^{-8} Torr. This is a small chamber consists of a six way cross mounted on top of a small ion pump (shown in Figure 2-22).
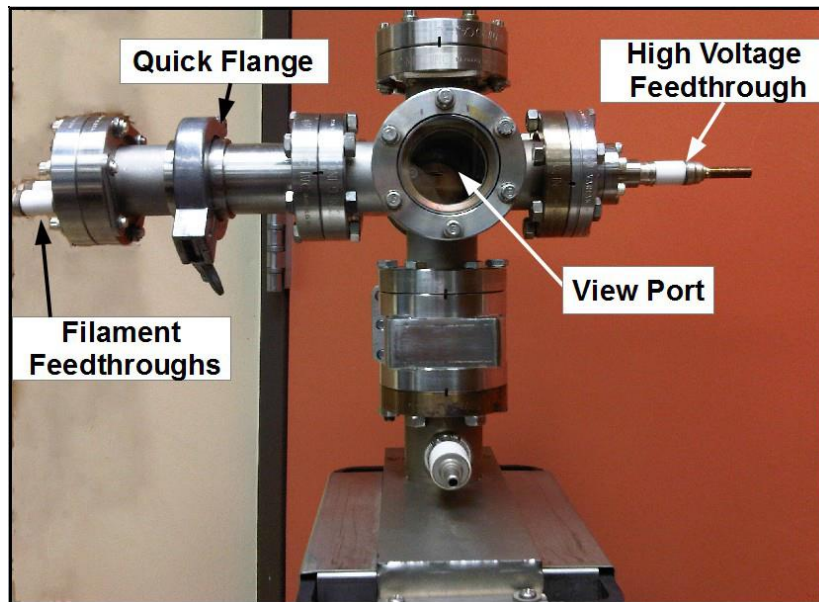
Figure 2-22 Photograph of the tip preparation chamber [3]

This chamber is equipped to both heat the sample and perform field emission experiments. A current feed through and a high-voltage feedthrough assembly is installed

in two different flanges facing each other. A copper disc collector is attached to the high

voltage feedthrough for measuring the field-emitted current. The current feedthrough is

attached to two copper rods at the end of which a heating nichrome filament is attached.

A stainless-steel capillary tube is spot welded to the heating filament, where the STM tip

is installed by simple friction fitting in place within the capillary (as shown in Figure 2-

23). A STM tip is installed in the capillary tube and the whole assembly is transferred

into the tip preparation chamber and the chamber is pump down to $\sim 5 \times 10^{-8}$ Torr. The

length of the copper rods is adjusted such that, when inside the vacuum chamber, the

separation between the apex of the STM tip and the copper disc collector is about ~ 2.5

cm.
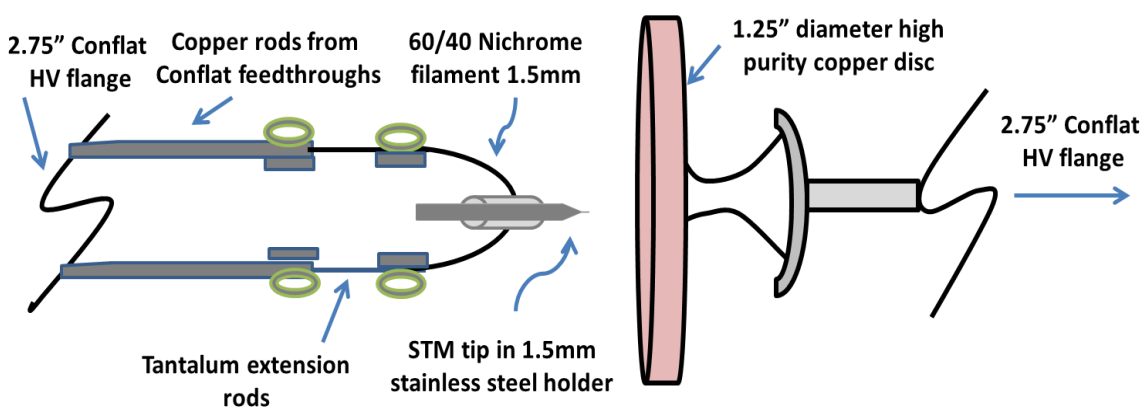
Figure 2-23 Construction details of the tip mounting system [3]

A current of $\sim 3A$ is passed through the nichrome heating filament to anneal the

tip to ~ 1100 K. When the tip glows dull red, it is estimated to be ~ 1200 K. After the tip is

heated to ~ 1200 K two to three times, field emission experiment was carried out by

applying a positive bias voltage to the tip with respect to the copper disc. A DC voltage

was applied through the high-voltage feedthrough and was increased slowly until a

detectable field emission current is measured. The voltage is increased step wise in a

small increment until a current of ~1 microamp is measured. The procedure was repeated

three to four times while annealing the tip to ~1200 K after each run. The voltage and

current were recorded during each step and the results were plotted as the Fowler

Nordheim plot. Figure2-24 show typical Fowler-Nordheim plots obtained for a STM tip.

Run	slope	R-value	Radius (nm)
1	-9072	0.98722	28
2	-6452	0.97716	20
3	-4526	0.96887	14
4	-3469	0.99495	11
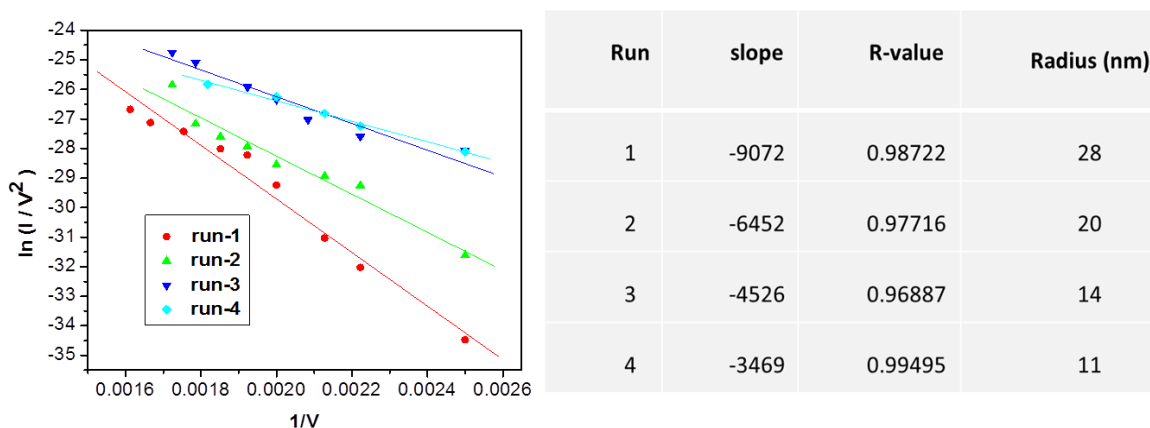
Figure 2-24 Typical results of a field emission tip conditioning method

From this Figure 2-24 it is clear that the slope of the line decreases from Run 1 to

Run 4 indicating a decrease in tip radius as a result of the field emission experiment.

From the slope of the F-N plot (equation 2.38), the tip radius can be calculated. By using

an average work function of tungsten to be ~4.5 eV, the value of α to be 1 and k to be 5,

the radius of the tip is calculated which are shown in the right. The radius of the tip

calculated for the first run is ~28 nm and for the fourth run is ~11 nm. There is a dramatic

reduction in the tip radius as a result of the field emission experiment and it has also been

observed from Run 1 to Run 4, the stability of the measured current increases, which

indicates that the tip becomes stable. The increase in stability can be explained by the so

called "electron wind force". When a positive bias is applied to the tip *versus* a negative

counter electrode, the positive nuclei experience a force aligned with the electric field

vectors. At the same time the electron cloud exerts a force of equal in magnitude but

opposite in direction (often called electron wind force) and as a result the bulk atoms experience no net movement. However, for the surface and low coordination atoms the electron wind force is no longer applicable so they will experience a net force drawing them in the direction of the applied electric field and forms a stable tip apex.[3,22]

In summary, the combination of tip annealing followed by field emission experiment helps to achieve a clean, stable and sharp tip. From our experience most of the tips prepared by this method perform well during STM imaging. The sharp tips are mounted in the RHK tip holder and transferred to the UHV-STM chamber. There are some additional tip conditioning is performed in situ for the optimum performance of the tip which are described below.

2.6.3.2   In Situ Tip Conditioning Methods

(1) Ion Bombardment

Tungsten is very reactive and when exposed to atmospheric condition even for a short period of time is coated with layers of oxide. Therefore we have tried to keep the time gap between cleaning the tips in the tip preparation chamber and transferring the tip into the STM chamber as short as possible. When imaging directly with the pre cleaned tips, the performance of the tips was poor, probably due to a small amount of contamination which prevents a clean tunneling junction. To remove the remaining contamination, the tips were Ar ions bombarded for short period of time (10 to 15 s) by using 500 to 1000 V. The idea of a gentle bombardment is to remove the contamination without affecting the shape of the tip. In some cases, when a well performing tip images poorly, probably due to some contamination or geometry change, a gentle Ar ion bombardment improves the performance drastically. After ion bombardment the tip is

transferred to the STM scan head and scanning is performed. A difficulty with using a tungsten tip is that, metallic tungsten is very reactive and it is extremely likely that once the tip is brought into the tunneling range and bias is applied, the organic species on the surface will be picked up by the tip and contaminate it. As a result the tip becomes very unstable and sometimes the tip does not conduct due to the presence of thick insulating layers. To maintain the optimum performance of the tip, there are some strategies for tip conditioning which are controlled by the RHK software and can be performed while the tip is in the scan head. In the section below presented some of the quick *in situ* tip conditioning methods that have proven successful.

(2) Controlled "Crash" into a Metal (F-Z curve)

The ion bombarded tips are usually "dipped" into a gold crystal before scanning. This is done by a controlled "crash" of the tip into the gold surface using a force-distance curve. Since Au is much softer than W, there is a little chance of damaging the tip in this process. The idea behind this method is to form a gold-coated tip with gold atoms at the apex which contributes to 99% of the tunneling. Gold is much less reactive than tungsten, so that the tip remains clean during scanning. This method has frequently been used to maintain the cleanliness of the tip and this method when applied to a contaminated tip can drastically improve its performance, probably due to picking up some gold atoms and/or leaving the contamination behind.[25]

(3) I-V Curve

A continuous curve of tunneling current *versus* bias voltage which is nearly vertical at the origin indicates a clean tip. I-V curve is a nondestructive method for cleaning tips and is done frequently to maintain the cleanliness of the tip.

(4) Voltage Pulsing

This is the easiest and a quickest method of tip conditioning and can be implemented while scanning. If, during scanning, the tip suddenly behaves poorly due to picking up contamination from the surface, by pulsing (quickly applying a high voltage) the tip to -4 to -5 V, helps to remove that contamination and sometimes drastically improves the image quality. By applying a high voltage at a fixed current, moves the tip away from the surface which makes a tip "crash" unlikely. The successes rates of the tips prepared and conditioned by the above described methods is satisfactory and often perform well during imaging.

2.7   References

1.   Burkholder, L.; The Surface Chemistry of Enantioselectively Modified Palladium (111) Systems. **2009**, Ph.D. dissertation, University of Wisconsin-Milwaukee

2.   Furlong, O.; Tribological and Tribichemical Precess in Sliding metal interfaces. **2010**. Ph.D. dissertation, University of Wisconsin-Milwaukee

 3.   Kestell, J.;The Surface Chemistry of Ad atom mediated Oligomers of Aromatic Disocyanides and dithiols on Au(111) and Granular Films. **2014**. Ph.D. dissertation, University of Wisconsin-Milwaukee

4.   Gast Mfg.; "Rotary Vane Compressors and Vacuum Pumps". **2012**.

5.   Pfeiffer Vauum; " Working with turbopumps". **2003**. Technical document PT 0053 available for download at *mmrc.caltach.edu/Vacuum/Pfeiffer%20Turbo/Turbos.pdf*

6.   Mattox, D.; Educational Guide to Vacuum Coating Procedures. **2001**. Society of Vacuum Coaters technical document

7.   Westinghouse Electric; Vacuum pump Setup. Operation and Maintenance. **1944**. Instruction book 5669-168

8.   Chambers, A.; Modern Vacuum Physics, **2005**, CRC Press

9.   Hudson, J.B. *Surface Science: An Introduction*, Butterworth-Heinemann, MA, **1992**

10.   Redhead, P.A. *Vacuum*, **1962**, 12, 203

11.   surface science website**:** http://www.chem.qmul.ac.uk/surfaces/scc/scat5_1.htm

12.   Auger, M.P. *Compt. Rend*., **1925**, 180

13.   Terenin, A.N. *Zh. Fiz. Khim*., **1940**, 14, 1362

14.   Eischens, R.P.: Pliskin, W.A: Francis S.A. *J Chem. Phys*., **1954**, 22, 1786

15.   Little, L.H. *Infrared spectra of Adsorbed Species*, Academics Press, London,

1966

16.   Greenler, R.G. *J Chem. Phys*., **1966**, 44, 310

17.   Binnig, G.; Rohrer, H.; Gerber, C.;Weibel,E., Surface Studies by Scanning

Tunneling Microscopy. *Physical review Letters* **1982**, 49, (1), 57.

18.   Woodruff, D.P.: Delchar, T.A. *Modern Techniques of Surface Science, (2nd ed)*,

Cambridge University Press, **1994**

19.   Boscoboinik, J.A.; Small Organic Molecues on Transition Metal Surfaces and

Monte Carlo Simulations of Surface Alloys. **2010**. Ph.D. dissertation, University of

Wisconsin-Milwaukee

20.   Surface Science Network. www. Surfacesciencenetwork.com

21.   Chambers, A.; Modern Vacuum Physics, **2005**, CRC Press

22.   Lucier, A.; Master's thesis, 2004, McGill University, Montreal, Qubec.

23.   Hockett, L.;Creager, S.;*Rev. Sci. Inst*. **1993**, 64, (1), 263-4.

24.   Ernst, S.; Optimization of the preparation process for tips in scanning tunneling

microscopy. **2006** Max Planck Institute for Chemical Physics of Solids, Dresden

and Department of Physics Faculty of Mathematics and Natural Sciences

Technical University at Dresden

25.   Winterlin, J.; Wiechers, j.; Hofer, H.; Bhem, R.; *Phys. Rev.Lett*. *1989*, 62, (1), 59-

63.

Chapter 3

Formation of Chiral Self-Assembled Structures
of α-Amino Acids on Pd (111)

3.1 Introduction

The importance of heterogeneous chiral catalysis and different approaches for achieving this is described in Chapter 1. Chiral modification of an achiral metal surface is one of the most successful approaches in the field of heterogeneous asymmetric catalysis. In this approach, chirality is imparted to an achiral metal surface by adsorbing a chiral molecule which is called a "chiral modifier" on a metal surface which breaks the symmetry of the underlying lattice and imparts asymmetry to the metal surface. The chirally modified surface, when exposed to another chiral probe molecule interacts differently with different enantiomers of the probe. The way in which chiral modification works is further classified into two broad categories. Either the modifier molecules function collectively to form self-assembled structures, called as "chiral pockets" which provides local chiral adsorption sites to allow the preferential adsorption of one enantiomer of a chiral probe molecule over the other, or alternatively they provide a direct 1:1 enantiospecific interaction with the probe molecule. Therefore the nature of the chiral modification controls the subsequent chiral interactions on the surface which emphasizes the importance of exploring the surface chemistry of the chiral modifiers on metal surfaces.

Amino acids provide the building block of life and all terrestrial proteins derive exclusively from L-amino acids and the participation of surface has been implicated for

the possible origin of homochirality.[1] Amino acids themselves have been used as both

chiral catalyst[2-4] and as a chiral modifier for the enantioselective hydrogenation of

isophorone.[5-10] Structural investigation of amino acids on transition metal surfaces is

largely focused on copper single crystal surfaces, where they adsorb in the anionic form

and provide long range ordered structure.[11-22] The adsorbate induced chirality on copper

has been discussed in terms of molecule's handedness (the intrinsic chirality of the

molecule) and footedness (the chirality induced by adsorption).[22-23] Density functional

theory calculations of amino acids on Ni(111) have examined the structure of the neutral

and zwitterionic forms of alanine.[24] Recent study of proline on Au(111) shows the

presence of neutral, zwitterionic and anionic species on the surface.[25]

Accordingly, this chapter provides a detail characterization of the α-amino acids

on a Pd (111) single crystal surface. Particular emphasis is given to a thorough

characterization of alanine, the smallest chiral amino acid. The surface chemistry of α-

amino acids have been studied previously[26-28] on Pd(111), and it was found to be

thermally stable at room temperature. Scanning tunneling microscopy study by A.

Boscoboinik [55] shows that amino acids do not form any long range order, but they self-

assemble to form ordered local structures which consists of tetrameric units and dimer

rows. This suggest that amino acids on Pd(111) could act as templates, proposed to occur

when several molecules act in concert to provide a chiral pocket or adsorption site.[29] This

is completely different to what has been observed on Cu surfaces, where the amino acids

form long range order. These results indicate that amino acids can form a wide range of

structures on transition metal surface depending on the nature of the substrate. This

chapter presents a combination of TPD, XPS, RAIRS, STM and DFT study of the amino

acids on Pd(111) surface. With the help of XPS and RAIRS we have identified the chemical nature, bonding and orientation of the adsorbed species on the surface. Additionally XPS is also used to calculate the absolute molecular coverage of the amino acids on Pd(111) surface. DFT calculations have been performed to identify the different surface structures observed in STM.[30]

3.2   Experimental Section

TPD, XPS, RAIRS and STM data were collected in three separate UHV chambers as described in Chapter 2. TPD experiments are carried out by using a heating rate of ~3 K/s and the desorbing species were detected by using a decor mass spectrometer which was placed close to and in-line-of sight of the sample front face.

XPS measurements were made using a MgKα source operating at a power of 250 W and the emitted photoelectrons were detected using a double pass cylindrical-mirror analyzer operating at a pass energy of 50 eV. The resulting spectra were fit using XPS PEAK fit program by initially performing a Shirley background subtraction. The components of the spectra were then fit using a fixed Lorentzian to Gaussian ratio of 0.3 and the width at half maxima and peak positions of the fitting components were initially fixed while allowing the heights and areas to vary. A final refinement was carried out by allowing all parameters to vary to provide the optimum fit. LEED experiments were carried out previously by L. Burkholder *et al*. which shows that alanine adsorbed on Pd(111) was extremely susceptible to electron-beam damage .Therefore LEED patterns were measured in a low current system with an incident beam current of ~500 fA. Similarly, the adsorbed amino acids could be modified by the photo emitted electrons during the XPS collection. While this effect was not studied in detail, no drastic changes

were observed in the XP spectra during data collection.

Infrared spectra were collected by using a Bruker Vertex infrared spectrometer operating at a resolution of 4 cm^{-1}, using a liquid-nitrogen-cooled mercury telluride detector, and spectra were typically collected for 1000 scans.

STM images were acquired using an electrochemically etched tip made from recrystallized tungsten wire. This was conditioned by a controlled interaction with a clean Au(111) single crystal. This is expected to result in a gold terminated tip. The absolute coverage was measured by taking a ratio between the number of adsorbed molecule to the Pd(111) substrate atom density.

The Pd(111) substrate was cleaned using a standard procedure consisting of cycles of argon sputtering and annealing in 3×10^{-8} Torr of oxygen at 1000 K and the cleanliness was judged either using X-ray photoelectron spectroscopy, Auger spectroscopy or temperature programmed desorption after dosing oxygen, where the absence of CO desorption indicated that the sample was carbon free.

Amino acids were dosed onto the sample by using a home built Knudsen source as described in Chapter 2. The compounds were generally outgassed over night at ~380 K before dosing onto the surface to remove contaminants, particularly water, and the temperature of the amino acids were adjusted to yield reasonable dosing rates.

3.3   Theoretical Methods

Density functional theory (DFT) calculations were performed with the projector augmented wave (PAW) method [31-32] as implemented in the Vienna ab initio simulation package, VASP.[33-34] The exchange correlation potential was described using the generalized gradient approximation (GGA) of Perdue, Burke and Ernzehof. [35] Hydrogen

bonding interactions are well reproduced (within ~ 4 kJ/mol) using this functional, although the accuracy deteriorates as the hydrogen bonds deviate from linear.[36] A cut off of 400 eV was used for the plane wave basis set, and the wave functions and electron density were converged to within 1×10^{-5} eV. The first Brillouin zone was sampled with a 4×4×1 Γ-centered k-point mesh. Geometric relaxations were considered to be converged when the force was less than 0.02 eV/Å on all unrestricted atoms. STM topography simulations were performed using both the Tersoff-Hamann[37] and Bardeen[38] approaches to tunneling using bSKAN 3.7.1.[39-40]

3.4 Experimental Results

3.4.1 Relative Coverage Measurement of Amino Acids
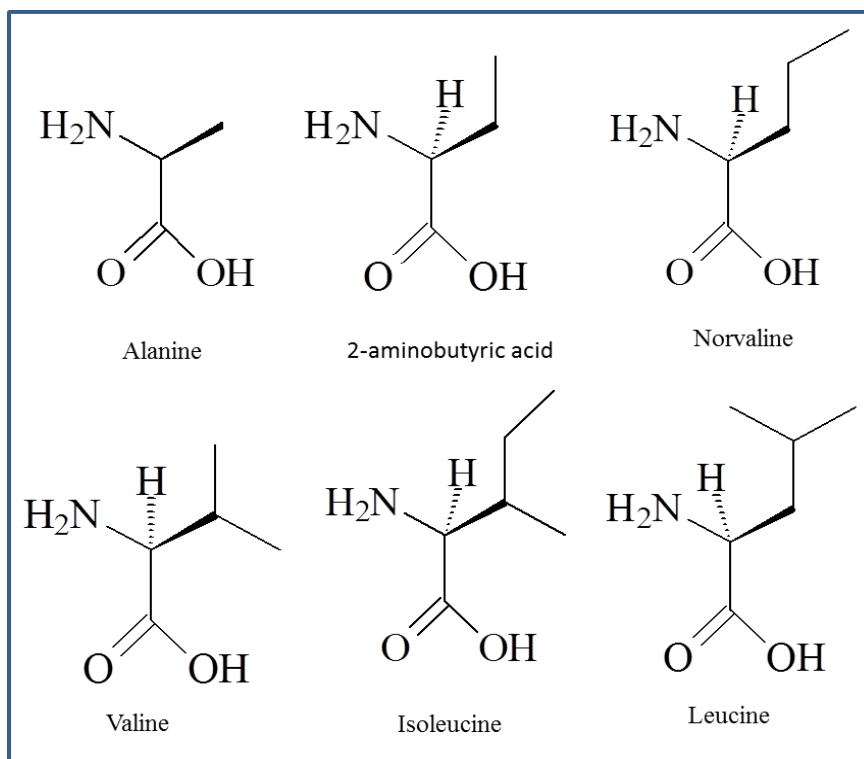
Figure 3-1 Selection of α-amino acids

Figure 3-1 shows all the amino acids studied in this chapter. The amino acids are

chosen starting from the simplest chiral amino acid alanine. Other amino acids are different from alanine in the sense that they have different (bulky) side groups. 2-amino butanoic acid and norvaline have simply $-C_2H_5$ and C_3H_7 groups respectively instead of a $-CH_3$ group in alanine. In Valine, isoleucine and leucine chain branching occurs at C3, C3 and C4 carbons respectively.

It has been previously observed by the Tysoe group that when amino acids are dosed onto the palladium surface at ~100 K, they adsorb to second layer and multilayers before the saturation of the monolayer, thus making it difficult to measure an accurate coverage from TPD.[26-28] For this reason, the relative coverage measurements of the amino acids were carried out by titrating it with CO using the fact that CO adsorbs on bare palladium sites but not on amino acid covered sites. By taking this approach, the amino acid monolayer is defined as the coverage which completely blocks CO adsorption. In this study, the relative coverages of the amino acids are measured using a similar approach but by titrating with propylene oxide. Propylene oxide adsorbs reversibly on a Pd(111) atop site and is used extensively as a chiral probe on amino acid modified palladium surfaces which is described in the following chapters. Figure 3-2 shows a typical plot for the integrated area of propylene oxide desorption yield as a function of alanine exposure which shows an exponential decay behavior. 85% of the propylene oxide is blocked after an alanine exposure of 4 minutes, suggesting the formation of a saturated alanine monolayer. With further increase in alanine dosing time propylene oxide desorption yield remains unchanged which suggests that there is some residual propylene oxide from the background condense onto the surface at liquid nitrogen temperature. Similar experiments are carried out for the relative coverage

measurement of other amino acids (data not shown).
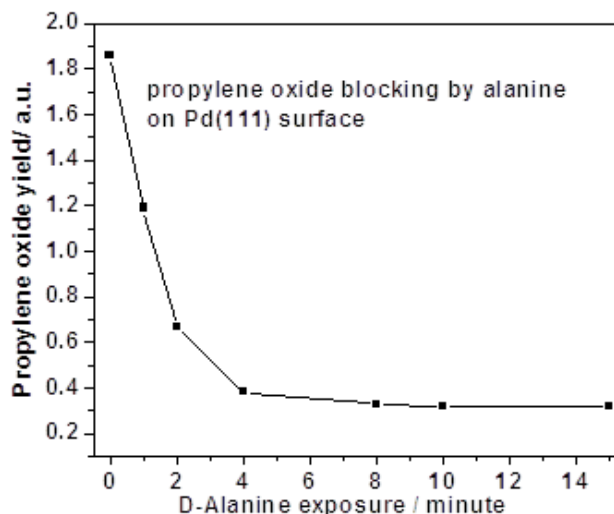
Figure 3-2 Plot of the integrated propylene oxide desorption yield of as a function of alanine exposure at 150 K.

However adsorbing amino acids onto a Pd(111) surface at ~300 K does not allow

the extensive adsorption of second layer or mulitilayers. Therefore when alanine is dosed

at 300 K, a TPD uptake profile can also be used to measure the relative coverage of the

amino acids where a monolayer is defined based on Langmuir adsorption isotherm.

Figure 3-3 shows the TPD profile of alanine on Pd(111) surface at various

coverages. The TPD spectra were obtained by dosing alanine onto a Pd(111) at 300 K

and then cooling down the surface to ~200 K. The surface chemistry and decomposition

pathways of alanine on Pd(111) has been studied previously [26] by dosing high coverages

at ~100 K, which suggests that alanine decompose at slightly above room temperature to

produce H_2,CO, CO_2 , HCN and $CH_3CH_2NH_2$. In this work, TPD has been performed by

dosing sub-monolayers to monolayer coverages of alanine on Pd(111) at room

temperature. The principal reason behind the TPD experiments is to measure relative

coverages of the adsorbate which will be used in the later work during enantioselective

measurement studies.
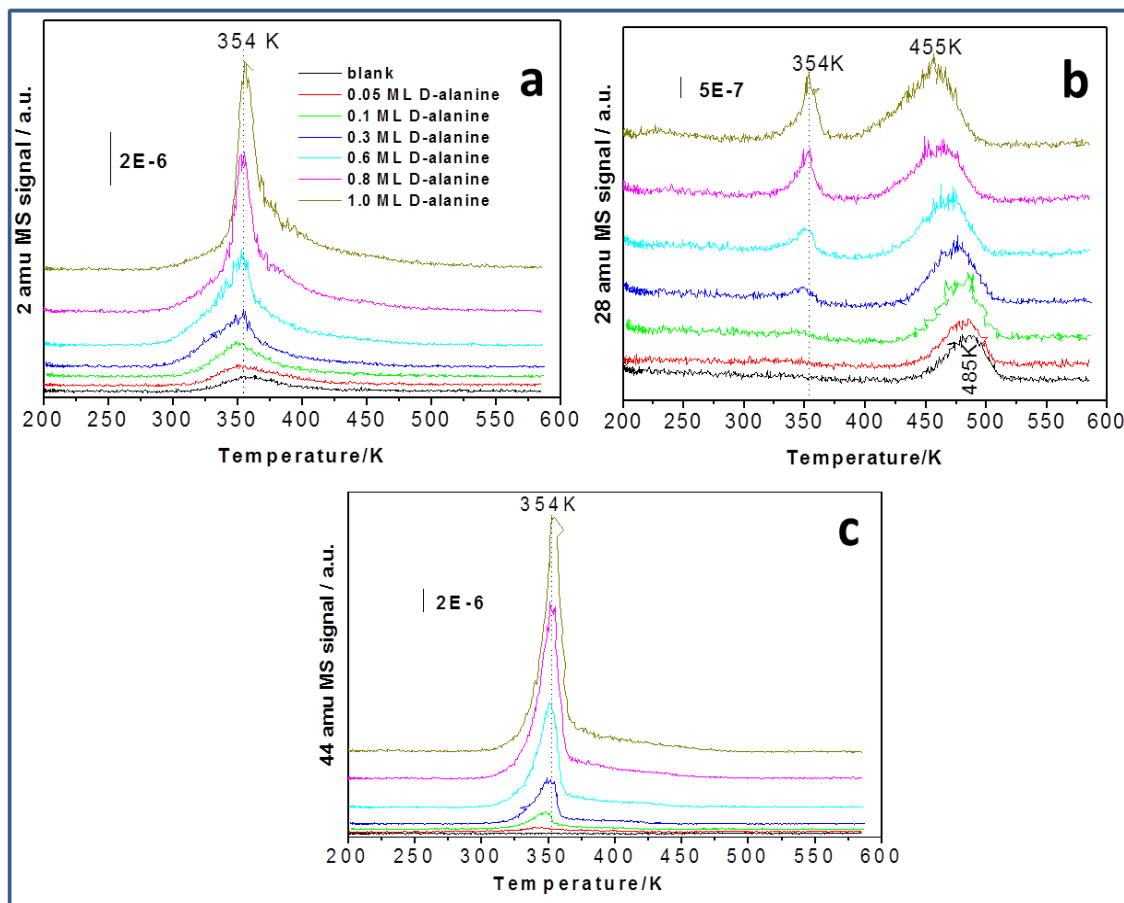
Figure 3-3 TPD profiles for various coverages of alanine on Pd(111) when dosed at ~ 300 K by monitoring (a) 2 amu (H_2) (b) 28 amu (CO) (c) 44 amu (CO_2). Data were collected by using a heating rate of 3 K/s

TPD spectra were collected for various coverages of alanine by monitoring three

key masses of 2, 28 and 44 amu by using a heating rate of ~3 K/s. Blank experiments

show that there is some background H_2 and CO adsorption on the Pd(111) surface.

Hydrogen desorbs at a temperature of 354 K due to the decomposition of alanine which is

in accord with desorption of CO_2 (44 amu) at the same temperature. At low coverages the

44 amu peak is centered at ~348 K and the temperature increase to ~354 K with increase

in coverage suggesting an attracting lateral interaction between the molecules in the monolayer regime. CO (28 amu) desorbs at two different temperatures; at low coverages a CO peak is observed at ~485 K which is close to the desorption temperature of CO from Pd(111) suggesting that the CO desorption is rate limited. At higher coverages another peak appears at 354 K which is a fragment of CO_2. 44 amu desorption peak profile is a good gauge of the amount of alanine on the surface. Although TPD has been done only for alanine, it is expected that all the other amino acids will follow the same decomposition pathway as observed previously when dosed at ~120 K.

3.4.2   XPS of α-Amino Acids on Pd(111)

XP spectra were collected by dosing various coverages of amino acids onto Pd(111) surface at ~290 K and then cooling the sample surface to ~100 K. The relative coverages are measured using propylene oxide blocking experiments as described above. Figure 3-4 shows the XP spectra of alanine on Pd(111) at various coverages. The C 1s spectra (Figure 3-4 (a)) display two distinct peaks at 285.2 ± 0.1 eV and 288.3 ± 0.1 eV binding energies (BE), where the binding energies were referenced to the most intense Pd $3d_{5/2}$ feature on clean Pd(111) at 334.8 eV. Based on previous assignments, carboxylate groups have a C 1s feature at ~288 eV, and the backbone carbons yield peaks between 285 and 286 eV BE. Thus, the feature at 285.2 eV BE is assigned to the α-carbon and the methyl group in alanine and the peak at ~288.3 eV BE to the carboxylate groups. The intensity of the α-carbon features is approximately twice that of the carboxylate carbon feature in accord with the composition of alanine and is in accord with its lack of thermal decomposition at 290 K.
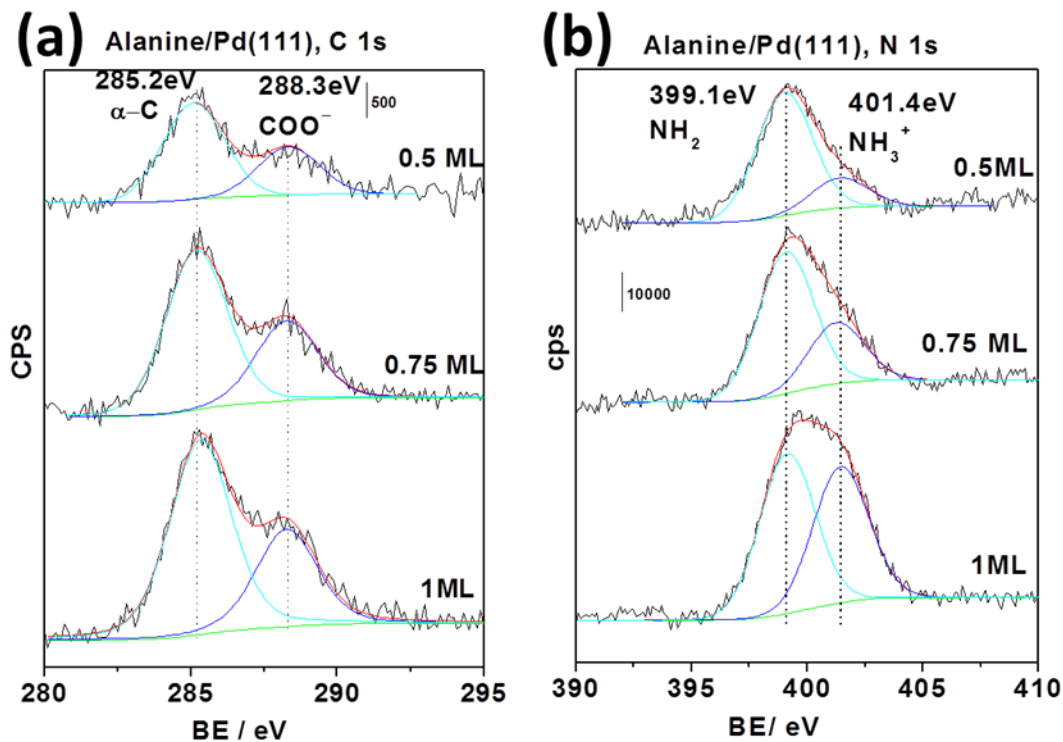
Figure 3-4 C 1s (a) and N 1s (b) photoelectron spectra of various relative coverages of alanine on Pd(111) at 290 K. The alanine coverages are displayed adjacent to the corresponding spectra. Shirley backgrounds are displayed on each of the spectra as well as fits to the individual components.

Figure 3-4 (b) shows the corresponding spectra for N 1s region which reveal the presence of two features at 399.1 ± 0.1 and 401.4 ± 0.1 eV BE. The N 1s spectral region provides straightforward identification of NH_2 (BE ~400 eV) and NH_3^+ (BE ~402 eV). [13, 16-17, 26-28, 41-43] Thus the feature at 399.1 eV BE is assigned to an amine group indicating the presence of a proportion of anionic species on the surface and the feature at ~401.4 eV BE is assigned to ammonium ions suggesting that a portion of the alanine on the surface is in the zwitterionic form. The proportion of zwitterion to anion species increases with increase in coverage probably due to the hydrogen adsorption into the amine group when the surface is crowded with hydrogen.

In a similar way, XP spectra were collected for 2-aminobutanoic acid adsorption

on Pd(111) and are presented in Figure 3-5. The C 1s spectra Figure 3-5 (a) display two

distinct peaks at 285.2 ± 0.1 eV and 288.3 ± 0.1 eV BE. The peak at 285.2 eV is assigned

to the α-carbon and the ethyl group in 2-aminobutyric acid and the peak at ~288.3 eV is

assigned to the carbon atoms of the carboxylate group. As expected, the intensity of the

α-carbon features is approximately three times that of the carboxylate carbon feature

consistent with the composition of the 2-aminobutanoic acid. Figure 3-5 (b) shows the

corresponding spectra for N 1s region which shows the presence of two features at 399.1

± 0.1 and 401.4 ± 0.1 eV BE, assigned to amine group and ammonium ion respectively.
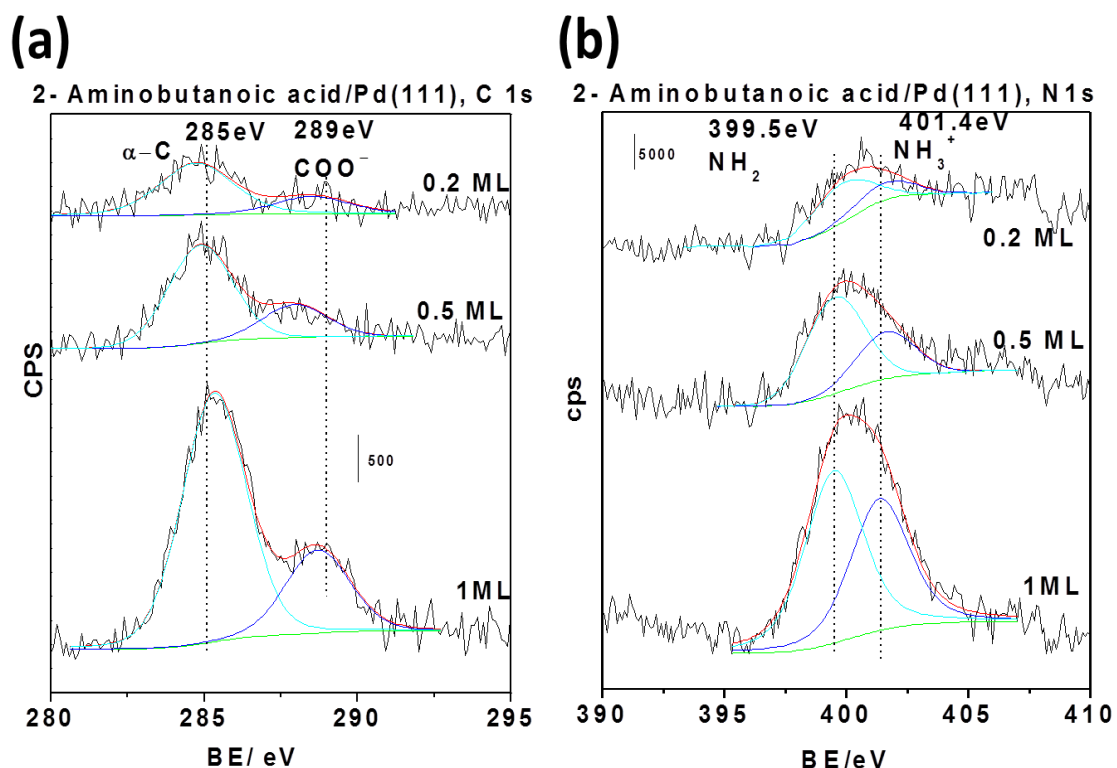
Figure 3-5 C 1s (a) and N 1s (b) photoelectron spectra of various relative coverages of 2-aminobutanoic acid on Pd(111) at 290 K. The coverages are displayed adjacent to the corresponding spectra. Shirley backgrounds are displayed on each of the spectra as well as fits to the individual components.

In a similar fashion XP spectra were collected for norvaline (Figure 3-6), valine

(Figure 3-7), isoleucine (Figure 3-8) and leucine (Figure 3-9).
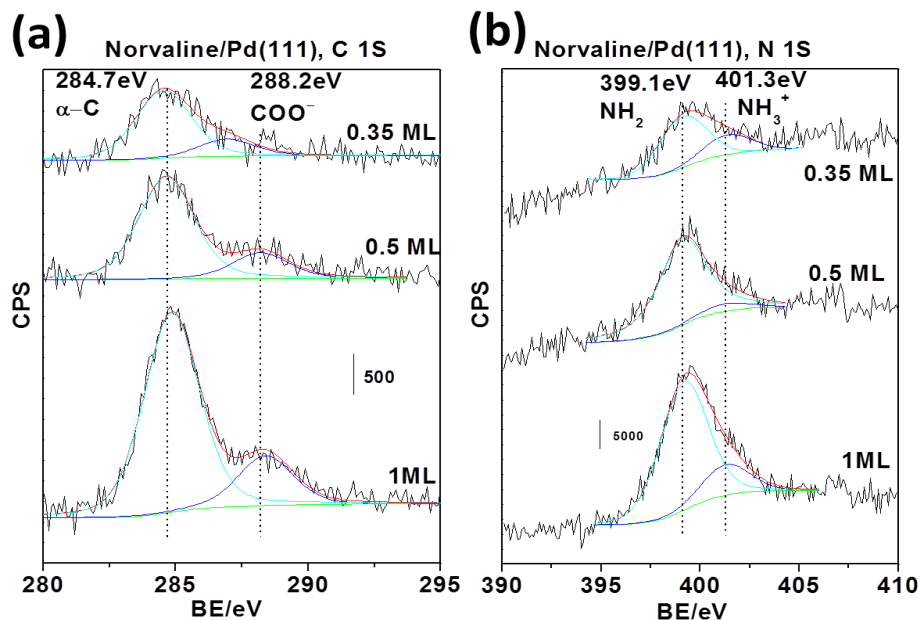
Figure 3-6 C 1s (a) and N 1s (b) photoelectron spectra of various relative coverages of norvaline on Pd(111) at 290 K. The norvaline coverages are displayed adjacent to the corresponding spectra. Shirley backgrounds are displayed on each of the spectra as well as fits to the individual components.

.
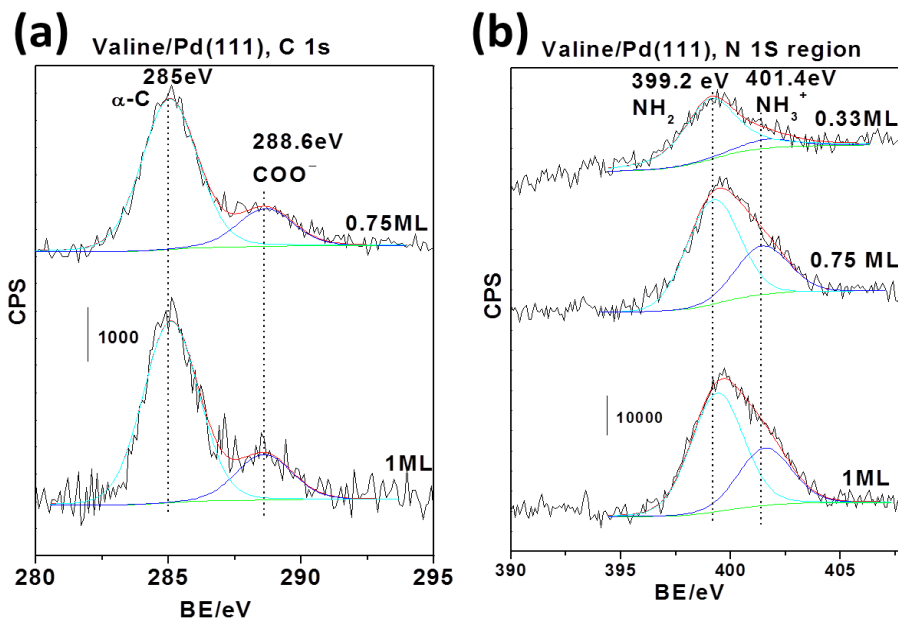
Figure 3-7 C 1s (a) and N 1s (b) photoelectron spectra of various relative coverages of valine on Pd(111) at 290 K. The coverages are displayed adjacent to the corresponding spectra. Shirley backgrounds are displayed on each of the spectra as well as fits to the individual components
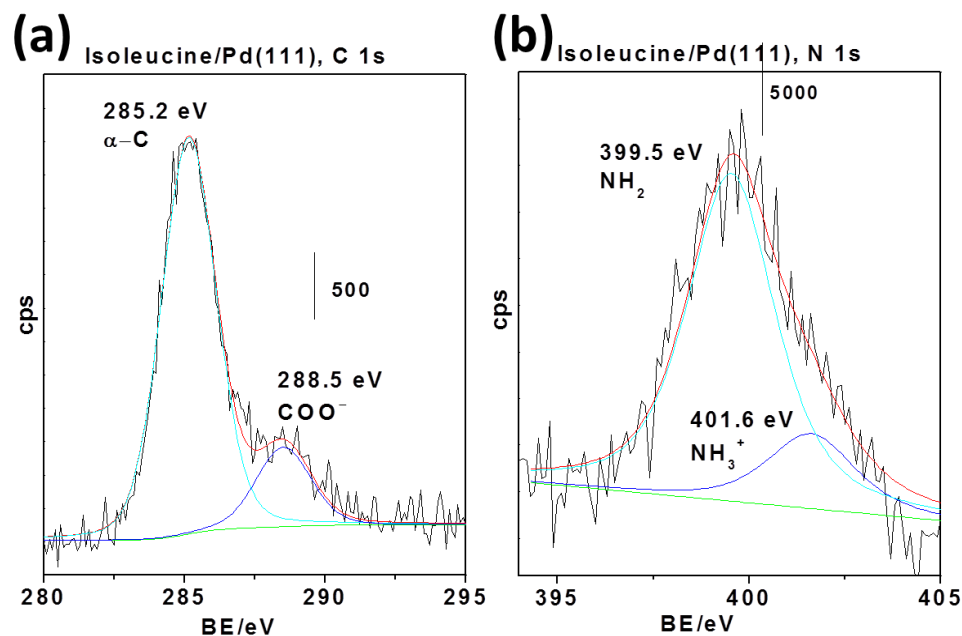
Figure 3-8 C 1s (a) and N 1s (b) photoelectron spectra of various relative coverages of isoleucine on Pd(111) at 290 K. The coverages are displayed adjacent to the corresponding spectra. Shirley backgrounds are displayed on each of the spectra as well as fits to the individual components
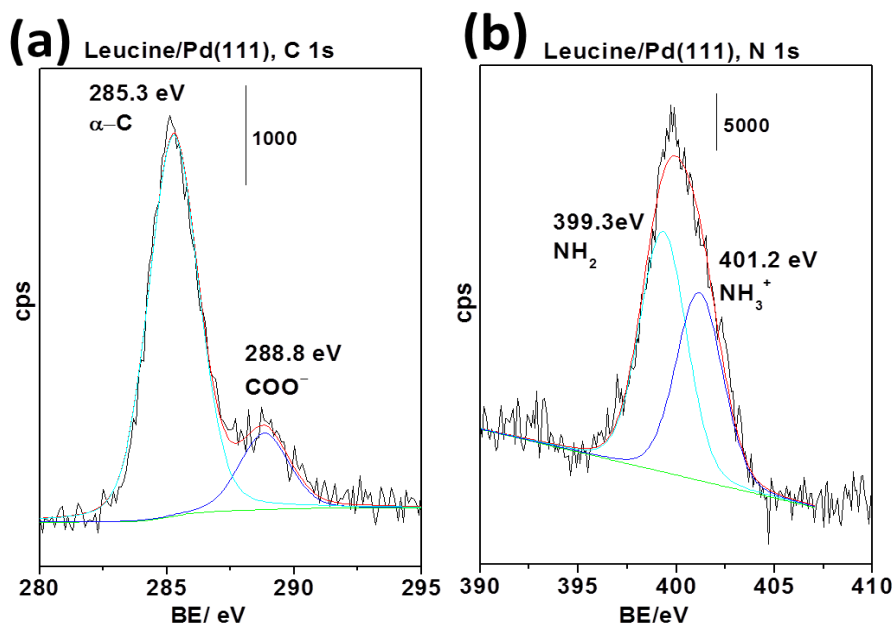
Figure 3-9 C 1s (a) and N 1s (b) photoelectron spectra of various relative coverages of leucine on Pd(111) at 290 K. The coverages are displayed adjacent to the corresponding spectra. Shirley backgrounds are displayed on each of the spectra as well as fits to the individual components

In all the cases similar behavior was observed: C 1s spectra are resolved to two distinct peaks assigned to the presence of α-carbons and carboxylate carbons. The ratio of peak intensity of the α-carbon peaks to the carboxylate carbon peaks for norvaline, valine, isoleucine and leucine are 1:4, 1:4, 1:5 and 1:5 respectively which are consistent with the composition of the respective amino acids. N 1s spectra show the presence of both anionic and zwitterionic species and the proportion of zwitterion to anion increases with coverage. The binding energies and the proportion of zwitterions and anions at various coverages are summarized in Table 3-1 and 3-2 respectively.

Amino Acid	C 1s (α-C) BE/eV	C 1s (COO^-) BE/eV	N 1s (NH_3^+) BE/eV	N 1s (NH_2) BE/eV
Alanine	285.2±0.1	288.3±0.1	401.4±0.1	399.1±0.1
2- aminobutanoic acid	285.0±0.2	288.7±0.2	401.4±0.1	399.5±0.2
Valine	285.0±0.1	288.6±0.1	401.4±0.2	399.2±0.1
Norvaline	284.7±0.2	288.2± 0.2	401.4±0.1	399.1±0.1
Leucine	285.3	288.8	401.2	399.3
Isoleucine	285.2	288.5	401.6	399.5

Table 3-1 C 1s and N 1s binding energies of amino acids on Pd(111)

In all the amino acids a similar trend is observed; anions predominate at low coverages

and the percentage of zwitterions to anions increases with increasing coverage.

Amino Acid	Relative Coverage (monolayer)	% Zwitterion	% Anion
Alanine	1.0	46±3.0	54±3.0
	0.75	30±2.0	70±2.0
	0.5	20±2.0	80±2.0
2-Amino Butanoic Acid	1.0	43±2.0	57±2.0
	0.5	33±3.0	67±3.0
	0.2	30±4.0	70±4.0
Valine	1.0	33±3.0	67±3.0
	0.75	32±2.0	68±2.0
	0.33	13±2.0	87±2.0
Norvaline	1.0	27±4.0	73±4.0
	0.5	20±3.0	80±3.0
	0.3	8±3.0	92±3.0
Leucine	1	44±2.0	56±2.0
Isoleucine	1	19±3.0	79±3.0

Table 3-2 Percentage of zwitterions and anions measured at various coverages for amino acid adsorption on Pd(111)

From the XPS signal intensity the absolute molecular coverage of the amino acids

for a saturated monolayer has been measured. This has been calculated by measuring the

ratio of the carbon 1s signal to the Pd $3d_{5/2}$ signal, calibrated using molecules of known

coverage on Pd(111): carbon monoxide at 300 K , $\theta_c = 0.55$ and the results are

summarized in table 3-3.

Amino Acid	Number of α-carbon atom	Absolute Coverage $\left(\dfrac{\theta_{sat}}{ML}\right)$
Alanine	1	0.34 ± 0.02
2-Amino Butanoic Acid	2	0.24 ± 0.03
Valine	3	0.23 ± 0.03
Norvaline	3	0.16 ± 0.02
Leucine	4	0.20 ± 0.02
Isoleucine	4	0.15 ± 0.01

Table 3-3 Absolute molecular coverages of the amino acids for a saturated monolayer measure by propylene oxide blocking

3.4.3 RAIRS of Alanine on Pd(111)

IR spectra were collected for alanine adsorbed on Pd(111) at 300 K as a function of exposure which is shown in Figure 3-10. The spectra are analyzed by comparison with the spectra for alanine on Cu(110) at low coverages,[13, 44-45] where it bonds to the surface *via* the carboxylate and the amine groups (η^3-alaninate) as well as nickel alaninate [46] and the frequencies and assignments are shown in Table 3-4. The infrared features for zwitterionic alanine have also been measured by a sample dissolution, spray, and deposition (DSD) technique,[47] and the frequencies measured by this method are also summarized in Table 3-4. The most intense modes in the spectra appear at ~3200 cm^{-1} and grow with increasing coverage, resolving into a clear doublet with peaks at 3226 cm^{-1} and 3183 cm^{-1} at higher coverage. In addition, a broad feature is found at ~1606 cm^{-1} and a sharper feature at 1402 cm^{-1}. The high frequency modes at 3226 cm^{-1} and 3183 cm^{-1} are completely absent in the spectra for alaninate species on Cu(110), where the adsorbed alanine only contains amine groups. Ammonium ions in zwitterions have intense stretching modes in this frequency range (Table 3-4) so that 3226 cm^{-1} is assigned to

asymmetric stretching mode and the 3183 cm^{-1} feature to the corresponding symmetric

stretching mode.
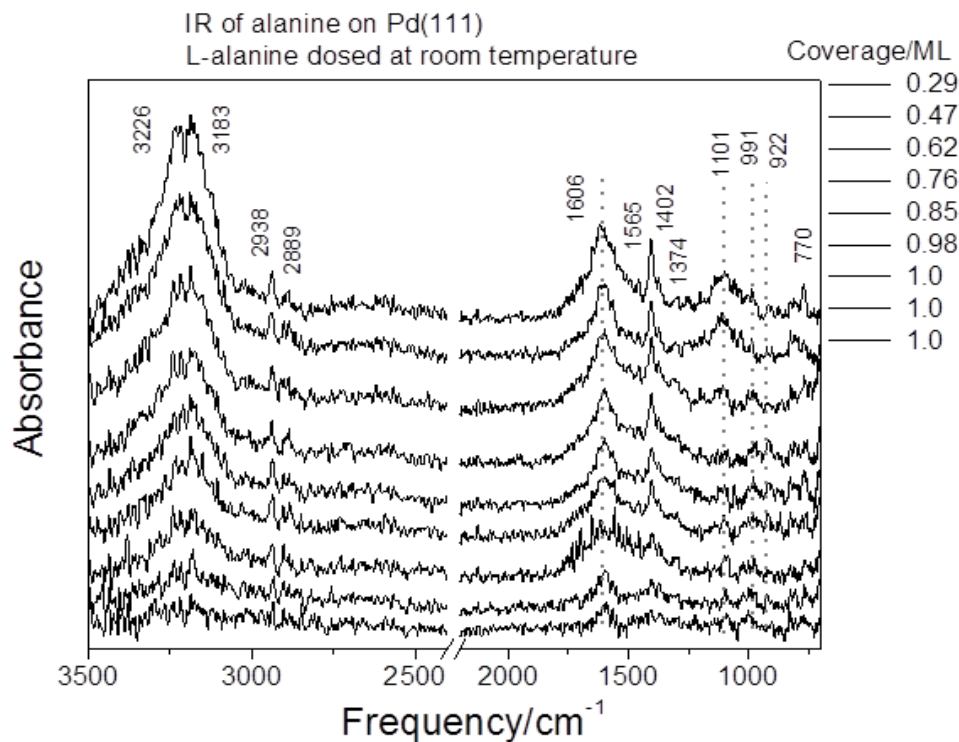
Figure 3-10 Infrared spectra of alanine adsorbed on Pd(111) at 300 K as a function of alanine coverage, where the relative coverages are displayed adjacent to the corresponding spectrum

Carboxylic acids rapidly deprotonate on clean Pd(111) to form carboxylate

species [48-49] consistent with the COO$^-$ mode being detected by XPS. The acetate species

adsorb with the oxygen atom located close to atop sites with the (COO)-CH$_3$ group

perpendicular to the surface.[50] This species exhibits an intense COO$^-$ symmetric

stretching mode at 1414 cm^{-1} [51-52] while the corresponding asymmetric stretching mode is

forbidden by the infrared selection rule.[53] A bidentate acetate adsorption geometry in

which the plane of the acetate group tilts with respect to the surface reduces the local

symmetry from C$_{2v}$ (for a perpendicular acetate group) to C$_S$ (for a tilted acetate group),

but still results in the symmetric acetate stretching mode being infrared active and the asymmetric mode being forbidden. Accordingly the mod at ~1402 cm^{-1} is assigned to a v_s (COO) vibration. The corresponding asymmetric stretching mode, which is infrared forbidden for an η^3-alaninate species, appears at ~ 1606 cm^{-1}. This indicates that a portion of the adsorbed alanine adopts a different geometry. A similar asymmetric stretching mode has been observed at 1613 cm^{-1} for alaninate species on Cu(110) at high coverages and ascribed to the presence of an η^2-alaninate species with the plane of the carboxylate group tilted with respect to the surface, proposed to coordinate to the surface through the amine group and an oxygen atom of the carboxylate.[44]

Vibrational Frequencies/cm^{-1}				
Alanine/Pd(111), 300 K	Alanine/Cu(110), low coverage	Ni-(L-ala)$_2$	Zwitterionic alanine	Assignment
3226	-	-	3300	$v_{as}(NH_3^+)$ **z**
3183	-	-	3240	$v_s(NH_3^+)$ **z**
2938	2935	-	2935	$v_s(CH_3)\ v(CH)$ **z**
2889	2876	-	2876	$2\delta(CH_3)\ v_s(CH_3)$ **z**
1606	1613	1588	1619	$v_{as}(COO^-)$
1565 (sh)	1576	1570	1574	$\delta(HN_2)\ \delta(HN_3^+)$ **z**
1402	1411	1402	1395	$v_s(OCO)+\delta_s(CH_3)$
1374	1373	1365	1358	$\delta_s(CH_3)+v_s(OCO)$
1101	1086	1086	1120	$v_{as}(CCN)\ \rho(CH_3)$ **z**
991	1011	-	-	-
922	919	919	929	$v(CN)\ \rho(NH_3^+)$ **z**
770	771	771	789,768	$\delta(OCO)\ v(CN)$ **z**

Table 3-4 Vibrational frequencies of Alanine on Pd(111) at 300 K. The experimental frequencies are compared with those of alanine on Cu(110) at low coverages,[44-45] where it forms η^3-alaninate, nickel alaninate,[46] and vibrational spectra of the zwitterionic form of alanine.[47] The assignments are given in the last column.

Additional less intense vibrational modes are detected at 2938 and 2889 cm^{-1} in the C-H stretching region. The intensity of these features varies slightly with alanine exposure. A shoulder is detected on the broad, intense asymmetric acetate mode at ~

1565 cm^{-1}, due to the NH$_2$ or NH$_3^+$ groups. A sharp feature also appears as shoulder on

the ~1402 cm^{-1} peak at ~1374 cm^{-1}, assigned to a methyl deformation mode (Table 3-4),

that only varies slightly in intensity as a function of alanine coverage. A broad feature is

also found at ~1101cm^{-1} at the highest alanine exposure and a small peak is observed at

922 cm^{-1} with an intensity that varies only slightly with coverage due to either the modes

involving C-N stretching in the anion or methyl or ammonium rocking modes in the

zwitterions. Finally a mode is detected at ~770 cm^{-1} due to either a COO bending (for the

anion) or CN stretching (for the zwitterion) mode. Thus, alanine contains only

carboxylate groups (giving modes at 1606 and 1402 cm^{-1}), in the anionic and zwitterionic

(with an ammonium group, 3326 and 3183 cm^{-1}) forms.

3.4.4 Scanning Tunneling Microscopy

Scanning tunneling microscopy images are collected following alanine adsorption

on Pd(111) under various dosing conditions. Adsorption of alanine on Pd(111) at low

temperatures (~120 K) resulted in a random surface distribution as shown in Figure 3-

11(a). Adsorption of high coverages of alanine at slightly above room temperature (~ 310

K) and scanning at room temperature resulted in polymerized structure on the surface as

shown in Figure 3-11 (b).The approximate sizes of the polymer islands are about ~3 nm

covering the whole surface and no individual molecules or any ordered structures are

found.
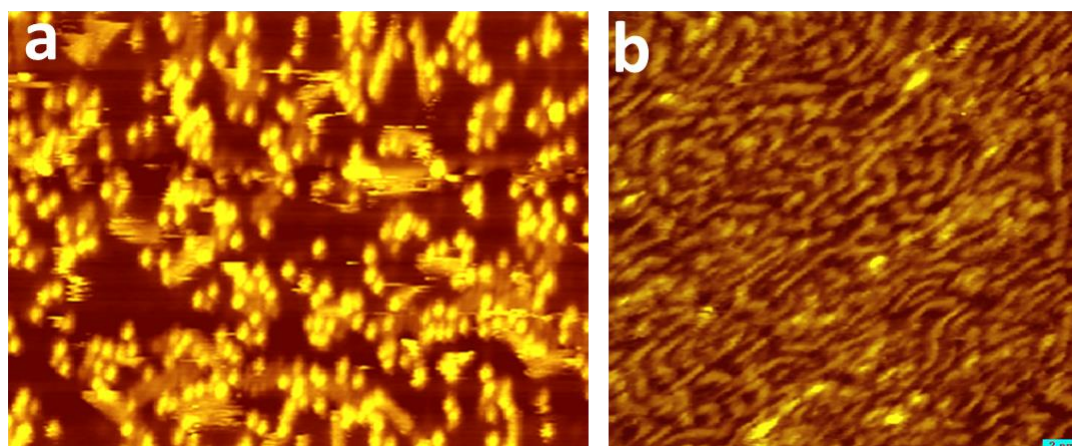
Figure 3-11 Alanine surface structures on Pd(111) (a) disordered over layer when dosed at ~120 K (b) polymerized structure when dosed high coverages at ~310 K (V_b= - 0.16 V, I_t= 40 pA)

However, initial adsorption of an absolute coverage of ~0.09 ML of alanine (measured from the STM image, where absolute coverages are referred to the number of surface palladium atoms) at ~270 K and then cooling the sample down to 120 K and imaging quickly at this temperature to avoid background contamination produced the STM images displayed in Figure 3-12. This resulted in some thermal drift while imaging. The orientation of the close packed $< 1\bar{1}0 >$ direction of the underlying lattice were found from the high resolution images of the clean surface. While a few isolated species and some alanine clusters are detected, the surface consists primarily of dimers. Vectors joining the bright spots of the dimer images are oriented at around $30 \pm 5^\circ$ relative to the closed packed direction although some thermal drift in the images results in some uncertainty in this value. Nevertheless, the image in Figure 3-12 provides clear evidence for the initial formation of dimeric species.
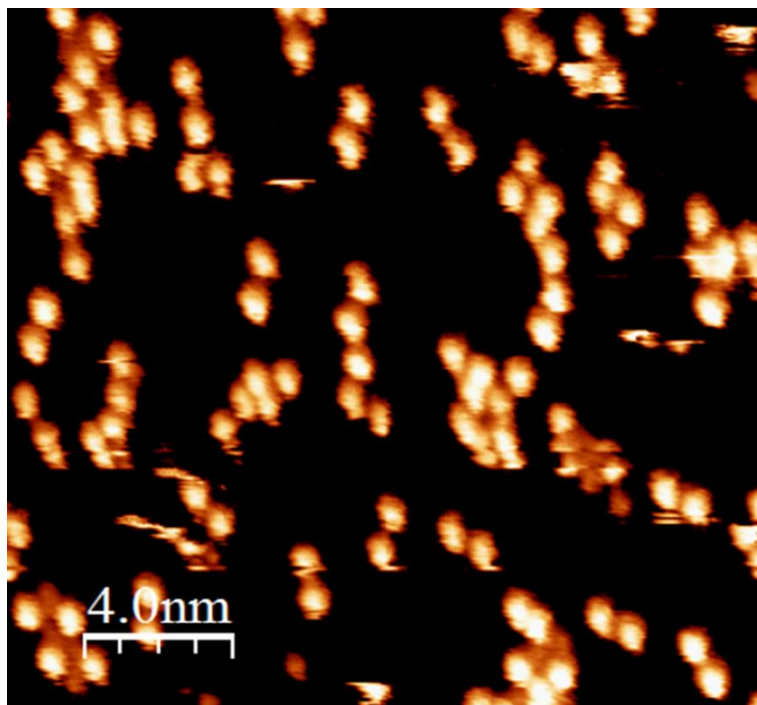
Figure 3-12 STM image of an absolute coverage of 0.09 ML of alanine on Pd(111) dosed at 270 K and then cooled to 120 K after 500 s at 270 K, and the sample imaged at 120 K. (V_b= 0.1 V, I_t= 187 pA).

More complex surface structures form when a Pd(111) surface is dosed and

imaged at ~290 K. A typical STM image for an absolute alanine coverage of 0.052 ML,

collected under this experimental condition is given in Figure 3-13. The inset shows an

atomic resolution image of the clean Pd(111) surface and the three equivalent $< 1\bar{1}0 >$

directions are indicated by arrows of different colors. Two different structural motifs can

be identified in this image. The first consists of dimer rows. Many of these comprise

hexamers (highlighted by rectangular boxes) although a number of longer dimer chains

also form. In all the cases, the long axes of the chains are oriented along one of the

$< 1\bar{1}0 >$ direction, so that a vector perpendicular to the chains is oriented at 30° to the

closed packed direction. Three of these dimer rows are indicated in the image by color-

coded arrows to the corresponding $< 1\bar{1}0 >$ direction. The intermolecular spacing along

the chains is 0.59 ± 0.02 nm, and perpendicular to the chain is 0.58 ± 0.01 nm. It can also

be seen that some of the dimer chains are terminated by a single alanine molecule and

some of these terminations are indicated by triangles. These terminal single molecules are

also sometimes associated with two rows with different directions as in the cases

indicated by the white stars in the image.
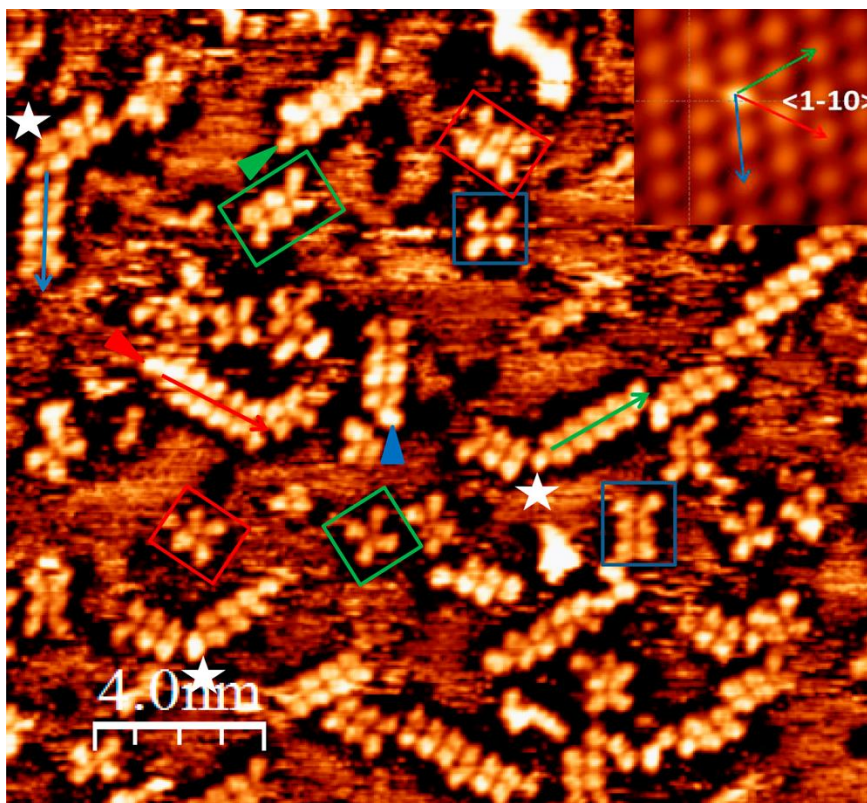
Figure 3-13 STM image of an absolute coverage of 0.052 ML of alanine on Pd(111) dosed and imaged at 290 K (V_b= -161 mV, I_t= 20.0 pA). (Image reproduced with permission ©) [30,55]

In addition to the dimer rows, distinct, rectangular tetramers are also observed

(highlighted by squares color-coded depending on their orientation). In all the cases, the

tetramers have one edge oriented along the close packed directions, with the other edge

oriented at $30°$ to this direction. The spacing between the brightest portions of the

tetramers is higher than in the dimer rows (0.65 ± 0.02 nm). Similar structures form at

higher and lower doses following alanine dosing at 290 K. However, when the surface approaches saturation the dimer row structures evolve into a disordered surface.

While the tetramers and dimer rows are stable over long period of scanning, some mobility of the tetramers was noted as illustrated by consecutive images in Figure 3-14 where image (b) was collected 104 s after the image (a). Examples of the observed motions are indicated in the image and highlighted by squares. Tetramer 1 remains in the same position, while tetramer 2 translate in a direction diagonal to the tetramer 1, and tetramer 4 translate along the direction parallel to its edge. Rotation of the tetramers is also found as illustrated by tetramer 3, which rotate by 30° in a clock wise direction.
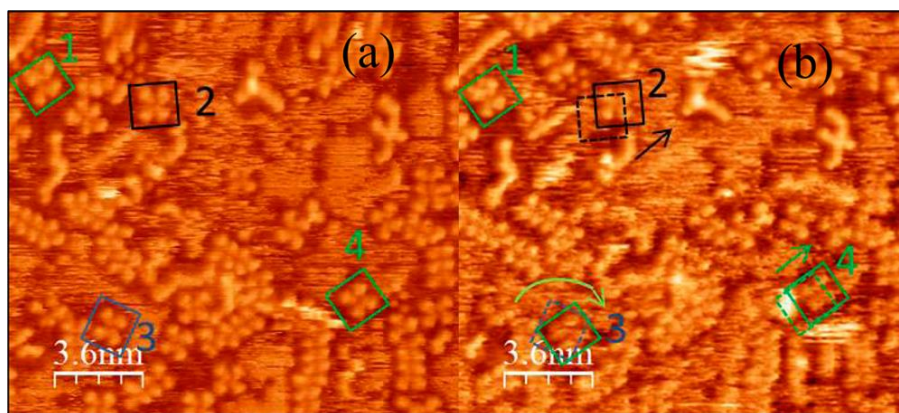
Figure 3-14 Two consecutive images of alanine on Pd(111) dosed and imaged to 290 K (V_b= -161mV, I_t= 20.0 pA), where image (b) was collected 104 second after image (b). The squares represent for arbitrarily chosen tetramers illustrating the motion of the tetramers. (Reproduced with permission from A. Boscoboinik PhD Thesis 2010 ©) [30,55]

3.5 Discussion

TPD and XPS studies show that amino acids are stable on the surface at ~300 K and decomposes at higher temperatures to mostly produce H_2, CO and CO_2 which is consistent with the previous results when amino acids were dosed at ~100 K.[26] Both anionic and zwitterionic form of amino acids were detected on the Pd(111) surface by

XPS. Assuming that all the amino acids would form similar chemistry on the surface, a through characterization of alanine was done by RAIRS, STM and DFT. The presence of zwitterionic form of alanine was evidenced by RAIRS from the NH_3^+ stretching modes at ~3226 and 3183 cm^{-1} and from the peaks at the ~ 401.4 eV BE feature in the N 1s XPS spectra. In order to gauge the relative stability of the anionic and zwitterionic alanine on Pd(111), DFT calculations were performed for isolated alanine species on a 7×7 slab corresponding to an absolute coverage of 0.02 ML, close to the experimental value. A relative large cell was used for the calculation to provide sufficient space for the subsequent calculations for the alanine derived dimers and tetramers to enable energies to be compared for the calculations of identical substrate cell sizes. Note that, while there may be some errors in the absolute energy of the different structures, relative energies for different alanine derived structures are reasonably accurate.

The calculations yielded adsorption energy of -47 kJ/mol for zwitterionic alanine and -68 kJ/mol for anionic alanine (with a co-adsorbed hydrogen on a 3-fold hollow site of the unit cell). Thus the anionic alanine is ~21 kJ/mol more stable than the zwitterionic form. Similar calculations for a slightly higher coverage using a 6×6 unit cell yielded similar results where the anionic species are ~22 kJ/ mol more stable than the zwitterionic species. DFT calculation by Sholl and James using a more crowded surface(using a 3×3 surface unit cell) yielding an absolute coverage of 0.111 ML shows that anionic species are more stable than zwitterionic species by ~44 kJ /mol.[18] While this is larger than the values found at low coverage, perhaps suggesting a strong interaction between the adsorbed species on surface.

The resulting calculated structures are depicted in Figure 3-15 where Figure 3-15

(a) shows the structure of anionic species and Figure 3-15(b) shows the zwitterionic species. In agreement with the work by Sholl and James, in both cases, the individual amino acids bond to Pd(111) through the carboxylate oxygen atoms located near atop sites of Pd and the amine group. The amine group is bonded to the palladium surface for both anionic and zwitterionic species. However, the amine group has a lone pair of electrons available on the nitrogen atom, which allows a strong bonding to the surface, while this bond will be weaker for an NH_3^+ group, accounting for the energy difference between the two forms.
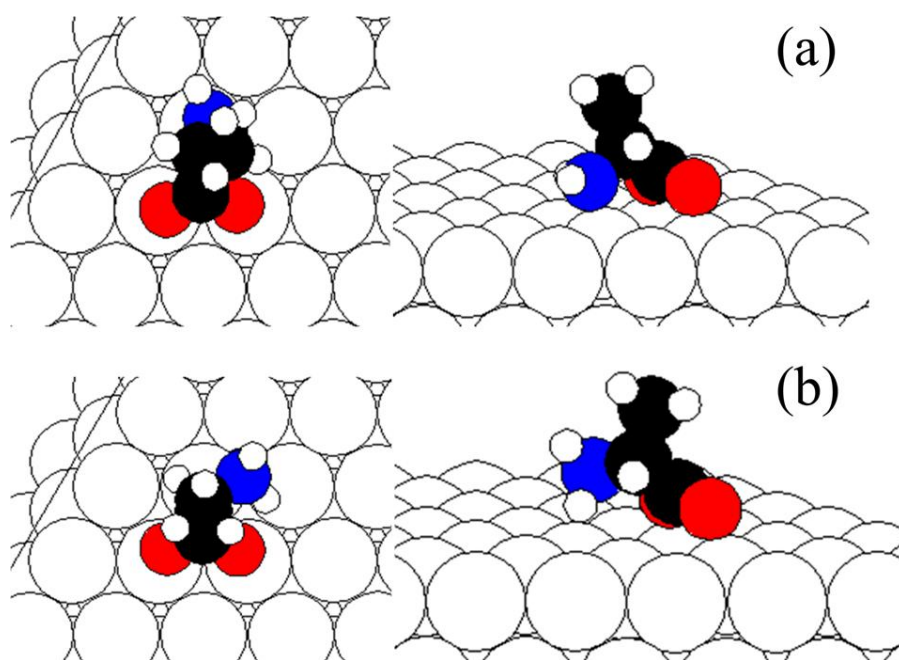
Figure 3-15 Structures of alanine on Pd(111) calculated for a 7×7 using cell from DFT calculations showing the top and side views for (a) the anionic and (b) the zwitterionic forms.

This result contradicts the XPS and RAIRS results, which provides clear evidence for the presence of both zwitterionic and anionic species on palladium surface. However STM shows the formation of dimers when the surface was dosed at ~270 K and cooled to ~120 K for imaging. Therefore a possible thought for the observation of zwitterions was

that the interaction between the anionic and zwitterionic alanine might lead to the formation of dimer pairs which stabilizes the zwitterionic form of alanine on the surface. Accordingly, the energies of alanine dimers were calculated using DFT for configurations consisting of two anions (A-A), two zwitterions (Z-Z), and one each, zwitterion and anion (Z-A) as shown in Figure 3-16. The structures were built by using the most stable structure of individual anion and zwitterion but carboxylate group was reoriented so that it moves away from the surface to interact with the amine or ammonium ion in the adjacent molecule.

It was fond that A-A dimer was less stable by ~15 kJ/mol than the individual anions. This suggests that the NH_2 – surface interaction is sufficiently strong to inhibit its reorientation. The dimer consisting of mixed Z-A pair was more stable by ~35 kJ/mol than the isolated species. The dimer consists of Z-Z pair showed similar stabilization energy as Z-A pair suggesting similar interaction between the Z-A and Z-Z dimers. The resulting most stable dimer configurations, along with their simulated images are given in Figure3-16. In all the cases, the simulated images resemble the experimental images of the dimer pairs and the long axes are similarly oriented at $30^{°}$ with respect to the close packed direction. From energetic point of view the formation of A-A dimer pairs are excluded while Z-Z and Z-A pairs are considered to be stable on the surface. However, since individual zwitterions are less stable on the surface compared to its anions, it is very likely that individual molecules stay on the surface predominately as anions. Therefore to form a A-A or Z-A dimer pair the more stable anion has to convert to less stable zwitterion which costs ~21 kJ/mol per one conversion. To construct one Z-A dimer pair one zwitterion needs to be formed which costs ~21 kJ/mol, thus energy for Z-A dimer

formation is exothermic by ~14 kJ/mol, while converting two zwitterions to make a Z-Z

dimer results in being endothermic by ~7kJ/mol. Further evidence to exclude the

possibility of Z-Z dimer pairs comes from the XPS and IR results which suggest the

presence of both zwitterions and anions.
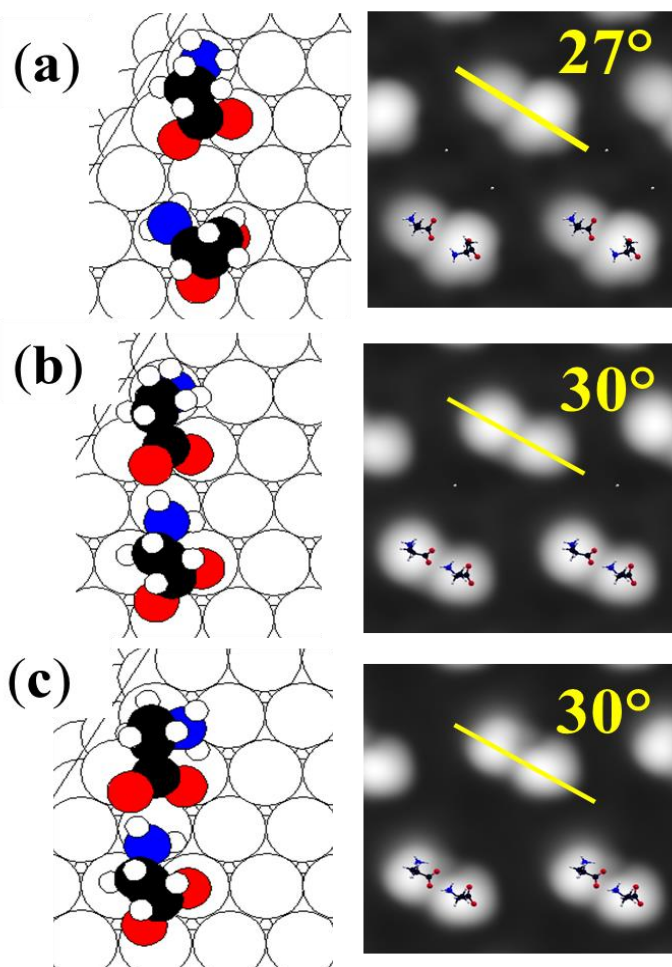
Figure 3-16 Simulated structures and STM images of alanine dimers on Pd(111) for (a) a fully anionic alanine dimer (b) mixed zwitterionic-anionic alanine dimer and (c) fully zwitterionic alanine dimer.

The Z-A dimer (Figure 3-16(b)) has one oxygen atom of the carboxylate group

moved away from the Pd atop site which is in accord with the detection of asymmetric

carboxylate stretch ($v_{as}(COO^-)$) at ~1606 cm^{-1} in RAIRS (Figure3-10, Table 3-4). The

average spacing between the lobes of all the most stable dimers in the simulated images

are 0.54 ± 0.02 nm. The Z-A dimer pair is stabilized by an interaction between the

carboxylate and the NH_3^+ groups, causing the carboxylate group to reorient. While there

is clearly a hydrogen bonding interaction between the two groups, the interaction is more

likely to have a significant electrostatic component between a formally negatively

charged COO^- and a positively charged NH_3^+. This provides sufficient stabilization

energy to overcome the penalty associated with cleaving an O-Pd bond in the carboxylate

group. Dimer structures have also been observed for amino acids adsorbed on gold.[54]

However, the interaction in this case is between the COOH group of the molecular form

of the amino acid, which is bonded to the surface via the NH_2 group, and is thus distinct

from the dimer species identified here.

Dosing and imaging alanine at ~290 K (Figure 3-13) results in the formation of

tetramers with one edge aligned along the $< 1\bar{1}0 >$ direction and the dimer chains with

the long axes of the chains oriented along the $< 1\bar{1}0 >$ direction. While these structures

do show some order, the coherence length perpendicular to the chain (of ~0.5 nm) will

not be sufficient to produce LEED structures as found experimentally by L. Burkholder.

The assembly of formation of dimer chains and tetramers are kinetically limited since

adsorbing alanine at ~270 K and immediately cooling down to ~120 K resulted in the

formation of dimers as shown in Figure 3-12. The motion of the tetramers is observe at

~290 K, where both translational and rotational motions are observed over a period of

~104 s. This suggests that the tetramers and dimer rows assemble relatively slowly from

Z-A dimers.

The geometries of the dimers were used to form tetrameric assemblies and their

stabilization energies calculated using DFT. Here, the initial geometries, based on the

dimer structures, were allowed to relax. For completeness, tetrameric structures comprising four anionic and four zwitterionic species were also explored. The tetrameric stabilization energy was calculated from $E_{ads, tetramer} - 4 E_{ads, monomer}$. As expected based on the energies calculated for the A-A dimers, all fully anionic tetramers were unstable while fully zwitterionic tetramers were found to be stable. However, all of the stabilization energies were less than ~21 kJ/mol (the largest being 19 kJ/mol), indicating that their formation from anionic alanine is endothermic. Accordingly, the energies of tetramers constructed from Z-A dimers were calculated by DFT. The resulting most stable structure and corresponding simulated images are given in Figure 3-17 and the stabilization energies are summarized in Table 3-5. Structure 1 comprise parallel Z-A dimers and has a calculated energy of -15.3 kJ/mol/molecule. Structure 2 and 3 are constructed from antiparallel Z-A dimers in different adsorption sites and have calculated stabilization energies of -16.2 and -17.6 kJ/mol/molecule, respectively. Structure 4 is similar to structure 3, but with molecules in the dimer placed closer to each other and yields the most stable stabilization energy of -25.8 kJ/mole/molecule. This structure is stabilized by the interaction between the NH_2 and NH_3^+ groups and carboxylate oxygen atoms. Taking into account for the energy needed to convert an anion to zwitterion, the formation energy of the mixed Z-A tetramers are exothermic by ~6kJ/mol/molecule for structure 1, 2 and 3 and by ~-15 kJ/mol/molecule for structure 4. In all cases the simulated STM images have one edge oriented at 30° with respect to the $< 1\bar{1}0 >$ direction.
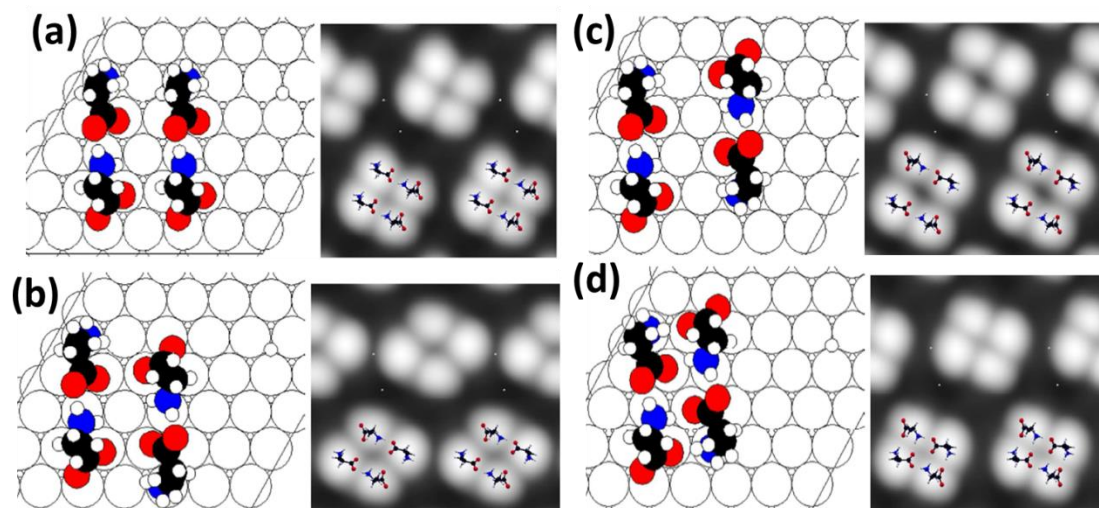
Figure 3-17 Structures (left panels) and simulated STM images (right panels) of mixed zwitterionic-anionic tetramers (a) structure1 (b) structure 2 (c) structure 3 (d) structure 4

anionic-zwitterionic tetramer, Configuration	tetramer stabilization energy, kJ/mol/molecule
structure 1	-15.3
structure 2	-16.2
structure 3	-17.6
structure 4	-25.8

Table 3-5 Energies of the most stable alanine tetramer structures

However, only structure 1 and 3 display rectangular images, with one edge parallel to $< 1\bar{1}0 >$ direction and the other edge oriented $30^{°}$ to it. Structure 1 consists of Z-A dimer pairs aligned in the same direction and structure 3 and 4 have Z-A dimer pairs aligned in the opposite direction. The spacing between the lobes in each of the calculated tetramers is ~0.55 nm. Both the shape and spacing of the simulated images differ from the isolated tetramers (highlighted by square boxes in Figure 3-13) observed experimentally.

However, the orientations, imaged intermolecular spacing and appearance of the

images are strikingly similar to the experimental images of alanine hexamers (highlighted by rectangular boxes in Figure 3-13) and dimer rows. Accordingly, DFT calculations were performed for dimer rows constructed of antiparallel Z-A dimers and parallel Z-A dimers. In these calculations, the surface unit cell was constructed to the repeat distances for each of the structures along the dimer rows. The most stable structures and the simulated STM images are displayed in Figure 3-18. Figure 3-18(a) shows the structure of the parallel Z-A dimer row as well as the unit cell used for the calculation, which yields stabilization energy of ~10 kJ/mol/molecule. The corresponding most stable structure for antiparallel Z-A dimers is shown in Figure 3-18(b), where the unit cell used for the calculation is also shown. This is a more stable structure and its formation is exothermic by ~15 kJ/mol/molecule. Clearly, in spite of the antiparallel dimer rows being more stable, the simulated images of the parallel dimer rows most closely resemble with the experimental dimer rows. This is emphasized by the plots shown in Figure 3-18(c) that shows the calculated profile along and perpendicular to the dimer rows. The spacing in the simulated image along the dimer rows is ~0.56 nm and perpendicular to them is ~0.6 nm which is in excellent agreement with the experimentally measured values. In addition, the simulated images of the dimer rows are oriented with the long axes of the chains along the $< 1\bar{1}0 >$ direction as found experimentally. This suggests that the dimer rows consist of parallel Z-A dimers.
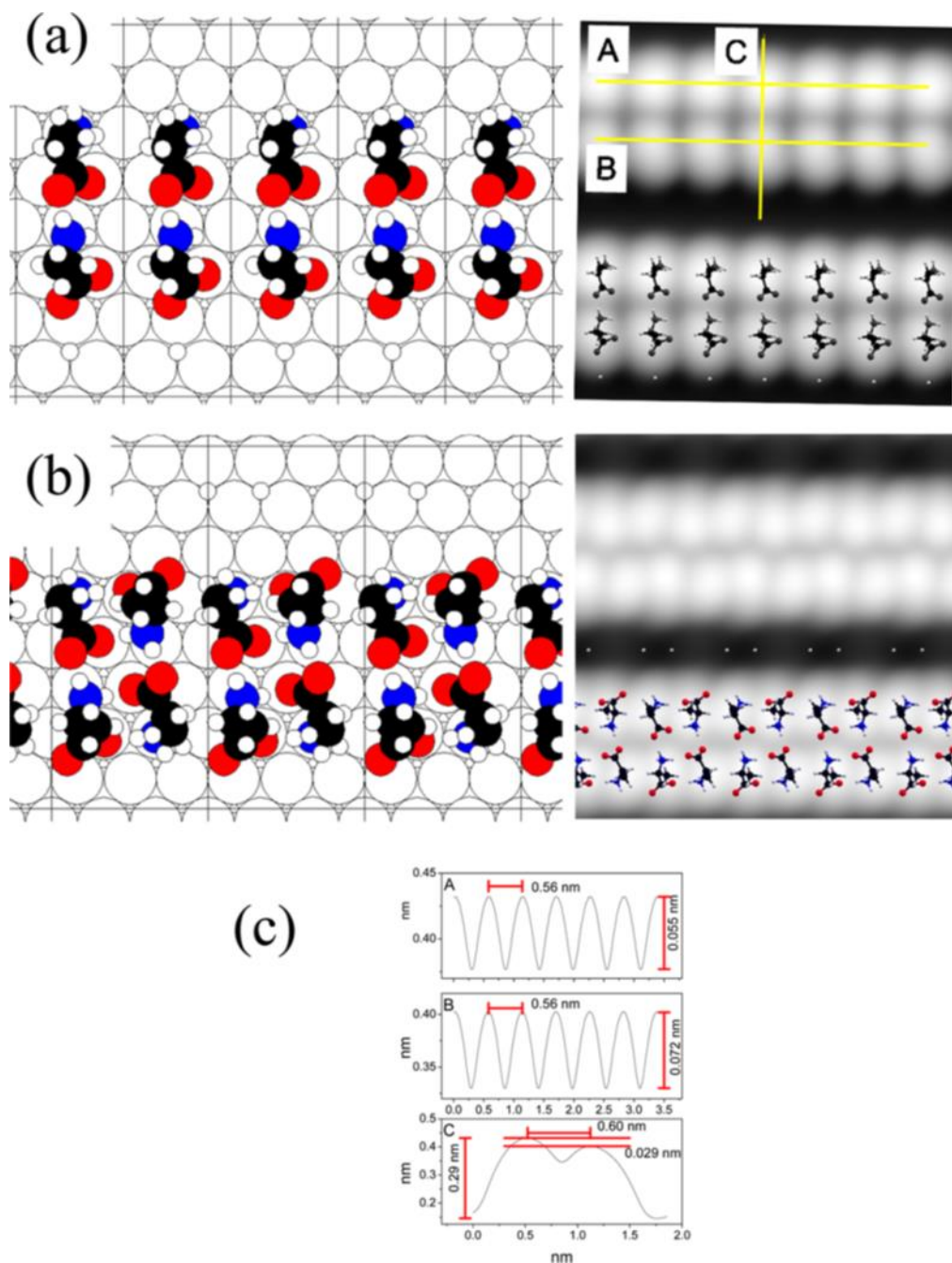
Figure 3-18 Structures (left panels) and simulated STM images (right panels) of mixed zwitterionic-anionic dimer rows showing (a) structures constructed from parallel Z-A dimers, (b) antiparallel Z-A dimers. Figure (c) plots the profiles along lines indicated by A, B and C in the simulated images in Figure 3-18 (a).

As noted above, none of the simulated images of the most stable mixed Z-A

tetramer structures agree with the isolated tetramers found experimentally. However, a

concerted rotation of the lower three alanines in the, antiparallel Z-A tetramers (Figure 3-

17(b)) by 30° enables the NH_3^+ groups to simultaneously interact with the carboxylate groups on the adjacent, anionic alanine species. Note that a similar concerted rotation is observed for the tetramers (Figure 3-14). The rotation is illustrated in Figure 3-19(a), where the tetramer (A) reproduce the structure of the mixed Z-A tetramer from Figure 3-17(b) and shows the structure resulting from the concerted motion of three alanines to yield the structure (B).
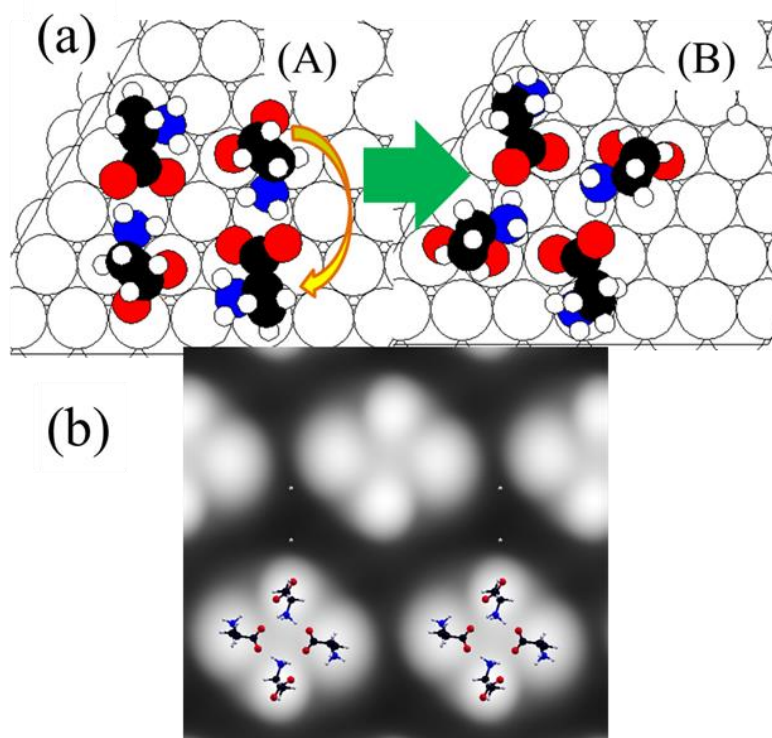
Figure 3-19 (a) Depicts the transformation of an alanine tetramer constructed from antiparallel A-Z dimers (Structure (A)) into a more stable tetramer that enables simultaneous interaction between a NH_3 group on the zwitterions with two oxygen atoms on adjacent carboxylate groups in anionic alanine (Structure (B)). Figure (b) shows the simulated STM image of the tetramer structure shown in Structure (B)

This process is calculated to be slightly exothermic by ~2 kJ/mol. The simulated image is shown in Figure3-19(b). The orientation and shape of the simulated images now agree well with the experimental images of the isolated tetramers and has the correct orientation with respect to the underlying lattice.

3.6   Conclusions

Both anionic and zwitterionic forms of amino acids are spectroscopically found on Pd(111) surface and the proportion of zwitterions to anions changes as a function of coverage. A thorough characterization of the simplest chiral amino acid alanine by DFT shows that isolated anionic species are significantly more stable than the zwitterions due to the bonding of the amine group to the surface. However, the zwitterions are stabilized by forming a bond between the NH_3^+ group in the zwitterion and one of the oxygen atoms of a reoriented carboxylate group of an anion. This result in accord with the detection of a NH_3^+ groups by XPS and RAIRS as well as the detection of a asymmetric carboxylate stretching mode in the RAIRS. This stable dimeric unit forms the basis for the complex structures seen in STM following alanine adsorption at room temperature. Parallel A-Z dimer pairs can form dimer rows that often lead to the formation of hexamers and longer dimer rows. Isolated tetramers also form on the surface from a concerted motion of three amino acid molecules in an antiparallel Z-A tetramers. These assignments are based on both the energies calculated by DFT and comparing the simulated images to the experimentally observed images. In spite of the fact that the dimer rows which consist of antiparallel Z-A pairs are energetically more favorable, those structures are excluded by comparison of the simulated image with the experimental image. One possible origin for the appearance of apparently less stable dimer row structure is that the conversion of tetramers formed from antiparallel arrangements of a Z-A pairs into the isolated interacting tetramers is sufficiently facile that they form preferentially to assembling as dimer rows. This concerted motion in the case of the parallel Z-A dimer rows does not result in the formation of such stable

structures, thereby leaving them available to coalesce into dimer rows. These structural results set the stage for measuring the enantioselectivity of amino acid modified surfaces using chiral probes to relate the presence of such surface structures to enantioselectivity and to establish whether they can act as chiral templates.

3.7   References

1.   Hazen, R. M.; Filley, T. R.; Goodfriend, G. A., Selective adsorption of l- and d-amino acids on calcite: Implications for biochemical homochirality. *Proceedings of the National Academy of Sciences* **2001,** *98* (10), 5487-5490.

2.   Duthaler, R. O., Proline-Catalyzed Asymmetric α-Amination of Aldehydes and Ketones—An Astonishingly Simple Access to Optically Active α-Hydrazino Carbonyl Compounds. *Angewandte Chemie International Edition* **2003,** *42* (9), 975-978.

3.   Levina, A.; Muzart, J., Enantioselective allylic oxidation in the presence of the Cu(I)Cu(II)-proline catalytic system. *Tetrahedron: Asymmetry* **1995,** *6* (1), 147-156.

4.   List, B., Proline-catalyzed asymmetric reactions. *Tetrahedron* **2002,** *58* (28), 5573-5590.

5.   Tóth, G.; Kovács, A.; Tarnai, T.; Tungler, A., Stereochemistry of the enantioselective reductive alkylation of proline with ketones. *Tetrahedron: Asymmetry* **1993,** *4* (3), 331-338.

6.   Tungler, A.; Tarnai, T.; Máthé, T.; Petró, J., Enantioselective hydrogenation of acetophenone in the presence of S-proline. *Journal of Molecular Catalysis* **1991,** *67* (2), 277-282.

7.   Tungler, A.; Tarnai, T.; Máthé, T.; Petró, J., Enantioselective hydrogenation of ethyl pyruvate. *Journal of Molecular Catalysis* **1991,** *70* (3), L5-L8.

8.   Tungler, A.; Fogassy, G., Catalysis with supported palladium metal, selectivity in the hydrogenation of C:C, C:O and C:N bonds, from chemo- to enantioselectivity. *Journal of Molecular Catalysis A: Chemical* **2001,** *173* (1-2), 231-247.

9.   Szöllösi, G.; Somlai, C.; Szabó, P. T.; Bartók, M., Heterogeneous asymmetric reactions: Part 21. Amino acid derived modifiers in the enantioselective hydrogenation of ethyl pyruvate over supported platinum catalyst. *Journal of Molecular Catalysis A:*

Chemical **2001,** *170* (1–2), 165-173.

10.   Tungler, A.; Kajtar, M.; Mathe, T.; Toth, G.; Fogassy, E.; Petro, J., Enantioselective hydrogenation of α-β-unsaturated ketones. *Catalysis Today* **1989,** *5* (2), 159-171.

11.   Marti, E. M.; Barlow, S. M.; Haq, S.; Raval, R., Bonding and assembly of the chiral amino acid S-proline on Cu(110): the influence of structural rigidity. *Surface Science* **2002,** *501* (3), 191-202.

12.   Barlow, S. M.; Raval, R., Complex organic molecules at metal surfaces: bonding, organisation and chirality. *Surface Science Reports* **2003,** *50* (6-8), 201-341.

13.   Barlow, S. M.; Louafi, S.; Le Roux, D.; Williams, J.; Muryn, C.; Haq, S.; Raval, R., Polymorphism in supramolecular chiral structures of R- and S-alanine on Cu(110). *Surface Science* **2005,** *590* (2-3), 243-263.

14.   Rankin, R. B.; Sholl, D. S., Structure of enantiopure and racemic alanine adlayers on Cu(110). *Surf Sci* **2005,** *574* (1), L1-L8.

15.   Rankin, R. B.; Sholl, D. S., First-principles studies of chiral step reconstructions of Cu(100) by adsorbed glycine and alanine. *J. Chem. Phys.* **2006,** *124* (7), 074703.

16.   Gladys, M. J.; Stevens, A. V.; Scott, N. R.; Jones, G.; Batchelor, D.; Held, G., Enantiospecific adsorption of alanine on the chiral Cu{531} surface. *Journal of Physical Chemistry C* **2007,** *111*, 8331-8336.

17.   Humblot, V.; Methivier, C.; Raval, R.; Pradier, C. M., Amino acid and peptides on Cu(110) surfaces: Chemical and structural analyses of L-lysine. *Surface Science* **2007,** *601* (18), 4189-4194.

18.   James, J. N.; Sholl, D. S., Density Functional Theory studies of dehydrogenated and zwitterionic glycine and alanine on Pd and Cu surfaces. *Journal of Molecular Catalysis A-Chemical* **2008,** *281* (1-2), 44-48.

19.   Cheong, W. Y.; Huang, Y.; Dangaria, N.; Gellman, A. J., Probing Enantioselectivity on Chirally Modified Cu(110), Cu(100), and Cu(111) Surfaces. *Langmuir* **2010,** *26* (21), 16412-16423.

20.   Clegg, M.; Morales de la Garza, L.; Karakatsani, S.; King, D.; Driver, S., Chirality in Amino Acid Overlayers on Cu Surfaces. *Top Catal* **2011,** *54* (19-20), 1429-1444.

21.   Han, J. W.; James, J. N.; Sholl, D. S., Chemical speciation of adsorbed glycine on metal surfaces. *J. Chem. Phys.* **2011,** *135* (3).

22.   Mark, A. G.; Forster, M.; Raval, R., Recognition and Ordering at Surfaces: The Importance of Handedness and Footedness. *ChemPhysChem* **2011,** *12* (8), 1474-1480.

23.   Forster, M.; Dyer, M. S.; Persson, M.; Raval, R., Tailoring Homochirality at Surfaces: Going Beyond Molecular Handedness. *Journal of the American Chemical Society* **2011,** *133* (40), 15992-16000.

24.   Ghiringhelli, L. M.; Schravendijk, P.; Delle Site, L., Adsorption of alanine on a Ni(111) surface: A multiscale modeling oriented density functional study. *Physical Review B* **2006,** *74* (3), 035437.

25.   Seljamäe-Green, R. T.; Simpson, G. J.; Grillo, F.; Greenwood, J.; Francis, S. M.; Schaub, R.; Lacovig, P.; Baddeley, C. J., Assembly of a chiral amino acid on an unreactive surface:(S)-proline on Au (111). *Langmuir* **2014,** *30* (12), 3495-3501.

26.   Gao, F.; Li, Z. J.; Wang, Y. L.; Burkholder, L.; Tysoe, W. T., Chemistry of Alanine on Pd(111): Temperature-programmed desorption and X-ray photoelectron spectroscopic study. *Surface Science* **2007,** *601* (15), 3276-3288.

27.   Gao, F.; Wang, Y. L.; Burkholder, L.; Tysoe, W. T., Chemistry of L-proline on Pd(111): Temperature-programmed desorption and X-ray photoelectron spectroscopic study. *Surface Science* **2007,** *601* (17), 3579-3588.

28.   Gao, F.; Li, Z. J.; Wang, Y. L.; Burkholder, L.; Tysoe, W. T., Chemistry of glycine on Pd(111): Temperature-programmed desorption and X-ray photoelectron spectroscopic study. *Journal of Physical Chemistry C* **2007,** *111* (27), 9981-9991.

29.   Sutherland, I. M.; Ibbotson, A.; Moyes, R. B.; Wells, P. B., Enantioselective hydrogenation. I. Surface conditions during methyl pyruvate hydrogenation catalyzed by cinchonidine-modified platinum/silica (EUROPT-1). *J. Catal.* **1990,** *125* (1), 77-88.

30.   Mahapatra, M.; Burkholder, L.; Bai, Y.; Garvey, M.; Boscoboinik, J. A.; Hirschmugl, C.; Tysoe, W. T., Formation of Chiral Self-Assembled Structures of Amino Acids on Transition-Metal Surfaces: Alanine on Pd (111). *The Journal of Physical Chemistry C* **2014,** *118* (13), 6856-6865.

31.   Kresse, G.; Joubert, D., From ultrasoft pseudopotentials to the projector augmented-wave method. *Physical Review B* **1999,** *59* (3), 1758-1775.

32.   Blöchl, P. E., Projector augmented-wave method. *Physical Review B* **1994,** *50* (24), 17953-17979.

33.   Kresse, G.; Furthmüller, J., Efficient iterative schemes for ab initio total-energy calculations using a plane-wave basis set. *Physical Review B* **1996,** *54* (16), 11169-11186.

34.   Kresse, G.; Furthmüller, J., Efficiency of ab-initio total energy calculations for metals and semiconductors using a plane-wave basis set. *Computational Materials Science* **1996,** *6* (1), 15-50.

35.   Perdew, J. P.; Burke, K.; Ernzerhof, M., Generalized Gradient Approximation Made Simple. *Physical Review Letters* **1996,** *77* (18), 3865-3868.

36.   Ireta, J.; Neugebauer, J.; Scheffler, M., On the Accuracy of DFT for Describing Hydrogen Bonds: Dependence on the Bond Directionality. *The Journal of Physical Chemistry A* **2004,** *108* (26), 5692-5698.

37.   Tersoff, J.; Hamann, D. R., Theory of the scanning tunneling microscope. *Physical Review B* **1985,** *31* (2), 805-813.

38.   Bardeen, J., Tunnelling from a Many-Particle Point of View. *Physical Review Letters* **1961,** *6* (2), 57-59.

39.   W.A, H., Challenges and errors: interpreting high resolution images in scanning tunneling microscopy. *Progress in Surface Science* **2003,** *71* (5-8), 147-183.

40.   Hofer, W. A.; Garcia-Lekue, A., Differential tunneling spectroscopy simulations: Imaging surface states. *Physical Review B* **2005,** *71* (8), 085401.

41.   Eralp, T.; Shavorskiy, A.; Zheleva, Z. V.; Dhanak, V. R.; Held, G., Hydrogen Bond-Induced Pair Formation of Glycine on the Chiral Cu{531} Surface. *Langmuir* **2010,** *26* (13), 10918-10923.

42.   Eralp, T.; Cornish, A.; Shavorskiy, A.; Held, G., The Study of Chiral Adsorption Systems Using Synchrotron-Based Structural and Spectroscopic Techniques: Stereospecific Adsorption of Serine on Au-Modified Chiral Cu{531} Surfaces. *Top Catal* **2011,** *54* (19-20), 1414-1428.

43.   Jones, G.; Jones, L. B.; Thibault-Starzyk, F.; Seddon, E. A.; Raval, R.; Jenkins, S. J.; Held, G., The local adsorption geometry and electronic structure of alanine on Cu{1 1 0}. *Surface Science* **2006,** *600* (9), 1924-1935.

44.   Williams, J.; Haq, S.; Raval, R., The bonding and orientation of the amino acid l-alanine on Cu{110} determined by RAIRS. *Surface Science* **1996,** *368* (1–3), 303-309.

45.   Haq, S.; Massey, A.; Moslemzadeh, N.; Robin, A.; Barlow, S. M.; Raval, R., Racemic versus enantiopure alanine on Cu(110): An experimental study. *Langmuir* **2007,** *23* (21), 10694-10700.

46.   Percy, G. C.; Stenton, H. S., Infrared band assignments for L-alanine and the nickel(II) and copper(II) complexes of L- and [small beta]-alanine. *Journal of the Chemical Society, Dalton Transactions* **1976,** (23), 2429-2433.

47.   Cao, X.; Fischer, G., New infrared spectra and the tautomeric studies of purine and αl-alanine with an innovative sampling technique. *Spectrochimica Acta Part A: Molecular and Biomolecular Spectroscopy* **1999,** *55* (11), 2329-2342.

48.   Li, Z.; Gao, F.; Tysoe, W. T., Surface chemistry of acetic acid on clean and oxygen-covered Pd. *Surface Science* **2008,** *602* (2), 416-423.

49.   Calaza, F.; Tysoe, W. T.; Stacchiola, D. J., Stabilization of Carboxylate Surface Species on Pd(111). *Adsorpt. Sci. Technol.* **2011,** *29* (6), 603-611.

50.   James, J.; Saldin, D. K.; Zheng, T.; Tysoe, W. T.; Sholl, D. S., Structure and binding site of acetate on Pd(1 1 1) determined using density functional theory and low energy electron diffraction. *Catalysis Today* **2005,** *105* (1), 74-77.

51.   Stacchiola, D.; Calaza, F.; Burkholder, L.; Tysoe, W. T., Vinyl Acetate Formation by the Reaction of Ethylene with Acetate Species on Oxygen-Covered Pd(111). *Journal of the American Chemical Society* **2004,** *126* (47), 15384-15385.

52.   Stacchiola, D.; Calaza, F.; Burkholder, L.; Schwabacher, A. W.; Neurock, M.; Tysoe, W. T., Elucidation of the Reaction Mechanism for the Palladium-Catalyzed Synthesis of Vinyl Acetate. *Angewandte Chemie International Edition* **2005,** *44* (29), 4572-4574.

53.   Greenler, R. G., Infrared Study of Adsorbed Molecules on Metal Surfaces by Reflection Techniques. *J. Chem. Phys.* **1966,** *44* (1), 310-315.

54.   Kuhnle, A.; Linderoth, T. R.; Hammer, B.; Besenbacher, F., Chiral recognition in dimerization of adsorbed cysteine observed by scanning tunnelling microscopy. *Nature* **2002,** *415* (6874), 891-893.

55.   Boscoboinik, J.A.; **2010**. Ph.D. dissertation, University of Wisconsin-Milwaukee

Chapter 4

Adsorption and Reaction Pathways of a Chiral Probe Molecule, S-glycidol on a Pd(111) Surface

4.1 Introduction

This chapter presents the adsorption and reaction pathways of a chiral probe molecule S-glycidol on a Pd(111) surface. As stated previously, one of the most successful approach for performing enantioselective catalysis in the heterogeneous phase is chiral modification of an achiral surface, where an active metal surface is used in combination with a chiral organic molecule (chiral modifier) and the metal-modifier system works together as a chiral catalytic system. Accordingly, the first step in this approach is to examine the surface chemistry of the chiral adsorbate (chiral modifier) on the metal surface to understand the nature of interaction between the adsorbate and metal. Amino acids and tartaric acid have been used extensively on transition-metal surfaces as chiral modifiers and a significant amount of work have been done to explore the surface chemistry on different metal surfaces.[1-19] The surface chemistry of α-amino acids and tartaric acid have been explored on a Pd(111) surface and is shown in the Chapters 3 and 6 of this dissertation respectively.[20] However, the chiral expression of the modified surface requires an understanding of the interactions between the chiral modifier and a prochiral reactant or a chiral probe molecule. Simply put, it is important to verify how the modified surface interacts with another co-adsorbed chiral probe molecule. One strategy for exploring such interaction is to expose the modified surface to both the enantiomers of a suitable chiral molecule (chiral probe) and measure the relative coverage of both the

enantiomers of the probe on surface modified with adsorbate of same or opposite

chirality. Enantioselectivity is measured from the enantioselectivity ratio (ER) which is

defined as the ratio of the coverages of the two enantiomers of the probe for the same

coverage of the modifier;

$$ER = [\theta_R \text{ (probe)}/ \theta_R \text{ (modifier)}] / [\theta_S \text{ (probe)}/ \theta_R \text{ (modifier)}]$$

The experiments has been carried out previously by the Tysoe group to measure

the enantioselectivity ratio by using propylene oxide as a chiral probe on 2-butanol

modified Pd(111) surface.[21-22] Similar experiments are carried out on different probe-

modifier systems to measure enantioselectivity ratio for example: 2-butanol as chiral

probe on proline modified Pd(111) surfaces,[23-24] propylene oxide and 2-butanol as chiral

probes on Pt surfaces modified with amino acids and naphthylethylamine respectively.[25-27]

These experiments require accurate coverage measurements of the modifier and

probe and selection of a suitable chiral probe molecule is crucial. Propylene oxide is an

ideal probe molecule on Pd(111), since it undergoes negligible thermal decomposition,

thereby allowing coverages to be measured using TPD. In addition, the infrared spectrum

of propylene oxide on Pd(111) surface exhibits reasonably intense vibrational modes,

allowing IR spectroscopy to also be used to monitor adsorbate coverage.[28] Propylene

oxide contains only one potential hydrogen-bonding acceptor site (the epoxide oxygen),

thereby limiting its use for investigating the stereochemistry of chiral interactions.

Nevertheless, it has been demonstrated that the enantioselective adsorption of propylene

oxide on R- or S-2-butanol modified Pd(111) surfaces is controlled by the hydrogen

bonding interaction between the –OH group of 2-butanol with the epoxide oxygen of the

propylene oxide.[22] However, this approach would be rendered more versatile by being able to tune the location of the hydrogen bonding donor and acceptor sites on the probe molecule to provide a more detailed understanding of the nature and stereochemistry of the interactions that lead to enantioselectivity. An attractive strategy for achieving this would be to replace the methyl group in propylene oxide with a hydrogen bond donor/acceptor , by using a chiral probe such as glycidol, (alternatively, oxiranylmethannol, 2,3-epoxy-1-propanol or 3-hydroxypropylene oxide) in which the – CH_3 group of propylene oxide is replaced by a $-CH_2$ -OH group (Figure 4-1). This molecule has been used to explore chiral recognition in the gas phase.[29-30]
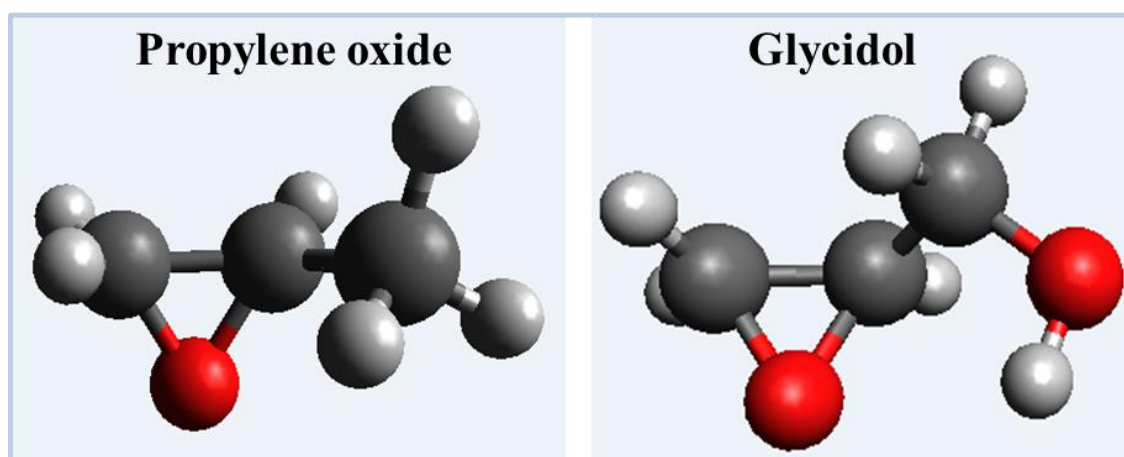
Figure 4-1 Chiral Probe propylene oxide *versus* glycidol

However, since alcohols undergo relatively facile deprotonation on Pd(111) [31-32] the resulting potentially stronger binding of the glycidate to the surface may facilitate side reactions that hamper its use as a chiral probe molecule because of the associated difficulties in precisely measuring adsorbate coverages using TPD. While such chemistry is anticipated to occur on Pd(111), if the extent of decomposition is minimal, it may still provide a useful chiral probe. In addition, insights into the reaction pathway of glycidol are useful for understanding non-selective pathways in the syntheses of ethylene oxide.[33-]

[34] Ethylene oxide decomposes on Pd(111) by an initial ring-opening reaction to form an oxametallacycle[35] that has been implicated as the central intermediate in the silver catalyzed epoxidation of ethylene.[36-37] Ethylene oxide forms from a reductive elimination of the oxametallacycle, which can also decompose by C-C or C-O bond scission or *via* a hydrogen-transfer reaction to produce acetaldehyde.[35] The desorption temperature of propylene oxide (~175 K) [38] on Pd(111) is lower than that of ethylene oxide (~255 K),[35] which facilitate the thermal decomposition in the latter case.

The goal of studying glycidol on Pd(111) [39] is twofold. The first is to characterize the adsorption of glycidol on Pd(111) and to measure its extent of thermal decomposition to explore whether it is suitable as a chiral probe molecule and second, to monitor the decomposition pathway on Pd(111) by using a combination of temperature programmed desorption spectroscopy and RAIRS.

4.2   Experimental Section

TPD and RAIRS experiments are carried out in the TPD chamber and RAIRS chamber respectively as described in Chapter 2. TPD experiments are performed by using a linear heating rate of ~3 K/s and the desorbing species were detected by using a Dycor mass spectrometer ,which was placed close to and in-line-of sight of the sample front face. Infrared spectra were collected using a Bruker Vertex infrared spectrometer operating at a resolution of 4 cm^{-1}, using a nitrogen cooled, mercury cadmium telluride detector, and spectra were typically collected for 1000 scans.

The Pd(111) single crystal was cleaned by using a standard procedure consisting of cycles of argon ion sputtering and annealing in 3×10^{-8} Torr of oxygen at 1000 K and the cleanliness was judged by using Auger spectroscopy or TPD after dosing with

oxygen, where the absence of CO desorption indicated that the sample was carbon free.

S-glycidol (Aldrich Chemical Co., 96%) was transferred to a glass vial and initially cleaned by several freeze pump thaw cycles in the gas line. The purity of the compound was checked by introducing a small amount to the vacuum chamber to see the mass spectrometer ionization fragmentation pattern. Glycidol has a vapor pressure of ~2 Torr at room temperature. The gas line was filled with glycidol and dosed onto the sample *via* a variable leak valve through a dosing tube directed towards the sample. Since this leads to an enhancement in the local pressure which has not been calibrated, glycidol exposures are quoted in units of Torr minutes, where the pressure is measured by a nude ionization gauge in the chamber.

4.3   Theoretical Methods

Density functional theory (DFT) calculations were performed with the projector augmented wave (PAW) method [40-41] using the Vienna ab initio simulation package, VASP. The exchange-correlation potential was descried using the generalized gradient approximation(GGA) of Perdew, Bruke and Ernzerhof.[42] A cutoff of 400 eV was used for the plane wave basis set, and the wave function and electron density was converged to within 1×10^{-5} eV. The first Brillouin zine was sampled with a $4 \times 4 \times 1$ Γ-centered k-point mesh. Geometric relaxations were considered to be converged when the force was less than 0.02 eV/Å on all unrestricted atoms.

4.4   Experimental Results

A series of TPD spectra were collected as a function of S-glycidol exposure for a number of key masses: 2 amu (hydrogen), 28 amu (glycidol and carbon monoxide), 29

amu, 30 amu (glycidol) and 46 amu (glycidol and ethanol) as shown in Figure 4-2. As indicated by the blank desorption profile (Figure 4-2(a)), there is a small amount of hydrogen adsorbs from the background. At a small exposure of glycidol, hydrogen desorbs at ~322 K and the desorption temperature decreases with increase in coverage to ~308 K. This temperature range is close to the temperature for hydrogen desorption on clean Pd(111), [43] indicating that the hydrogen is desorption rate limited, implying that this arises from S-glycidol that has undergone some decomposition below this temperature. The integrated intensity of the hydrogen desorption peak decreases with increase in coverage which suggests that the extent of decomposition decreases with increase in coverage. At higher coverages, a sharp peak appears at ~191 K which grows with exposure and is assigned to the presence of multilayer. At high coverages, a peak appears at ~452 K, indicative of the dehydrogenation of more strongly bound species or due to sub surface hydrogen. The corresponding 29 and 30 amu are the mass spectrometer ionizer fragments of molecular glycidol, which are shown in Figure 4-2(c) and (d) respectively. In both 29 and 30 amu, at low exposures a broad peak appears at ~250 K which is assigned to molecular glycidol desorption from the Pd(111) surface. This peak shifts to lower temperature (~244 K) at higher coverages suggesting some lateral interaction or geometry changes occurring at higher coverages.
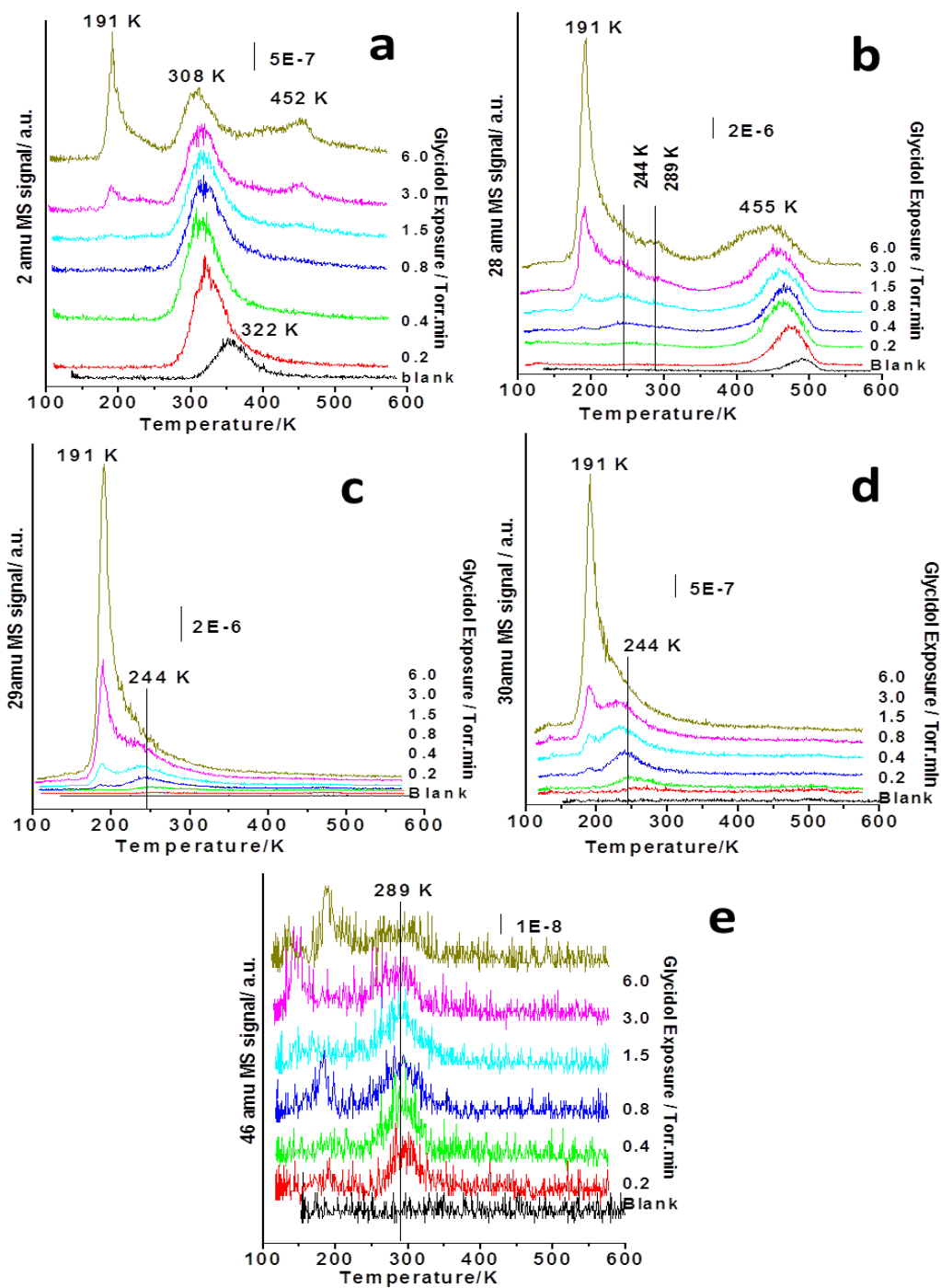
Figure 4-2 Temperature-programmed desorption profiles following the adsorption of S-glycidol on Pd(111) at ~120 K, as a function of S-glycidol dose (in Torr. min×10^{-9} Torr), which are displayed adjacent to the corresponding desorption profile. The results were collected using a heating rate of 3 K/s and by monitoring (a) 2 amu (b) 28 amu (c) 29 amu (d) 30 amu (e) 46 amu. Scale bars are included in each spectrum.

A second glycidol feature appears at higher coverages with a peak temperature of ~191 K, which continually grows in intensity, indicating the desorption from multilayer. The integrated intensities of the ~250 K and 191 K features vary in exactly the same manner with the increase in exposure, and the intensities at various masses also agree well with the mass spectrometer ionizer fragmentation pattern of S-glycidol, indicating that both the features are due to S-glycidol desorption. The corresponding 28 amu signals are plotted in Figure 4-2(b). The high temperature features at ~455 K is due to the CO desorption arising from S-glycidol decomposition. The ~191 K and 244 K peaks are assigned to the mass spectrometer ionization fragments of S-glycidol as discussed above, and an additional, relatively weak feature is detected at ~289 K at higher exposures. This is assigned to ethanol desorption as confirmed by the 46 amu desorption profile plotted in Figure 4-2 (e), since it shows a peak at a similar temperature. 46 amu (Figure 4-2(e)) is assigned to the desorption of ethanol as a thermal decomposition product of glycidol.

In order to gain insight into the surface reaction pathways, infrared spectra were collected following glycidol adsorption on Pd(111). Figure 4-3 shows an infrared spectra for multilayer glycidol adsorbed on Pd(111) at 100 K. The vibrational frequencies of the glycidol multilayer spectra is compared to the frequencies of the liquid glycidol [44] and summarized in Table 4-1. The close correspondence between the spectra of the adsorbed species and liquid glycidol confirms that pure S-glycidol adsorbs onto the surface.
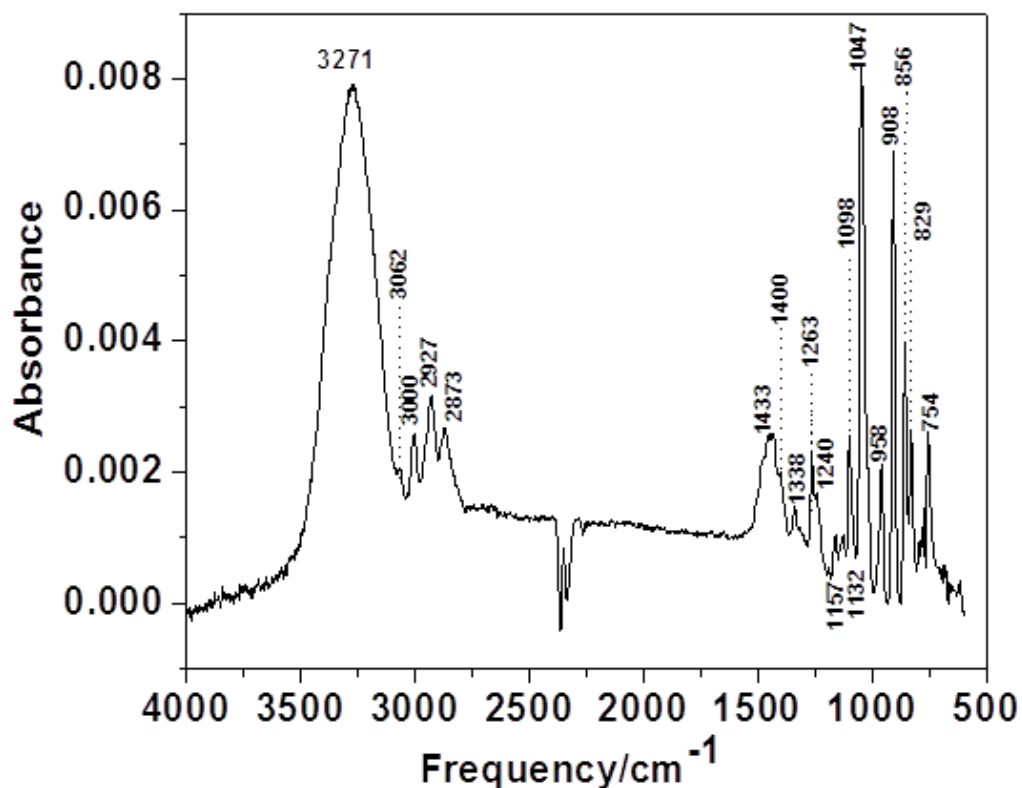
Figure 4-3 Reflection absorption infrared spectra for multilayer glycidol adsorbed on Pd(111) at 100 K

In order to understand the surface decomposition pathway and the formation of

intermediates, the Pd(111) surface was saturated with S-glycidol at ~100 K, and then

heated to various temperatures. The results of this experiment are displayed in Figure 4-4,

where the annealing temperatures are displayed adjacent to the corresponding spectra.

Essentially identical spectra were measured at ~100 K and 177 K, and the observed

frequency modes are identical to that observed with multilayer glycidol adsorption

(Figure 4-3, Table 4-1) .When the sample was annealed between 181 to 187 K, the IR

signal intensity decreases by a factor of 3 which is consistent with the desorption of

multilayer in TPD at ~191 K.
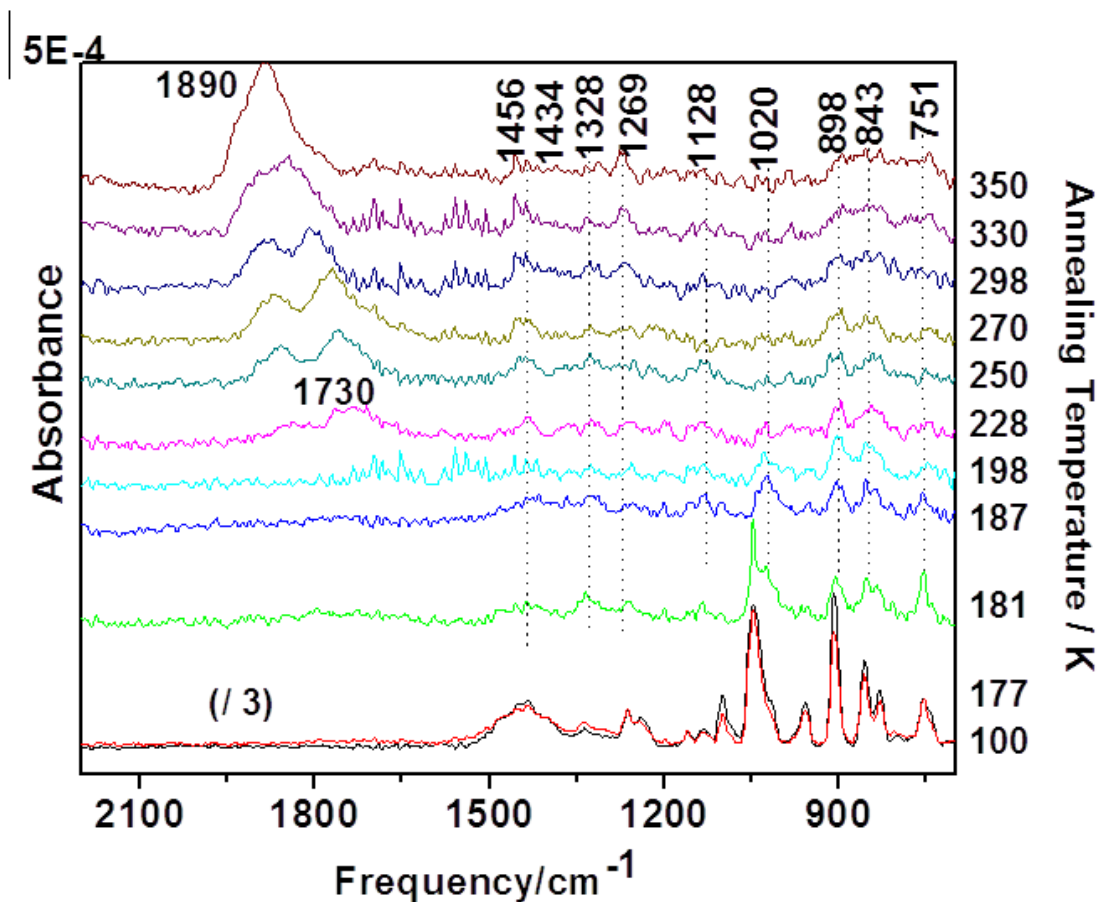
Figure 4-4 Reflection absorption infrared spectra of 2×10^{-9} Torr.min of S-glycidol adsorbed on Pd(111) at 100 K and then heated to various temperatures, which are indicated adjacent to the corresponding spectrum.

A number of relatively weak features are detected as the temperature increases from ~197 to 228 K at 751, 843, 898, 1020.1128, 1269 and 1328 cm^{-1} with a broad feature at 1430 cm^{-1}. The low signal intensity of the spectra upon annealing makes it difficult to assign the bands. However, by looking at the spectra carefully it is found that these frequencies correspond rather closely to those for molecular glycidol and the frequencies for the features within the sample temperature range from ~197 K to 228 K are indicated in parentheses in Table 4-1.

Vibrational Frequency/cm^{-1} glycidol/Pd(111), 100-177 (187-228) K	Liquid glycidol Frequency/cm^{-1}	Assignments
3271	3420, vs, brd	O-H stretch
3062	3062, m	ν_a (CH$_2$) (Ring)
3000	2999, s	ν_s (C-H and CH$_2$)(Ring)
	2999. s	ν_s (CH$_2$ (Ring) and C-H)
2927	2927, s	ν (CH$_2$ (methanol))
2873	2873, s	ν (CH$_2$ (methanol))
1433 (brd)	1427, s	δ(O-H + Ring)
1400 (~1400)	1400, s	δ (CH$_2$ (methanol) + Ring)
1338 (1328)	1338, w	δ (O-H + CH$_2$(methanol))
1263 (1269)	1260, s	δ (CH(Ring))
1240	1233, sh	δ (CH$_2$ (methanol))
1157	1156, w	δ (CH$_2$ (Ring))
1132 (1128)	1133, m	δ (CH + CH$_2$ (Ring))
1098 (1020)	1098, s	ν(C- O stretch) + δ (C-H)
1047	1041, vs	δ (O-H +CH$_2$ (methanol)) + δ (CH$_2$ (Ring))
958	956, s	δ (CH (Ring))
908 (898)	905, vs	Ring breathing
856 (843)	848, s	ν_a(Ring)
829	832, s	
	797, m	
754 (751)	750	δ (Ring)

Table 4-1 Comparison of the vibrational frequencies of S-glycidol on Pd(111) between ~100 K and 177 K, compared with the spectrum of liquid glycidol.[44] The measured IR frequencies for sample temperatures between ~187 and 228 K are indicated in the parentheses. (Sh, shoulder; v, very; s, strong; m, medium; brd, broad; w, weak; ν, stretch; δ, deformation)

Annealing the sample to further higher temperature results in the appearance of a

broad feature centered at ~1730 cm^{-1} that increases in frequency at higher annealing

temperatures. The close correspondence between the modes found after annealing the

sample between ~187 and 228 K indicates that S-glycidol molecular backbone remains

intact. However, evidence for deprotonation is provided by the absence of the intense ~1047 cm^{-1} mode observed at low temperature spectra and the attenuation of the ~1433 cm^{-1} feature. In this case, the mode appearing at ~1020 cm^{-1} is due to a shift in the C-O stretching mode(from ~1098 cm^{-1}) [45] due to the formation of a S-glycidate. The spectral changes are therefore consistence with S-glycidol deprotonation at ~190 K as molecular S-glycidol desorbs. The peaks at ~1440 cm^{-1} (1454 and 1437 cm^{-1}) are most likely due to CH$_2$ modes and the features at ~1328 cm^{-1} is assigned to a symmetric methyl deformation mode.[46] A higher frequency mode appears at higher annealing temperature (> 250 K). This feature appears at ~1890 cm^{-1}, due to the C-O stretch of carbon monoxide, when the sample is heated to ~350 K and dominates the spectrum.

4.5   Discussion

From the TPD results it is observed that glycidol desorbs molecularly and also undergoes decomposition at high temperatures to produce hydrogen, carbon monoxide and ethanol as gas phase products. The principal reason of studying glycidol on Pd(111) is to use it as a chiral probe; because it is chemically similar to propylene oxide but it has an additional hydrogen bonding donor and acceptor site. Propylene oxide has been used as an ideal chiral probe in the past because it undergoes negligible decomposition on Pd(111), thereby allowing the accurate coverage measurement in TPD and RAIRS. On the contrary glycidol decompose to some extent on Pd(111) surface. The extent of S-glycidol decomposition cab be gauged from the relative intensities of the hydrogen and molecular glycidol from the TPD spectra. Accurately making these measurements require values for the ionization gauge sensitivities for hydrogen (~0.4) and glycidol, which is

not available. [47] However, the sensitivity factor for propylene oxide is ~3.9, providing a likely lower limit for the sensitivity of glycidol. The results of these measurement suggests that ~8% of the glycidol decompose during the desorption sweep on Pd(111). Thus, while the extent of decomposition is higher than that for propylene oxide, it is still sufficiently low to allow TPD to be used for measuring its coverage on chirally modified surfaces to gauge chemisorptive enantioselectivity.

RAIRS suggests that a small fraction of the glycidol molecules undergo deprotonation reaction at ~190 K to form glycidate species, which is evidenced by the absence of the intense ~1047 cm^{-1} mode and the attenuation of the 1433 cm^{-1} feature. Based on the chemistry found previously for epoxide on Pd(111),[35-37] it is anticipated that ring opening should occur at ~220 K and should be accompanied by a hydrogen transfer reaction to form an aldehyde or ketone, consistent with the detection of C=O stretching frequency at 1730 cm^{-1}.

Based on TPD and IR results the proposed reaction pathways of glycidol on a Pd(111) surface is illustrated in Figure 4-5.
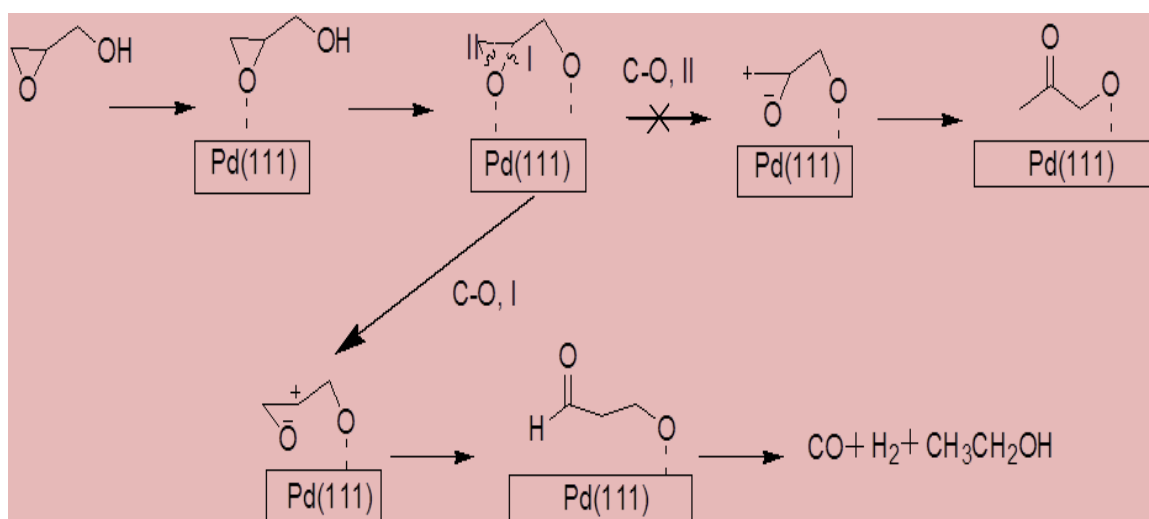
Figure 4-5 A Schematic illustration of the reaction pathways of S-glycidol on Pd(111).

Depending on which of the C-O bond cleaves in the epoxide ring, this can result in the formation of a ketone or an aldehyde. If the C-O bond indicated by I cleaves, this would result in the formation of a secondary carbocation, which will then undergo a facile hydrogen transfer reaction to form an aldehyde like intermediate (Figure 4-5). Alternatively, if the C-O bond cleaves at II, this would form a primary carbocation, which will undergo a similar hydrogen transfer reaction to form a ketone. Since secondary carbocations are more stable than primary carbocations, it is more likely that the epoxide ring cleaves at C-O bond I to preferentially form an aldehyde like intermediate.

This reaction pathway is consistent with the appearance of C=O stretching mode at ~1730 cm^{-1}. When the surface is heated to above ~350 K, the peak at ~1890 cm^{-1} (C-O stretch for CO molecule) dominates the spectrum indicating the complete decomposition of the aldehyde like intermediate. The resulting CO desorbs at ~450 K. This presumably arises from the decomposition of the aldehyde group and the remainder of the molecule desorbs as a small amount of ethanol.[48] The reaction pathway for S-glycidol on Pd(111) is thus analogous to that found for ethylene oxide on Pd(111) [35] since decomposition occurs via C-O bond cleavage of the epoxide ring. However, in the case of the non-equivalent C-O bonds in the stabilized glycidate species, the reaction pathway is controlled by the stability of the intermediate carbocation, which then undergoes a hydrogen transfer reaction to yield an aldehyde like intermediate.

First-principle DFT calculations were carried out for adsorption of S-glycidol on a 6×6 Pd(111) slab. Propylene oxide adsorbs on Pd(111), where the epoxide oxygen bonds to a palladium atop site. [49] Based on that, a similar adsorption geometry is

expected for glycidol, where the epoxide oxygen bonds to a palladium atop site and the resulting most stable structure is given in Figure 4-6. However, in contrast to propylene oxide, the –CH$_2$-OH group of glycidol, has an additional agostic interaction with the surface resulting in an overall adsorption energy of -22 kJ/mol. The bond distance between the epoxide oxygen and palladium atop is ~2.3 Å. The Hydrogen atom of the –OH group points down and is approximately at a distance of ~ 3 Å from the surface Pd atoms.
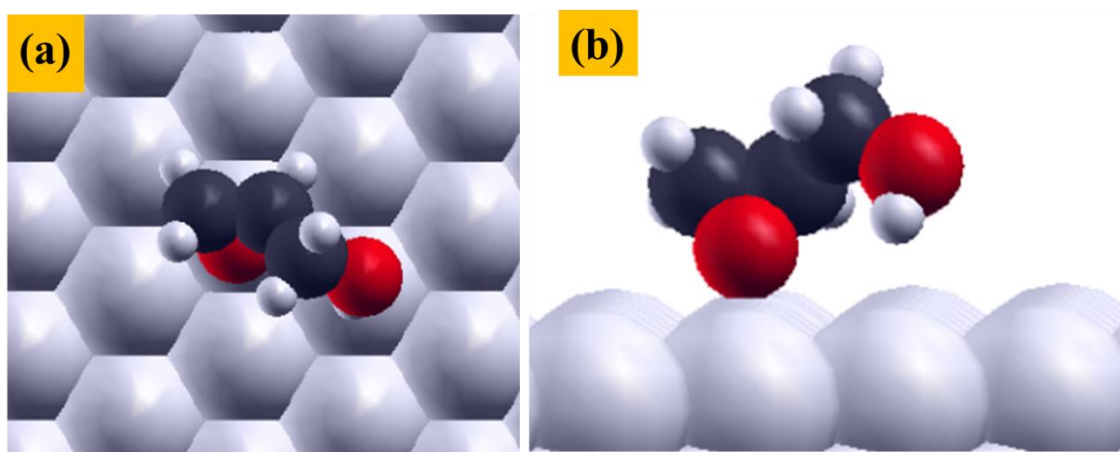
Figure 4-6 Depiction of the most stable structure of R-glycidol on Pd(111) obtained using DFT calculations showing (a) the top view and (b) the side view

Similar calculations were performed for the glycidate species on Pd(111) (with a co-adsorbed hydrogen atom on a threefold hollow site) with the same adsorption geometry as the most stable glycidol structure (Figure 4-6). The resulting relaxed structure is shown in Figure 4-7. This structure yields an adsorption energy of 142 kJ/mol. However, when the oxygen atom was brought closer to Pd (2 Å) as shown in Figure 4-8, the resulting structure was somewhat stabilized due to the interaction of the oxygen lone pair of electron with the surface, which yield an adsorption energy of ~15 kJ/mol. These calculations indicate that the formation of glycidate species on Pd(111) is

highly endothermic and thus its formation on the surface is not energetically favorable.
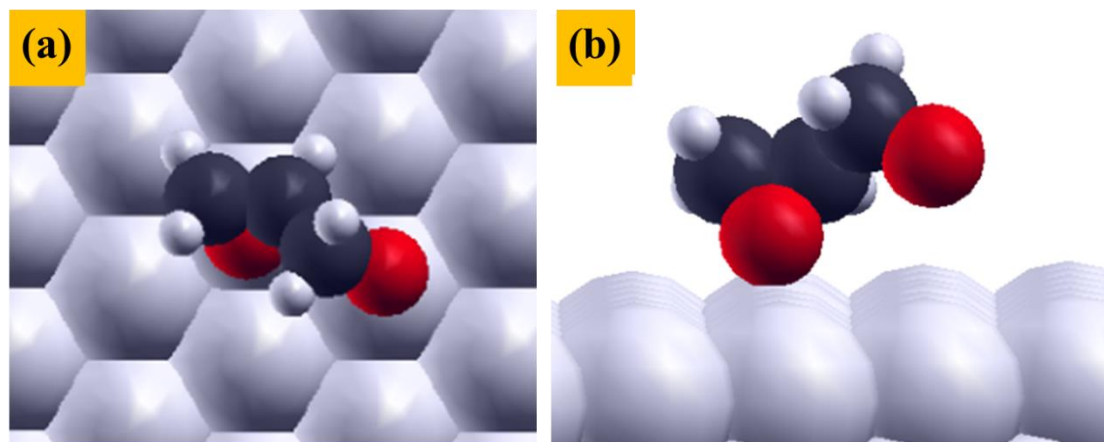
Figure 4-7 Depiction of the structure of R-glycidate species derived from the most stable glycidol structure (a) top view (b) side view
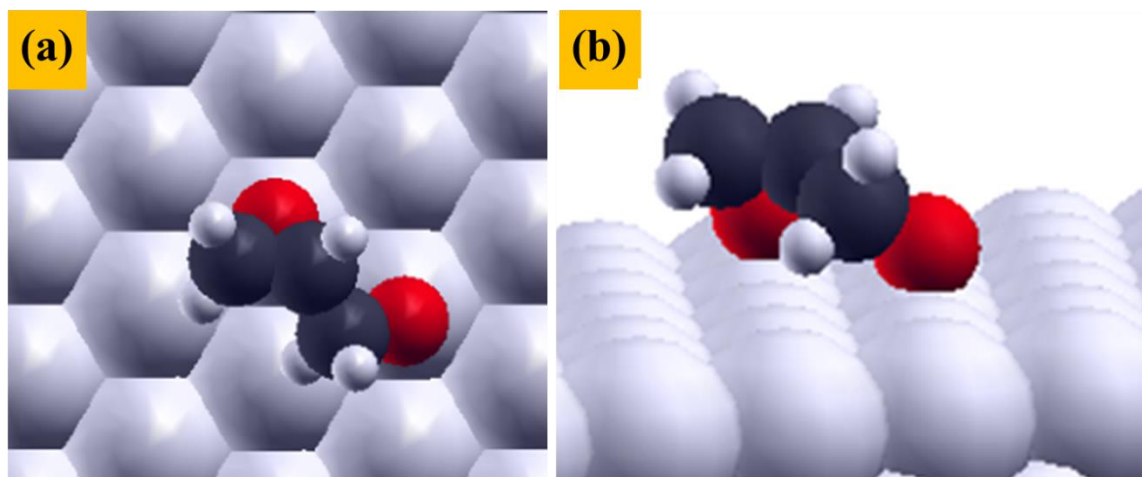
Figure 4-8 R-glycidate species on Pd(111) (a) top view (b) side view

IR results suggest that a small fraction of the adsorbed glycidol decompose on the surface as a result of heating, which is initiated by the formation of a glycidate species. DFT and IR results have good agreement; DFT predicts the formation of glycidate from glycidol is not energetically favorable, which suppress the decomposition pathway and

the majority of the glycidol species desorb intact from the surface as observed in the IR results.

4.6 Conclusions

S-glycidol adsorbs relatively strongly on Pd(111) and desorbs intact at ~244 K. A small fraction of the molecules undergo decomposition reaction which is initiated by the dehydrogenation of the glycidol to glycidate species below 200 K. The S-glycidate intermediate further reacts via C-O bond scission in the epoxide ring to preferentially form an ethoxy aldehyde intermediate in a pathway that is controlled by the stability of the carbocation. This thermally decomposes to desorb hydrogen and carbon monoxide with a small amount of ethanol. However, comparing the desorption yield of S-glycidol with that of molecular hydrogen suggest that less than ~8% of the adsorbed S-glycidol decomposes suggesting that it is a suitable chiral probe. DFT calculations predict that the formation of S-glycidate from S-glycidol is highly endothermic on the Pd(111) surface, which suppress the decomposition pathways, resulting in intact molecular desorption.

4.7 References

1.   Williams, J.; Haq, S.; Raval, R., The bonding and orientation of the amino acid l-alanine on Cu{110} determined by RAIRS. *Surface Science* **1996,** *368* (1–3), 303-309.

2.   Lorenzo, M. O.; Haq, S.; Bertrams, T.; Murray, P.; Raval, R.; Baddeley, C. J., Creating chiral surfaces for enantioselective heterogeneous catalysis: R,R-Tartaric acid on Cu(110). *J. Phys. Chem. B* **1999,** *103* (48), 10661-10669.

3.   Raval, R., Assembling molecular guidance systems for heterogeneous enantioselective catalysis. *Cattech* **2001,** *5* (1), 12-28.

4.   Humblot, V.; Haq, S.; Muryn, C.; Hofer, W. A.; Raval, R., From local adsorption stresses to chiral surfaces: (R,R)-tartaric acid on Ni(110). *Journal of the American*

Chemical Society **2002,** *124* (3), 503-510.

5.   Marti, E. M.; Barlow, S. M.; Haq, S.; Raval, R., Bonding and assembly of the chiral amino acid S-proline on Cu(110): the influence of structural rigidity. *Surface Science* **2002,** *501* (3), 191-202.

6.   Barlow, S. M.; Raval, R., Complex organic molecules at metal surfaces: bonding, organisation and chirality. *Surface Science Reports* **2003,** *50* (6-8), 201-341.

7.   Raval, R., Chiral expressions at metal surfaces. *Current Opinion in Solid State & Materials Science* **2003,** *7* (1), 67-74.

8.   Humblot, V.; Barlow, S. M.; Raval, R., Two-dimensional organisational chirality through supramolecular assembly of molecules at metal surfaces. *Progress in Surface Science* **2004,** *76* (1-2), 1-19.

9.   Humblot, V.; Haq, S.; Muryn, C.; Raval, R., (R,R)-tartaric acid on Ni(110): the dynamic nature of chiral adsorption motifs. *Journal of Catalysis* **2004,** *228* (1), 130-140.

10.   Humblot, V.; Raval, R., Chiral metal surfaces from the adsorption of chiral and achiral molecules. *Applied Surface Science* **2005,** *241* (1-2), 150-156.

11.   Mark, A. G.; Forster, M.; Raval, R., Recognition and Ordering at Surfaces: The Importance of Handedness and Footedness. *ChemPhysChem* **2011,** *12* (8), 1474-1480.

12.   Forster, M.; Dyer, M. S.; Persson, M.; Raval, R., Tailoring Homochirality at Surfaces: Going Beyond Molecular Handedness. *Journal of the American Chemical Society* **2011,** *133* (40), 15992-16000.

13.   Jones, T. E.; Baddeley, C. J.; Gerbi, A.; Savio, L.; Rocca, M.; Vattuone, L., Molecular ordering and adsorbate induced faceting in the Ag{110}-(S)-glutamic acid system. *Langmuir* **2005,** *21* (21), 9468-9475.

14.   Jones, T. E.; Urquhart, M. E.; Baddeley, C. J., An investigation of the influence of temperature on the adsorption of the chiral modifier, (S)-glutamic acid, on Ni{111}. *Surface Science* **2005,** *587* (1-2), 69-77.

15.   Parschau, M.; Romer, S.; Ernst, K. H., Induction of homochirality in achiral enantiomorphous monolayers. *Journal of the American Chemical Society* **2004,** *126* (47), 15398-15399.

16.   Parschau, M.; Kampen, T.; Ernst, K. H., Homochirality in monolayers of achiral meso tartaric acid. *Chemical Physics Letters* **2005,** *407* (4-6), 433-437.

17.   Ernst, K. H., Supramolecular surface chirality. In *Supramolecular Chirality*, 2006; Vol. 265, pp 209-252.

18.   Behzadi, B.; Ferri, D.; Baiker, A.; Ernst, K. H., Adsorption mode of the chiral modifier cinchonidine on Au(111). *Applied Surface Science* **2007,** *253* (7), 3480-3484.

19.   Ernst, K. H., Expression and amplification of chirality in two-dimensional molecular crystals. *Chimia* **2008,** *62* (6), 471-475.

20.   Mahapatra, M.; Burkholder, L.; Bai, Y.; Garvey, M.; Boscoboinik, J. A.; Hirschmugl, C.; Tysoe, W. T., Formation of Chiral Self-Assembled Structures of Amino Acids on Transition-Metal Surfaces: Alanine on Pd (111). *The Journal of Physical Chemistry C* **2014,** *118* (13), 6856-6865.

21.   Stacchiola, D.; Burkholder, L.; Tysoe, W. T., Probing enantio selective chemisorption in ultrahig vacuum. *Journal of Molecular Catalysis A-Chemical* **2004,** *216* (2), 215-221.

22.   Gao, F.; Wang, Y. L.; Burkholder, L.; Tysoe, W. T., Enantioselective chemisorption of propylene oxide on a 2-butanol modified Pd(111) surface: The role of hydrogen-bonding interactions. *Journal of the American Chemical Society* **2007,** *129* (49), 15240-15249.

23.   Gao, F.; Wang, Y. L.; Tysoe, W. T., Enantioselective chemisorption and reactions on model chirally modified surfaces: 2-butanol on L-proline templated Pd(111) surfaces. *Journal of Physical Chemistry C* **2008,** *112* (15), 6145-6150.

24.   Gao, F.; Wang, Y. L.; Li, Z. J.; Furlong, O.; Tysoe, W. T., Enantioselective reactions on a Au/Pd(111) surface alloy with coadsorbed chiral 2-butanol and propylene oxide. *Journal of Physical Chemistry C* **2008,** *112* (9), 3362-3372.

25.   Sales, J. L.; Gargiulo, V.; Lee, I.; Zaera, F.; Zgrablich, G., Monte Carlo modeling of the enantioselective adsorption of propylene oxide on 1-(1-naphthyl)ethylamine-modified Pt(1 1 1) surfaces. *Catalysis Today* **2010,** *158* (1-2), 186-196.

26.   Lee, I.; Zaera, F., Chiral Templating of Surfaces: Adsorption of (S)-2-Methylbutanoic Acid on Pt(111) Single-Crystal Surfaces. *Journal of the American Chemical Society* **2006,** *128* (27), 8890-8898.

27.   Zaera, F., Chiral Modification of Solid Surfaces: A Molecular View†. *The Journal of Physical Chemistry C* **2008,** *112* (42), 16196-16203.

28.   Stacchiola, D.; Burkholder, L.; Tysoe, W. T., Enantioselective chemisorption on a chirally modified surface in ultrahigh vacuum: Adsorption of propylene oxide on 2-butoxide-covered palladium(111). *Journal of the American Chemical Society* **2002,** *124* (30), 8984-8989.

29.   Borho, N.; Suhm, M. A., Glycidol dimer: anatomy of a molecular handshake. *Physical Chemistry Chemical Physics* **2002,** *4* (12), 2721-2732.

30.   Maris, A.; Giuliano, B. M.; Bonazzi, D.; Caminati, W., Molecular Recognition of Chiral Conformers: A Rotational Study of the Dimers of Glycidol. *Journal of the American Chemical Society* **2008,** *130* (42), 13860-13861.

31.   Davis, J. L.; Barteau, M. A., Decarbonylation and decomposition pathways of alcohol's on Pd(111). *Surface Science* **1987,** *187* (2–3), 387-406.

32.   Gao, F.; Wang, Y. L.; Burkholder, L.; Hirschmugl, C.; Saldin, D. K.; Poon, H. C.; Sholl, D.; James, J.; Tysoe, W. T., The structure and reactivity of 2-butanol on Pd(111). *Surface Science* **2008,** *602* (13), 2264-2270.

33.   Grant, R. B.; Lambert, R. M., Mechanism of the silver-catalysed heterogeneous epoxidation of ethylene. *Journal of the Chemical Society, Chemical Communications* **1983,** (12), 662-663.

34.   Grant, R. B.; Lambert, R. M., A single crystal study of the silver-catalysed selective oxidation and total oxidation of ethylene. *Journal of Catalysis* **1985,** *92* (2), 364-375.

35.   Lambert, R. M.; Ormerod, R. M.; Tysoe, W. T., Thermal Decomposition of Ethylene Oxide on Pd(111): Comparison of the Pathways for the Selective Oxidation of Ethylene and Olefin Metathesis. *Langmuir* **1994,** *10* (3), 730-733.

36.   Linic, S.; Barteau, M. A., Formation of a Stable Surface Oxametallacycle that Produces Ethylene Oxide. *Journal of the American Chemical Society* **2001,** *124* (2), 310-317.

37.   Linic, S.; Barteau, M. A., Control of Ethylene Epoxidation Selectivity by Surface Oxametallacycles. *Journal of the American Chemical Society* **2003,** *125* (14), 4034-4035.

38.   Bustos, V.; Linares, D.; Rebaza, A. G.; Tysoe, W. T.; Stacchiola, D.; Burkholder, L.; Zgrablich, G., Monte Carlo Theory Analysis of Thermal Programmed Desorption of Chiral Propylene Oxide from Pd(111) Surfaces. *Journal of Physical Chemistry C* **2009,**

113 (8), 3254-3258.

39.   Mahapatra, M.; Tysoe, W. T., Adsorption and reaction pathways of a chiral probe molecule, S-glycidol on a Pd (111) surface. *Catalysis Science & Technology* **2015**.

40.   Blöchl, P. E., Projector augmented-wave method. *Physical Review B* **1994,** *50* (24), 17953-17979.

41.   Kresse, G.; Joubert, D., From ultrasoft pseudopotentials to the projector augmented-wave method. *Physical Review B* **1999,** *59* (3), 1758-1775.

42.   Perdew, J. P.; Burke, K.; Ernzerhof, M., Generalized Gradient Approximation Made Simple. *Physical Review Letters* **1996,** *77* (18), 3865-3868.

43.   Conrad, H.; Ertl, G.; Latta, E. E., Adsorption of hydrogen on palladium single crystal surfaces. *Surface Science* **1974,** *41* (2), 435-446.

44.   Badawi, H. M.; Ali, S. A., A study of internal rotations and vibrational spectra of oxiranemethanol (glycidol). *Spectrochimica Acta Part A: Molecular and Biomolecular Spectroscopy* **2009,** *74* (2), 558-562.

45.   Stacchiola, D.; Burkholder, L.; Tysoe, W. T., Enantioselective chemisorption on a chirally modified surface in ultrahigh vacuum: Adsorption of propylene oxide on 2-butoxide covered Pd(111). *Journal of the American Ceramic Society* **2002,** *124*, 8984-8989.

46.   Colthup, N. B. D. L. H. W. S. E., *Introduction to infrared and Raman spectroscopy*. Academic Press: N.Y.

47.   Summers, R. L. U. S. N. A.; Space Administration, L. R. C. Empirical observations on the sensitivity of hot cathode ionization type vacuum gages. http://ntrs.nasa.gov/archive/nasa/casi.ntrs.nasa.gov/19690019953_1969019953.pdf.

48.   Marshall, S. T.; Horiuchi, C. M.; Zhang, W.; Medlin, J. W., Common Decomposition Pathways of 1-Epoxy-3-butene and 2-Butenal on Pd(111). *The Journal of Physical Chemistry C* **2008,** *112* (51), 20406-20412.

49.   Roma, F.; Zgrablich, G.; Stacchiola, D.; Tysoe, W. T., Theoretical analysis of the coverage dependence of enantioselective chemisorption on a chirally templated surface. *Journal of Chemical Physics* **2003,** *118* (13), 6030-6037.

Chapter 5

Formation of Induced-Fit Chiral Templates by Amino Acid Functionalized Pd(111) Surfaces

5.1   Introduction

Amino acids have been shown to be potential chiral modifiers on transition metal surfaces especially on copper [1-4] and a large amount of surface science research have been carried out in this field to gain mechanistic insights into these phenomena. A substantial amount of the work in this dissertation consists of using α-amino acids, especially alanine as a chiral modifier on a Pd(111) single crystal surface. Accordingly, the surface chemistry of α-amino acids has been explored on Pd(111),[5] which is described in Chapter-3. It has been observed that alanine does not form any long range order on Pd(111) unlike copper surfaces, where ordered layers are reported. However, alanine self-organize on Pd(111) to form discrete chiral assemblies that comprise of tetrameric units and dimer rows from alanine anionic-zwitterionic pairs.[5] The pocket formed at the center of the alanine tetramer provides an attractive candidate for a chiral template. Testing this idea requires enantioselectivity measurement of the overlayer to be correlated with the presence of surface ensembles. The chemisorptive enantioselectivity of the chiral overlayer is measured by chiral titration TPD, where the chirally modified surface is exposed to both the enantiomers of a suitable chiral probe molecule and TPD has been performed to measure the relative desorption yield of both enantiomers of the probe. Enantioselectivity is measured from enantioselectivity ratio, which is simply the

ratio of the probe coverages of both the enantiomer. Previously propylene oxide has been used extensively as a chiral probe molecule to measure the enantioselectivity of 2-butanol modified Pd(111) surface where the measured enantioselectivity is a result of the hydrogen bonding interaction between the epoxide oxygen of the propylene oxide and the –OH group of the 2-butanol. Chapter 4 of this dissertation presents the surface chemistry of the chiral probe molecule S-glycidol [6] and it has been demonstrated that glycidol can be used as a potential chiral probe molecule because it has a –CH_2OH group (replaced by the -CH_3 group in propylene oxide), which has a both hydrogen bonding donor and acceptor site, enhancing the hydrogen bonding interaction with the modifier.

This chapter presents the study of enantioselectivity measurements of amino acid modified Pd(111) surfaces by using both propylene oxide and glycidol as chiral probe molecules. Chiral titration TPDS are performed to measure the chemisorptive enantioselectivity of the alanine overlayer by using the chiral probe glycidol. The results are compared to the enantioselectivity measurements done by L. Burkholder, [22] by using propylene oxide as a chiral probe. The measured enantioselectivity is correlated to the STM surface structures of the amino acids studied by A. Boscoboinik.[25] DFT calculations were carried out to explore the adsorption of the chiral probe molecule inside the chiral pocket formed by alanine on Pd(111).

5.2 Experimental Section

Chiral titration experiments are carried out in the TPD chamber as described in Chapter-2. The Pd(111) single crystal was initially cleaned by using a standard procedure which consists of cycles of argon ion sputtering and oxygen roasting. To maintain the cleanliness of the sample, the sample was briefly oxygen cleaned in between each

experiment. At first, the sample was flashed to ~1000 K in vacuum and as the sample was cooling down an oxygen pressure of 3×10^{-8} Torr was introduced into the vacuum chamber while holding the sample temperature at ~800 K for ~1 minute by using a DC power supply. Then the power supply was turned off and the sample was allowed to cool to ~400 K with oxygen. Finally oxygen flow was stopped and the sample was flashed to ~1000 K in vacuum. The same cycle was repeated twice in between each TPD. It takes relatively long time for the sample to cool down to room temperature after heating it to ~1000 K. Since CO and hydrogen from the UHV background can adsorb onto Pd(111) readily below ~450 K and ~350 K respectively, the sample gets contaminated while it is cooling down to ~ 300 K or lower. Therefore, the sample was usually flashed again to ~500 K just before dosing any reactants, the idea is to allow the sample cool faster to the dosing temperature to minimize background CO and hydrogen adsorption.

The amino acids were dosed onto the sample by using a home built Knudsen source as described in Chapter 2. They were extensively outgassed prior to deposition to remove contaminants, particularly water, and the temperature of each of the amino acids were adjusted to yield reasonable dosing rates. Once the desirable dosing rate is achieved, the amino acid source temperature was maintained at that value for a series of titration experiments for achieving consistent dosing rate. The Knudsen source temperature was maintained between 100 to 102° C during all the titration experiments presented in this chapter.

R- and S- glycidol were introduced into the chamber from a gas line through a leak valve which is attached to a direct dosing tube. Both the enantiomers are introduced through the same leak valve during consecutive experiments. The gas line is filled first

with one enantiomer of glycidol to perform the experiment and then evacuated to fill the other enantiomer.

Previous experiments are carried out by L. Burkholder [24] to measure the coverages of R- and S-propylene oxide on a wide range of amino acid modified Pd(111) surfaces by using King and Wells method, where a beam of propylene oxide impinge on the chirally modified Pd(111) surface and measuring the integrated area of the pressure drop when moving the sample to intercept the beam of propylene oxide. The slow pumping speed of glycidol in the UHV chamber precluded the King and Wells method from being used to measure enantioselectivity. Therefore the coverage measurement was obtained from the integrated area of the R- and S- glycidol TPD profile over a Pd(111) surface modified with D- or L- alanine.

STM images of the amino acid-covered surfaces were acquired at a sample temperature of ~290 K using an electrochemically etched tip made from recrystallized tungsten wire. Experiments were performed using a scanning tunneling microscope housed in the STM chamber as described in Chapter 2.

5.3 Theoretical Methods

DFT calculations were performed with the projector augmented wave (PAW) method [7-8] using the Vienna ab initio simulation package, VASP. [9-11] The exchange correlation potential was described using the generalized gradient approximation (GGA) of Perdew, Burke and ERNzerhof. [12] A cut off of 400 eV was used for the planewave basis set and the wave functions and electron density were converged t within 1×10^{-5} eV. The first Brillouin zine was sampled with a $4 \times 4 \times 1$ Γ-centered k-point mesh. Geometric relaxations were considered to be converged when the force was less than 0.02 eV/Å on

all unrestricted atoms. Van der Waals corrections were included using the method of

Tkatchenko and Scheffler (TS)[13]

5.4   Experimental Results

Previous TPD experiments show that of Glycine[14], alanine[15] and proline[16] are

stable on Pd(111) to ~360 K, and the saturation coverages are gauged by monitoring

propylene oxide blocking by the amino-acid covered surface and the results are

summarized in Chapter 3. The C 1s and N 1s XPS of the amino acids used in this work

are shown in Chapter 3, and provide a homologous series of amino acids with n-alkyl

functional groups((alanine (CH_3-), 2-aminobutanoic acid (C_2H_5-) and norvaline (C_3H_5-)),

and the branched side chains ((valine (-$CH(CH_3)_2$), isoleucine (-$CH(CH_3)CH_2CH_3$) and

leucine (-$CH_2CH(CH_3)_2$)). XPS reveals that they adsorb as both zwitterions and anions.

Previous DFT calculations have shown that anionic alanine is more stable than the

zwitterion [5] due to the stronger binding of the NH_2 than the NH_3^+ group to the surface.

However, alanine forms zwitterion-anion dimer pairs where the zwitterion is stabilized by

the COO^- group of the anionic alanine rotating away from the surface to interact with the

$NH3^+$ group of the zwitterion. The dimers further assemble to form tetramer and longer

dimer chains. The tetramers consists of antiparallel alanine anion-zwitterion dimers

(Figure 5-1(a)) in which three of the alanines undergo a concerted translational motion to

form a stable tetramer to optimize the interactions between adjacent amino acids as

shown in Figure 5-1(b). DFT calculations indicate that this isomerization results in slight

energy gain of ~2 kJ/mol. Although, DFT calculations has not been performed for other

amino acids, but the presence of both zwitterions and anionic forms in all the systems

imply that zwitterions are similarly stabilized by interacting with an anionic species for

all the amino acids.
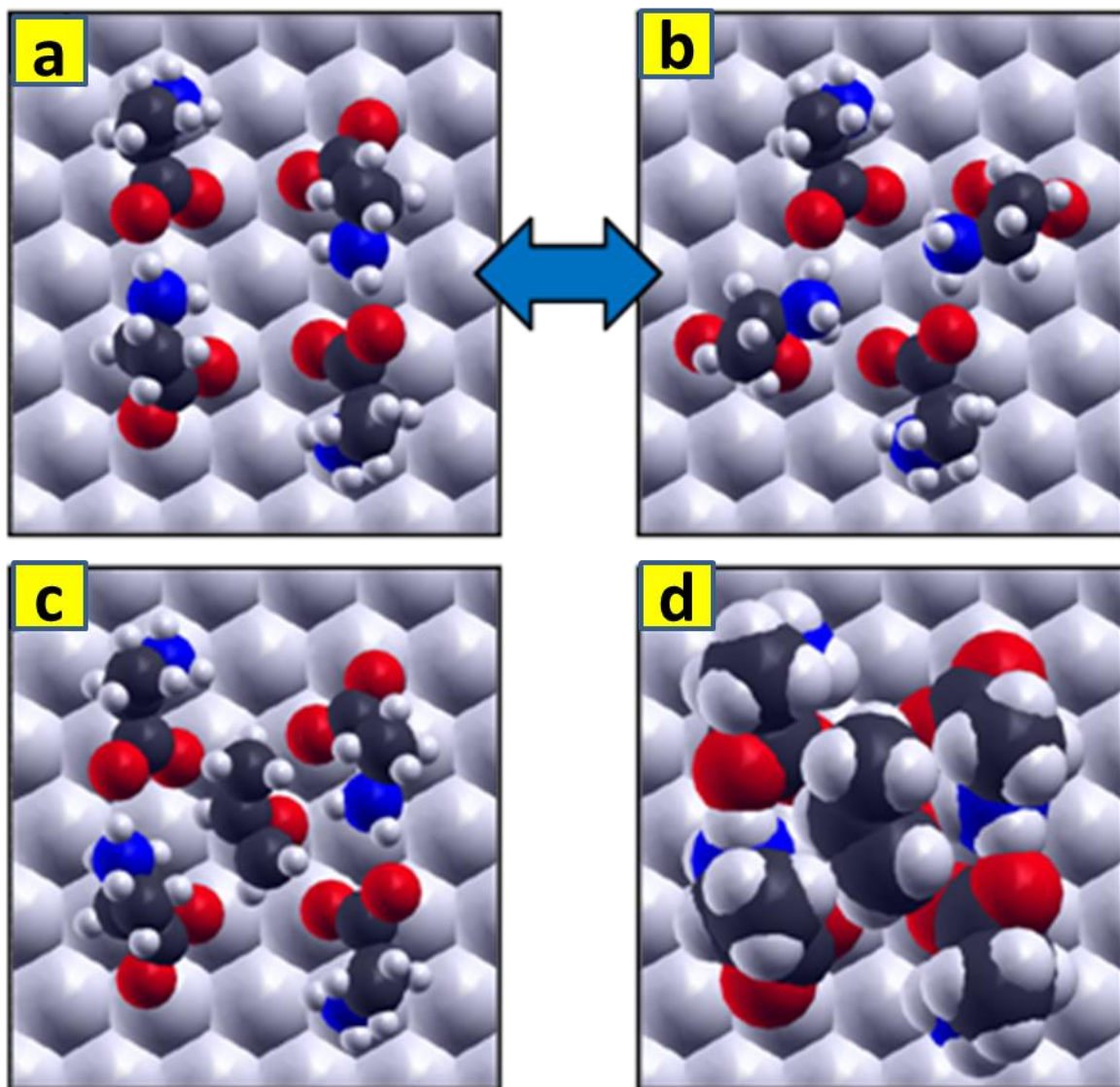
Figure 5-1 (a) shows the Structure of the initial antiparallel anion-zwitterion dimer pairs in which three of the amino acids then undergo a concerted rotation on the surface to form the most stable tetramer (b), (c) Depiction of the proposed structure of R-propylene oxide in the chiral pocket of the metastable tetrameric unit constructed from antiparallel D-alanine anion-zwitterion dimer pairs showing the epoxide oxygen bound to the most stable palladium atop site, which also can interact with the NH_3^+ groups of the adjacent alanine zwitterions. (d) Shows the structure displayed in (c), using van der Waals radii to illustrate how chirality is imparted by the fit of the chiral probe molecule into the groove of the tetramer.

Previously experiments are carried out by L. Burkholder, [22] to measure

enantioselectivity of the amino acid modified Pd(111) surfaces by King and Wells method by using propylene oxide as a chiral probe. Enantioselectivity was measured from enantioselective ratio Re, defined as: $R_e = \Theta_D^R / \Theta_D^S = \Theta_L^S / \Theta_L^R$) where Θ is the probe molecule saturation coverage and the superscripts (S or R) are the chirality of the probe (in this case propylene oxide) and the subscript (D or L) are those of the modifier. In all the cases, R_e varies as a function of amino acid coverages from $R_e = 1$ with no modifier present, to a maximum at a relative amino acid coverage of ~0.5 ML, and then decreases at higher coverages. The maximum *Re* values for all the amino acids are summarized in table 5-1. Amino acids with n-alkyl side chains have relatively large, $R_e{}^{max}$ value (~1.6 to 2.0) while amino acids containing branched groups with the secondary carbon adjacent to the chiral center are not enantioselective.

In order to explore whether the enantioselectivity was influenced by replacing the methyl group in the probe molecule by $-CH_2-OH$, R_e values were measured for R and S-glycidol on D-alanine modified Pd(111), where the coverages are measured by using TPD. Glycidol TPD experiments are carried out on clean Pd(111) (Chapter-4) by dosing at a crystal temperature of ~100 K, which shows that the monolayer glycidol desorption peak occurs at ~240 K and multilayer desorbs at a temperature of ~190 K. For these titration experiments glycidol is dosed at a crystal temperature of ~190 K, to avoid populating the multilayer.

Amino acid	R_e^{max} value (Propylene oxide) [22-23]	R_e^{max} value (Glycidol)	Amino acid Structure
Alanine	2.0 ± 0.2	2.16 ± 0.15	Tetramers and dimer rows
2-aminobutanoic acid	1.7 ± 0.1	-	Tetramers
Norvaline	1.6 ± 0.1	-	Tetramers and some dimers
Isoleucine	1.3 ± 0.1	-	Tetramers and some dimers
Valine	1.0	-	Dimers
Leucine	1.0	-	Dimers

Table 5-1 Maximum enantioselectivity ratio (R_e^{max}) values for R- or S-propylene oxide [21-23] adsorbed on Pd(111) surfaces modified by various amino acids, and for R- and S-glycidol adsorbed on alanine-modified surfaces. The observed surface structures are also indicated.

The chiral titration experiments are carried out by following the protocol as described below. A small coverage of D-alanine was dosed onto a Pd(111) surface at a sample temperature at ~295 K following which the sample was cooled and held at ~190 K to dose a saturated monolayer of R- or S- glycidol. The sample was further cooled to ~125 K, following which a TPD was carried out by monitoring 44 amu (to gauge alanine coverage) and 29 amu (to gauge glycidol coverage). Then the sample was briefly oxygen cleaned to maintain the cleanliness. The next experiment done was identical to the previous one except the opposite enantiomer of glycidol is used. Similar sets of experiments are carried out for various increasing coverages of D-alanine till the coverage is high to block glycidol adsorption.
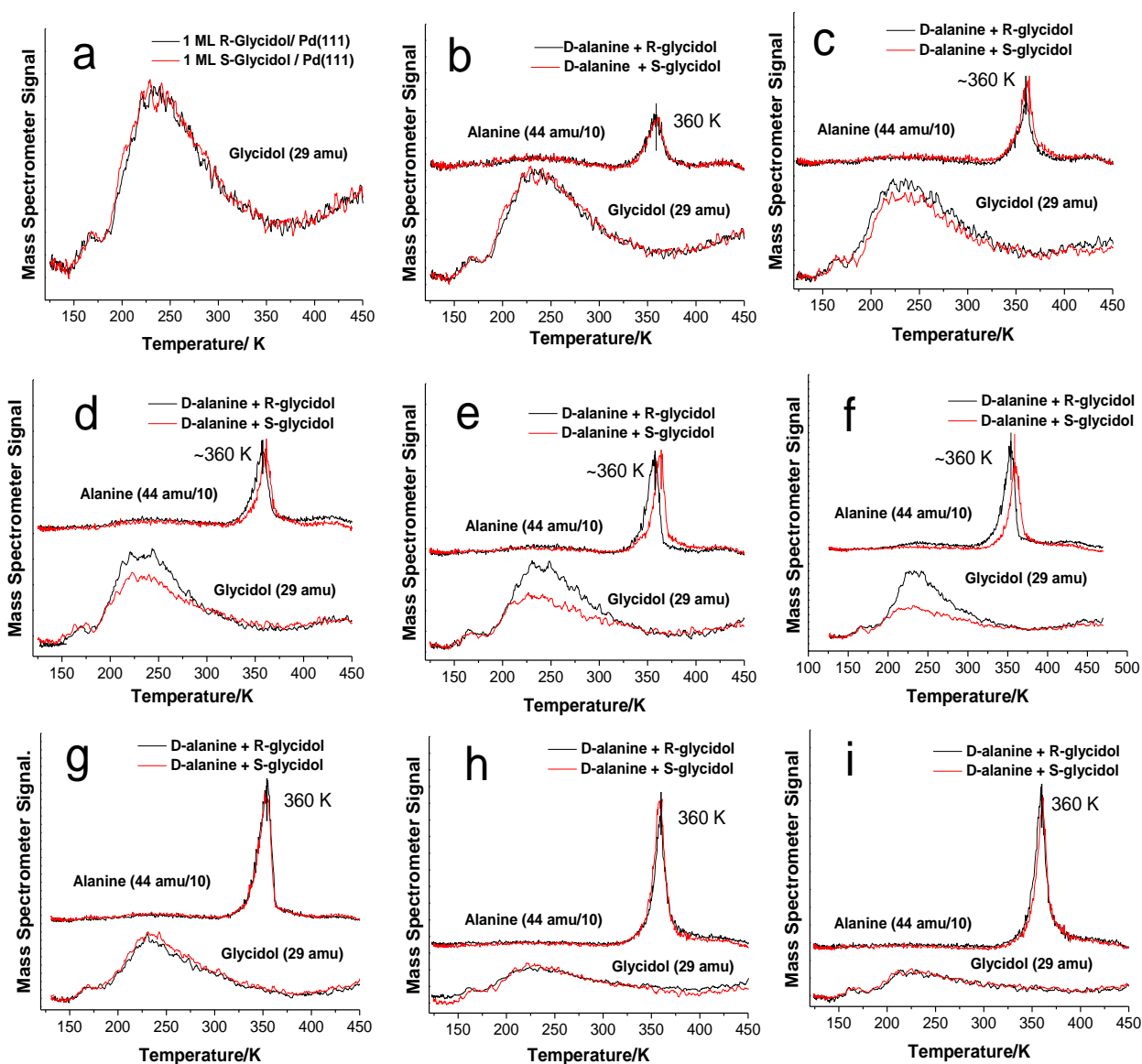
Figure 5-2 Temperature-programmed desorption profiles collected at a heating rate of 3 K/s for R-glycidol (black traces) and S-glycidol (red traces) adsorbed on Pd(111) surfaces that are precovered with D-alanine, collected at 44 (alanine) and 29 amu (glycidol). (a) shows the desorption of glycidol from the clean Pd(111)surface and D-alanine was exposed for (b) 5, (c) 10, (d) 15, (e) 25, (f) 30, (g) 35, (h) 40 and (i) 50 s.

Figure 5-2 shows the results of the glycidol titration TPDS. On clean Pd(111)

(Figure 5-2(a)) as expected identical desorption profile are found for R- and S-glycidol,

which demonstrates the reproducibility of the experiments. Glycidol saturated monolayer

desorbs at ~240 K and a very small peak appears below ~190 K probably due to a small amount of glycidol adsorption into the second layer. In Figure 5-2(b) to (i) the coverage of alanine was increased gradually, which is evidenced by the increase in signal intensity of 44 amu (top two spectra in Fig5-2 (b) to (i)) and at the same time decrease in overall signal intensity of 29 amu (bottom two spectra of Fig 5-2(b) to (i)) compared to the signal intensity of glycidol desorption on clean Pd(111) due to site blocking by D-alanine. However, alanine induced a difference in the relative desorption yields (saturation coverages) of R- and S-glycidol over a range of alanine dose between 10 to 40 s. At very low coverage (5 s dose) and higher coverage (> 40 s) of alanine, the R- and S- glycidol desorption spectra were identical indicating no enantioselectivity at high or low coverages.
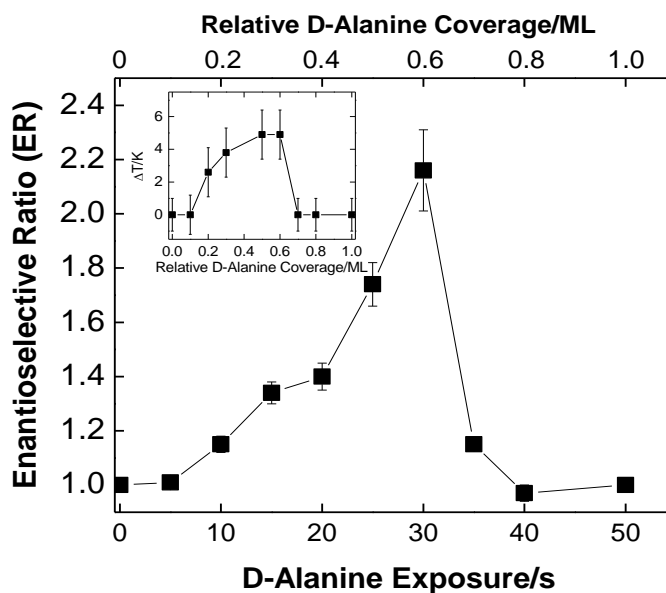
Figure 5-3 Plot of enantioselective ratio (R_e) for glycidol versus D-alanine exposure obtained from the data shown in Figure5-2. The top axis displays the corresponding relative coverage of D-alanine. Shown as an inset is the temperature difference ΔT between the D-alanine desorption states in Figure 5-2 plotted *versus* D-alanine coverage.

Figure 5-3 plots the glycidol R_e value verses D-alanine exposure. The R_e value

remains 1 at very low dose of alanine and gradually increase with increasing alanine dose and attain a maximum value of ~2.16 for a alanine dose of 30 s and then goes to one at higher doses. The variation in R_e with D-alanine coverage when using glycidol mimics the results found for propylene oxide with $R_e^{max} = 2.16 \pm 0.15$, in agreement with the value measured when using propylene oxide as a chiral probe. The D-alanine (44 amu) desorption peak centered at ~360 K increases in intensity with increasing alanine dose but, for doses greater than ~10 s, D-alanine desorbs at slightly lower temperature when exposed to R-glycidol. The temperature difference increases as the amino acid coverages increases, but disappears at higher D-alanine doses. However, there are no significant differences between the glycidol desorption temperature on clean and alanine-modified surfaces. An inset to Figure 5-3 shows the temperature difference ΔT between the D-alanine desorption peaks for clean and R- and S-glycidol covered surfaces, which vary in a similar manner with D-alanine coverage as the R_e values.

STM images of various amino acids on Pd(111) studied by A. Boscoboinik, [21,23] are displayed in Figure 5-4. Correlating the STM structures with measured enantioselectivity shows that the enantioselective amino acids (alanine (Figure 5-4(a)), 2-aminobutanoic acid (Figure 5-4(b)), norvaline (Figure 5-4(c)) and Isoleucine (Figure 5-4(f)) exhibit tetrameric structures and dimeric units. In contrast, non-enantioselective amino acids (valine (Figure 5-4(e)) consist only of dimers. The results are summarized in Table 5-1.
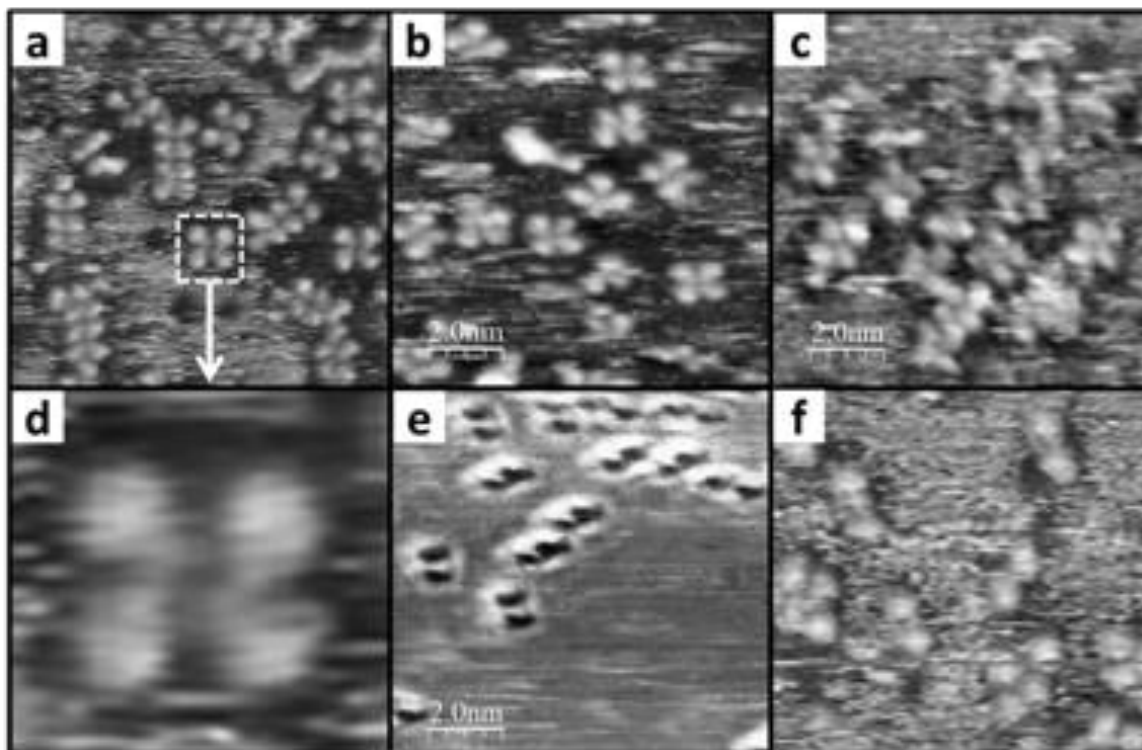
Figure 5-4 10 nm×10nm STM images of various amino acids adsorbed on Pd(111) at 290 K following the adsorption of (a) alanine (b), 2-aminobutanoic acid, (c) norvaline, (d) stable alanine tetramer, (e) isoleucine, and (f) leucine. [23]

The variation in number of tetramers for a 2-aminobutanoic acid on Pd(111) was

followed as a function of amino acid coverage and correlated with the R_e values as shown

in Figure 5-5. The tetramer coverage increases to the point at which the maximum R_e

value is reached, while at higher coverages (above 0.5 ML relative coverage), when the

R_e ratio decreases, the tetramers disappear due to the formation of a compressed

overlayer.
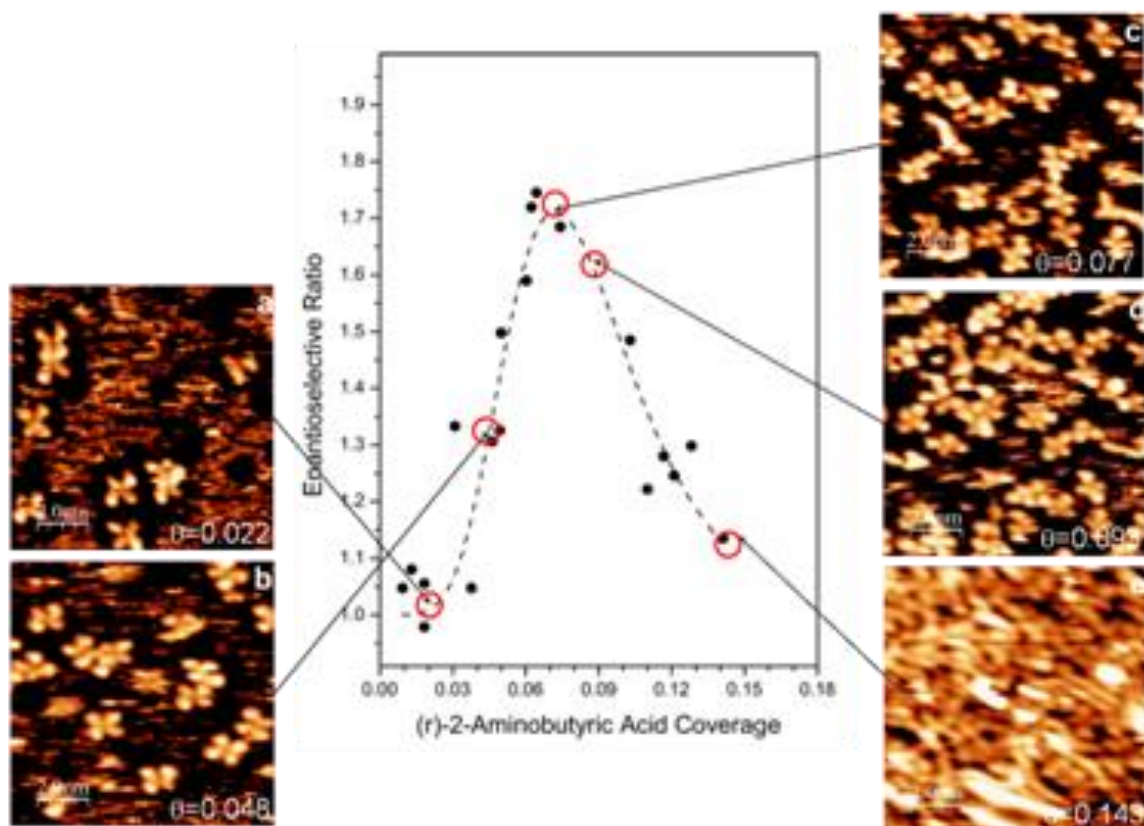
Figure 5-5 Plot of enantioselective ratio (R_e) as a function of 2-aminobutanoic acid coverage (●) where a dashed line is shown plotted though the data as a guide to the eye. Shown also are STM images of various coverages of 2-aminobutanoic acid on Pd(111) where the coverage on the plot of R_e *versus* coverage is indicated by an arrow for each image (V_b = -209 mV, I_t = 19.7 pA).[21,22,23] (reproduced with permission[23] ©)

5.5 Discussion

The results provide a clear correlation between the presence of amino acid (2-amino butanoic acid) tetramers and the enantioselective adsorption of propylene oxide and glycidol on amino acid functionalized tetramers. The amino acids which show the presence of both tetramers and dimers are enantioselective to PO adsorption while the amino acids which show only dimers are not enantioselective. This is further evidenced by the correspondence between the tetramer coverage and measured enantioselectivity of

2-aminobutanoic acid (Figure 5-5). Identical enantioselectivities are found when using both propylene oxide and glycidol as chiral probes on alanine modified surface; where the interaction is dominated by the steric effects and the presence of an additional potential hydrogen-bonding donor and acceptor group ($-CH_2-OH$) in glycidol did not influence the enantioselectivity.

DFT calculations have been carried out to explore the adsorption of R-propylene oxide inside the chiral pocket formed by D-alanine tetramers. Propylene oxide adsorbs at an atop site on Pd(111).[17] The most stable alanine tetramer does not contain any atop palladium site in the center. Therefore when propylene oxide was placed in the center of the most stable alanine tetramer (Figure 5-1(b)), the structure was unstable because of the unfavorable adsorption site and also the size of the pocket is too small to accommodate a propylene oxide. Additional calculations were carried out by constraining the epoxide oxygen of the propylene oxide in the center of the tetramer to be 0.25 nm from the palladium surface, and by allowing the remaining atoms to relax, which caused the tetramer to be disrupted.

Similar DFT calculations were performed for R-propylene oxide on the D-metastable tetramer (Figure 5-1(a)) that has a more open structure and also exposes the favorable atop propylene oxide adsorption site. This structure was found to be stable and the most stable geometry is depicted in Figure 5-1(c) and (d), where Figure 5-1(d) displays the van der Waal radii of the atoms. The energy of the tetramer/PO complex was ~50 kJ/mol more stable than the isolated tetramer, which indicates that R-PO is stable at this site.

The binding energy of the R-PO in the pocket was calculated using DFT by including van der Waals interactions from the energy difference between the structure depicted in Figure 5-1(c), and the energy of the gas phase PO and the frozen structure of the tetramer to mimic adiabatic PO desorption which yields a binding energy of ~-75 kJ/mol, indicating that the homochiral propylene oxide is stable at this site. Previous calculations of the binding energy of PO on Pd(111) did not include van der Waals interaction, so that its biding energy was recalculated with these interactions included. It was found that this did not influence the adsorption geometry and the atop sites were again found to be the most stable, and the binding energy was calculate to be slightly larger at ~-75 kJ/mol. Thus the binding energy of the R-propylene oxide in the pocket of the metastable D-alanine tetramer is isoenergetic with the binding energy of the R-propylene oxide on clean Pd(111). Since glycidol also adsorbs onto Pd(111) by the palladium atop site in a similar way to propylene oxide, it is expected that the homochiral glycidol can adsorb inside the alanine tetramer in a similar fashion to propylene oxide. The similarity in energy between propylene oxide binding energy in the tetramer and on clean Pd(111) is in accord with the lack of change in the glycidol desorption temperature (Figure 5-2). Propylene oxide adsorbs on the atop site and the epoxide oxygen interacts with the adjacent NH_3^+ group (Figure 5-1(c)), and chirality is imposed by the groove defined by the van der Waals radii between pairs of anion-zwitterion dimers and propylene oxide a shown in Figure 5-1(d). The location of methyl group is such that replacing it by CH_2-OH (in the case of glycidol) causes no additional interactions with the adjacent amino acid molecules, accounting for the identical R_e^{max} values for propylene oxide and glycidol Table 5-1.

The energy difference between the two tetrameric forms of alanine (Figure 5-1(a), (b)) is sufficiently small to enable fluctuations between the two isomers to occur to provide a chiral templating adsorption site; the structure is stabilized once propylene oxide or glycidol occupies this site. The structural transformation was proposed based on the rotation of alanine tetramers observed in STM, (data shown in Chapter 3) which occurred in images taken ~100 s apart suggesting that the fluctuations are relatively slow and the process is activated.[5] The difference in D-alanine desorption temperature following either R- or S-glycidol adsorption (Figure 5-3, inset) is in accord with enantioselective adsorption of R-glycidol in the pocket of a metastable D-alanine tetramer. The time delay between glycidol and alanine desorption in the data shown in Figure 5-2 is ~30 s implying that the metastable tetramer does not have sufficient time to relax into the most stable state after the probe molecule has desorbed, causing it to be more weakly bound as found experimentally. The energy difference between the two alanine desorption states can be estimated from the desorption temperature difference ΔT to be ~1.6 kJ/mol for first-order desorption, assuming a typical pre-exponential factor of 1×10^{13} s^{-1}, [18] in reasonable agreement with the energy difference of ~2 kJ/mol found by DFT calculations.

Finally, the adsorption energy of the most stable structure of S-PO in the metastable D-alanine tetramer was estimated using DFT calculations. This provided a somewhat stable structure, in which the S-propylene oxide tilted to allow the epoxide oxygen to interact with the zwitterionic alanine, with a binding energy of ~40 kJ/mol. This would result in a desorption temperature of ~120 K, lower than that at which King and Wells and TPD experiments were performed, and thus not adsorb.

Efforts were made to directly image propylene oxide at the center of the alanine tetramers. However, because of the small size of the propylene oxide, it was not possible to unequivocally distinguish between propylene oxide and other molecules adsorbed at the center of the amino acid tetramer.

5.6 Conclusions

The results clearly demonstrates the existence of chiral templates for the enantiospecific adsorption of propylene oxide and glycidol where the templates form from the self-assembly of amino-acids on a Pd(111) surface into a tetrameric structure. However, the template is provided by a metastable tetramer that exposes the most stable palladium adsorption site and exposes a sufficiently large pocket to accommodate the epoxide, where chirality is imposed by van der Waal's interaction between the epoxide and the surrounding amino acids. The most stable alanine tetramer contains a pocket that is too small to accommodate PO while the metastable precursor structure exposes a palladium atop site at the center into which both PO and glycidol can adsorb enantiospecifically. Both molecules are stabilized by interactions between NH_3^+ group of a zwitterion and the epoxide oxygen, and chirality is induced by fitting the chiral probe into the groove defined by the adjacent amino acid dimers. The fluctuation between the two isomers of the amino acid tetramers is sufficiently slow that the destabilized amino acids persist for a sufficient time to desorb at a slightly lower temperature than the most stable tetramer. Thus the amino acid tetrameric templates do not behave as a lock-and–key [19] in which the modifier provides a static configuration into which the probe molecule can fit, but is reminiscent of the induced–fit model [20] for enzymes in which fluctuations enable reactant (substrate) binding. DFT calculations reveal that S-propylene

oxide in the pocket of the D-alanine tetramer structure is sufficiently weakly bound that it will not adsorb at the experimental temperature of 150 K whereas R-propylene oxide can adsorb.

It is not clear why the presence of secondary alkyl groups in the amino acid inhibits tetramer formation. The most obvious candidate for this effect is steric hindrance imparted by bulkier side groups but the methyl groups in both tetramer structures are oriented away from the surface, suggesting that such steric hindrance is not responsible.

5.7   References

1.   Williams, J.; Haq, S.; Raval, R., The bonding and orientation of the amino acid l-alanine on Cu{110} determined by RAIRS. *Surface Science* **1996,** *368* (1–3), 303-309.

2.   Lorenzo, M. O.; Baddeley, C. J.; Muryn, C.; Raval, R., Extended surface chirality from supramolecular assemblies of adsorbed chiral molecules. *Nature* **2000,** *404*, 376-378.

3.   Marti, E. M.; Barlow, S. M.; Haq, S.; Raval, R., Bonding and assembly of the chiral amino acid S-proline on Cu(110): the influence of structural rigidity. *Surface Science* **2002,** *501* (3), 191-202.

4.   Barlow, S. M.; Louafi, S.; Le Roux, D.; Williams, J.; Muryn, C.; Haq, S.; Raval, R., Polymorphism in supramolecular chiral structures of R- and S-alanine on Cu(110). *Surface Science* **2005,** *590* (2-3), 243-263.

5.   Mahapatra, M.; Burkholder, L.; Bai, Y.; Garvey, M.; Boscoboinik, J. A.; Hirschmugl, C.; Tysoe, W. T., Formation of Chiral Self-Assembled Structures of Amino Acids on Transition-Metal Surfaces: Alanine on Pd(111). *The Journal of Physical Chemistry C* **2014,** *118* (13), 6856-6865.

6.   Mahapatra, M.; Tysoe, W., Adsorption and Reaction Pathways of a Chiral Probe Molecule, S-glycidol on a Pd(111) Surface. *Catal. Sci. Technol* **2014,** *Submitted*.

7.   Blöchl, P. E., Projector augmented-wave method. *Physical Review B* **1994,** *50* (24), 17953-17979.

8.   Kresse, G.; Joubert, D., From ultrasoft pseudopotentials to the projector

augmented-wave method. *Physical Review B* **1999,** *59* (3), 1758-1775.

9.		Kresse, G.; Hafner, J., Ab initio molecular dynamics for liquid metals. *Physical Review B* **1993,** *47* (1), 558-561.

10.		Kresse, G.; Furthmüller, J., Efficient iterative schemes for ab initio total-energy calculations using a plane-wave basis set. *Physical Review B* **1996,** *54* (16), 11169-11186.

11.		Kresse, G.; Furthmüller, J., Efficiency of ab-initio total energy calculations for metals and semiconductors using a plane-wave basis set. *Computational Materials Science* **1996,** *6* (1), 15-50.

12.		Perdew, J. P.; Burke, K.; Ernzerhof, M., Generalized Gradient Approximation Made Simple. *Physical Review Letters* **1996,** *77* (18), 3865-3868.

13.		Tkatchenko, A.; Scheffler, M., Accurate Molecular Van Der Waals Interactions from Ground-State Electron Density and Free-Atom Reference Data. *Physical Review Letters* **2009,** *102* (7), 073005.

14.		Gao, F.; Li, Z. J.; Wang, Y. L.; Burkholder, L.; Tysoe, W. T., Chemistry of glycine on Pd(111): Temperature-programmed desorption and X-ray photoelectron spectroscopic study. *J. Phys. Chem. C* **2007,** *111* (27), 9981-9991.

15.		Gao, F.; Li, Z. J.; Wang, Y. L.; Burkholder, L.; Tysoe, W. T., Chemistry of Alanine on Pd(111): Temperature-programmed desorption and X-ray photoelectron spectroscopic study. *Surface Science* **2007,** *601* (15), 3276-3288.

16.		Gao, F.; Wang, Y. L.; Burkholder, L.; Tysoe, W. T., Chemistry of L-proline on Pd(111): Temperature-programmed desorption and X-ray photoelectron spectroscopic study. *Surface Science* **2007,** *601* (17), 3579-3588.

17.		Bustos, V.; Linares, D.; Rebaza, A. G.; Tysoe, W. T.; Stacchiola, D.; Burkholder, L.; Zgrablich, G., Monte Carlo Theory Analysis of Thermal Programmed Desorption of Chiral Propylene Oxide from Pd(111) Surfaces. *J. Phys. Chem. C* **2009,** *113* (8), 3254-3258.

18.		Redhead, P. A., Thermal desorption of gases. *Vacuum* **1962,** *12*, 9.

19.		Fischer, E., Einfluss der Configuration auf die Wirkung der Enzyme. *Berichte der deutschen chemischen Gesellschaft* **1894,** *27* (3), 2985-2993.

20.		Koshland, D. E., Application of a Theory of Enzyme Specificity to Protein

Synthesis. *Proceedings of the National Academy of Sciences* **1958,** *44* (2), 98-104.

21.   Boscoboinik, J.A.; Small Organic Molecues on Transition Metal Surfaces and Monte Carlo Simulations of Surface Alloys. **2010**. Ph.D. dissertation, University of Wisconsin-Milwaukee

22.   Burkholder, L.; The Surface Chemistry of Enantioselectively Modified Palladium (111) Systems. **2009**, Ph.D. dissertation, University of Wisconsin-Milwaukee

23.   Mahapatra, M.; Burkholder, L.; Devarajan, S. P.; Boscoboinik, A.; Garvey, M.; Bai, Y.; Tysoe, W. T., Formation of Induced-Fit Chiral Templates by Amino Acid-Functionalized Pd (111) Surfaces. *The Journal of Physical Chemistry C* **2015,** *119* (7), 3556-3563.

Chapter 6

Structure and Decomposition Pathways of D-(-)-Tartaric Acid on Pd(111): A TPD and RAIRS Study

6.1 Introduction

As it has been stated previously, the principal focus of this dissertation is to use suitable chiral modifiers for imparting chirality to the achiral Pd(111) surface and then measure the resulting enantioselectivity of the chirally modified surface by probing with suitable chiral probe molecules. So far, we have extensively used α-amino acids as chiral modifiers on Pd(111) surface. It has been observed that amino acids self-organize on a Pd(111) surface to form tetrameric units [1] (Chapter 3) which act as chiral templates and provide enantiospecific adsorption towards the chiral probe molecules propylene oxide and glycidol (Chapter 5). Thus amino acid tetramers impart organizational chirality to the Pd(111) surface as described in Chapter 5.

Modification of an achiral surface by using a chiral modifier is the most successful approach to achieve heterogeneous chiral catalysis but remains a challenge at the present stage. To date, only two systems based on this concept have resulted in relatively high value of enantiomeric excess in the products. The first is the so called Orito-reaction in which α-keto esters hydrogenate over cinchona modified supported platinum catalyst [2-4] and the second is the tartaric acid modified nickel catalyst for the hydrogenation of β-keto esters.[5-6] Tartaric acid has been extensively studied as a chiral modifier on various transition metal surfaces to gain insight into the ability to create

highly enantioselective heterogeneous catalysis. The surface chemistry of tartaric acid

has been explored on Cu [7-11] and Ni [12-15] surfaces. In both the metal surfaces the nature of

the surface species depends on the temperature of the crystal surface at which tartaric

acid is dosed and the coverage. The chemistry is dominated by the presence of bitartrate

species at low coverage or upon annealing the surface to high temperature. Monotartrate

species dominates at high coverages and biacidic species are observed when dosed at low

temperatures and for multilayer coverages. The main difference between nickel and

copper is the temperature range over which these processes occur. The thermal

decomposition of the enantiopure versus racemic tartaric acid has been studied on

Cu(110) surface [16-17] and in both the cases surface explosion reaction of monotartrate

species is reported.

This chapter presents the adsorption of a chiral molecule D-(‑)-tartaric acid on

Pd(111). The main purpose of this study is to characterize the modifier molecule (D-(-)-

tartaric acid) on a Pd(111) surface which will set the basics for the future study of

enantioselective measurement of D-(‑)-tartaric acid modified palladium surface using

chiral probe molecules. The thermal stability and decomposition pathway of tartaric acid

has been explored by TPD. RAIRS has been performed to understand the orientation and

bonding of the surface species at various coverages.[18]

6.2 Experimental Section

TPD and RAIRS data were collected in the TPD and RAIRS chambers

respectively as described in Chapter-2. TPD experiments are carried out by using a

heating rate of ~2 K/s and the desorbing species were detected by using a Dycor mass

spectrometer which was placed close to and in-line-of sight of the sample front face.

Infrared spectra were collected using a Bruker Vertex infrared spectrometer operating at a resolution of 4 cm^{-1}, using a nitrogen cooled, mercury cadmium telluride detector, and spectra were typically collected for 1000 scans. The light path was purged by nitrogen boiled off from a liquid-nitrogen reservoir or using dry air.

The Pd(111) single crystal was cleaned by using a standard procedure consisting of cycles of argon ion sputtering and annealing in 3×10^{-8} Torr of oxygen at 1000 K and the cleanliness was judged by using Auger spectroscopy or TPD after dosing with oxygen, where the absence of CO desorption indicated that the sample was carbon free.

D-(-)-tartaric acid (Aldrich Chemical CO., 99%) was dosed onto the sample using a home-built Knudsen source. The tartaric acid was attached to the Knudsen source by a blank Swagelok fitting. The source was outgassed at ~400 K to remove contaminants, primarily water. It was finally outgassed at ~380 K overnight prior to dosing onto the sample. The Knudsen source temperature was maintained at 385 to 390 K during the TPD and RAIRS experiment.

6.3   Experimental Results

6.3.1   TPD Results

Temperature programmed desorption spectra were collected by dosing D-(-)-tartaric acid onto a Pd(111) surface at various temperatures. The TPD profile following D-(-)-tartaric acid adsorption at 200 K is summarized in Figure 6-1, for increasing dosing time from the Knudsen source. The only products found to desorb from the surface are hydrogen, water, carbon monoxide and carbon dioxide.
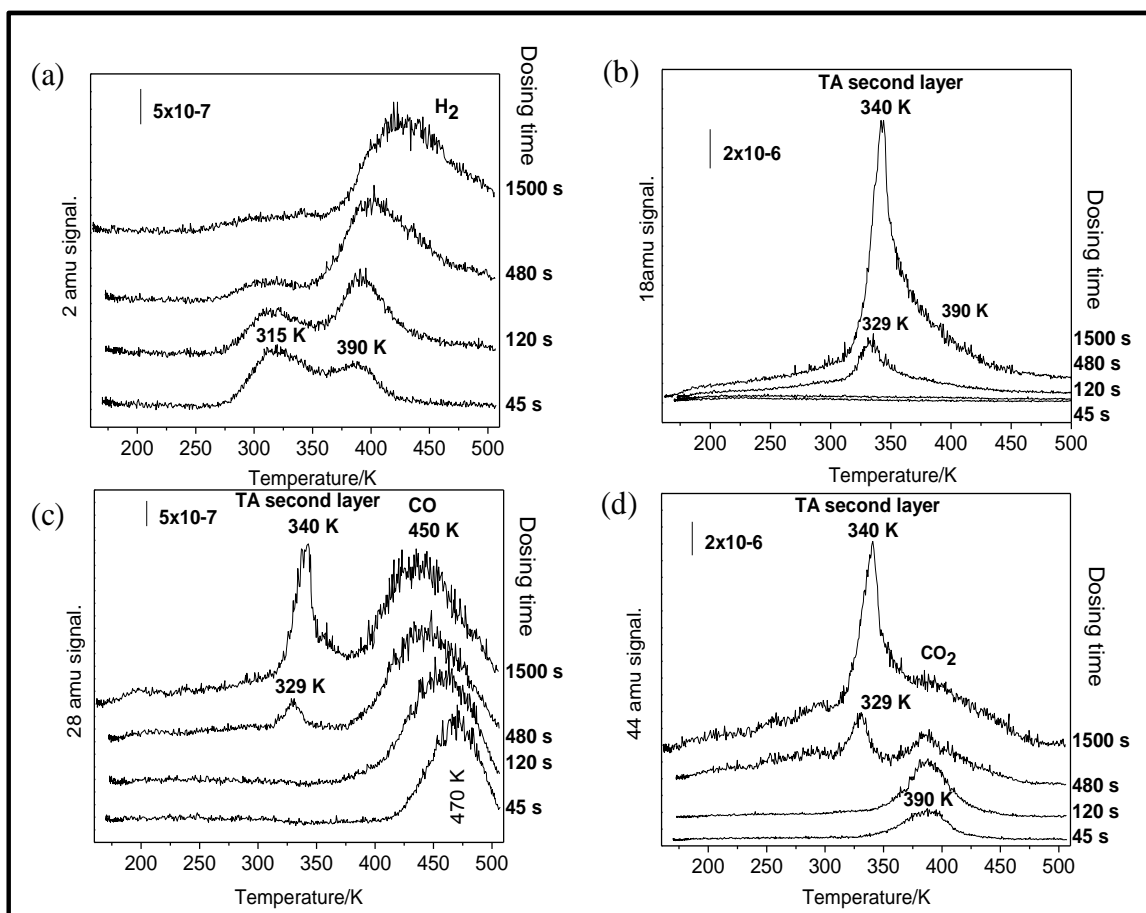
Figure 6-1 TPD profiles as a function of D-(-)-tartaric acid exposure on Pd(111) at ~200 K, collected at (a) 2 (H_2), (b) 18 (H_2O), (c) 28 (CO) and (d) 44 (CO_2) amu using a heating rate of 2 K/s. The dosing times are indicated on the desorption profiles

Hydrogen desorbs at low coverages (after 45 s dosing) in two states centered at

~315 K and ~390 K, and is accompanied by CO_2 desorption at ~390 K, indicating

complete thermal decomposition at that temperature. Carbon monoxide desorbs at ~470

K, the desorption temperature found for CO on clean Pd(111), [19-20] and is thus desorption

rate limited. At low coverages no observable water is seen in the desorption profiles. As

the D-(-)-tartaric acid dosing time increases, the low temperature hydrogen desorption

state decreases in peak temperature and intensity, while the higher temperature state

increases in intensity and desorption temperature. The peak temperature of the CO_2

desorption state remains reasonably constant with increasing dosing time, but broadens to

higher temperatures at the highest exposures (1500 s) and the intensity of the CO

desorption state increases with increase in exposure. A small amount of water signal is

observed at ~390 K with higher tartaric acid dosing times ($\geq$ 480 s). At dosing time of

480 s and greater, an additional peak appears at ~329 to 340 K in the 18, 28 and 44 amu

spectra due to the mass spectrometer ionization fragmentation of the molecular tartaric

acid, indicating D-(-)-tartaric acid adsorption into the second layer. The increase in

tartaric acid desorption temperature with increase in second layer coverage is due to

relatively strong lateral interaction between the adsorbate molecules.

Tartaric acid contains three chemically distinct hydrogen species; the hydroxyl

and the C-H hydrogens, and the hydrogen on the carboxylic acid group. Based on the

previous work of tartaric acid on transition metal surfaces, where it reacts via

deprotonation of the carboxylic acid groups, the low temperature hydrogen (~315 K) is

assigned to the deprotonation of the carboxylic acid group, and the high temperature

feature is due to the decomposition of the remaining surface species from tartaric acid.

This conclusion is confirmed by detecting CO_2 desorption at approximately the same

temperature as hydrogen (~390 K) and the evolution of carbon monoxide at higher

temperatures, likely due to the decomposition of the carboxyl and C-O-H groups,

respectively. The low temperature hydrogen peak temperature is close to that found for

hydrogen on Pd(111) [21], suggesting that it is desorption rate limited. Thus the ratio of the

~315 and 390 K hydrogen desorption features provides some indication of the extent of

tartaric acid deprotonation, with a lower intensity of the ~315 K peak suggesting a

smaller extent of deprotonation. This suggests that the extent of deprotonation decreases

as the D-(-)-tartaric acid coverage increases, and commence below ~300 K.

To provide additional insights into the chemistry occurring following D-(-)-tartaric acid adsorption at 300 K, TPD data were collected following adsorption at this temperature as a function of D-(-)-tartaric acid dosing time, and the results are summarized in Figure 6-2.
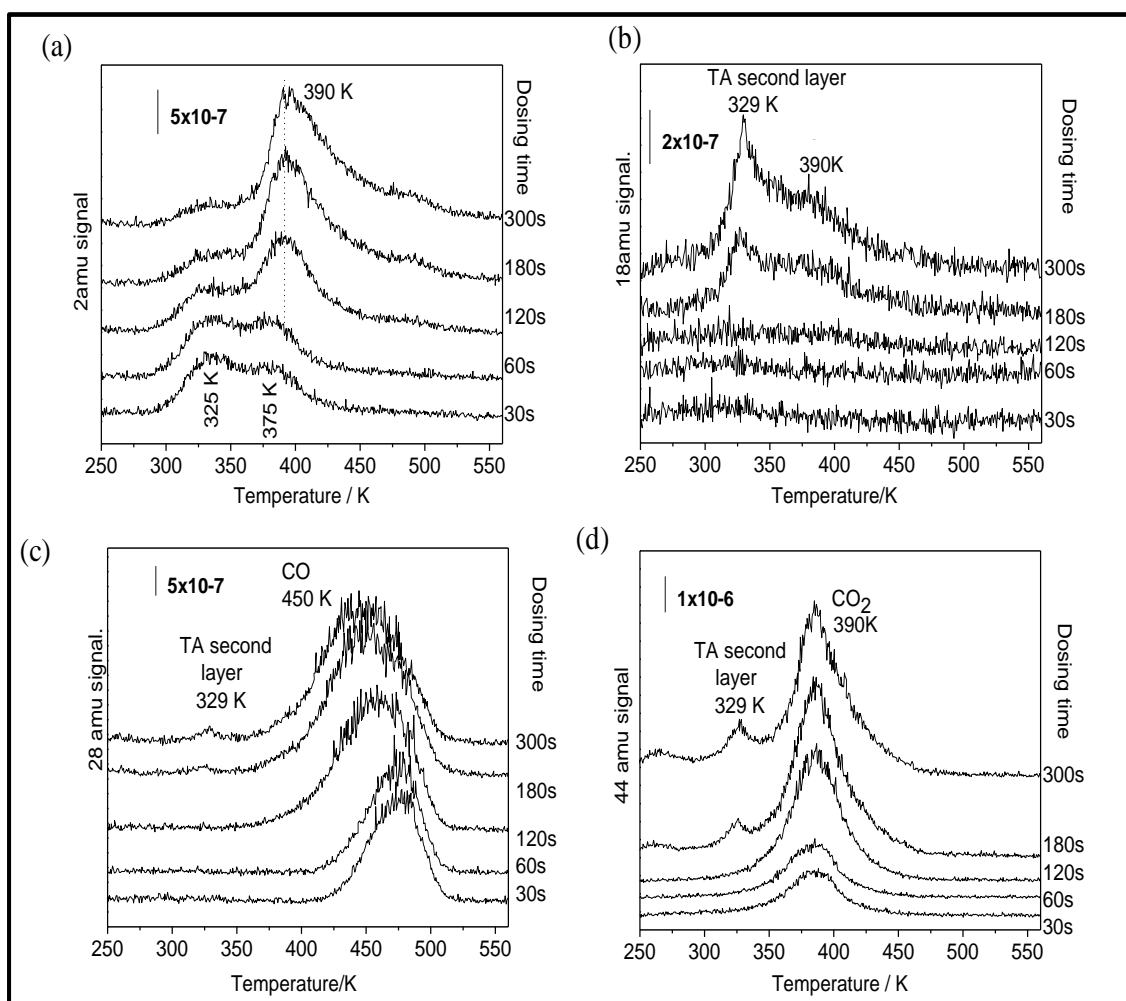
Figure 6-2 TPD profiles as a function of D-(-)-tartaric acid exposure to Pd(111) at 300 K, collected at (a) 2 (H_2), (b) 18 (H_2O) (c) 28 (CO) and (d) 44 (CO_2) amu using a heating rate of 2 K/s. The dosing times are indicated on the desorption profiles.

H_2O (desorbing at 329 and 390 K), CO (desorption temperature between ~440 to ~470 K) and CO_2 (desorption temperature ~390 K) profiles are similar to those found following adsorption at ~200 K (Figure 6-1). The 2 amu (hydrogen) desorption profile

show two states at ~325 and 375 K where the low temperature state decreases in intensity with increase in tartaric acid coverage, while the high temperature state continue to grow. This indicates a higher level of deprotonation at lower than at high coverage.

6.3.2 RAIRS Experiment

RAIRS was used to further explore the nature of the surface species formed from D-(-)-tartaric acid on Pd(111). Figure 6-3 shows the infrared spectra for the tartaric acid adsorbed at ~100 K as a function of exposure time.
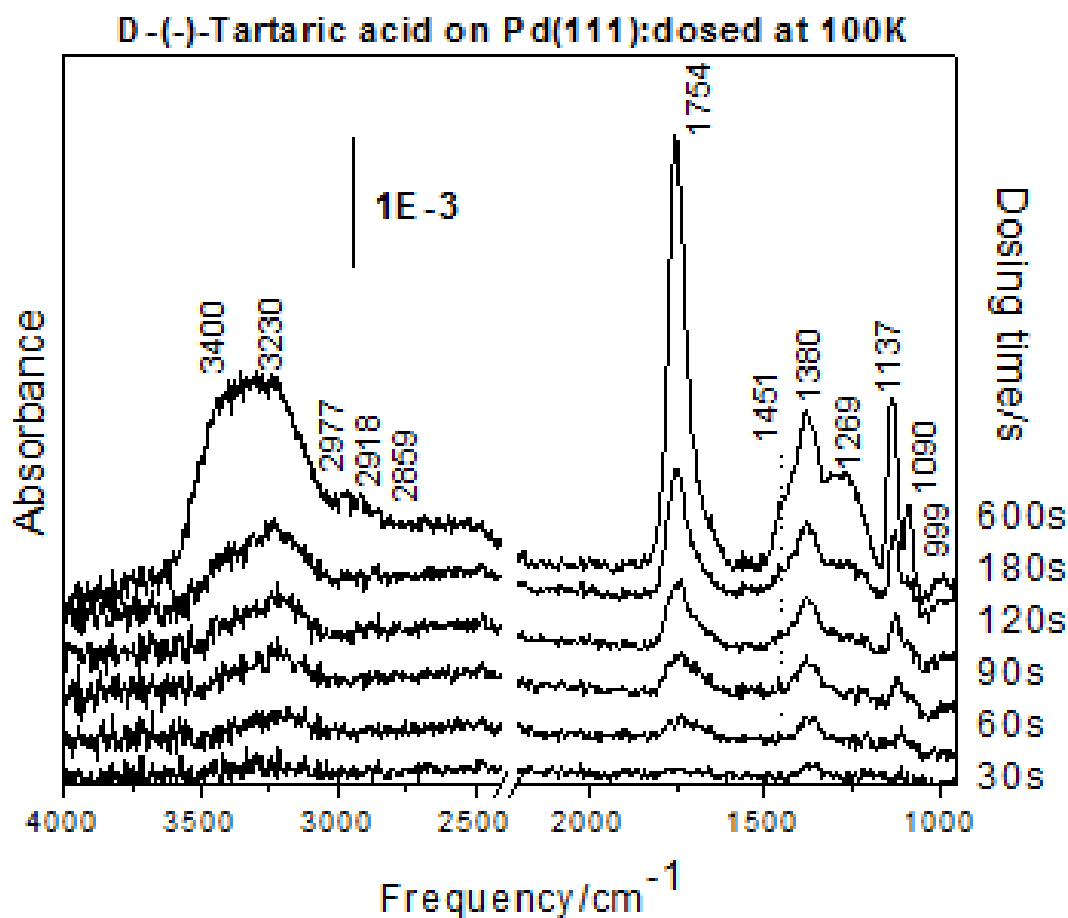
Figure 6-3 Infrared spectra of D-(-)-tartaric acid adsorbed on Pd(111) at 100 K as a function of tartaric acid exposure, where the dosing times are indicated adjacent to the spectra.

This displays a number of features that grow in intensity as the dosing time increases, which are assigned by comparison of the spectra for the biacid.[22] The frequencies measured in Figure 6-3 are compared to those of the tartaric acid powder in Table 6-1 along with the assignments. The broad high frequency modes at ~3400 and 3200 cm^{-1} are assigned to OH stretching mode, and their relative breadths indicate hydrogen bonding interactions between –OH groups, consistence with the temperature shift of the second layer desorption state in TPD. Weak features are seen in the C-H region at ~2977, 2918 and 2859 cm^{-1}. [23] The most intense peak occurs at ~1754 cm^{-1} due to the C=O stretching mode of the carboxylic acid group and a shoulder at ~1451 cm^{-1} is due to the associated C-O vibration. In principle, since the identical C-H and C-O-H groups are attached to the same carbon atom on the tartaric acid backbone, coupling between the vibrational modes of these groups should cause a split in the features, with the antisymmetric combination having a higher frequency than the isolated species, and the symmetric combination moving to lower frequency.[23] The ~1380 and the 1269 cm^{-1} modes are assigned to the wagging modes of the –OH group of the alcohol and the C-H group respectively. While they should in principle be split into two modes, they are not resolved in the spectra, but appear as broadened features. This effect is however, seen for the doublets at ~1090 and 1137 cm^{-1} due to the C-O stretching mode of the alcohol C-O-H groups. Finally, the weak feature at ~999 cm^{-1} is assigned to the backbone carbon-carbon stretching vibrations.[23] The close correspondence between the spectrum of D-(-)-tartaric acid on the surface and the bulk material indicates that pure tartaric acid adsorbs on the surface at ~100 K. The frequency assignments in the Table 6-1 provide the basis for following the decomposition pathways at higher temperatures.

Pd(111)/Vibrational frequency/cm^{-1}	Tartaric acid powder [22] frequency/cm^{-1}	Assignments
~3400	3388	ν_{OH}^{alc}
~3230	3193	ν_{OH}^{acid}
2977	2972	ν_{CH}
2918	2939	ν_{CH}
2859	-	-
1754	1741	$\nu_{C=O}$
1451 (shoulder)	1453	ν_{CO}^{acid}
1380	1375	δ_{OH}^{alc}
1269 (broad)	1255	δ_{CH}
1137	1134	ν_{CO}^{alc}
1090	1087	ν_{CO}^{alc}
999	992	ν_{CC}

Table 6-1 Assignments of the vibrational frequencies of tartaric acid adsorbed on Pd(111) at 100 K (Figure 6-3) with that due to a biacid powder of tartaric acid [22] ν-stretching vibration, δ-wagging vibration.

Since TPD data suggests that deprotonation of the carboxylic acid group starts below ~300 K, D-(-)-tartaric acid was dosed onto Pd(111) at ~300 K. The infrared results collected as a function of D-(-)-tartaric acid dosing time are shown in Figure 6-4. At small doses (up to 90 s), small peaks are detected at ~1910 and ~1840 cm^{-1} which corresponds to the CO adsorption in different sites, [24-25] which indicate that either there is a small amount of tartaric acid decomposition or that some CO has adsorbed from the background. Since the CO peaks attenuate at higher tartaric acid doses, this suggests that the CO is due to the background adsorption and is displaced from the surface by subsequent tartaric acid adsorption. The spectra also show a broad peak at ~1370 and a peak at ~1108 cm^{-1}. Based on the assignments for multilayer tartaric acid on Pd(111) at 100 K (Figure 6-3 and Table 6-1), these features are due to the δ_{OH} and ν_{CO} modes of the alcohol groups. However, no features due to the carboxylic acid groups are detected at ~1700 cm^{-1}.
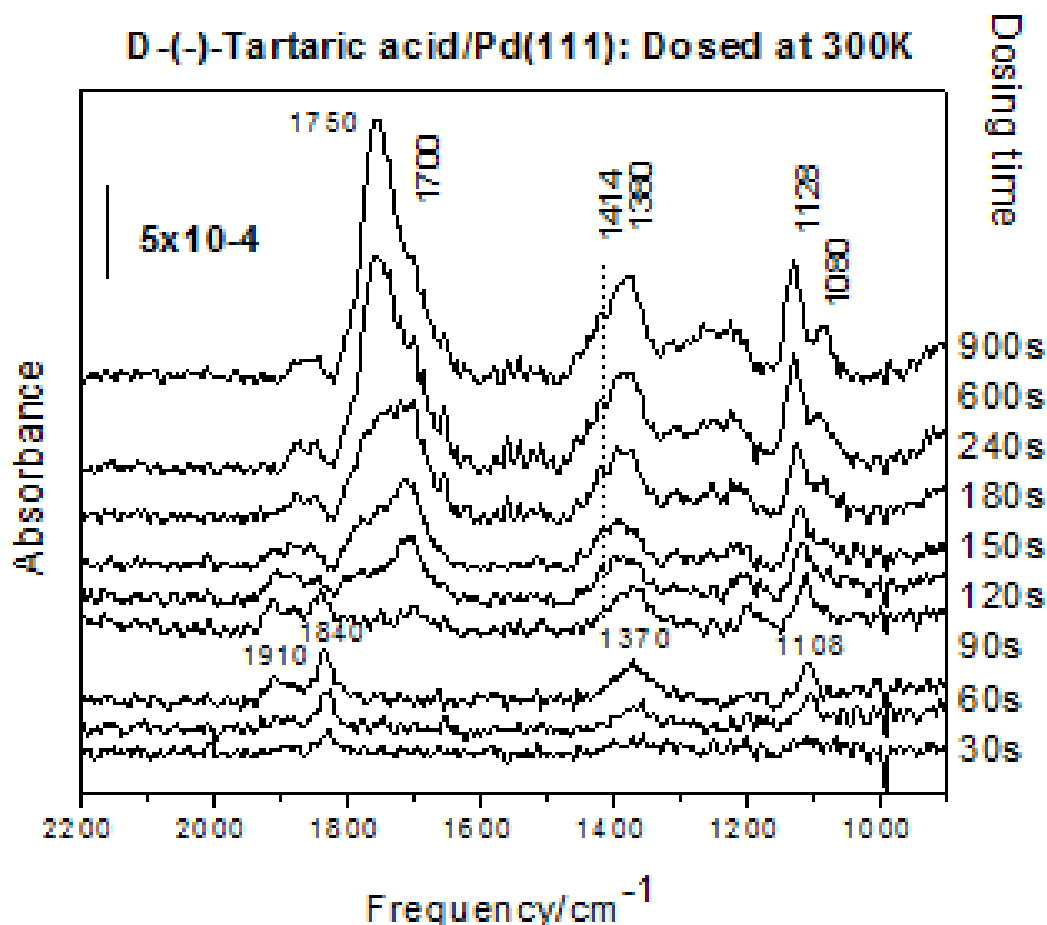
Figure 6-4 Infrared spectra of D-(-)-tartaric acid adsorbed on Pd(111) at 300 K as a function of tartaric acid exposure, where the dosing times are indicated adjacent to the spectra.

Addition of further tartaric acid for a total of 240 s results in the appearance of and additional feature at 1700 cm^{-1}, and the shift of the ~1370 cm^{-1} peak to a slightly higher frequency of ~1380 cm^{-1}. Further addition of tartaric acid to a total exposure of ~900 s results in a feature growing at ~1750 cm^{-1}, an intensification of the peak at ~1380 cm^{-1}, and a splitting of the ~1108 cm^{-1} feature into a doublet at ~1128 and 1080 cm^{-1}. The spectrum following higher exposures is essentially identical to that formed at ~100 K (Figure 6-3) and is due to adsorption of the biacid into the second layer. Based on the TPD data (Figure 6-2), the multilayer desorbs at ~329 K from a surface dosed at ~300 K.

This starts to appear at a tartaric acid exposure of ~240 s, suggesting that a saturated

monolayer forms after an exposure of ~200 s. It thus appears that one species forms on

the surface for exposures between 0 and 100 s, which shows no intensity at ~1700 cm^{-1},

and a second state for exposures between ~100 and 200 s which exhibits a C=O

stretching frequency of ~1700 cm^{-1}.

      We first focus on the species that appears for exposures between 100 and 200 s.

The ~1700 cm^{-1} peak is due to a C=O stretching mode of a carboxylic group, but is

shifted from the value of ~1750 cm^{-1} in the biacid due to adsorption of the other

carboxylate group to the surface and probably due to hydrogen bonding between the

adsorbates. The modes for all identical species (C-H, C-OH, and COOH) couple in

tartaric acid to produce a symmetric and antisymmetric combination of vibrational

modes. The coupling causes a split in the frequency with the antisymmetric combination

having a higher frequency than the isolated species and the symmetric combination

moving to lower frequency. In crystalline tartaric acid, the coupled modes appear at

~1743 and 1697 cm^{-1}.[22] Assuming that they split symmetrically, the free carboxylic acid

mode would have a frequency of ~1720 cm^{-1}, close to the value of 1700 cm^{-1} found at

low exposures at 300 K (Figure 6-4), suggesting the formation of monotartrate. The

remainder of the molecule is identical to the biacid leading to a straightforward

assignment, and the measured frequencies are compared with those for the monotartrate

on Cu(110) [7] and Ni(111) [13] in Table 6-2. The close correspondence with the data on

copper and nickel indicate that the monotartrate has formed for dosing time between 100

and 200 s.

Vibrational Frequency/Pd(111) /cm^{-1}	Monotartrate/Cu(110)/ cm^{-1}	Monotartrate/Ni(111)/ cm^{-1}	Assignment
1700	1711	1656	$\nu_{C=O}$
~1414 (shoulder)	1437	1428	ν_{OCO}^{Sym}
1380	1398	1380	δ_{OH}^{alc}
-	1338	-	
-	1300	-	$\delta\nu_{OH}^{acid}+\delta_{CH}$
-	1234	-	
1204	1197	1194	
1117	1101	1113	ν_{CO}^{alc}

Table 6-2 Infrared vibrational frequencies for high coverages of tartaric acid adsorbed on Pd(111) at 300 K (Figure 6-4) compared with the assignments for monotartrate species on Cu(110) [7] and Ni(111).[13] ν-stretching vibration, δ-wagging vibration.

Insight into the species formed at low tartaric acid dosing times (< 100 s) at 300 K comes from the shift in frequency of the 1380 cm^{-1} (found at higher coverages) to 1370 cm^{-1} as well as the absence of a ~1700 cm^{-1} mode. This might be the reason that there is a hydrogen-bonding interaction between the OH group on the carbon adjacent to the surface carboxylate group and the C=O group that causes it to be oriented parallel to the surface and is therefore infrared forbidden. Subsequently, crowding caused by additional tartaric acid adsorption causes the carboxylic acid group to move so that it becomes closer to perpendicular to the surface and then becomes infrared active. An alternative explanation is that surface bitartrate species are formed at low coverages. By comparing the low coverage frequencies of the Cu(110) [7] and Ni(111) [13] with the low coverage frequencies found on Pd(111), it is confirmed that surface bitartrate species are formed at low coverages on Pd(111) at 300 K. The low coverage frequencies of Pd(111) at 300 K and the comparison with that for Cu(110) and Ni(111) are given in Table 6-3 along with their assignment. These assignments will form the basis for analyzing the subsequent spectra.

Vibrational Frequency/Pd(111)/ cm^{-1}	Bitartrate/Cu(110)/cm^{-1}	Bitartrate/Ni(111)/cm^{-1}	Assignment
1414	1430	1434	ν_{OCO}^{Sym}
1390	1410	1401	ν_{OCO}^{Sym}
1370	1375	1370, 1325	δ_{OH}^{alc}
1200	1200	1272	δ_{CH}
1108	1113	1110	ν_{CO}^{alc}
-	-	999	ν_{CC}

Table 6-3 Infrared vibrational frequencies for low coverages of tartaric acid adsorbed on Pd(111) at 300 K (Figure 6-4) compared with the assignments for bitartrate species on Cu(110) [7] and Ni(111).[13] ν- stretching vibration, δ-wagging vibration.

The effect of heating a low coverage (90 s dosing time) of D-(-)-tartaric acid on Pd(111) adsorbed at ~300 K is shown in Figure 6-5. An initial dose of ~90 s of tartaric acid on Pd(111) is very similar to the low coverage spectra shown in Figure 6-4, except that there is a small peak at ~1705 cm^{-1} peak suggest that the dose is closer to ~120 s in Figure 6-4. Based on the above assignments (Table 6-3), this is due to the formation of bitartrate species on the surface with some monotartrate species (Table 6-2). The effect of temperature on the adsorbed layer was followed by heating the sample to the indicated temperature for ~20 s and allowing the sample to cool once again and then recording the infrared spectrum. Heating the sample causes various changes. First, the ~1705 cm^{-1} feature, due to monotartrate species, increases in intensity. Second, the ~1370 cm^{-1} feature shifts to ~1380 cm^{-1}, providing further evidence for monotartrate formation. This suggests that the hydrogen present on the surface can rehydrogenate the bitartrate that forms at ~300 K to reform a monotartrate species. Similar behavior is seen for acetate species on Pd(111) that can rehydrogenate to reform acetic acid.[26-28] In addition, a number of other sharp features grow at 1309, 1252 and 1209 cm^{-1} as the sample is warmed. Note that these features are not associated with the monotartrate since the 1705

cm^{-1} feature decreases in intensity at ~350 K, while these additional features remain

constant in intensity. The origin of these features will be discussed in greater detail

below.
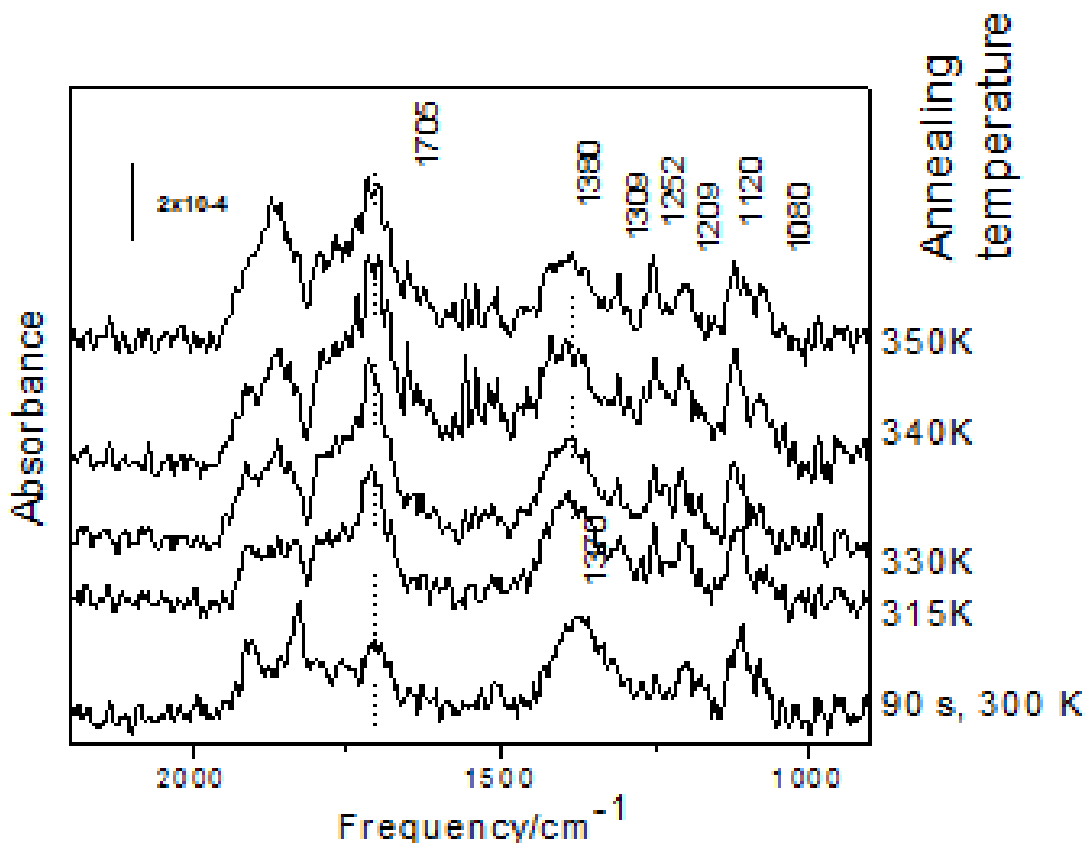
Figure 6-5 Infrared spectra illustrating the effect of heating a Pd(111) surface exposed to ~90 s (~0.5 ML) of D-(–)-tartaric acid heated to various temperatures. The annealing temperatures are indicated adjacent to the spectra.

This new intermediate species can be obtained by dosing a sample at ~100 K with

tartaric acid for ~300 s and heating as shown in Figure 6-6. Again the sample was heated

for ~20 s to the indicated temperature, and then allowed to cool to 100 K, following

which the spectrum was recorded.
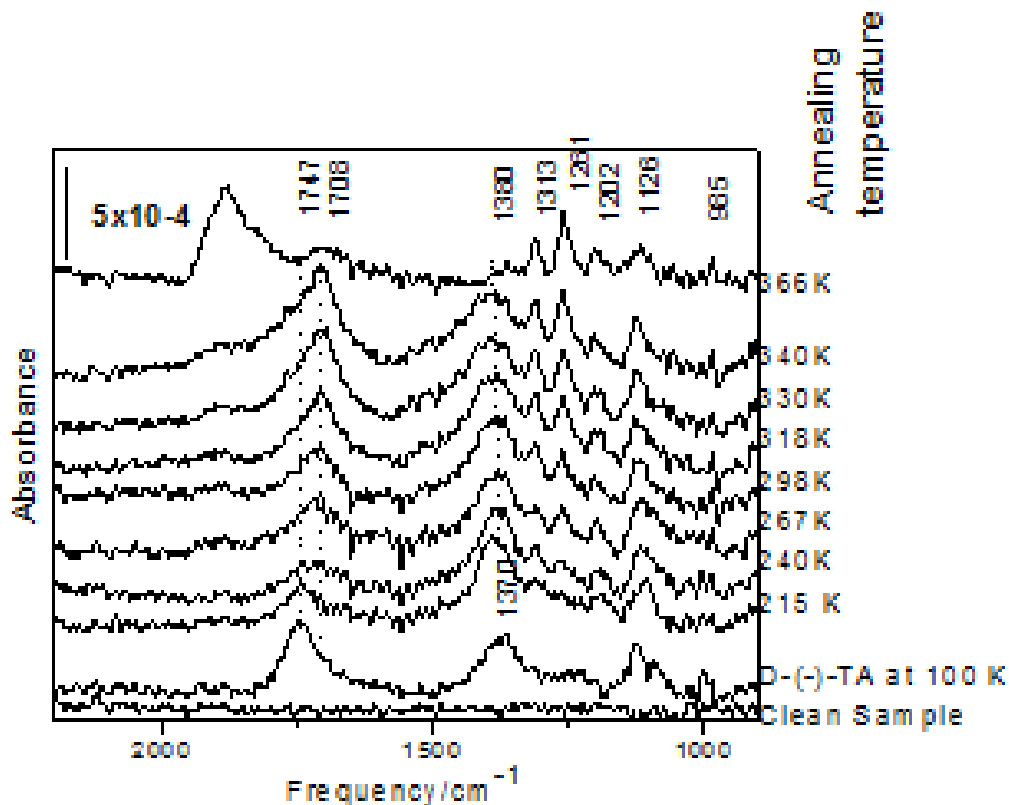
Figure 6-6 Infrared spectra of Pd(111) exposed to 300 s of D-(-)-tartaric acid at ~100 K heated to various temperatures. The annealing temperatures are indicated adjacent to the spectra.

Based on the above discussion, a dosing time of ~300 s should lead to the saturation of the first layer and the formation of some second-layer biacidic species. The initial spectrum (Figure 6-6) is in accord with that observed following adsorption at 100 K (Figure 6-3), which shows a major pear at ~1750 cm^{-1} due to the carboxylic acid groups. Heating to ~215 K causes the ~1747 cm^{-1} peak to decrease in intensity, while the ~1380 cm^{-1} feature increases. Based on TPD results, no desorption occurs over this temperature range (Figure 6-1) suggesting that the tartaric acid in the second layer reorients such that the carboxylic acid groups are more parallel to the surface. Heating to ~267 K causes a shift in the 1747 cm^{-1} mode to ~1708 cm^{-1}, indicative of monotartrate

formation, while from the TPD data, the second layer is still present. This indicates that deprotonation of the tartaric acid occurs between ~240 and ~267 K, consistent with the 2 amu TPD profile. Warming from ~298 to ~340 K results in features at ~1313, 1261 and 1202 cm^{-1} growing, while a small amount of hydrogen desorbs from the surface (Figure 6-1). Any second-layer tartaric acid desorbs at ~330 K (Figure 6-1). In addition, no CO is found on the surface when heating to ~340 K. Drastic changes occur on heating to ~366 K, where all of the monotartrate species disappear, as indicated by the absence of the ~1708 cm^{-1} peak and a significant amount of formation of CO species as indicated by the presence of a broad peak at ~1850 cm^{-1}. However, there is clearly a second decomposition pathway at higher coverages *via* a surface intermediate that has peaks at ~1313, 1261, 1202 and a broad feature at ~1126 cm^{-1}. Further heating of the sample to ~450 K causes these features to disappear, resulting in a flat baseline (data not shown). Additional evidence for such an alternative pathway comes from the TPD data (Figure 6-1), where for tartaric acid doses up to ~120 s (thus for sub monolayer coverages), CO_2 and hydrogen desorb simultaneously in a rather symmetric state centered at ~280 K. A high-temperature tail appears in both of these peaks at higher coverages (480 and 1500 s doses), presumably due to the decomposition of the surface species found after annealing to ~366 K. The absence of any intensity at ~1700 or ~1400 cm^{-1} suggest that the intermediate contains no carboxylic or carboxylate groups. Comparison with the assignments for the various tartaric-acid derived species on Pd(111) suggests that the 1313, 1261 and 1202 cm^{-1} features are δ_{CH} modes and the 1116 mode is due to a ν_{CO}^{alc} vibration. This may therefore be due to a decarboxylated tartaric acid, resembling the adsorption of 1,2-dihydroxyethylene (1,2-ethendiol).

6.3.3 Effect of Tartaric Acid Dosing Flux

It has been found on Ni(111) that the rate of impingement of tartaric acid on the surface can affect the nature of the surface species that are formed.[13] The formation of a bitartrate species must occur in two steps with sufficient sites being available to deprotonate the second carboxylic acid group. A higher arrival rate can potentially block those sites before the bitartrate has had an opportunity to form. The infrared spectra of tartaric acid adsorbed on Pd(111) using higher dosing fluxes are displayed in Figure 6-7, and are compared with similar data collected using a lower flux at ~300 K (Figure 6-4).
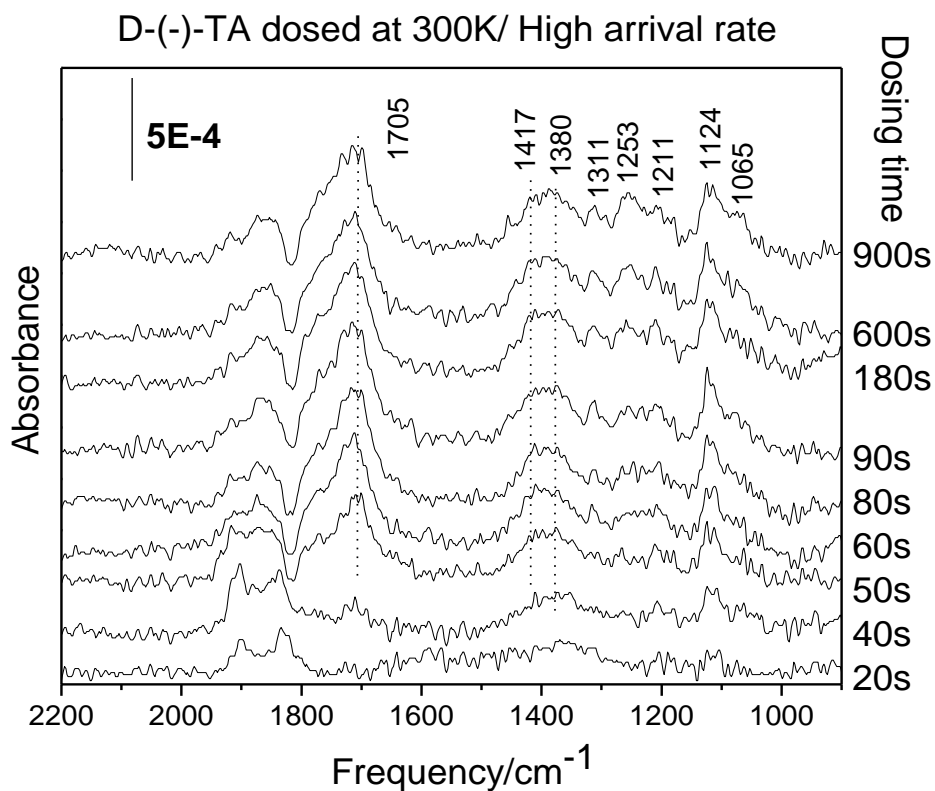
Figure 6-7 Infrared spectra collected as a function of D-(-)-tartaric acid exposure to Pd(111) at 300 K, where the exposure times are indicated adjacent to the spectra.

Several differences are indeed noted. Bitartrate species do form initially at lower

coverages as evidenced by the absence of features at ~1700 cm^{-1}, while the monotartrate starts to form after an exposure of ~40 s at higher flux (compared with ~100 s at a lower flux, Figure 6-4). This difference can be ascribed to changes in incident flux, and it is not clear from these data whether the onset of bitartrate formation differs. However, a larger amount of thermal decomposition occurs at higher flux as evidenced by the appearance of intense peaks due to adsorbed CO. Interestingly, no tartaric acid adsorbed in the second layer and the features are observed at 1313, 1261 and 1202 cm^{-1} further indicating the formation of the same intermediate detected in the previous IR profiles when the surface was dosed at ~100 K and annealed to higher temperatures (Figure 6-6). This suggests that the nature of the species formed on the surface (mono *versus* bitartrate) is not strongly influenced by the tartaric acid flux, but second layer adsorption is suppressed at higher fluxes, and the extent of surface decomposition increases.

6.4   Discussion

The general chemical reactivity of D-(–)-tartaric acid on Pd(111) is similar to that seen previously for chemically similar Ni(111).[13] The thermal stability and decomposition pathways are followed using TPD (Figure 6-1 and 6-4). Hydrogen desorbs on two states at ~315 and ~390 K, where the temperature of the latter state is coincident with the desorption of carbon dioxide and is thus ascribed to the total thermal decomposition of surface D-(–)-tartaric acid derived species. The low-temperature hydrogen desorption state is due to adsorbed hydrogen and indicates the extent of deprotonation, which decreases with increasing coverage. This is quite similar to the behavior seen on Ni(111) where simultaneous hydrogen and CO$_2$ desorption are observed at between 430 and 440 K, so that the D-(–)-tartaric acid species are slightly more

reactive on Pd(111) than on Ni(111). Similarly, adsorbed biacid, monotartrate and bitartrate species are identified on the surface, depending on the dosing or annealing temperatures and coverage. A thermodynamically stable bitartrate tends to form at lower coverages, while the monotartrate preferentially forms at higher coverages due to steric effects that inhibit the removal of the second proton at higher coverages.[7] It is also found that the bitartrate appears to rehydrogenate to a monotartrate species on Pd(111). The major difference between the chemistry found previously between nickel [12-13] and palladium is the formation of an intermediate seen most clearly when a monolayer of D-(-)-tartaric acid is adsorbed on Pd(111) at ~100 K and heated to ~366 K (Figure 6-6). This is not due to a bitartrate species since all of the bitartrate species have decomposed by this annealing temperature. Additional evidence for such an alternative pathway comes from the TPD data (Figure 6-1), where for D-(-)-tartaric acid doses up to ~120 s (for submonolayer coverages), CO_2 and hydrogen desorb simultaneously in a rather symmetric state centered at ~380 K and no water is observed. A high-temperature, tail appears in both of these peaks at higher coverages (480 and 1600 s doses) with a small amount of water being formed, presumably due to the decomposition of the surface species found after annealing to ~366 K. This is consistent with the disappearance of this species on heating to ~450 K. The absence of any intensity at ~1700 or ~1400 cm^{-1} suggests that the intermediate contains no carboxylic acid or carboxylate groups.

This annealing temperature range from ~ 366 to ~450 K coincides with the higher-temperature desorption states of CO_2 and water of ~390 K (Figures 6-1 and 6-4) observed at higher dosing times. The absence of any modes due to carboxyl or carboxylate groups on heating to ~366 K suggests that the adsorbed tartaric acid species

have decarboxylated to produce the intermediate. However, a small amount of this species also seems to form after dosing at ~300 K and heating to ~315 K and above (Figure 6-5). The intermediate is characterized by modes at ~1313, 1261, 1202 and 1116 cm^{-1} most clearly seen in Figure 6-6. Comparison with the assignments for the various tartaric-acid derived species on Pd(111) (Table 6-1, 6-2 and 6-3) suggests that the 1313, 1261 and 1202 cm^{-1} features are δ_{CH} modes and the 1116 cm^{-1} mode is due to a ν_{CO}^{alc} vibration. There is also the suggestion of a feature at ~985 cm^{-1}, detected slightly above the background noise in Figure 6-6 suggesting that the carbon backbone remains intact. Such an intermediate may suggest that tartaric-acid derived species initially decompose by decarboxylation, with the remaining hydrocarbon fragment decomposing to give hydrogen, water and carbon monoxide. It is noted that this intermediate also contains a chiral center.

6.5 Conclusions

D-(-)-tartaric acid adsorbs on a Pd(111) surface predominantly *via* deprotonation of the carboxylic acid group in a chemistry directly analogous to that found previously on nickel and copper surfaces. Adsorbed monotartrate species form at higher D-(-)-tartaric acid coverages and the bitartrate formed at lower coverages. However, the bitartrate appears to rehydrogenate to monotartrate species on heating. Biacidic tartaric acid adsorbs into the second layer at higher coverages and desorbs between ~329 and 340 K depending on the second-layer coverage, indicative of attractive interactions between the tartaric acid molecules. Hydrogen evolves on heating in two features at ~320 and 390 K. The lower-temperature feature is ascribed to hydrogen from the carboxylate groups and the higher-temperature state assigned to the decomposition of the remainder of the

molecule since it desorbs at the same temperature as carbon dioxide and some water at higher D-(-)-tartaric acid coverages. The relative intensity of the low-temperature state decreases compared to the high-temperature state as the D-(-)-tartaric acid coverage increases consistent with a lower extent of carboxylic acid group deprotonation and the presence of a higher proportion of monotartrate species at higher dosing times. Carbon monoxide desorbs at ~450 K is a desorption-rate limited process. A decomposition intermediate is detected by dosing D-(-)-tartaric acid at low temperatures (~100 K) and heating to ~300 K or by dosing at ~300 K and heating to ~320 K, and is characterized by modes at ~1313, 1261, 1202 and 1116 cm^{-1} assigned to δ_{CH} modes and a ν_{CO}^{alc} vibration suggesting that the intermediate may form by removal of the –COO group.

6.6   References

1.   Mahapatra, M.; Burkholder, L.; Bai, Y.; Garvey, M.; Boscoboinik, J. A.; Hirschmugl, C.; Tysoe, W. T., Formation of Chiral Self-Assembled Structures of Amino Acids on Transition-Metal Surfaces: Alanine on Pd(111). *The Journal of Physical Chemistry C* **2014,** *118* (13), 6856-6865.

2.   Orito, Y.; Imai, S.; Niwa, S., Asymmetric Hydrogenation of Methyl Pyruvate Using Pt-C Catalyst Modified with Cinchonidine. *J. Chem. Soc. Jpn.* **1979,** (8), 1118-1120.

3.   Orito, Y.; Imai, S.; Niwa, S.; Nguyengiahung, Asymmetric Hydrogenation of Methyl Benzoylformate Using Platinum-Carbon Catalysts Modified with Cinchonidine. *Journal of Synthetic Organic Chemistry Japan* **1979,** *37* (2), 173-174.

4.   Orito, Y.; Imai, S.; Niwa, S., Asymmetric hydrogenation of a-keto esters using a platinum-alumina catalyst modified with cinchona alkaloid. *J. Chem. Soc. Jpn.* **1980,** (4), 670-2.

5.   Harada, T.; Izumi, Y., Improved Modified Raney-Nickel Catalyst for Enantioface-Differentiating (Asymmetric) Hydrogenation of Methyl Acetoacetate. *Chemistry Letters* **1978,** (11), 1195-1196.

6.	Izumi, Y., Modified Raney-Nickel (Mrni) Catalyst - Heterogeneous Enantio-Differentiating (Asymmetric) Catalyst. *Advances in Catalysis* **1983,** *32*, 215-271.

7.	Lorenzo, M. O.; Haq, S.; Bertrams, T.; Murray, P.; Raval, R.; Baddeley, C. J., Creating chiral surfaces for enantioselective heterogeneous catalysis: R,R-Tartaric acid on Cu(110). *J. Phys. Chem. B* **1999,** *103* (48), 10661-10669.

8.	Lorenzo, M. O.; Baddeley, C. J.; Muryn, C.; Raval, R., Extended surface chirality from supramolecular assemblies of adsorbed chiral molecules. *Nature* **2000,** *404*, 376-378.

9.	Lorenzo, M. O.; Humblot, V.; Murray, P.; Baddeley, C. J.; Haq, S.; Raval, R., Chemical transformations, molecular transport, and kinetic barriers in creating the chiral phase of (R,R)-tartaric acid on Cu(110). *Journal of Catalysis* **2002,** *205* (1), 123-134.

10.	Raval, R., Chiral expressions at metal surfaces. *Current Opinion in Solid State & Materials Science* **2003,** *7* (1), 67-74.

11.	Humblot, V.; Lorenzo, M. O.; Baddeley, C. J.; Haq, S.; Raval, R., Local and global chirality at surfaces: Succinic acid versus tartaric acid on Cu(110). *Journal of the American Chemical Society* **2004,** *126* (20), 6460-6469.

12.	Humblot, V.; Haq, S.; Muryn, C.; Hofer, W. A.; Raval, R., From local adsorption stresses to chiral surfaces: (R,R)-tartaric acid on Ni(110). *Journal of the American Chemical Society* **2002,** *124* (3), 503-510.

13.	Jones, T. E.; Baddeley, C. J., A RAIRS, STM and TPD study of the Ni{111}/R,R-tartaric acid system: Modelling the chiral modification of Ni nanoparticles. *Surface Science* **2002,** *513* (3), 453-467.

14.	Humblot, V.; Haq, S.; Muryn, C.; Raval, R., (R,R)-tartaric acid on Ni(110): the dynamic nature of chiral adsorption motifs. *Journal of Catalysis* **2004,** *228* (1), 130-140.

15.	Jones, T. E.; Baddeley, C. J., An investigation of the adsorption of (R,R)-tartaric acid on oxidised Ni{111} surfaces. *Journal of Molecular Catalysis A-Chemical* **2004,** *216* (2), 223-231.

16.	Behzadi, B.; Romer, S.; Fasel, R.; Ernst, K.-H., Chiral recognition in surface explosion. *Journal of the American Chemical Society* **2004,** *126* (30), 9176-9177.

17.	Romer, S.; Behzadi, B.; Fasel, R.; Ernst, K. H., Homochiral conglomerates and racemic crystals in two dimensions: tartaric acid on Cu (110). *Chemistry-A European*

Journal **2005,** *11* (14), 4149-4154.

18.   Mahapatra, M.; Tysoe, W. T., Structure and decomposition pathways of D-(−)-tartaric acid on Pd (111). *Surface Science* **2014**.

19.   Kuhn, W. K.; Szanyi, J.; Goodman, D. W., CO adsorption on Pd(111): the effects of temperature and pressure. *Surface Science* **1992,** *274* (3), L611-L618.

20.   Voogt, E. H.; Coulier, L.; Gijzeman, O. L. J.; Geus, J. W., Adsorption of Carbon Monoxide on Pd(111) and Palladium Model Catalysts. *Journal of Catalysis* **1997,** *169* (1), 359-364.

21.   Conrad, H.; Ertl, G.; Latta, E. E., Adsorption of hydrogen on palladium single crystal surfaces. *Surface Science* **1974,** *41* (2), 435-446.

22.   Bhattacharjee, R.; Jain, Y. S.; Bist, H. D., Laser Raman and infrared spectra of tartaric acid crystals. *Journal of Raman Spectroscopy* **1989,** *20* (2), 91-97.

23.   Colthup, N. B. D. L. H. W. S. E., *Introduction to infrared and Raman spectroscopy*. Academic Press: N.Y.

24.   Bradshaw, A. M.; Hoffmann, F. M., The chemisorption of carbon monoxide on palladium single crystal surfaces: IR spectroscopic evidence for localised site adsorption. *Surface Science* **1978,** *72* (3), 513-535.

25.   Surnev, S.; Sock, M.; Ramsey, M. G.; Netzer, F. P.; Wiklund, M.; Borg, M.; Andersen, J. N., CO adsorption on Pd(1 1 1): a high-resolution core level photoemission and electron energy loss spectroscopy study. *Surface Science* **2000,** *470* (1–2), 171-185.

26.   Davis, J. L.; Barteau, M. A., Hydrogen bonding in carboxylic acid adlayers on Pd(111): evidence for catemer formation. *Langmuir* **1989,** *5* (6), 1299-1309.

27.   Haley, R.; Tikhov, M.; Lambert, R., The Surface Chemistry of Acetic Acid on Pd{111}. *Catalysis Letters* **2001,** *76* (3-4), 125-130.

28.   Hansen, E.; Neurock, M., First-Principles Based Kinetic Simulations of Acetic Acid Temperature Programmed Reaction on Pd(111). *The Journal of Physical Chemistry B* **2001,** *105* (38), 9218-9229.

Chapter 7
STM and DFT of D-(–)-tartaric acid on Pd(111)

7.1   Introduction

Asymmetric hydrogenation of β-keto esters over tartaric acid modified nickel catalysts is one of the most successful examples in the field of heterogeneous asymmetric catalysis. Tartaric acid has been extensively studied as a chiral modifier on various transition-metal surfaces to gain insight into the nature of the species which provide highly enantioselective chiral sites. In the previous chapter we have explored the surface chemistry of tartaric acid on Pd(111) surface[1] by spectroscopic methods and the results are consistent with the previous surface science studies carried out on Cu [2-12] and Ni [2-4, 6, 9, 11, 13-14] surfaces. On all the three metal surfaces (Cu, Ni and Pd), the nature of the surface species depends on the temperature of the sample at which tartaric acid is dosed and the coverage. On the Pd(111) surface; the overall chemistry is dominated by the presence of bitartrate species at low coverage, monotartrate species at high coverages and biacidic species for multilayer coverages which is similar to the results obtained on Cu and Ni surfaces.

A large number of STM studies have been performed on single crystal Cu and Ni surfaces to investigate the surface structure of tartaric acid on metal surfaces. Tartaric acid forms extended ordered supramolecular assemblies on Cu(110) surfaces, which destroys the existing symmetry elements of the underlying metal surfaces and directly bestow chirality to the modified surface.[2-3] Different 2-dimensional ordered structures are

reported which are formed either from the singly deprotonated monotartrate or doubly deprotonated bitartrate species depending on the tartaric acid coverage and annealing temperature. Recently it is been reported that singly deprotonated monotartrate species reconstruct the Cu(110) surface with proper annealing treatment and the resulting structure is ordered and chiral.[15] However, the major drawback of these studies in terms of catalytic importance is that copper is a poor hydrogenation catalyst. The STM images of tartaric acid on Ni(111) suggests that extend of ordering is much less on nickel than copper and is attributed to the fact that nickel surface is more reactive than copper.[13] Tartaric acid exists predominately in its bitartrate form on Ni(110) surface, which provides chiral motifs but does not show any long-range ordering. Those chiral motifs induce local reconstruction of the metal atoms to relive the adsorption-induced strain and provides global chirality to the metal surface.[9]

Accordingly, this chapter presents a STM study of D-(-)-tartaric acid on a Pd(111) surface at various coverages under different experimental conditions. The surface structures formed as a function of modification time and temperature are investigated. The main purpose of this study is to characterize the modifier molecule (D-(-)-tartaric acid) on a Pd(111) surface and to identify different surface structures by correlating them with the previous spectroscopic study (Chapter 6). The other motivation is to directly observe the nature of the chiral modification and to identify the catalytic sites which will set the stage for the future study of enantioselective measurement of D-tartaric acid modified palladium surfaces using chiral probe molecules.[1] STM results are complemented by DFT calculations which are also discussed in this chapter.

7.2   Experimental and Theoretical Methods

The Pd(111) single crystal was cleaned by using a standard procedure consisting of cycles of argon ion sputtering and annealing in 3×10^{-8} Torr of oxygen at 1000 K and the cleanliness was judged by using Auger spectroscopy.

Scanning Tunneling Microscopy experiments were performed using a scanning tunneling microscope housed in an UHV chamber operating at a base pressure of 2×10^{-10} Torr following bake-out as described in Chapter 2. STM images were acquired using an electrochemically etched tip made from recrystallized tungsten wire. This was conditioned by a controlled interaction with a clean Au(111) single crystal and is expected to result in a gold terminated tip.

D-(-)-tartaric acid (Aldrich Chemical, 99%) was dosed onto the sample using a home-built Knudsen source. The tartaric acid was placed in the Knudsen source using a blank Swagelok fitting. The source was outgassed at ~400 K to remove contaminants, primarily water. It was finally outgassed at ~380 K overnight prior to dosing onto the sample. The Knudsen source temperature was adjusted to achieve the desired dosing rate. STM experiments are carried out by maintaining the source temperature in the range of 385 to 395 K.

Density functional theory (DFT) calculations were performed with the projector augmented wave (PAW) method [16-17] as implemented in the Vienna ab initio simulation package, VASP.[18-19] The exchange correlation potential was described using the generalized gradient approximation (GGA) of Perdue, Burke and Ernzehof. [20] Hydrogen bonding interactions are well reproduced (within ~ 4 kJ/mol) using this functional, although the accuracy deteriorates as the hydrogen bonds deviate from linear.[21] A cut off

of 400 eV was used for the plane wave basis set, and the wave functions and electron density were converged to within 1×10^{-5} eV. The first Brillouin zone was sampled with a $4\times4\times1$ Γ-centered k-point mesh. Geometric relaxations were considered to be converged when the force was less than 0.02 eV/Å on all unrestricted atoms.

7.3   Experimental Results

STM images were collected by dosing D-(-)-tartaric acid onto a Pd(111) surface in order to explore the distribution on the surface.
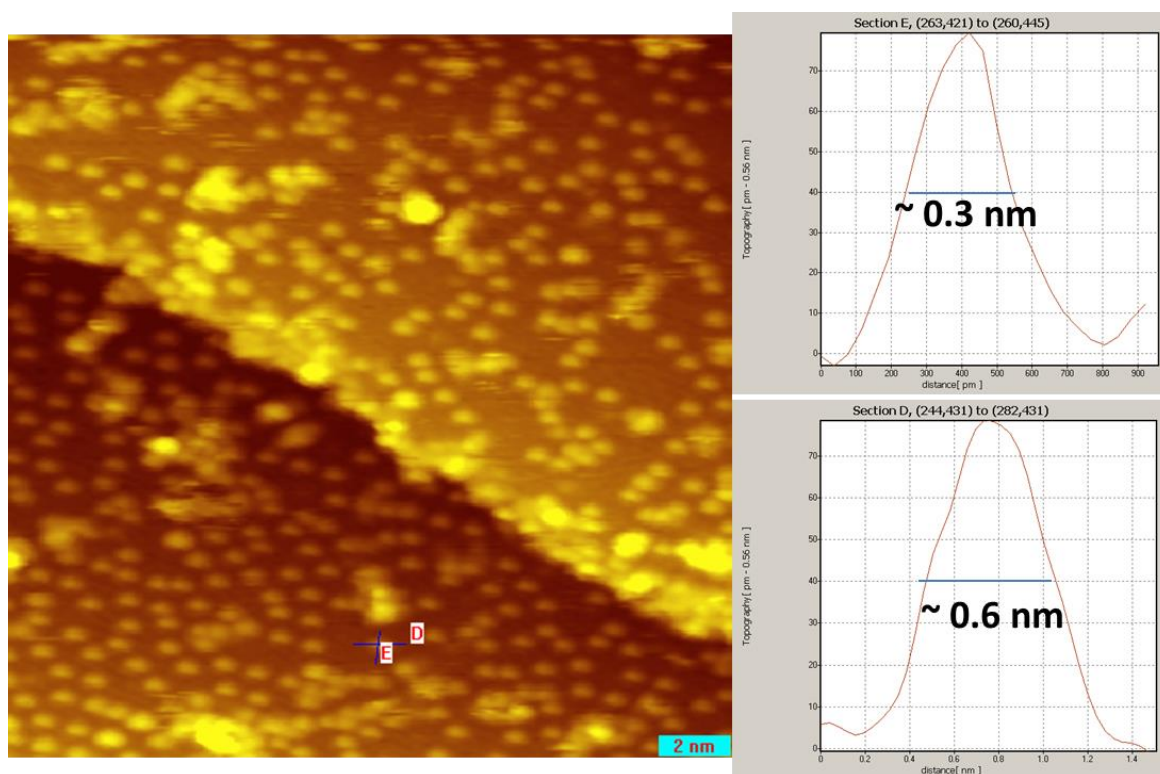
Figure 7-1 A STM image of D-(-)-tartaric acid dosed onto a Pd(111) surface at ~300 K following which the sample was cooled to ~120 K for imaging (V_b=0.9 V, I_t=380 pA).

An image of a low coverage of tartaric acid dosed at ~300 K (Pd sample temperature) and then cooled to ~120 K, at which temperature the image was collected is shown in Figure 7-1.This shows the presence of individual elliptical structures assigned to the presence of bitartrate species on the surface. Line profiles of the elliptical

structures suggest that they are ~3 Å across and ~6 Å long. The size of the observed

structure is in accord with the size of the bitartrate species observed on Cu(110) and

Ni(110) surfaces.[2-3, 9, 11]

Under the same preparation condition, other features were found on the surface

which appears to be bilobed as shown in Figure 7-2 (a) and (b).
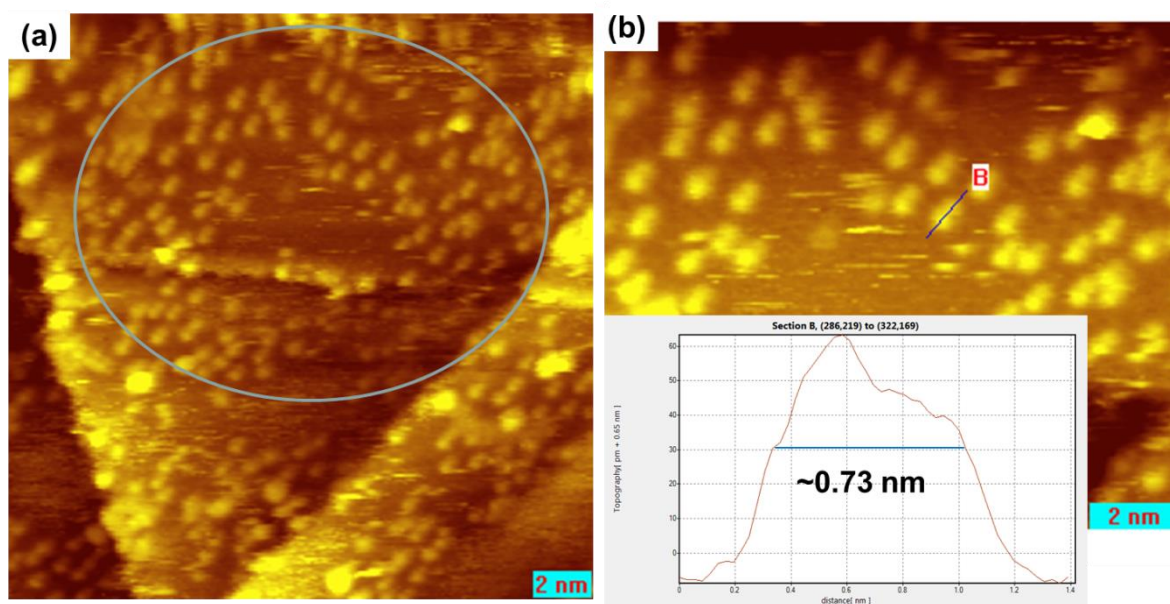
Figure 7-2 (a) A STM image of D-(-)-tartaric acid dosed onto a Pd(111) surface at ~300 K following which the sample was cooled to ~120 K for imaging (V_b=0.9 V, I_t=380 pA). (b) A zoomed in image for the area highlighted in blue oval in (a) and the line profile measurement across the dimer structure is shown.

Those features are imaged as two lobes, where one lobe appears brighter than the

other as indicated by the line profile measurement in Figure 7-2 (b). We have assigned

those structures to the formation of monotartrate dimers where the free –COOH group of

one monotartrate hydrogen bonds to the –OH group of another monotartrate. The

monotartrate species with free –COOH group images brighter than the other. A similar

dimer structure has been proposed for tartaric acid on Cu(110) surface.[2]

STM images are collected following dosing various coverages of D-(-)-tartaric acid at 300 K and scanning at the same temperature. The most commonly observed images are summarized in Figure 7-3.
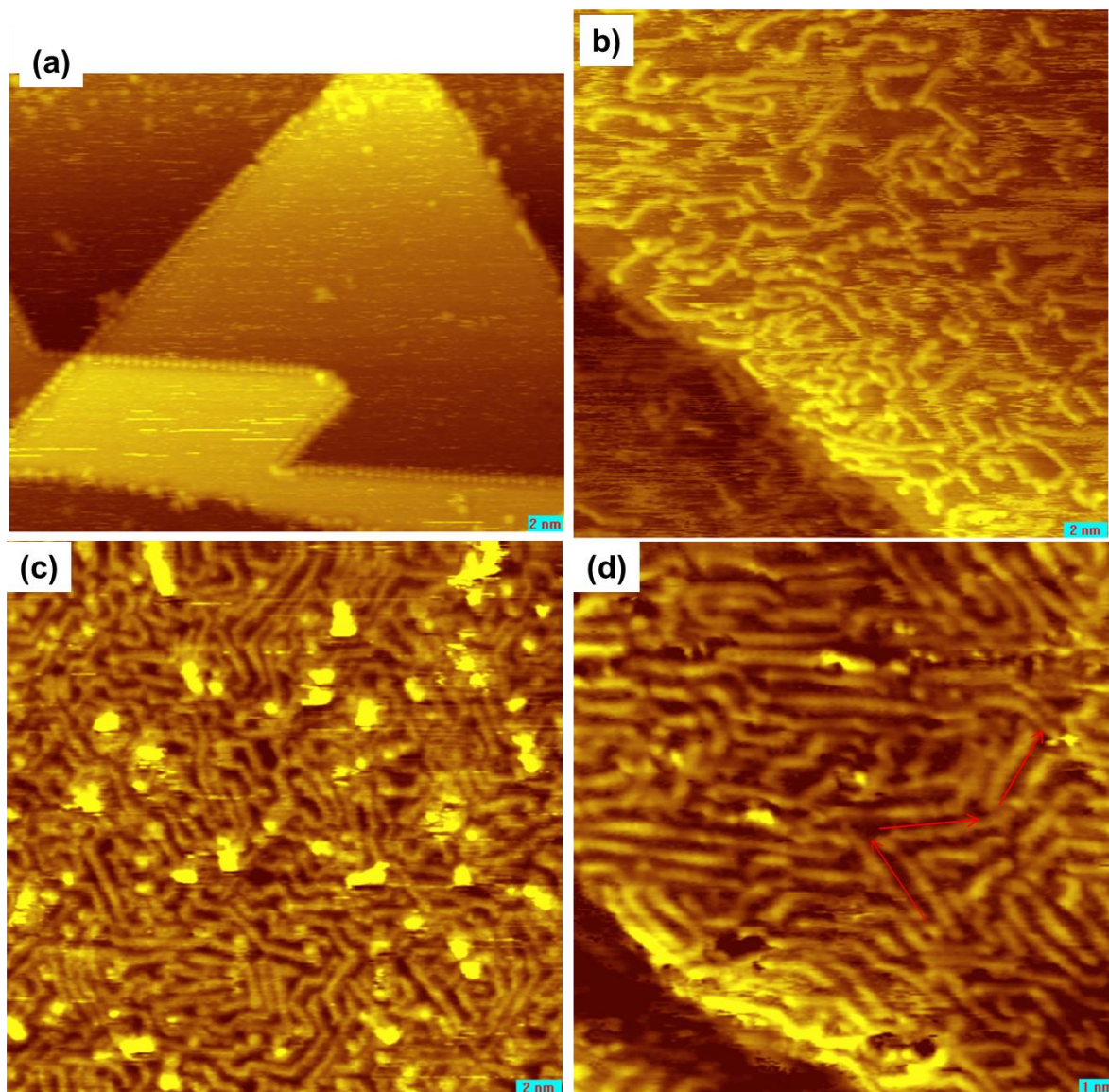
Figure 7-3 (a) to (c) STM images of D-(-)-tartaric acid on a Pd(111) surface as a function of increasing coverage. Images are collected when D-(-)-tartaric acid was dosed and imaged at 300 K (a) at low coverages the molecules are lined up on the step edge (b) and (c) show the formation of oligomers (d) zoomed in image for the same area as (c) ((a), (b),V_b=0.9 V, I_t=380 pA and (c) and (d) V_b= -0.32 V, I_t=80 pA).

At low coverages, the molecules are lined up on the step edges (Figure 7-3 (a)). In addition, a few individual monomers and dimers are also observed on the terrace. Streaky lines are observed in the scanning direction on the terrace indicating the presence of some mobile species on the surface. When the coverage was increased (Figure 7-3 (b) and (c)), the terrace was covered with oligomers of different size. Those oligomeric species are the most common surface structure observed in the moderate (Figure 7-3(b)) to high coverage regime, (Figure 7-3 (c)) and they are oriented along the $< 1\bar{1}0 >$ surface crystallographic directions. Similar oligomeric species are reported for intermediate coverages of tartaric acid on Ni(111) surface and are proposed to consist of monotartrate species.[13] Figure 7-3 (d) is a higher magnification image of the same area as in Figure 7-3 (c), which clearly shows the growth of the oligomeric species in three directions. It has been observed that a linear chain growing in one direction ends arbitrarily and another chain grows at an angle of 120° to it. An example is highlighted by red arrows, where three different oligomeric chains grow 120° to each other. The average size of the oligomers is about 3 to 4 nm. Based on the previous TPD and IR study, at intermediate to high coverages the surface contains predominately monotartrate species. Therefore the oligomeric chains are assigned to the hydrogen-bonded monotartrate species, where hydrogen bonding occurs between the carboxylic acid groups and the α-hydroxy groups or between two α-hydroxy groups of the neighboring monotartrate species. Previous IR results (Chapter 6) show a C=O stretching frequency for the carboxylic acid group of monotartrate species at ~1708 cm^{-1}, which is downshifted from a value of ~1750 cm^{-1} for a free carboxylic acid group, is indicative of the hydrogen bonding interactions between

the molecules in the adlayer. Thus, the STM results are in accord with the previous IR study.[1]

The growth of the oligomeric species on the surface increases with time. Figure 7-4 (a) to (c) show three consecutive images collected for the same surface at eight minute intervals.
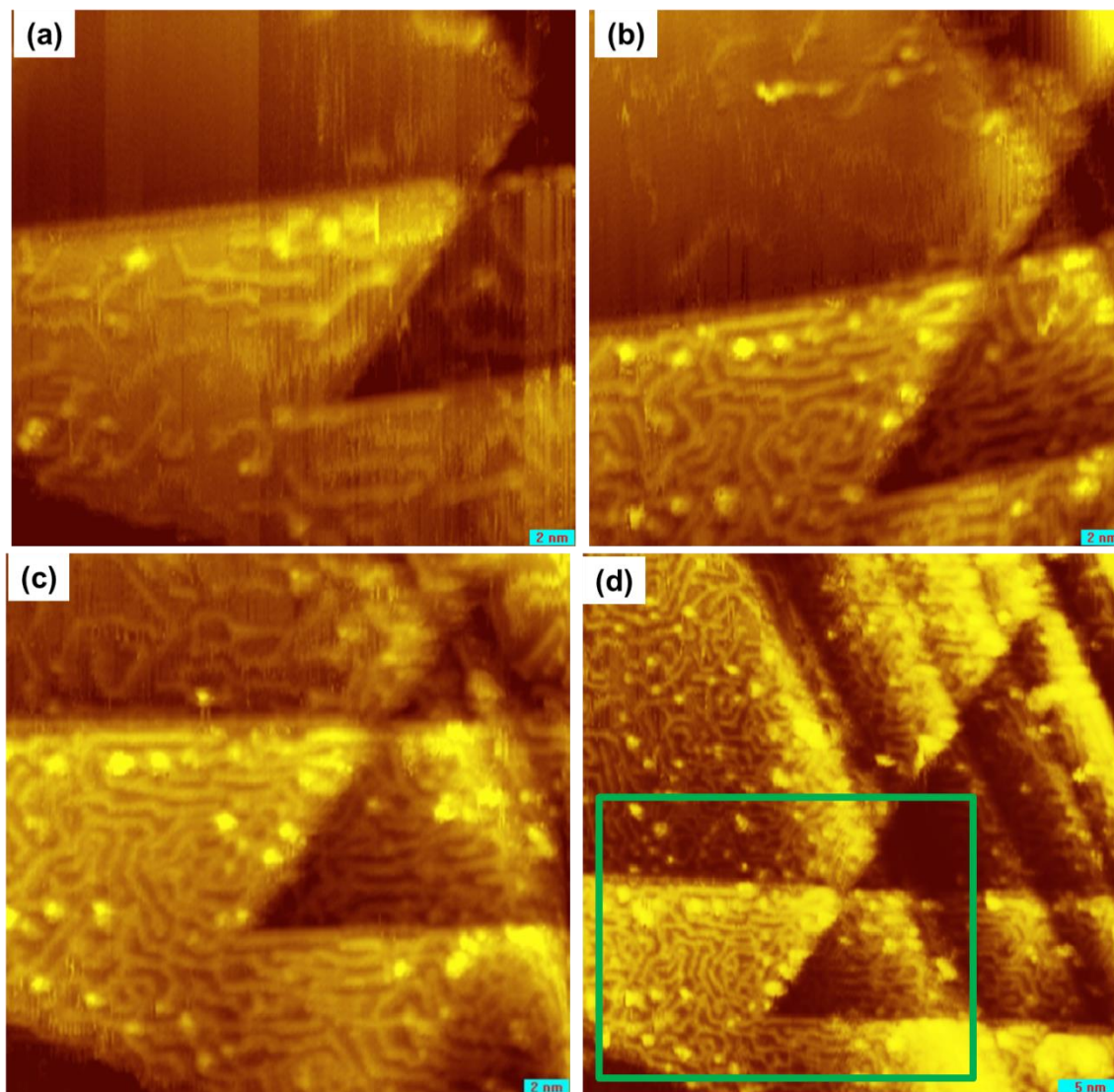
Figure 7-4 STM Images of D-(-)-tartaric acid when dosed onto a Pd(111) surface at 300 K and imaged at the same temperature. Figure 7-4 (a) to (c) shows the growth of the oligomeric chains in consecutive scan. Figure 7-4 (d) is a larger scan area which contains the previously repeated scan area (highlighted in green rectangle) (V_b= 1 V, I_t=180 pA).

In the first scan, there are few oligomers on the surface but with continuous scanning, the surface becomes more crowded with relatively short linear oligomers, where the length of the oligomers increases with time. During the initial growth of the oligomers, the coverage appears higher on the top terrace than on the bottom. The oligomers are quite stable on the surface, once formed can be imaged for very long period of time.

To understand if the growth of the oligomeric chains is a kinetic effect or induced by the tip, a STM image is collected for a larger scan area which contains the smaller repeatedly scanned area (highlighted in green rectangle in Figure 7-4 (d)). The resulting image (Figure 7-4 (d)) shows that the whole surface is covered with oligomers. This suggests that the growth of the oligomers is a kinetic effect and that they form slowly on the surface over time. However, when images are collected for a scan area which is farther (~100 nm or more) away from the previous repeatedly scanned area, again the growth of the oligomers was observed with time. Therefore, it appears though the tip is also enhancing the rate of formation of the oligomer chains. This process is independent of the bias polarity and occurs with both positive and negative biases. Similar behavior has been observed by glutaric acid on a Cu(110) surface, [22] where ordered structures appear as a result of electric field between the tip and the sample. The enhancement of the rate of evolution of the oligomer chains on Pd(111) can be explained by a similar effect. When a bias is applied between the tip and the sample, the diffusing molecules accumulate under the tip. When the local coverage is greater than a certain threshold value, diffusion ceases and molecules pair up with each other to form oligomers.

In addition to oligomeric structure, at intermediate coverages, a small fraction of the surface contains two different kinds of ordered structure which are shown in Figure 7-5 and 7-6. The formation of these structures is kinetically limited on the surface and only appears after a long period of time.

Figure 7-5 shows an ordered two-dimensional network, which arises due to mutual hydrogen bonding interaction between the monotartrate species.
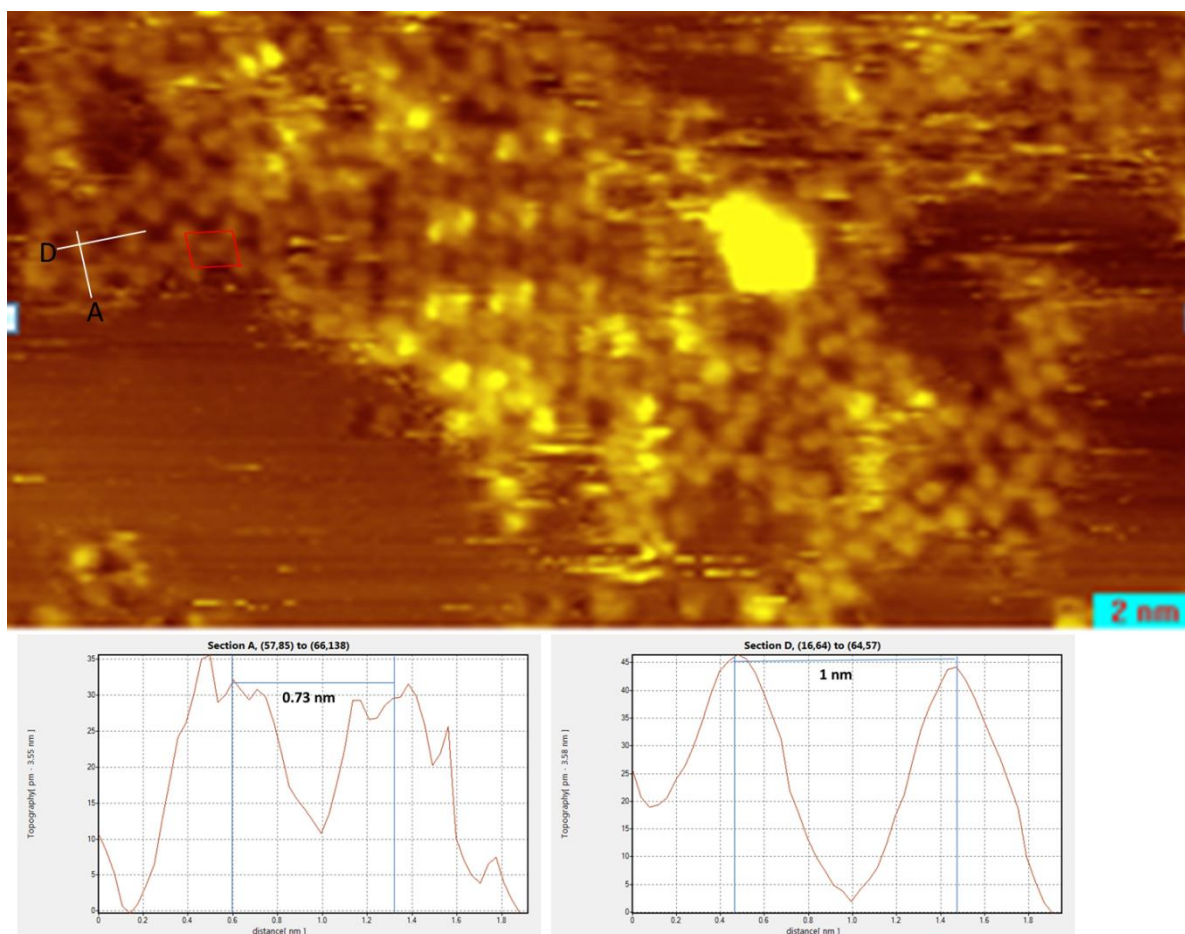
Figure 7-5 A STM image showing two dimensional ordered structure formed from tartaric acid adsorption on Pd(111) surface at 300 K. (V_b= -0.32 V, I_t=80 pA) The unit cell for the over layer structure is shown in the same figure. Line profile measurements shown in the bottom are indicated by white lines in the image.

The structure shows a clear relation between neighboring molecules and is characterized by adjacent features. It appears to consist of a central molecule which is

surrounded by four molecules, which are rotated by 60° with respect to it. It is proposed that this structure arises when all the functional groups of each monotartrate species takes part in hydrogen bonding interactions while the carboxylate group bonds to the surface. The unit cell for the over layer structure is shown in the Figure 7-5. By carefully measuring the distance between the species, it appears that this ordered structure consists of a unit cell which has a relationship with the underlying substrate given by the matrix notation (4 -1, -1 3).

Figure 7-6 shows the second type of observed ordered structure, which consists of dimer rows with empty channels between the rows. The local coverage is much smaller in this ordered domain than the structure observed in Figure 7-5; therefore this is proposed to occur from bitartrate species. There is no obvious linkage between the dimers which leads to long-range ordering. The unit cell for this structure is shown in Figure 7-6. Figure 7-6 (c) is a Fourier filter image which clearly shows the periodicity of the dimeric structure. There are some dark features observed in between the dimer rows and it is periodic, one dark spot corresponds to one dimer pair. The origin of those dark features is not completely understood at this moment, but might be the adsorbed hydrogen atoms as observed on a Ni(110) surface.[9] The distance between the bitartrate species reveal that the ordered structure consists of a (6 0, -1 5$\sqrt{3}$) unit cell.
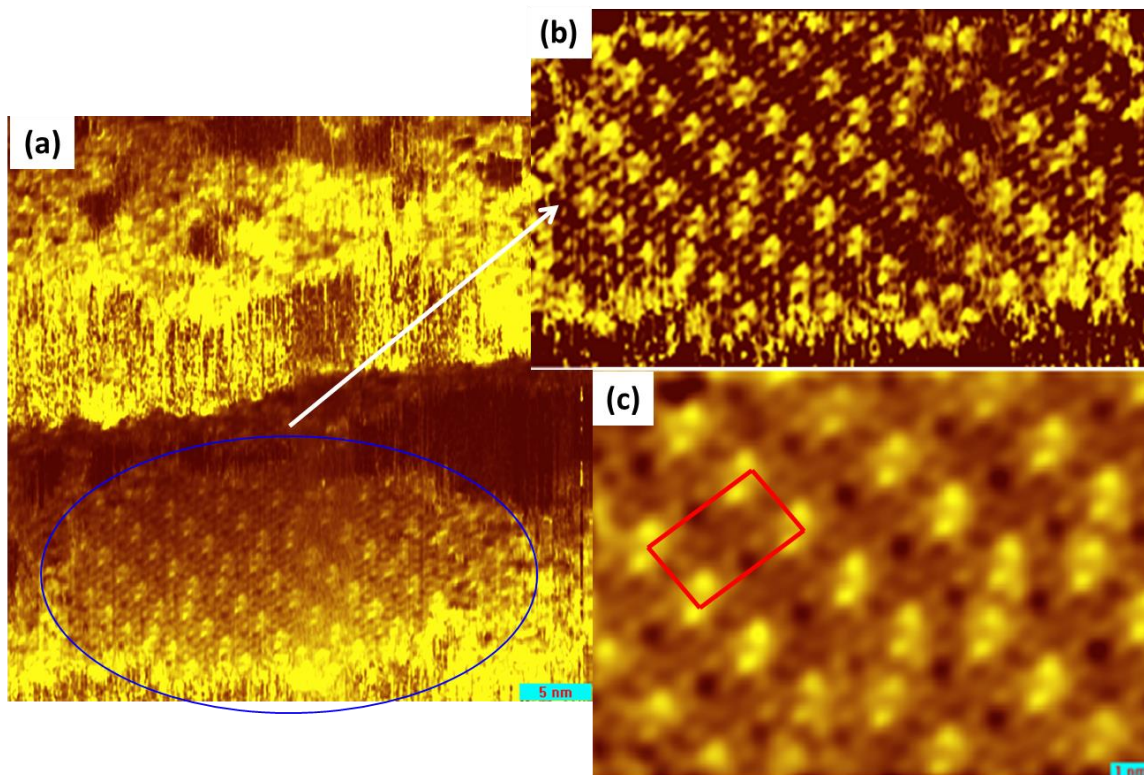
Figure 7-6 (a) A large scan area STM image showing two dimensional ordered structure (on the bottom terrace) formed from tartaric acid adsorption on Pd(111) at 300 K. (b) Cropped image as highlighted in blue oval in (a) showing clearly the dimer features and ordered assembly. (c) The image 7-6 (b) is Fourier filtered to eliminate the noise and in the same image, unit cell for the overlayer structure is shown (V_b= 1 V, I_t=80 pA).

7.4 Discussion

Tartaric acid shows the formation of several surface structures at different coverages. At low coverages, individual species were found on the surface whereas, at higher coverages, the surface primarily consists of oligomeric chain structures. The sample temperature and the time have a large effect on the formation of ordered structures. The ordered structures form over a very long period of time, only when the surface was dosed at 300 K, which emphasizes the importance of temperature. At low temperatures, the molecules are not sufficiently mobile to self-organize into two dimensional ordered patterns. Previous spectroscopic study shows that on a Pd(111)

surface, the surface contains bitartrate species at low coverages and monotartrate species at higher coverages. First principle DFT calculations were carried out to characterize different surface structures observed in STM and to confirm the structural assignments made above.

7.4.1   DFT Calculations for the Bitartrate Species

DFT calculations were performed for an isolated bitartrate species adsorbed on a 6×6 Pd(111) slab with co-adsorbed hydrogen atoms on three-fold hollow sites, and the most stable structure is shown in Figure 7-7.
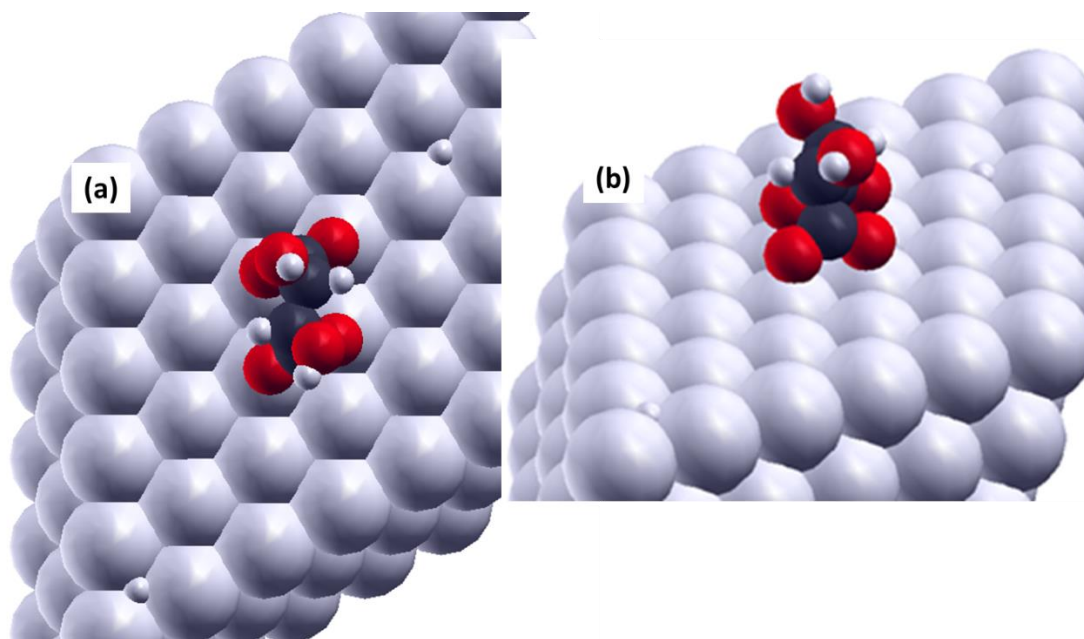
Figure 7-7 Depiction of the most stable structure of D-(-)-bitartrate on Pd(111) obtained using DFT calculations showing (a) the top view and (b) the side view.

The calculation shows atop adsorption of the carboxylate oxygen atoms with the hydroxyl groups oriented along the long axis of the bitartrate species. The size of the calculated structure is in accord with the size of the image observed by STM (Figure 7-1). The molecule is somewhat strained to accommodate the hexagonal (111) surface and the adsorption energy calculated from the difference between the energies of the structure

shown in Figure 7-7 and the sum of the energies of clean Pd(111) and gas-phase tartaric acid, is -44 kJ/mol. Note that, while there may be some errors in the absolute energy of the different structures, relative energies for different tartaric acid derived structures are essentially accurate.

To characterize the different dimeric structures and oligomeric species observed in STM, calculations were carried out for bitartrate dimeric species. Four different adsorption geometries were considered for bitartrate dimer structures and the final converged structures are shown in Figure 7-8 (a) to (d) and the lateral interaction energies between the bitartrate species in the dimeric pair are indicated in the respective structures. In Figure 7-8 (a) two bitartrate species are placed in adjacent rows parallel to each other such that four carboxylate oxygen atoms bind to the Pd atoms of the same row in the horizontal direction. The interaction energy is calculated to be highly endothermic and is 28 kJ/mol. In Figure 7-9 (b) two bitartrate species are placed diagonal to each other such that they share one row of Pd atoms in the vertical direction. The α-hydroxy groups of the bitartrate species are located within hydrogen-bonding interaction distance. The interaction energy is less repulsive than structure (a) but is still endothermic by 7 kJ/mol. In Figure 7-9 (c), two bitartrate species are placed vertically in the same row, and the α-hydroxy groups are positioned such that hydrogen bonding can occur between the –OH groups in a head-to-tail manner. This structure is somewhat iso energetic to structure (b) and yielded a repulsive interaction energy of 6 kJ/mol. Figure 7-9 (d) has a similar adsorption geometry as Figure 7-9 (c) but one of the bitartrate species is moved down by one Pd spacing. This structure is found to be less repulsive than the other three structures and yields a repulsive interaction energy of 3 kJ/mol.
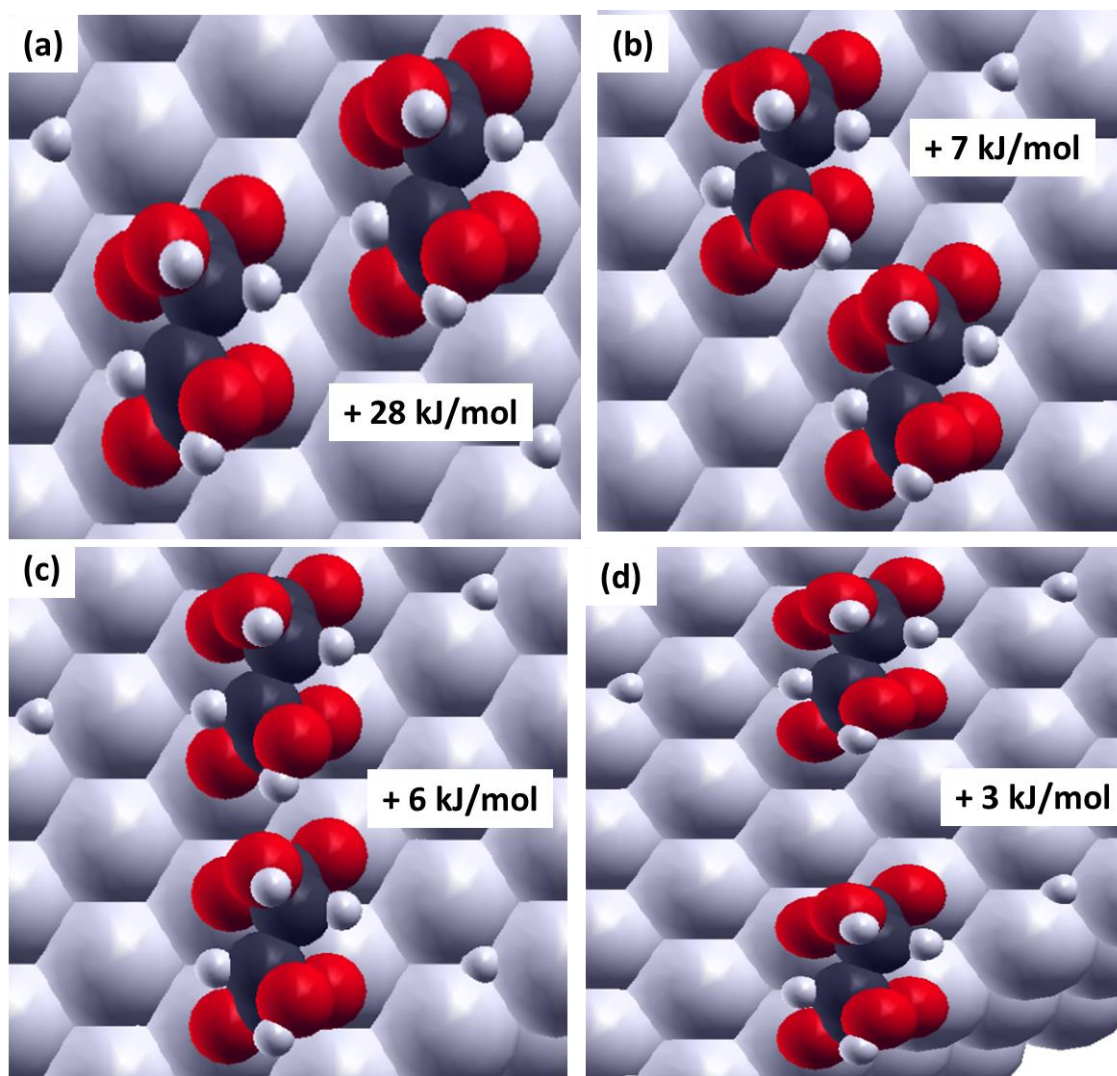
Figure 7-8 Depiction of the four different relaxed structure of D-(-)-bitartrate dimers on Pd(111) obtained using DFT calculations. Lateral interaction energy (dimer formation energy) is reported in kJ/mol.

The dimer structure shown in Figure 7-8 (d) is less endothermic than (c). This is surprising since in (c) the –OH groups are located within hydrogen-bonding interaction distances, while in (d) they are farther away. Thus, it appears that hydrogen-bonding interactions do not occur between neighboring bitartrate species since the dimer formation is endothermic on the surface. This is consistent with the observed STM image (Figure 7-1), where individual bitartrate motifs were found on the surface at 120 K.

Figure 7-9 shows the bitartrate species on Pd(111) (reproducing the image as shown in Figure 7-7), where the surface Pd atoms are numbered for clarity. Upon measuring the top layer Pd-Pd distance which contains a bitartrate species, it was observed that the spacing between the Pd atoms which accommodate the oxygen atoms of a carboxylate group expand by ~0.04 Å (distance between Pd atom 1-2 and 3-4), and the spacing between the Pd atoms which accommodate oxygen atoms of one carboxylate group each expand by 0.09 Å (1-3 and 2-4) with respect to the clean metal Pd-Pd lattice spacing. The measurements are shown in the table adjacent to the Figure 7-9.
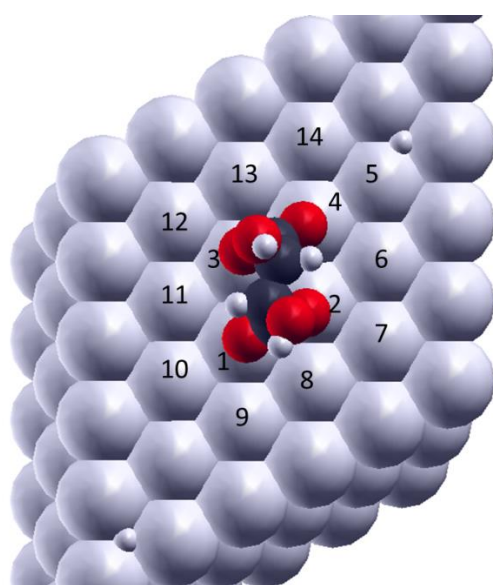
Pd-Pd spacing	Å
1-2	2.83
3-4	2.84
1-3	2.88
2-4	2.88
2-8	2.79
1-9	2.78
4-14	2.8
3-13	2.81
2-7	2.78
4-6	2.84
1-11	2.83

Figure 7-9 DFT structure of Bitartrate species on a Pd(111) surface, Pd surface atoms are numbered and the table on the right shows the measured neighboring Pd-Pd lattice spacing in Å. The Pd-Pd lattice spacing of a clean Pd(111) is calculated to be 2.8 Å.

By measuring the spacing between the neighboring Pd atoms surrounding the bitartrate species, it was observed that the atoms rearrange slightly by moving closer or farther away to distribute an even lattice spacing. When another bitartrate species is adsorbed adjacent to the existing bitartrate species, the surface atoms cannot relax, which

leads to high surface stress energy. Thus, it indicates that bitartrate species disrupt the surface crystal lattice locally, which does not favor the adsorption of another bitartrate species nearby and adsorption-induced surface stress accounts the less favorable formation of the bitartrate dimers on a Pd(111) surface. The surface stress energy was calculated by removing the bitartrate species from the surface and running a single point calculation to obtain the energy change of the palladium substrate, which was found to be 8 kJ/mol. This is in accord with the calculated interaction energies which were found to be less repulsive when two bitartrate species were placed further apart (Figure 7-8 (d)) than when they were placed next to each other. In Figure 7-8 (a), where the bitartrate species were placed horizontally on adjacent rows, the interaction energy was more repulsive compared with the structure, where they were placed vertically (Figure 7-8 (b), (c) and (d), which indicates that the surface stress is greater in the direction parallel to the bitartrate species. A similar surface stress has been reported for bitartrate adsorption on a Cu(110) surface using DFT calculations. [23-24] The ordered (9 0,1 2) bitartrate phase observed on Cu(110) surface [2] was initially reported by Raval *et. al* and was attributed to hydrogen bonding interactions between the bitartrate species. However, recent DFT calculations [23-24] suggests that the observed ordered (9 0,1 2) phase is originated to release adsorption-induced surface stress; having two or more bitartrate species close to each other results in a surface having very high stress energy. This stress is released if two or more copper atoms are left vacant between them, which leads to the formation of ordered (9 0,1 2) domains with vacant channel in between the rows. Bitartrate species also induce stress upon adsorption onto Ni(110) surface and in this case, locally reconstruct the surface.[9]

To understand the ordered structures observed on the surface as shown in Figure 7-6, DFT calculations were performed by adsorbing a bitartrate dimers on a 6×10 Pd(111) slab which is the repeat distance for the observed STM image. The adsorption energy of the individual bitartrate species on 6×10 slab was found to be 45 kJ/mol which is slightly higher than the value obtained on a 6×6 slab (44 kJ/mol).
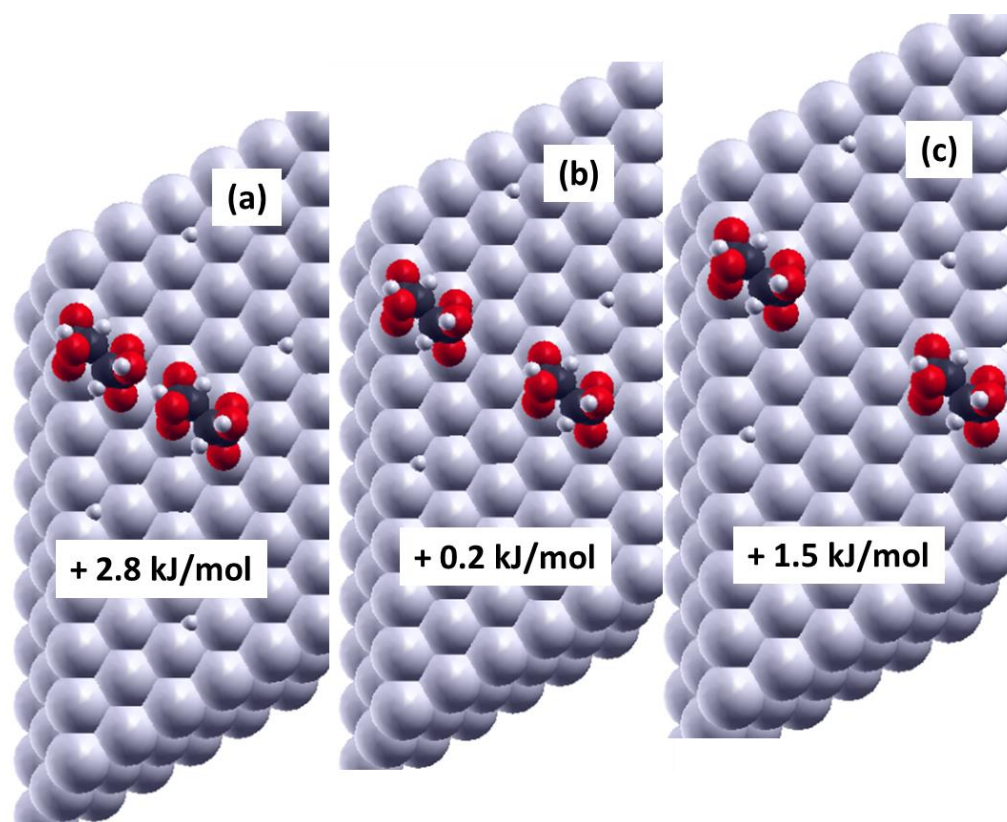
Figure 7-10 Depiction of the most stable structure of D-(-)-bitartrate dimers on a 6×10 Pd(111) slab obtained using DFT calculations. Interaction energies (dimer formation energies) are reported in kJ/mol.

The bitartrate dimer adsorption geometry was maintained as for the most stable structure obtained on a 6×6 slab (Figure 7(d)), where the bitartrate species are located vertically in the same row with one Pd lattice spacing between the two bitartrate species. The resulting converged structure and the interaction energy is shown in Figure 7-10 (b). This dimer structure yields an interaction energy of 0.2 kJ/mol which is slightly more

attractive than the value obtained on a 6×6 slab (3 kJ/mol), suggesting that at low coverages the dimer formation is slightly more favorable and that accounts for a less stressed surface due to low coverage of bitartrate species.

Two other adsorption geometries were chosen for bitartrate dimer structure based on the spacing in between the bitartrate. Moving the two species closer (Figure 7-10(a)) or farther apart (Figure 7-10 (c)) results in a slight increase in energy. Therefore, it is clear that within an ordered domain, the molecules are rearranged to minimize the surface strain energy. Within this domain, the large spacing between the dimers in the horizontal direction (~10 Pd spacing) compare to that in the vertical direction (6 spacing) can be rationalized based on the surface stress energy, which is higher in the horizontal direction than in the vertical direction as found by the DFT calculations (Figure 7-8). None of the bitartrate dimers formed on the surface was found to be attractive and the dimer formation energy within the observed ordered domain was found to be least repulsive (Figure 7-10 (b). Thus, the formation of the ordered structure as shown in Figure 7-6 occurs by minimizing the surface-induced stress provided by closely spaced bitartrate species and the stress is released when multiple Pd atoms between them are left free. The calculated structure, which mimics the observed STM image, is shown in Figure 7-11.
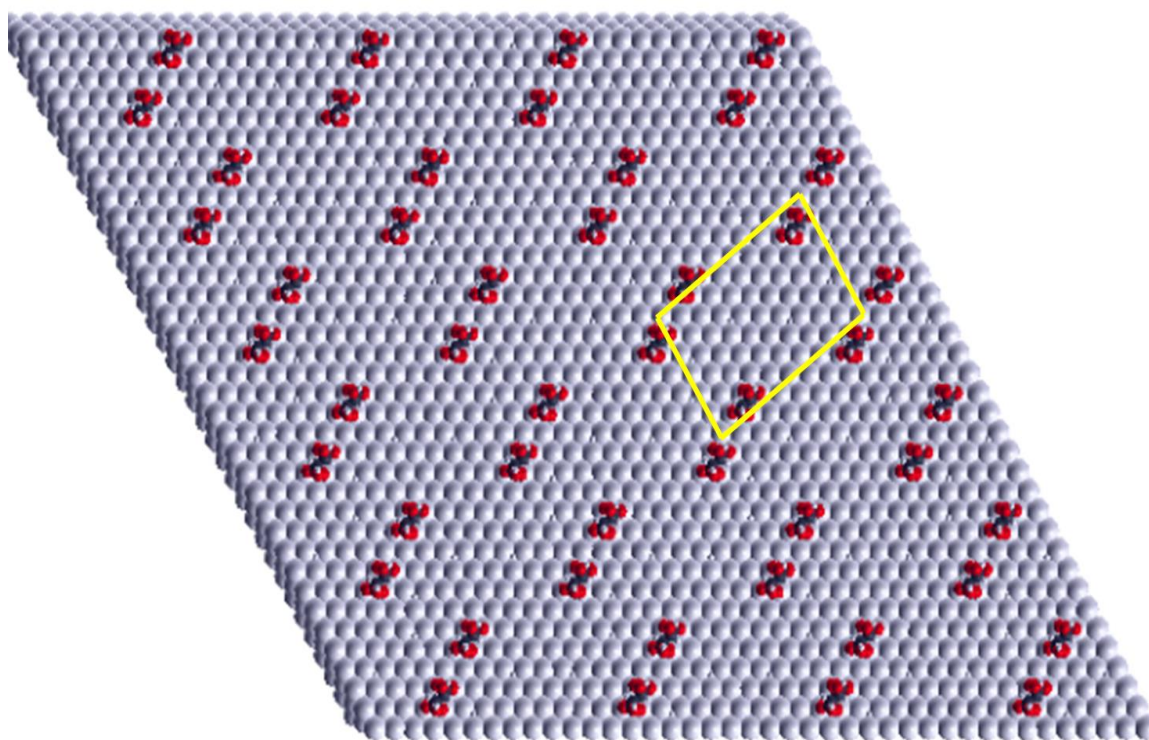
Figure 7-11 A DFT calculated structure for the experimentally observed bitartrate (5√3 1, 0 6) ordered domain. The unit cell for the calculated structure is also shown in the Figure.

7.4.2 DFT Calculations for the Monotartrate Species

Similar DFT calculations were carried out for the monotartrate species (with a co-adsorbed hydrogen atom on a three-fold hollow site) on a 6×6 Pd(111) slab. The most stable structure is shown in Figure 7-12. The monotartrate species adsorbs with the carboxylate oxygen atoms bonded to atop palladium sites, while the carboxylic acid group is upright at an angle of ~90° to the surface plane. The –OH group is oriented downwards which allows an intramolecular hydrogen-bonding interaction to occur with the carboxylate oxygen atom. This structure yields an adsorption energy of -37 kJ/mol.
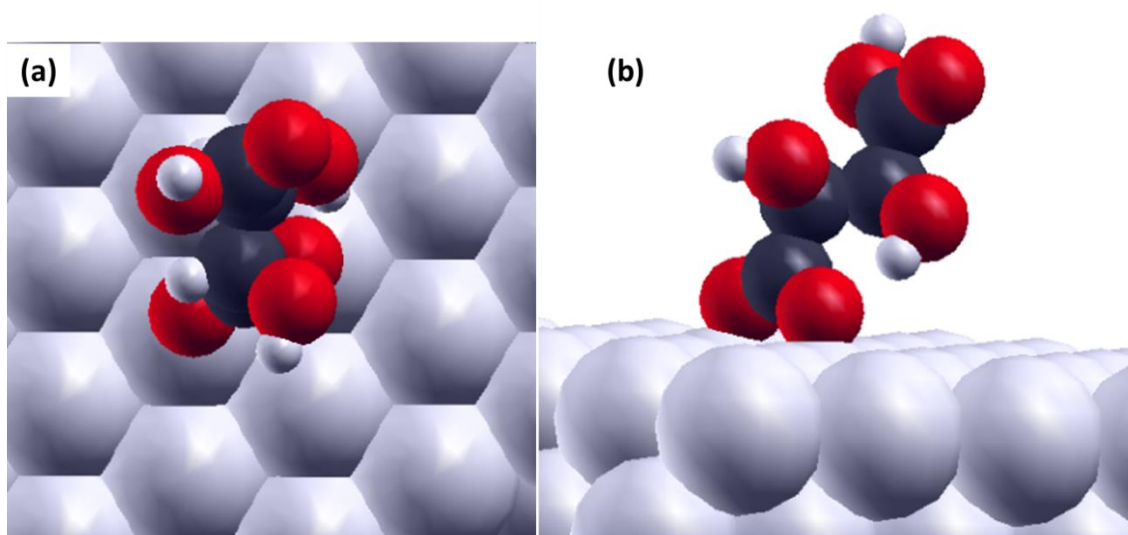
Figure 7-12 Depiction of the most stable structure of D-(-)-monotartrate on Pd(111) obtained using DFT calculations showing (a) the top view and (b) the side view.

DFT calculations were performed for three different monotartrate dimer structures, which either allows hydrogen-bonding interactions between the α-hydroxy groups or between the carboxylic acid groups and α-hydroxy groups. The dimer structures were constructed using an initial geometry of the most stable monomer structures (Figure 7-12).

Figure 7-13 shows a dimer structure in which two monotartrate monomers are placed adjacent to each other vertically in the same row. This allows hydrogen-bonding interaction between the –COOH group of one monotartrate species with the –OH group of the other (shown as a green dotted line). The energy to form a dimeric pair (interaction energy) was found to be highly exothermic by -33 kJ/mol.
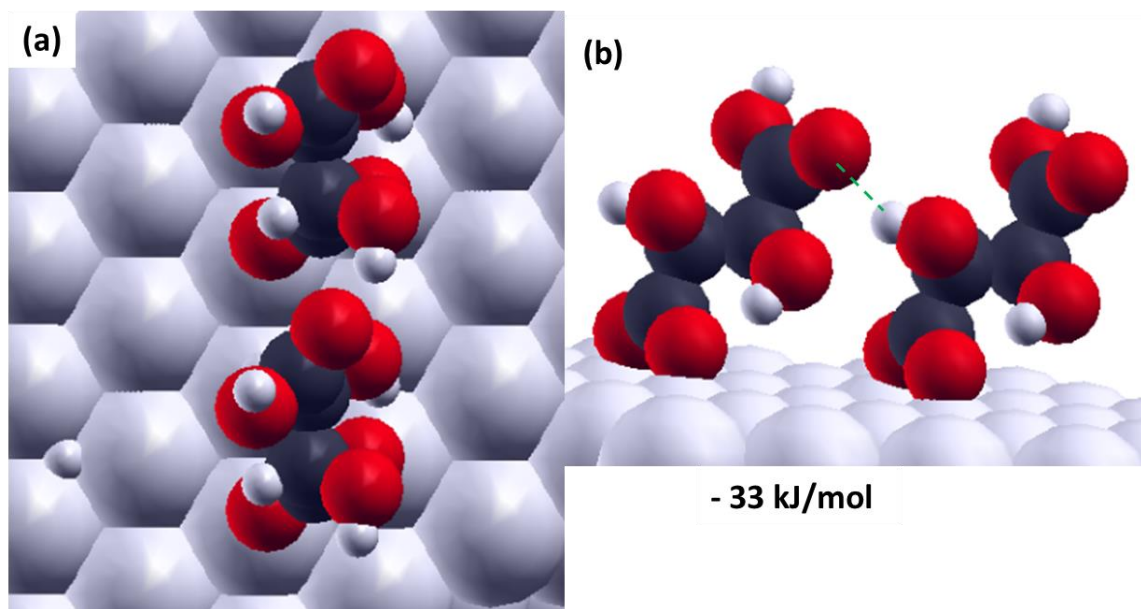
Figure 7-13 Depiction of a relaxed monotartrate dimer structure on Pd(111) obtained using DFT calculations showing (a) the top view and (b) the side view. The hydrogen bonding interaction between the –COOH and –OH groups is shown in green dotted line. The interaction energy (dimer formation energy) is reported in kJ/mol.

Figure 7-14 shows a second dimer structure, in which the molecular backbone axis of one monotartrate is oriented at an angle of 120° to the other. This structure allows a hydrogen-bonding interaction between the α-hydroxy groups. The interaction energy was found to be -57 kJ/mol.

These calculations are in accord with the observed STM images collected at room temperature (Figure 7-3 (d)), which shows linear chain structures (oligomers) running in three different surface crystallographic directions. The hydrogen-bonding interaction between –COOH group and –OH group allows the growth of linear chains along one crystallographic direction since the structure is such that the hydrogen-bonding interaction can be propagated. When a linear chain growing in one crystallographic direction meets another monotartrate species which is oriented at an angle of 120° to it, hydrogen bonding occurs through –OH –OH interaction and the chain stops growing in that direction because all of the functional groups are occupied by hydrogen-bonding

interactions and another chain propagates at an angle of 120° to it. This has been

observed in the STM images at room temperature (Figure 7-3). This structure is in good

agreement with the RAIRS result where a frequency mode of ~1708 cm^{-1} is observed due

to the C=O stretching frequency of the carboxylic acid groups. RAIRS show a frequency

of ~1708 cm^{-1} which is downshifted from the value of ~1750 cm^{-1} found for a

monomeric carboxylic acid group and suggests intermolecular hydrogen bonding

interactions in the islands.

- 57 kJ/mol
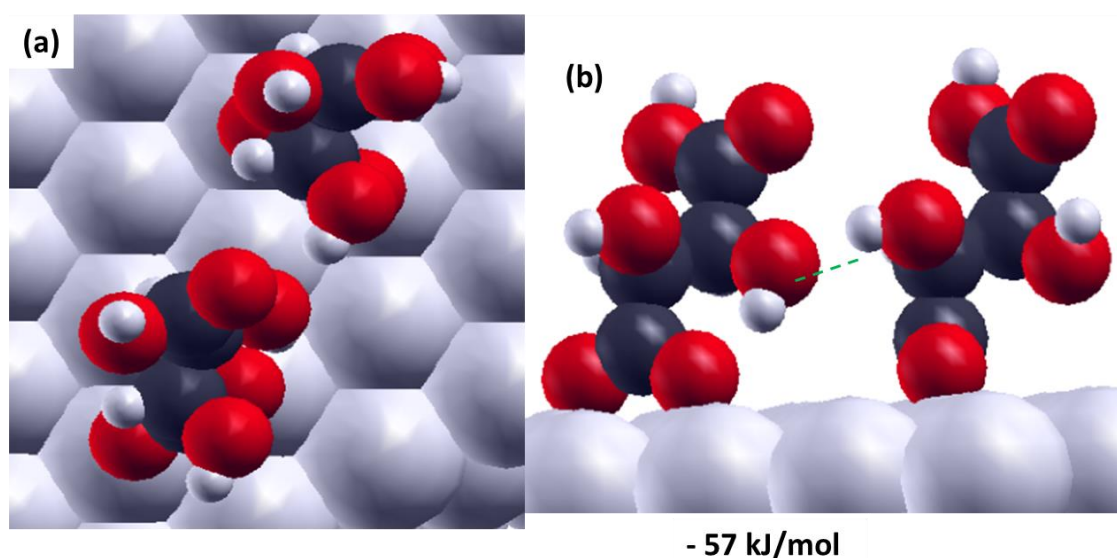
Figure 7-14 Depiction of a relaxed monotartrate dimer structure on Pd(111) obtained using DFT calculations showing (a) the top view and (b) the side view. The hydrogen bonding interaction between the –OH and –OH groups is shown in green dotted line. The interaction energy (dimer formation energy) is reported in kJ/mol.

A third dimer structure was calculated, where two monotartrate structures are

placed in adjacent rows running in the same crystallographic direction. The resulting

converged structure is shown in Figure 7-15. The α-hydroxy group, which is pointed

downwards, facilitates intermolecular hydrogen bonding to the carboxylate oxygen of the

neighboring monotartrate. This structure yields an interaction energy of -12 kJ/mol.
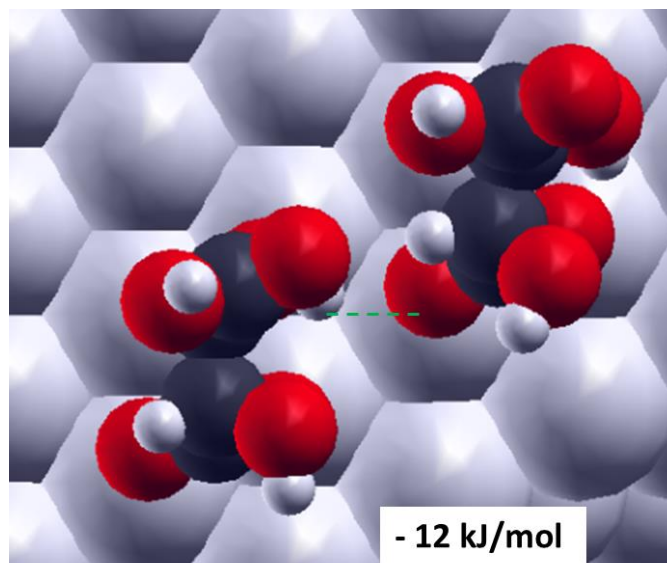
Figure 7-15 Depiction of a relaxed monotartrate dimer structure on Pd(111) obtained using DFT calculations. The hydrogen bonding interaction between –OH and –O is shown in green dotted line. The interaction energy (dimer formation energy) is reported in kJ/mol.

Finally, DFT calculations were carried out for a so-called cyclic dimer structure that involves mutual hydrogen bonding interaction through carboxylic acid groups. Two different types of cyclic dimer structures were considered and are shown in Figure 7-16 and 7-17.

Two monotartrate species are placed in a row such that the molecular axis of one is rotated 180° with respect to the other. This allows hydrogen-bonding interactions between the two carboxylic acid groups. This structure was found to be less attractive than other dimeric structures. This is may be due to the orientation of the monocarboxylate species. The carboxylic acid groups are perpendicular to the surface plane and face each other vertically, which does not allow an optimal hydrogen bonding interactions between the carboxylic acid groups.
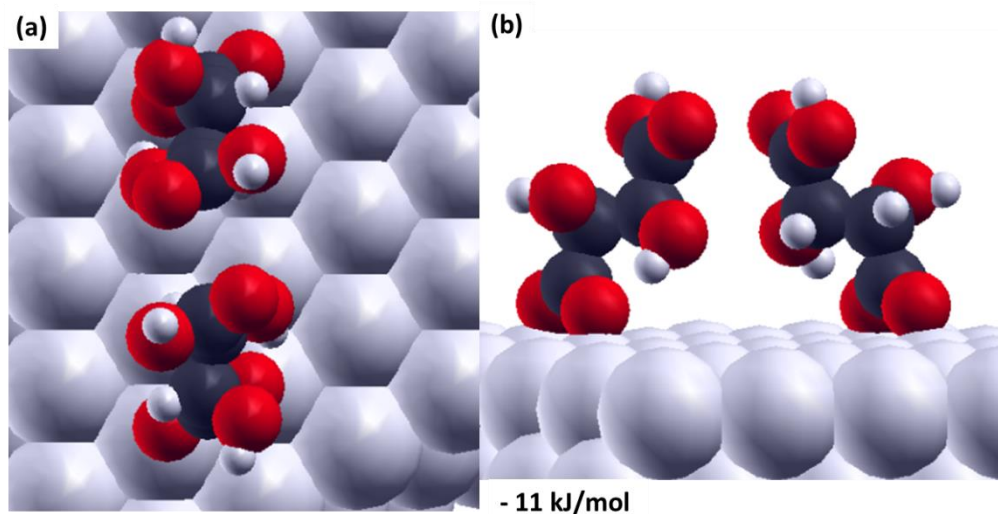
Figure 7-16 Depiction of a cyclic dimer structure which consists of the most stable D-(-)-monotartrate monomers on Pd(111) obtained using DFT calculations showing (a), the top view and (b) the side view. The interaction energy (dimer formation energy is reported in kJ/mol.

A second cyclic dimer structure was considered in which the C-C bond was rotated such that three carbon atoms lie in the same plane and the carboxylic acid groups are close to parallel to the surface plane. The resulting converged structure is shown in Figure 7-17.
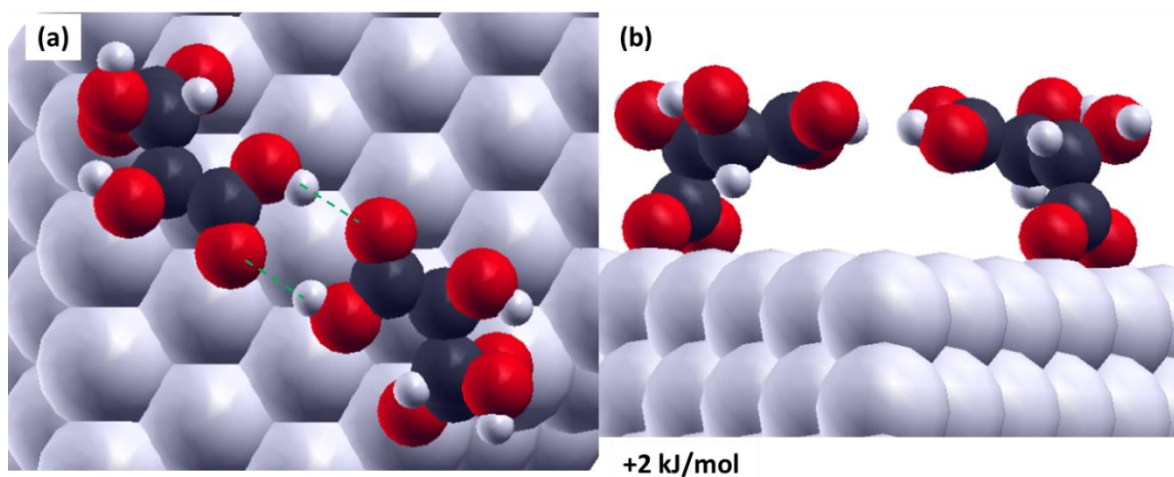
Figure 7-17 Depiction of a second cyclic dimer structure, where the –COOH groups are parallel to the surface. (a) the top view and (b) the side view. The interaction energy (dimer formation energy is reported in kJ/mol).

This structure yields an interaction energy which is slightly repulsive. Therefore it is very unlikely that this type of cyclic dimer structure will form on the surface from the most stable monotartrate monomer structures (Figure 7-12). This is surprising since the cyclic dimer structures from carboxylic acids is a very common phenomenon in both gas and solution phase. It is possible that, to form a cyclic dimer as shown in Figure 7-17, the most stable monomer species has to rotate by ~ 60° which is energetically unfavorable. However, if there are some monotartrate species present on the surface in which the – COOH group is tilted towards the surface, instead of standing upright, that might allow the formation of cyclic dimer as shown in Figure 7-17. These possibilities are currently under investigation. A monotartrate cyclic dimer structure was proposed to form on Cu(110) surface [2] based on their STM results which was confirmed by the presence of a C=O stretching frequency of the carboxylic acid group at ~1650 cm^{-1}, downshifted from a value of 1750 cm^{-1} for a free carboxylic acid group due to very strong hydrogen bonding interactions. In our infrared study, there is no evidence of any IR frequency observed at ~1650 cm^{-1}, and a C=O stretching frequency is observed only at ~1710 cm^{-1}, suggesting hydrogen-bonding interactions through –COOH and –OH groups or between the –OH groups.

The ordered structure observed in the STM (Figure 7-5) has a high local coverage, which eliminates the possibility that this structure comprise bitartrate species. Therefore it is proposed that this ordered phase occurs as a result of mutual hydrogen-bonding interactions between the monotartrate species, where the carboxylate groups bonds to the surface and the other three functional groups participate in hydrogen-bonding interactions. A plausible model for the structure is shown in Figure7-18. The

monotartrate species are slightly tilted, which allows hydrogen-bonding interactions through the three functional groups. The (4 -1, -1 3) unit cell and the direction of hydrogen bonding are indicated in the Figure 7-18. The spacing and orientation of the proposed model match with the experimentally observed STM image (Figure 7-5).
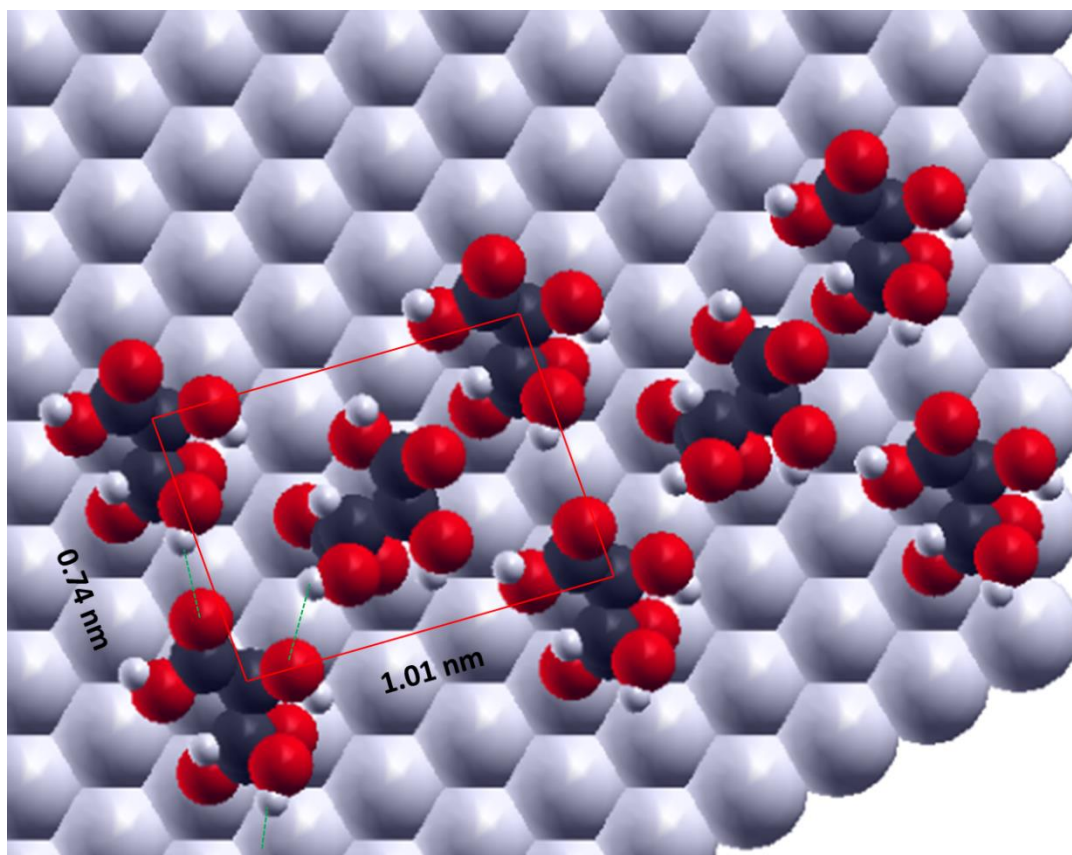
Figure 7-18 A proposed model for the observed monotartrate (4 -1, -1 3) ordered domain in STM, the unit cell is also shown in the Figure.

Overall, the results indicate that the extent of ordering of tartaric acid on Pd(111) is very small compare to Cu and Ni surfaces, which can be ascribed to the high reactivity of Pd surface. At room temperature, monotartrate species undergo extensive hydrogen bonding interaction and form oligomeric species, which is modeled by DFT calculations, showing that the formation of the monotartrate dimeric structures is highly exothermic. Thus the dominant surface structure was found to be the monotartrate oligomeric chains.

Only a fraction of the surface contains ordered domains. At low coverages individual bitartrate chiral motifs were found on the surface

With respect to real catalytic systems, the original enantioselectivity measurements of the R,R-tartaric acid modified Ni catalysts were conducted by dosing tartaric acid onto a supported Ni catalyst from solution phase, which shows a strong dependence on temperature, pH, modifier concentration and modification time. Our model studies of D-(-)-tartaric acid on Pd(111) rationalizes these effects by demonstrating that varying the adsorbate coverage (concentration), temperature, adsorbate flux and the modification time can have a large effect on the nature of the adsorbate species. These different adlayers will provide different docking sites for the incoming chiral probe molecule.

7.5 Conclusions

D-(-)-tartaric acid shows a number of adsorbate structures and dynamics on Pd(111) surface, where the chemical identity and the one-dimensional and two-dimensional ordering of the adsorbed species varies significantly with coverage, sample temperature and reaction time. At low coverages, the surface predominately consists of individual bitartrate species. At intermediate and high coverages, the dominant surface structure was monotartrate oligomeric chains. The formation of ordered structures was observed at intermediate coverages over a very long period of time and only occurs when the surface is dosed at ~300 K, which strongly suggests that the formation of those structures is kinetically limited. The formation of oligomeric chains and a (4 -1, -1 3) ordered phase is ascribed to hydrogen-bonding interactions between the monotartrate species, which is energetically highly favorable as predicted by DFT calculations.

Bitartrate species locally disrupt the Pd lattice structure which leads to surface strain; the bitartrate dimer structures are not energetically favorable. The ordered domain observed by the bitartrate species is proposed to occur by releasing the surface strain energy in a similar manner to what was observed on a Cu(110) surface.

7.6 References

1.   Mahapatra, M.; Tysoe, W. T., Structure and decomposition pathways of D-(−)-tartaric acid on Pd (111). *Surface Science* **2014**.

2.   Lorenzo, M. O.; Haq, S.; Bertrams, T.; Murray, P.; Raval, R.; Baddeley, C. J., Creating chiral surfaces for enantioselective heterogeneous catalysis: R,R-Tartaric acid on Cu(110). *J. Phys. Chem. B* **1999,** *103* (48), 10661-10669.

3.   Lorenzo, M. O.; Baddeley, C. J.; Muryn, C.; Raval, R., Extended surface chirality from supramolecular assemblies of adsorbed chiral molecules. *Nature* **2000,** *404*, 376-378.

4.   Lorenzo, M. O.; Humblot, V.; Murray, P.; Baddeley, C. J.; Haq, S.; Raval, R., Chemical transformations, molecular transport, and kinetic barriers in creating the chiral phase of (R,R)-tartaric acid on Cu(110). *Journal of Catalysis* **2002,** *205* (1), 123-134.

5.   Raval, R., Chiral expressions at metal surfaces. *Current Opinion in Solid State & Materials Science* **2003,** *7* (1), 67-74.

6.   Humblot, V.; Lorenzo, M. O.; Baddeley, C. J.; Haq, S.; Raval, R., Local and global chirality at surfaces: Succinic acid versus tartaric acid on Cu(110). *Journal of the American Chemical Society* **2004,** *126* (20), 6460-6469.

7.   Ernst, K.-H., Supramolecular surface chirality. In *Supramolecular chirality*, Springer: 2006; pp 209-252.

8.   Ernst, K.-H., Molecular chirality in surface science. *Surface science* **2013,** *613*, 1-

9.   Humblot, V.; Haq, S.; Muryn, C.; Hofer, W. A.; Raval, R., From local adsorption stresses to chiral surfaces: (R,R)-tartaric acid on Ni(110). *Journal of the American Chemical Society* **2002,** *124* (3), 503-510.

10.   Barlow, S. M.; Raval, R., Complex organic molecules at metal surfaces: bonding, organisation and chirality. *Surface Science Reports* **2003,** *50* (6), 201-341.

11.   Humblot, V.; Haq, S.; Muryn, C.; Raval, R., (R,R)-tartaric acid on Ni(110): the dynamic nature of chiral adsorption motifs. *Journal of Catalysis* **2004,** *228* (1), 130-140.

12.   Raval, R., Chiral expression from molecular assemblies at metal surfaces: insights from surface science techniques. *Chemical Society Reviews* **2009,** *38* (3), 707-721.

13.   Jones, T. E.; Baddeley, C. J., A RAIRS, STM and TPD study of the Ni{111}/R,R-tartaric acid system: Modelling the chiral modification of Ni nanoparticles. *Surface Science* **2002,** *513* (3), 453-467.

14.   Jones, T. E.; Baddeley, C. J., An investigation of the adsorption of (R,R)-tartaric acid on oxidised Ni{111) surfaces. *Journal of Molecular Catalysis A-Chemical* **2004,** *216* (2), 223-231.

15.   Lawton, T. J.; Pushkarev, V.; Wei, D.; Lucci, F. R.; Sholl, D. S.; Gellman, A. J.; Sykes, E. C. H., Long Range Chiral Imprinting of Cu (110) by Tartaric Acid. *The Journal of Physical Chemistry C* **2013,** *117* (43), 22290-22297.

16.   Kresse, G.; Joubert, D., From ultrasoft pseudopotentials to the projector augmented-wave method. *Physical Review B* **1999,** *59* (3), 1758-1775.

17.   Blöchl, P. E., Projector augmented-wave method. *Physical Review B* **1994,** *50* (24), 17953-17979.

18.   Kresse, G.; Furthmüller, J., Efficient iterative schemes for ab initio total-energy calculations using a plane-wave basis set. *Physical Review B* **1996,** *54* (16), 11169-11186.

19.   Kresse, G.; Furthmüller, J., Efficiency of ab-initio total energy calculations for metals and semiconductors using a plane-wave basis set. *Computational Materials Science* **1996,** *6* (1), 15-50.

20.   Perdew, J. P.; Burke, K.; Ernzerhof, M., Generalized Gradient Approximation Made Simple. *Physical Review Letters* **1996,** *77* (18), 3865-3868.

21.   Ireta, J.; Neugebauer, J.; Scheffler, M., On the Accuracy of DFT for Describing Hydrogen Bonds: Dependence on the Bond Directionality. *The Journal of Physical Chemistry A* **2004,** *108* (26), 5692-5698.

22.   Park, E. H.; Min, Y. H.; Kim, S., Self-Assembled and Field-Induced 2D Structures of Glutaric Acid on Cu (110). *The Journal of Physical Chemistry C* **2014,** *118* (13), 6719-6725.

23. Barbosa, L. A. M.; Sautet, P., Stability of chiral domains produced by adsorption of tartaric acid isomers on the Cu (110) surface: A periodic density functional theory study. *Journal of the American Chemical Society* **2001,** *123* (27), 6639-6648.

24. Hermse, C. G.; van Bavel, A. P.; Jansen, A. P.; Barbosa, L. A. M.; Sautet, P.; van Santen, R. A., Formation of chiral domains for tartaric acid on Cu (110): A combined DFT and kinetic Monte Carlo study. *The Journal of Physical Chemistry B* **2004,** *108* (30), 11035-11043.

Chapter 8

Chemisorptive Enantioselectivity of Chiral Epoxides on Tartaric acid Modified Pd(111); Three-Point Bonding

8.1   Introduction

Hydrogenation of β-keto esters on tartaric acid modified Ni catalyst is one of the most successful examples in the field of enantioselective heterogeneous catalysis.[1-3] This is been achieved by carrying out the reaction under ambient conditions on a tartaric acid modified Ni catalyst, where R,R-tartaric acid was dosed from the solution phase. The enantioselectivity measurement showed a strong dependence on temperature, pH, modifier concentration and modification time. One of the fundamental questions in this field remains unanswered: how do the modifiers provide chirality to the achiral metal surface and what is the nature of the active sites present on the modified surface. Due to the complexity associated with the real catalytic system in ambient pressure it is not well understood. However to address this problem, a vast number of research has been carried out over the years by adsorbing tartaric acid (from the gas phase) on model single crystal surfaces under UHV conditions and identifying the nature of the adsorbed species as a function of adsorbate coverage, dosing flux, dosing temperature of the crystal to mimic the experimental conditions of the real catalytic system.

Accordingly, the surface chemistry of tartaric acid has been explored on Pd(111) single crystal surface [4] by using TPD, RAIRS and STM which is described in Chapters 6 and 7 of this thesis. It has been observed that varying the adsorbate coverage

(concentration), temperature of the crystal, adsorbate flux and the modification time have a large effect on the nature of the adsorbate species and the formation of two dimensional ordered structure. On Pd(111), at low coverages, bitartrate phase dominates, while at higher coverages the surface mostly consists of monotartrate species. STM images (Chapter 7) show the presence of different surface structures at different coverages. Low coverage STM images showed the presence of individual bitartrate species, while higher coverages showed the presence of oligomeric species due to hydrogen bonding interactions between the monotartrate species. At intermediate coverages, two different kinds of two dimensional ordered structures are observed which breaks the underlying symmetry of the metal surface. These different adlayers will provide different docking sites for the incoming chiral probe molecule.

This chapter presents the study to test if the tartaric acid modified Pd(111) surface shows chiral behavior towards the adsorption of another incoming chiral molecule. This has been achieved by measuring the enantioselectivity of the tartaric acid modified Pd(111) surface by using two different chiral probes: propylene oxide and glycidol. The enantioselectivity is measured by chiral titration TPDS as described previously, where the modified surface is dosed with both the chirality of the probe molecule (in two different experiments) and TPD has been performed by monitoring the desorption yield of the probe. For the same coverage of the modifier if there is any difference in the desorption yield of the two enantiomers of the probe, is attributed to the presence of the chiral modifier. Enantioselectivity is measured from enantioselectivity ration (R_e), which is the ratio of the different enantiomer probe coverage for the same coverage of the modifier. The enantioselectivity of the tartaric acid modified surface is measured at various

coverages to identify the chiral site by correlating the measured enantioselectivity ratio with the observed surface structure in STM and spectroscopic studies. The TPD results are supplemented by DFT calculations to understand the chiral interactions.

The chiral probe molecules, propylene oxide and glycidol adopt identical adsorption sites on a Pd(111) surface by bonding through the epoxide oxygen to a palladium atop site. However, the $-CH_3$ group in the propylene oxide is replaced by a $-CH_2OH$ group in glycidol, which has both hydrogen bonding donor and acceptor site. It has been shown before that propylene oxide shows enantioselective chemisorption on 2-butanol modified Pd surface due to the hydrogen bonding interaction between the probe and the modifier.[19] However, propylene oxide only allows hydrogen bonding interaction with the epoxide oxygen, therefore glycidol where the methyl group is replaced by a CH_2-OH group can be a more versatile chiral probe since it is capable of an additional hydrogen-bonding interaction through the hydroxyl group.

Chapter 5 shows that both propylene oxide and glycidol shows identical enantioselectivity measurement for a Pd surface modified with alanine. Alanine self-assemble on a Pd(111) surface to form tetramers, which act as chiral templates. Both propylene oxide and glycidol of suitable enantiomer can adsorb inside the chiral pocket which exposes a palladium atop site and the structure is stabilized by the hydrogen bonding interaction between the epoxide oxygen and the ammonium ion of the adjacent alanine. The presence of the methyl group is far from the surface and does not interact with the other molecules, therefore replacing it with a $-CH_2OH$ group in the case of glycidol does not affect the measured enantioselectivity.

However, this is particularly important when using tartaric acid as a chiral

modifier; since its hydroxyl groups, which provide potential hydrogen-bonding loci, are located far from the surface in all of its adsorbed form. Both propylene oxide and glycidol adsorb reversibly and undergoes negligible thermal decomposition on Pd(111) [5] surface thereby allowing the accurate coverage measurement by TPD by monitoring the molecular desorption yield.

8.2   Experimental Section

Experiments were carried out in the TPD chamber as described in Chapter 2. The Pd(111) substrate was cleaned using a standard procedure consisting of cycles of argon ion sputtering and annealing in 3×10^{-8} Torr of oxygen at 1000 K, where the sample cleanliness was judged either using Auger spectroscopy or temperature-programmed desorption (TPD) after dosing with oxygen, where the absence of CO desorption indicated that the sample was carbon free.

R- and S-propylene oxide (Aldrich, 99%) and R- and S-glycidol (Aldrich, 96%) were dosed onto the sample *via* a variable leak valve through a dosing tube directed towards the sample. Since this leads to an enhancement in the local pressure at the sample, which has not been calibrated, both propylene oxide and glycidol exposures are quoted in units of Torr.minutes, where the pressure is that measured by a nude ionization gauge in the chamber. (S,S)-tartaric acid (Aldrich, 99%) was dosed onto the sample by using a home built Knudsen source. The tartaric acid source was repeatedly outgassed at ~380 K to remove contaminants, primarily water. It was finally outgassed overnight at this temperature prior to dosing into the sample. The temperature of the source was adjusted to get the desirable dosing rate and once the desired dosing rate is achieved, the Knudsen source temperature was maintained at that value for consistent results. The

source temperature was maintained between 105° C and 110° C throughout all the experiments.

8.3 Theoretical Methods

Density functional theory (DFT) calculations were performed with the projector augmented wave (PAW) method [6-7] using the Vienna ab initio simulation package, VASP.[8-10] The exchange correlation potential was described using the generalized gradient approximation (GGA) of Perdew, Burke and Ernzehof.[11] [11] A cutoff of 400 eV was used for the planewave basis set, and the wave functions and electron density were converged to within 1×10^{-5} eV. The first Brillouin zone was sampled with a $4\times4\times1$ Γ-centered k-point mesh. Hydrogen bonding interactions are reasonably well reproduced (within ~ 4 kJ/mol) using this functional, although the accuracy deteriorates as the hydrogen bonds deviate from linear.[12] Geometric relaxations were considered to be converged when the force was less than 0.02 eV/Å on all unrestricted atoms.

8.4 Experimental Results

TPD experiments are performed to measure the enantioselectivity of tartaric acid modified-Pd(111) by using propylene oxide as a chiral probe. The Pd(111) surface is dosed with certain coverage of (S,S)-tartaric acid at ~300 K, following which the sample is cooled to ~150 K to dose a monolayer of one enantiomer of propylene oxide. Propylene oxide is dosed at ~150 K to avoid the condensation of the multilayer. TPD experiments are performed afterwards by monitoring 44 (tartaric acid) and 58 (propylene oxide) amu. The surface is then cleaned and another experiment was repeated for the same coverage of tartaric acid, but using the opposite enantiomer of propylene oxide.

Similar experiments are carried out for various doses of tartaric acid. For the same coverage of the modifier (in this case, (S,S)-tartaric acid) the ratio between the coverage of the two enantiomers of the probe (in this case propylene oxide) is denoted as the enantioselectivity ratio, R_e.
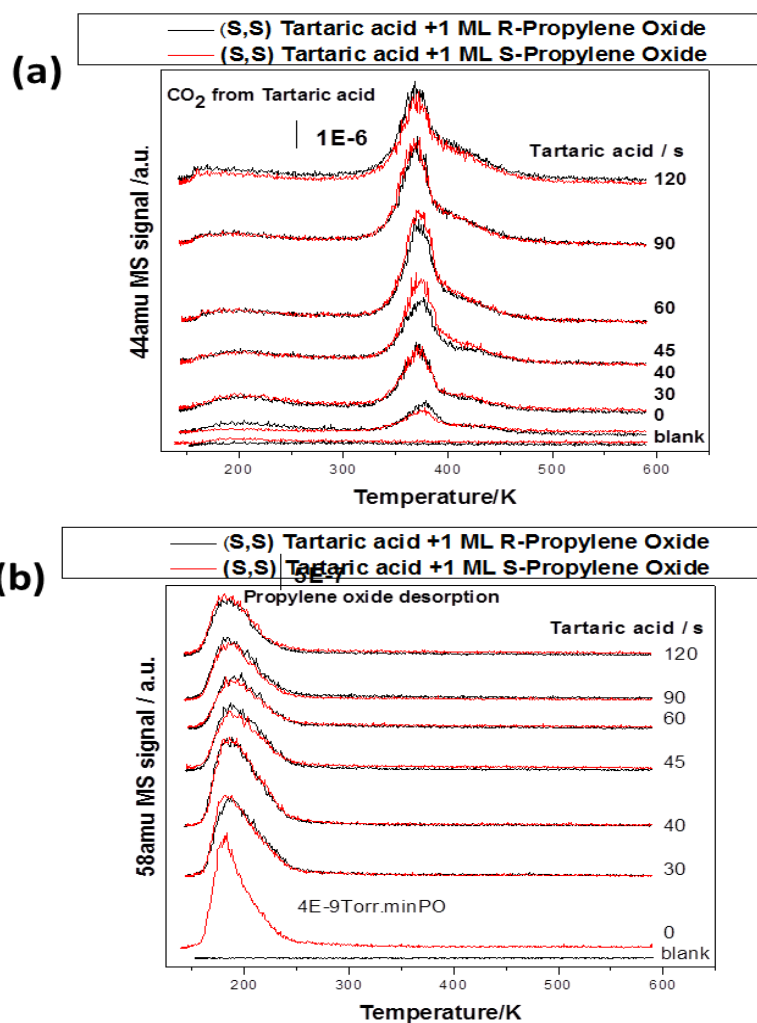
Figure 8-1 Temperature programmed desorption spectroscopy following the adsorption of (S,S)-tartaric acid and a monolayer of R- or S- propylene oxide on Pd(111), as a function of (S,S)-tartaric acid exposure in seconds. The spectra which correspond to R- or S- propylene oxide are color coded by black and red respectively. The results were collected by using a heating rate of ~3 K/s and by monitoring (a) 44 amu and (b) 58 amu

Figure 8-1(a) shows the TPD results plotted as a function of tartaric acid dosing time in seconds, where the black and red curves correspond to experiments with R- and S-propylene oxide, respectively. The curves for tartaric acid are essentially identical indicating that the modifier coverages during the enantioselectivity measurements were identical. Fig. 8-1(b) plots the corresponding desorption profiles for PO (58 amu).The bottom profile in Fig 8-1(b) is for the two enantiomers of PO adsorbed on clean Pd(111) and are identical, confirming the reproducibility of the experiment. However, as the tartaric acid coverage increases, while there is a decrease in the PO coverage due to site blocking, again the desorption profiles for R- and S-PO are identical; no enantioselectivity was observed when using PO as a chiral probe.

Similar experiments are carried out when using glycidol as a chiral probe. The surface chemistry of glycidol on Pd(111) indicates that glycidol desorbs molecularly at ~200 K and undergoes some decomposition reaction at higher temperature. However, only a maximum of ~8% of the glycidol decomposes during the desorption sweep on Pd(111).[5] While the extent of S-glycidol decomposition is higher than propylene oxide, it is sufficiently low to enable TPD experiments to be used to measure its coverage on chirally modified surfaces.

Figure 8-2 shows the enantioselective chemisorption of glycidol on (S,S)-tartaric-acid modified Pd(111). For these experiments, glycidol is dosed at ~200 K to avoid populating the multilayer.
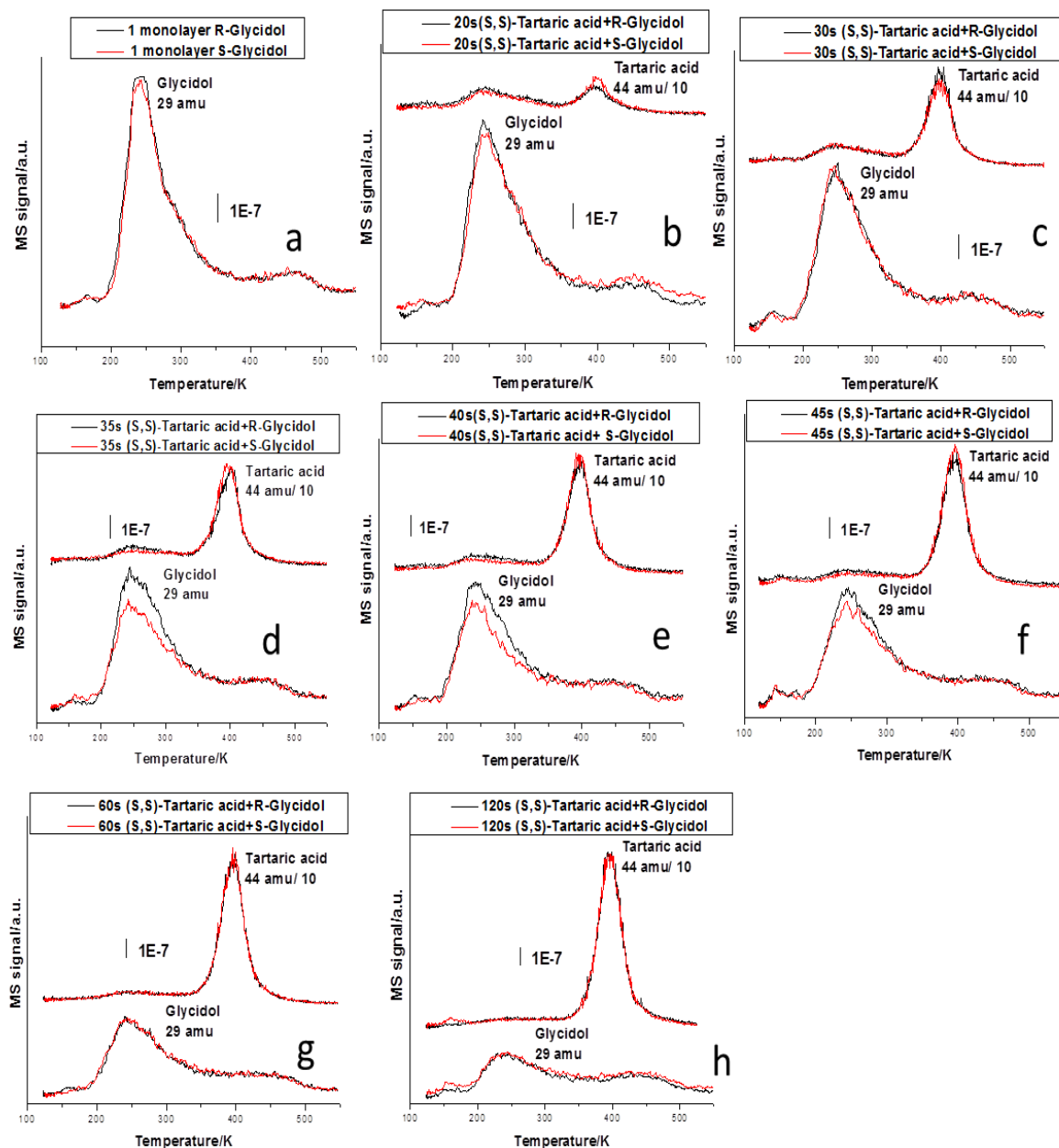
Figure 8-2 Temperature programmed desorption spectroscopy following the adsorption of (S,S)-tartaric acid and a monolayer of R- or S- glycidol on Pd(111), as a function of (S,S)-tartaric acid exposure in seconds. The spectra which correspond to R- or S- glycidol are color coded by black and red respectively. The results were collected by using a heating rate of ~3 K/s and by monitoring 44 amu and 58 amu. Figure 8-2 (a) shows the desorption profile of R and S glycidol from clean Pd(111), in Figure (b) to (h), the tartaric acid dosing time was increases from 20 s to 120 s.

Figure 8-2 a shows the desorption profiles of both enantiomers of glycidol on clean Pd(111), which are identical, again demonstrating the reproducibility of the experiment. Figure 8-2 b to h compare the desorption profiles for both glycidol enantiomers from tartaric-acid-modified Pd(111). The bottom spectra, color coded in black and red, are the desorption profiles for R- and S-glycidol, respectively, while the top two spectra are due to tartaric acid. This indicates that identical coverages of tartaric acid were used for each experiment and the feature increases with tartaric acid dose. For tartaric acid doses between 35 and 45 s (Figures 8-2 d to f), there is a clearly discernible preferential adsorption of R-glycidol on a (S,S)-tartaric-acid modified surface. For higher doses (Figure 8-2 g and h), the spectra for the two enantiomers of glycidol overlap, indicating no enantioselectivity.
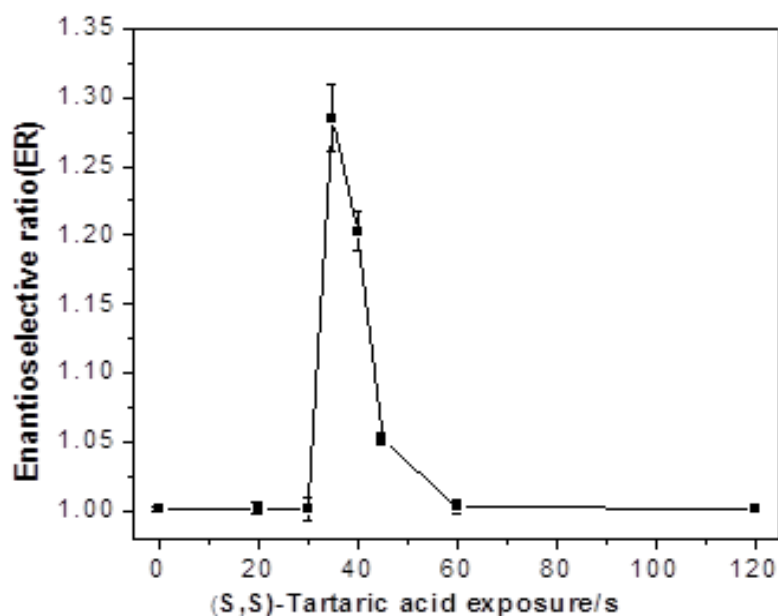
Figure 8-3 Plot of the enantioselectivity ratio R_e for glycidol as a function of tartaric acid coverage. R_e is 1 up to tartaric acid exposure of 25 s and reaches to a maximum value of ~1.29 at an exposure of ~40 s and again decreases to unity for higher doses.

The resulting value of the enantioselective ratio (R_e, defined as $R_e =$

$\Theta^R_{(S,S)}/\Theta^S_{(S,S)} = \Theta^S_{(R,R)}/\Theta^R_{(R,R)}$) where Θ is the probe coverage and the superscripts (*S* or

R) are the chiralities of the probe and the subscripts ((*S,S)* or (*R,R)*) are those of the

modifier) of glycidol on tartaric acid-modified Pd(111) surfaces is shown in Figure 8-3,

showing a maximum value of ~1.3 at a (S,S)-tartaric acid dose of ~40 s.

8.5 Discussion

No enantioselectivity was observed for propylene oxide on tartaric-acid modified

surfaces, whereas glycidol shows modest enantioselectivity over a narrow range of the

tartaric acid coverages (Figure 8-3). Based on previous studies, the surface contains

predominantly bitartrate species [4] in the coverage range over which enantioselectivity is

detected. The STM images collected when a smaller coverage of tartaric acid was dosed

at ~300 K and then cooled to ~120 K, individual bitartrate species were observed on the

surface (Chapter 7).

The observation that PO does not adsorb enantioselectively, while glycidol does

indicates that hydrogen-bonding interaction occur between the OH groups of glycidol and

bitartrate species.

First-principles DFT calculations were carried out to explore possible

enantioselective interactions between R-glycidol and (S,S)-bitartrate species. The most

stable calculated structure of bitartrate species on Pd(111) is depicted in Chapter-7,

showing atop adsorption of the carboxylate oxygen atoms with the hydroxyl groups

oriented along the long axis of the bitartrate species which yield an adsorption energy of

~-43 kJ/mol.[13-14]

Similar calculations were carried out for glycidol on Pd(111) and is shown in

Chapter 4. The epoxide oxygen adsorbs on a palladium atop site, as found for PO.[15]

However, in contrast to PO, the CH$_2$–OH group has an additional agostic interaction with

the surface resulting in an overall binding energy of ~22 kJ/mol.

In order to explore the interactions between R-glycidol and (S,S)-bitartrate

species on Pd(111), a glycidol molecule was placed at various locations around the

bitartrate species and the geometry was allowed to relax. The most stable structure

comprising (S,S)-bitartrate species interacting with R-glycidol is depicted in Figure 8-4.
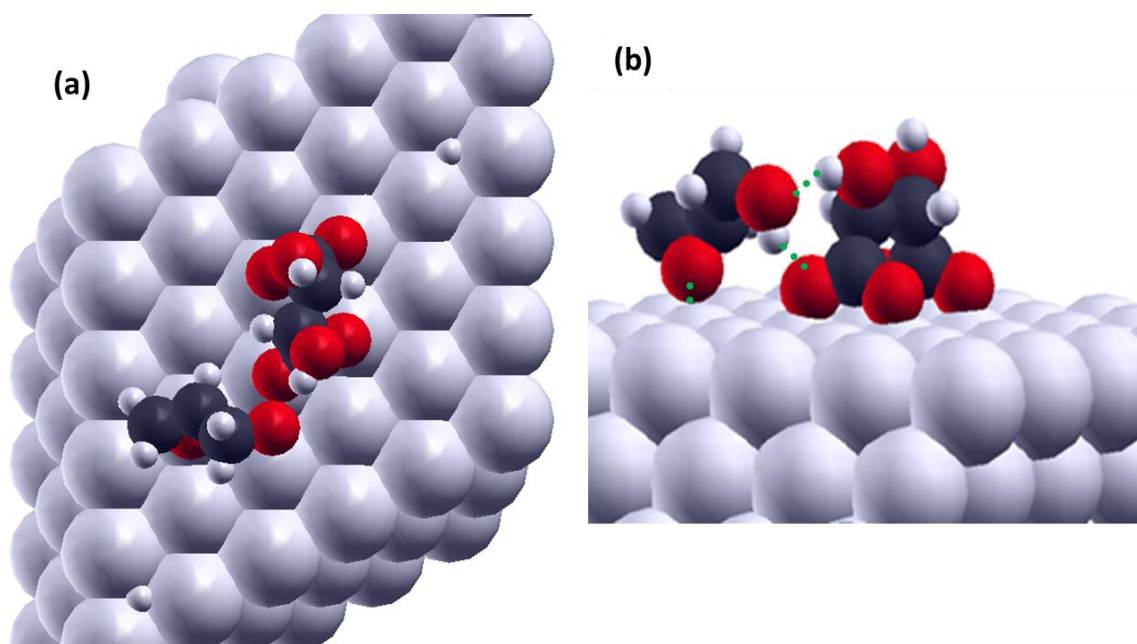
Figure 8-4 Depiction of the most stable structure of (S,S)-bitartrate+R-glycidol on
Pd(111) showing (a), a top view and (b), a side view, where the interactions are indicated
by dotted lines.

Here the epoxide oxygen is located at the most stable atop site, which dictates the

stereochemistry of the interactions between the CH$_2$–OH group and the bitartrate. This

comprises a simultaneous hydrogen-bonding donor interaction between the CH$_2$–OH

group and an oxygen atom of the carboxylate, and a hydrogen-bonding acceptor

interaction between the hydroxyl group of the bitartrate and the oxygen of the CH$_2$–OH

group. This involves a tilt of the R-glycidol molecule away from the surface to allow the hydroxyl group to interact with the carboxylate oxygen of the (S,S)-bitartrate species. This geometry is in accord with the three-point bonding rule, [16-17] where the bonds are indicated in dotted line in Figure 8-4. The distances between the hydrogens and oxygens are relatively close (~2 Å), thereby facilitating such interactions. The energy gain due to this interaction, calculated from the difference in energy of the (S,S)-bitartrate and R-glycidol structures, and the sum of the energies of isolated (S,S)-bitartrate species and R-glycidol, is ~-19 kJ/mol.

The corresponding structure from an interactions between (S,S)-bitartrate and S-glycidol is shown in Figure 8-5.
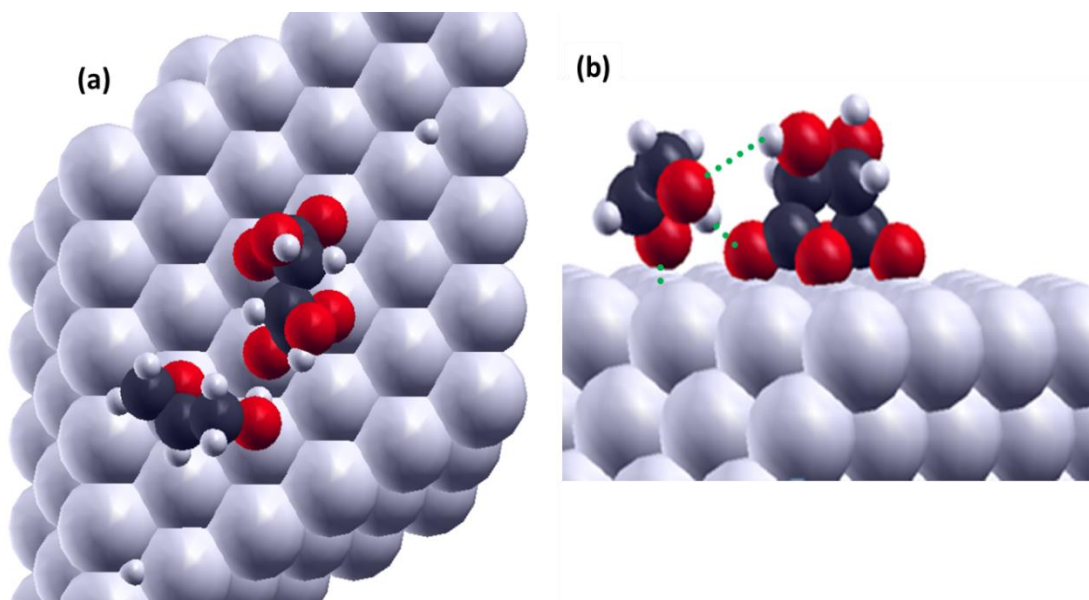
Figure 8-5 Depiction of the most stable structure of (S,S)-bitartrate+S-glycidol on Pd(111) showing (a), a top view and (b), a side view, where the interactions are indicated by dotted lines.

Glycidol still adsorbs on the atop palladium site, which then controls the stereochemistry of the subsequent intermolecular hydrogen-bonding interactions since the

glycidol binding energy of ~-22 kJ/mol is larger than the energies of typical hydrogen-bonding interactions.[18] S-glycidol still has a hydrogen-bonding donor interaction between the CH$_2$–OH group and the (S,S)-bitartrate carboxylate oxygen. However, the structural constraints now imposed by the S-enantiomer of the bitartrate means that the distance between its hydrogen and the CH$_2$–OH oxygen is 2.93 Å, which is much larger than in the most stable structure (Figure 8-4) where the corresponding distance is 1.87 Å, thereby reducing the interaction energy to ~-13 kJ/mol. Interestingly, the stabilization of the R-glycidol by interaction with the (S,S)-bitartrate species is not reflected in the desorption temperature of glycidol from the surface (Figure 8-2); the glycidol desorption temperature over the bitartrate coverage range where enantioselectivity is measured (Figures.8-2 d to f) is identical to that on the clean surface (Figure 8-2 a). This suggests that the relatively weak bonding in the glycidol-bitartrate complexes allows it to dissociate below the desorption temperature, during heating.

No enantioselectivity was observed for higher coverages of tartaric acid. Previous TPD and RAIRS studies (Chapter-6) show that at high coverages, tartaric acid predominately exist in the monotartrate form, where it bonds to the surface by two oxygen atoms of the carboxylate group. Therefore in principle, an isolated monotartrate species has the same functional groups available as the bitartrate species to hydrogen bond to glycidol. However, STM images show that the monotartrate species hydrogen bond with each other through COOH·····OH or OH·····OH interactions and form oligomers on the surface. Thus all the functional groups of the monotartrate species are used up in hydrogen bonding to each other and do not provide enantioselectivity towards the chemisorption of glycidol. The enantioselectivity measurement is highly dependent

on tartaric acid coverage. Therefore it is possible that the reaction environment such as temperature and the nature of the solvent will have a strong influence on the surface structure not captured by the experiments carried out in UHV.

8.6 Conclusions

Glycidol adsorbs enantioselectively on tartaric-acid modified Pd(111) while propylene oxide does not. The tartaric acid coverage at which enantioselectivity is measured indicates that the bitartrate species provides the chiral modifier; while other tartaric-acid derived structures are not enantioselective. Under the conditions where enantioselectivity is measured (dosing at ~300 K and cooling to ~120 K), isolated bitartrate species form on the surface and no ordered structures are found. At higher tartaric acid coverages, the surface is predominately covered with monotartrate species which oligomerize on the surface due to strong hydrogen bonding interactions with the neighboring monotartrate species such that all the functional groups are used up; thus does not provide hydrogen bonding to the chiral probe glycidol. These results clearly indicate that the local interaction between CH_2–OH group in the heterochiral complex formed between R-glycidol and (S,S)-bitartrate is responsible for the enantioselectivity and is modeled using DFT calculations. In both glycidol enantiomers, the binding is dominated by the relatively strong adsorption of the epoxide oxygen to the palladium atop site, and the structure is controlled by hydrogen-bond donation from the CH_2–OH hydrogen in R-glycidol to an oxygen atom of the carboxylate group and by donation from the (S,S)-bitartrate hydroxyl to the oxygen of the R-glycidol CH_2–OH group. In the heterochiral complex, formed between R-glycidol and (S,S)-bitartare, this structure stabilizes hydrogen bonding between a bitartrate –OH and the CH_2–OH oxygen, which

become disfavored in the homochiral complex between S-glycidol and (S,S)-bitartrate.

Thus, the three-point bonding is dominated by the strongest binding of the chiral probe (or a prochiral reactant) to the surface and the ability of a group (or groups) in the probe or reactant to be correctly positioned to simultaneously undergo two distinct bonding interactions with the chiral center. In the case of glycidol, these are hydrogen-bonding interactions. These energies (of a few kJ/mol) are sufficiently large to provide significant stabilization while not being so strong as to inhibit catalytic reactions.

8.7 References

1. Izumi, Y., Modified Raney-Nickel (Mrni) Catalyst - Heterogeneous Enantio-Differentiating (Asymmetric) Catalyst. *Advances in Catalysis* **1983,** *32*, 215-271.

2. Keane, M. A.; Webb, G., The Enantioselective Hydrogenation of Methyl Acetoacetate over Supported Nickel-Catalysts .1. the Modification Procedure. *Journal of Catalysis* **1992,** *136* (1), 1-15.

3. Baddeley, C. J., Fundamental investigations of enantioselective heterogeneous catalysis. *Topics in Catalysis* **2003,** *25* (1-4), 17-28.

4. Mahapatra, M.; Tysoe, W. T., Structure and decomposition pathways of D-(−)-tartaric acid on Pd(111). *Surface Science* **2014,** *629* (0), 132-138.

5. Mahapatra, M.; Tysoe, W., Adsorption and Reaction Pathways of a Chiral Probe Molecule, S-glycidol on a Pd(111) Surface. *Catal. Sci. Technol* **2014,** *Submitted*.

6. Blöchl, P. E., Projector augmented-wave method. *Physical Review B* **1994,** *50* (24), 17953-17979.

7. Kresse, G.; Joubert, D., From ultrasoft pseudopotentials to the projector augmented-wave method. *Physical Review B* **1999,** *59* (3), 1758-1775.

8. Kresse, G.; Hafner, J., Ab initio molecular dynamics for liquid metals. *Physical Review B* **1993,** *47* (1), 558-561.

9. Kresse, G.; Furthmüller, J., Efficient iterative schemes for ab initio total-energy calculations using a plane-wave basis set. *Physical Review B* **1996,** *54* (16), 11169-11186.

10.   Kresse, G.; Furthmüller, J., Efficiency of ab-initio total energy calculations for metals and semiconductors using a plane-wave basis set. *Computational Materials Science* **1996,** *6* (1), 15-50.

11.   Perdew, J. P.; Burke, K.; Ernzerhof, M., Generalized Gradient Approximation Made Simple. *Physical Review Letters* **1996,** *77* (18), 3865.

12.   Ireta, J.; Neugebauer, J.; Scheffler, M., On the Accuracy of DFT for Describing Hydrogen Bonds: Dependence on the Bond Directionality. *The Journal of Physical Chemistry A* **2004,** *108* (26), 5692-5698.

13.   Barbosa, L. A. M. M.; Sautet, P., Stability of Chiral Domains Produced by Adsorption of Tartaric Acid Isomers on the Cu(110) Surface: A Periodic Density Functional Theory Study. *Journal of the American Chemical Society* **2001,** *123* (27), 6639-6648.

14.   Hermse, C. G. M.; van Bavel, A. P.; Jansen, A. P. J.; Barbosa, L. A. M. M.; Sautet, P.; van Santen, R. A., Formation of Chiral Domains for Tartaric Acid on Cu(110): A Combined DFT and Kinetic Monte Carlo Study. *The Journal of Physical Chemistry B* **2004,** *108* (30), 11035-11043.

15.   Roma, F.; Zgrablich, G.; Stacchiola, D.; Tysoe, W. T., Theoretical analysis of the coverage dependence of enantioselective chemisorption on a chirally templated surface. *Journal of Chemical Physics* **2003,** *118* (13), 6030-6037.

16.   Easson, L. H.; Stedman, E., Studies on the relationship between chemical constitution and physiological action: Molecular dissymmetry and physiological activity. *Biochem. J.* **1933,** *27* (4), 1257-1266.

17.   Ogston, A. G., Interpretation of experiments on metabolic processes, using isotopic tracer elements. *Nature* **1948,** *162* (4129), 963.

18.   Pimentel, G. C. M. A. L., *The hydrogen bond*. W.H. Freeman; trade distributor: Reinhold Pub. Corp., New York: San Francisco, 1960.

19.   Gao, F.; Wang, Y. L.; Burkholder, L.; Tysoe, W. T., Enantioselective chemisorption of propylene oxide on a 2-butanol modified Pd(111) surface: The role of hydrogen-bonding interactions. *Journal of the American Chemical Society* **2007,** *129* (49), 15240-15249.

Chapter 9

Surface chemistry of Aspartic acid on a Pd(111) Surface

9.1   Introduction

In the previous chapters the surface chemistry of alanine and tartaric acid have been explored as chiral modifiers on Pd(111) and the resulting enantioselectivity of the modified surface was measured by using propylene oxide and glycidol as chiral probe molecules. From the STM results, it was clear that both alanine and tartaric acid form different surface structures depending on the dosing temperature of the sample and surface coverage. By correlating the surface structures observed in STM with the measured enantioselectivities, it was concluded that alanine bestows chirality to the surface by forming chiral templates (chiral pockets), which allow the preferential adsorption of one enantiomer of the probe molecules.[1-2] On the other hand, tartaric acid under the enantioselective conditions does not form any ordered structures, but individual bitartrate species interact with the chiral probe in a 1:1 fashion.[3] Thus alanine and tartaric acid behave very differently on a Pd(111) surface, the reason being the presence of different functional groups on both the compounds. Alanine self-assembles to form tetramers (chiral templates) and dimer rows due to strong hydrogen bonding interactions between the carboxylate groups and ammonium group. Tartaric acid STM images show the presence of individual bitartrate molecules at low coverages, but at higher coverages, oligomeric structures are observed proposed to occur, due to the hydrogen-bonding interactions between two –OH groups and between the COOH $\cdots$ OH groups of the

monotartrate species.

In this chapter, the surface chemistry of aspartic acid on Pd(111) is investigated with the motivation to gain insights into whether it can be used as a chiral modifier. Aspartic acid has bonding moieties similar to both tartaric acid and alanine: two COOH groups as in tartaric acid and one –NH$_2$ group as in alanine. Infrared spectroscopy has been used to characterize the bonding and orientation of aspartic acid on a Pd(111) surface. STM images were also collected following aspartic acid adsorption to characterize the surface structures and compare them with those of alanine and tartaric acid.

Aspartic acid is one of the most abundant amino acids in nature. The three-dimensional structure of aspartic acid is shown in Figure 9-1. It has three functional groups; the α-amino (α-NH$_2$), the α-carboxyl (the α-COOH) and the β-carboxyl *(β-COOH)* groups. Aspartic acid has been used as a potential chiral modifier for Ni catalyst for enantioselective hydrogenation of β-keto esters.[4-5]
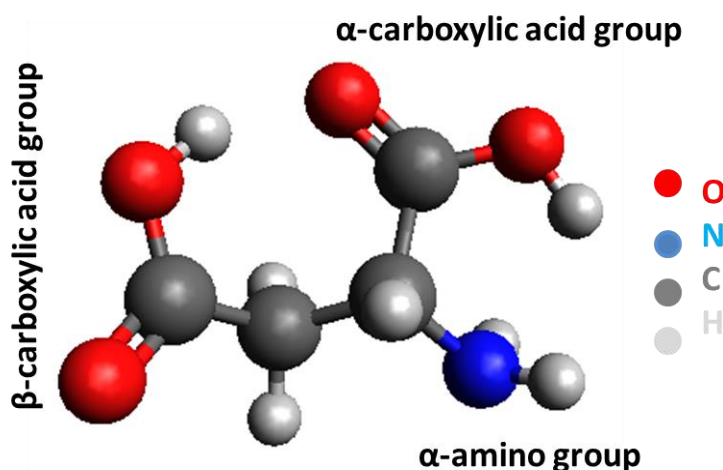
Figure 9-1 Three-dimensional structure of an aspartic acid molecule

There are many examples of UHV-based studies performed by adsorbing aspartic

acid on a Ni surface with the aim of gaining insight into the role of the chiral modifier in achieving enantioselective behavior.[6-10] The adsorption of aspartic acid was studied on Ni(111) under UHV conditions by RAIRS, STM and TPD.[10] At low coverages, aspartic acid polymerizes to form oligosuccinimide species at surface defects and, at higher coverages, the surface was filled with mono-aspartate species, which bond to the surface through the amine group and carboxylate oxygens. It has been speculated that the origin of enantioselectivity in the Ni/aspartate system is the formation of oligosuccinimide clusters at low coverage which creates docking sites for methylacetoacetate.

The orientation and bonding of aspartic adsorption from solution phase has been studied in detailed on rutile TiO_2 films and γ-Al_2O_3 surfaces.[7, 11-12] On both surfaces the dominant adsorption geometry is reported in which both the carboxylate groups of aspartic acid are involved in bonding to the surface atoms. Recently, DFT calculations have been performed for aspartic acid adsorption on rutile (110) surface,[11] which suggests that the strongest adsorption occurs when both the amino and carboxyl groups of aspartic acid approached the rutile (110) surface and formed a bidentate coordination to two surface Ti atoms. Therefore it seems that the geometry and bonding of aspartic acid is highly dependent on the nature of the surface.

9.2   Experimental Section

Infrared spectra were collected in the RAIRS chamber as described in Chapter 2. The spectra were collected by using a Bruker Vertex infrared spectrometer operating at a resolution of 4 cm^{-1}, using a liquid-nitrogen-cooled, mercury cadmium telluride detector, and spectra were typically collected for 1000 scans.

Scanning Tunneling Microscopy experiments were performed in the STM

chamber as described in Chapter 2. STM images were acquired using an electrochemically etched tip made from recrystallized tungsten wire.

The Pd(111) substrate was cleaned using a standard procedure consisting of cycles of argon ion sputtering and annealing in 3×10^{-8} Torr of oxygen at 1000 K and the cleanliness was judged either using X-ray photoelectron spectroscopy, Auger spectroscopy or temperature-programmed desorption after dosing with oxygen, where the absence of CO desorption indicated that the sample was carbon free.

L-aspartic acid (Aldrich, 99% purity) was dosed onto the sample by using home built Knudsen source attached to the respective vacuum chambers. The aspartic acid source was generally outgassed overnight at 400 K before being dosed onto the surface to remove contaminants, particularly water, and the temperature of the source was adjusted to yield reasonable dosing rates. The temperature of the Knudsen source was maintained between ~400 to ~410 K for the STM experiments and 390 to 395 K for the RAIRS experiments.

9.3 Experimental Results

9.3.1 RAIRS of L-Aspartic Acid on Pd(111) at 120 K

Infrared spectra were collected following adsorption of L-aspartic acid on a Pd(111) surface at 100 K as a function of increasing exposure and is shown in Figure 9-2.
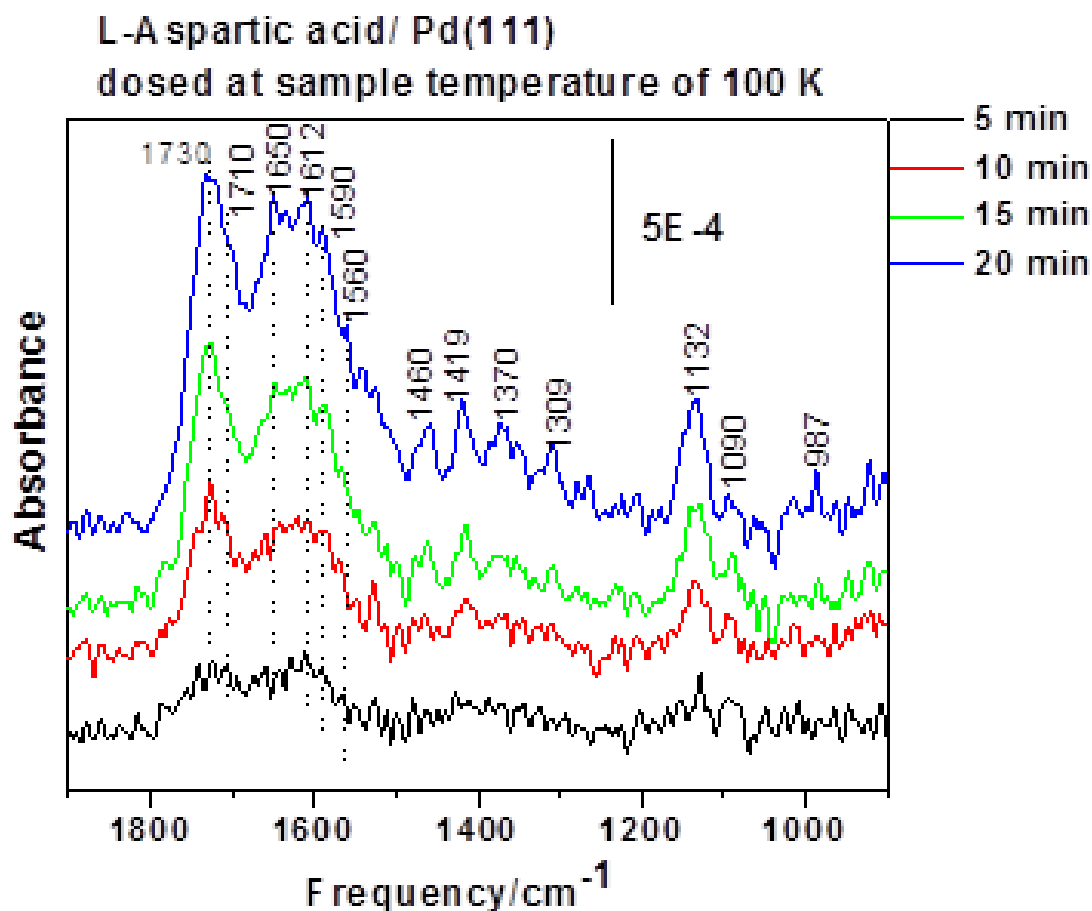
Figure 9-2 Infrared spectra of L-aspartic acid adsorbed on Pd(111) at 100 K as a function of exposure, and the dosing times are displayed in the spectra.

At all exposures, there are three broad peaks appear which are centered on ~1730 cm^{-1}, 1620 cm^{-1} and 1414 cm^{-1}. The peak at 1730 cm^{-1} corresponds to the C=O stretch of the carboxylic acid group and the peaks at 1620 cm^{-1} and 1414 cm^{-1} are characteristic of asymmetric and symmetric COO^- stretching modes respectively. Therefore IR suggests the presence of both carboxylic acid groups and carboxylate groups due to deprotonation of one of the carboxylic acid groups on Pd(111) surface. This is typical behavior of carboxylic acids on metal surfaces, where carboxylic acid group dehydrogenates and form carboxylate species.[13-14] The presence of symmetric OCO stretch mode at 1414 cm^{-1}

indicates that a portion of the adsorbed species adopts an η^3 geometry, where bonding to the surface occurs through both the carboxylate oxygen atoms and the amine group. The corresponding asymmetric stretching mode, which is infrared forbidden according to the surface infrared selection rule for a η^3 aspartate species appears at 1612 cm^{-1}. This indicates that a portion of the adsorbed aspartate adopts a different geometry. A similar asymmetric stretching mode has been observed at ~1606 cm^{-1} for alaninate species on Pd(111) [2] and at 1613 cm^{-1} on Cu [15] and ascribed to the adsorption of η^2-alaninate species with the plane of the carboxylate group inclined to the surface, proposed to coordinate to the surface through the amine group and an oxygen atom of the carboxylate. The peak intensity of the 1612 cm^{-1} peak is much higher than 1412 cm^{-1} peak at all coverages, which suggests that proportion of the η^2 aspartate species is greater than the η^3 aspartate at 100 K. The 1612 cm^{-1} peak is broadened due to the contribution of the asymmetric δ (NH$_3{}^+$) band which is usually observed at 1650 cm^{-1}. The small peak at ~1520 corresponds to the symmetric δ (NH$_3{}^+$) band. Therefore the IR data is indicative of the presence of zwitterionic species at low temperature. In addition, there are three shoulders found at 1710 cm^{-1}, 1590 cm^{-1} and 1560 cm^{-1}. The 1710 cm^{-1} peak is characteristics of the presence of a C=O mode of a carboxylic acid group while the 1590 and 1560 cm^{-1} frequencies corresponds to antisymmetric carboxylate stretch, probably arising from aspartate species adopting a different adsorption geometry. There are some additional bands observed in the low-frequency region. The peak at 1454 cm^{-1} corresponds to CH$_2$ bend of the side chain and the peak observed at 1309 cm^{-1} corresponds to the coupled mode of the CH$_2$ bend, C-C and C-N stretch. Finally a sharp peak is observed at 1132 cm^{-1} which is due to a for CCN stretching mode.

Broadly speaking at 100 K, the surface layer predominantly consists of monoaspartate species, where the bonding occurs through the amine group and the oxygen atoms of a carboxylate, in a similar manner to the adsorption geometry of alanine on Pd(111).[2] The majority of the surface species adopt an η^2 adsorption geometry, while there are some species on the surface which adopts a η^3 adsorption geometry as evidenced by the presence of both asymmetric (1612 cm^{-1}) and symmetric (1414 cm^{-1}) OCO$^-$ stretching modes. The frequency and assignments are given in Table 9-1.

Vibrational frequency/cm^{-1} at 120 K	Vibrational frequency/cm^{-1} at 300 K	Assignments
-	1763	ν_{as} (C=O) imide
-	1743	ν_s (C=O) imide
1730	1730	ν (C=O) α-carboxylic acid
1710	1710	ν (C=O) β-carboxylic acid
1650	1650	δ_{as} (NH$_3^+$)
1612	1600,1618	ν_{as} (COO$^-$) β-carboxylate
1590	1580	ν_{as} (COO$^-$) α-carboxylate
1560		δ_{as} (NH$_2$)
1527	1525	δ_s (NH$_3^+$)
1460		
1419	1419 (sh)	δ (CH$_2$)
	1400	ν_s (COO$^-$) α and β carboxylate
1370	1360	ω(CH$_2$)
1309		δ (CH$_2$)+ ν (C-C) + ν (C-N)
	1254	N(C-O) +δ (OH)
1132	1120	ν (CCN)
1090	1087	
987		ν (C-C)

Table 9-1 Vibrational frequencies and the assignments of L-aspartic acid on Pd(111) at 100 K and 300 K.

9.3.2 RAIRS of L-Aspartic Acid on Pd(111) at 300 K

Figure 9-3 shows the RAIRS spectra collected following aspartic acid adsorption at 300 K. The major bands at all exposures are observed at ~1730 cm^{-1}, 1600 cm^{-1}.and

1400 cm^{-1}. Based on the low-temperature spectra, the 1735 cm^{-1} peak is assigned to the

C=O stretch of the carboxylic acid group and the 1600 cm $^{-1}$ and 1400 cm^{-1} peaks are the

asymmetric and symmetric stretch of the carboxylate groups respectively. The 1735 cm^{-1}

peak is broadened in comparison to the band observed at 100 K. There are two shoulders

that appear at 1760 and 1743 cm^{-1}.
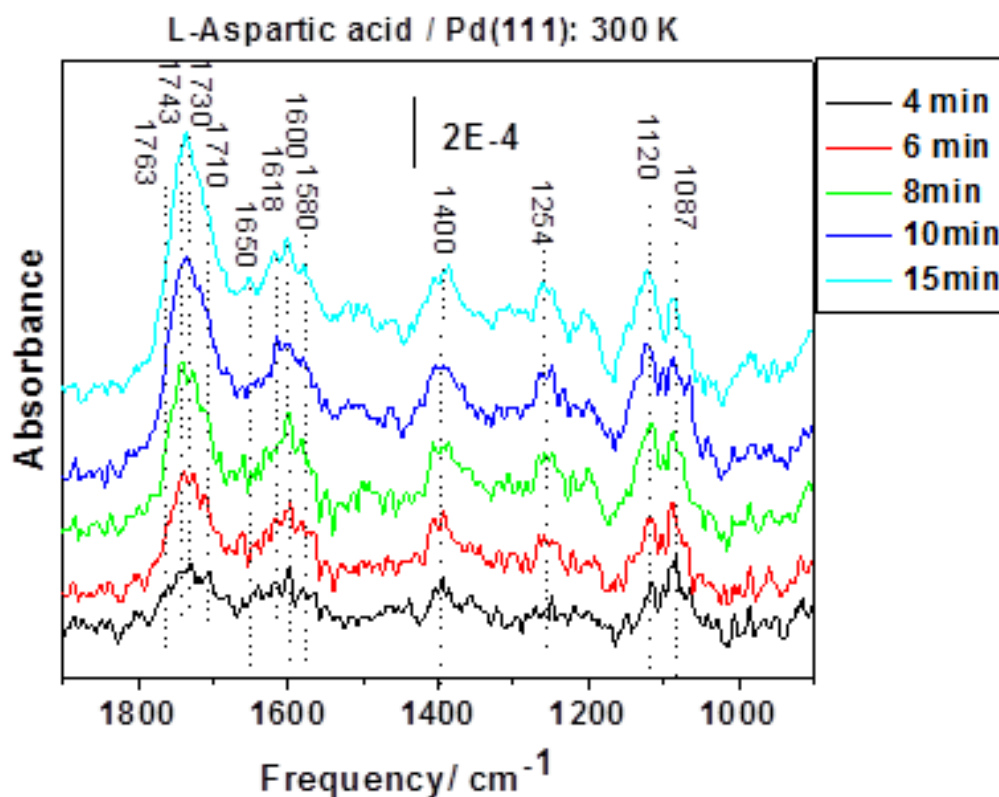
Figure 9-3 Infrared spectra of L-aspartic acid adsorbed on Pd(111) at 300 K as a function of exposure, and the dosing times are displayed in the spectra.

The 1760 and 1743 cm^{-1} peaks are due to the contribution of asymmetric and

symmetric C=O stretches of the cyclic imide structure, respectively. A similar IR

frequency has been reported for low-coverage adsorption of aspartic acid on Ni(111) at

~300 K.[10] The peak at 1650 cm^{-1} which corresponds to the asymmetric δ (NH$_3^+$) mode is

missing at low coverages following room-temperature adsorption and only a very small

peak appears at higher exposures. This indicates that the proportion of zwitterionic species is very low at room temperature in comparison to low-temperature adsorption. The peak at 1254 cm^{-1} arises due to the coupled interaction of the δ(OH) and ν(COO) modes of the carboxylic acid groups and, similar to the low-temperature spectra, a peak is observed at 1120 cm^{-1} due to a C-N stretching mode.

Overall, IR spectra collected at room temperature suggests the presence of two different kinds of surface species. The presence of two shoulders at 1760 and 1743 cm^{-1} features indicate that a portion of the absorbed species undergo a polycondensation reaction to form a cyclic imide structure and the reaction scheme for this process is shown in figure 9-4.
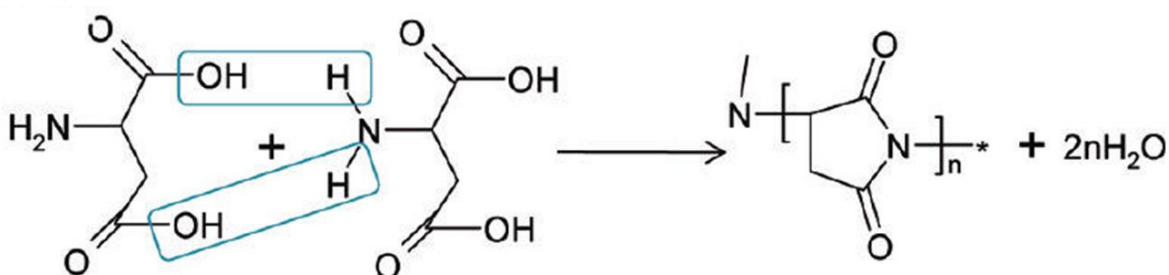
Figure 9-4 Reaction scheme representing the polycondensation of aspartic acid to polysuccinimide [10]

The majority of the overlayer consists of aspartate species with two different adsorption geometries, similar to the results obtained at low temperatures. In the first, bonding occurs via the amine group and the carboxylate oxygen atoms (η^3 aspartate) and, in the second, bonding occurs via the amine group and one of the oxygen atoms of the carboxylate group (η^2 aspartate) as evidenced by the presence of both asymmetric (1600 cm^{-1}) and symmetric (1400 cm^{-1}) carboxylate stretch. However, unlike low temperature spectra, the proportion of η^2 aspartate and η^3 aspartate species are equal at 300 K.

9.3.3   STM Study Following L-aspartic acid Adsorption at 120 K

STM images are collected for various coverages of aspartic acid adsorption at low

temperatures on Pd(111). Figure 9-5 (a) to (c) show the surface topology as a function of

increasing coverage. The most common surface structure observed at all coverages is the

honeycomb motif as shown in Figure 9-5. At low coverages, as shown in Figure 9-5 (a),

some individual molecules are observed which are imaged as bright, oval-shaped

features. In addition, one-dimensional ladder structures and small honeycomb islands are

also observed. With a slight increase in coverage (Figure 9-5 (b), the islands grow larger

in size and they are oriented along three crystallographic directions which are at 120° to

each other. The molecules form extended two-dimensional islands with smooth borders.

Within the islands, the molecules are organized in a honeycomb pattern with a periodicity

of ~1.1 nm. These islands propagate from step edges and run along the terraces. Figure 9-

5 (c) shows a larger-area STM image for a high coverage of aspartic acid dosed and

imaged at 120 K, which again shows the extended growth of islands. Figure 9-5 (d) is a

magnified region of the same surface as in Figure 9-5 (c), which shows the individual

honeycomb motif within the island. There are two large islands on the top and bottom

portions of image 9-5 (d) and those two islands are connected by some small islands. In

addition to the two-dimensional honeycomb islands, there are some one-dimensional

chain structures also present.
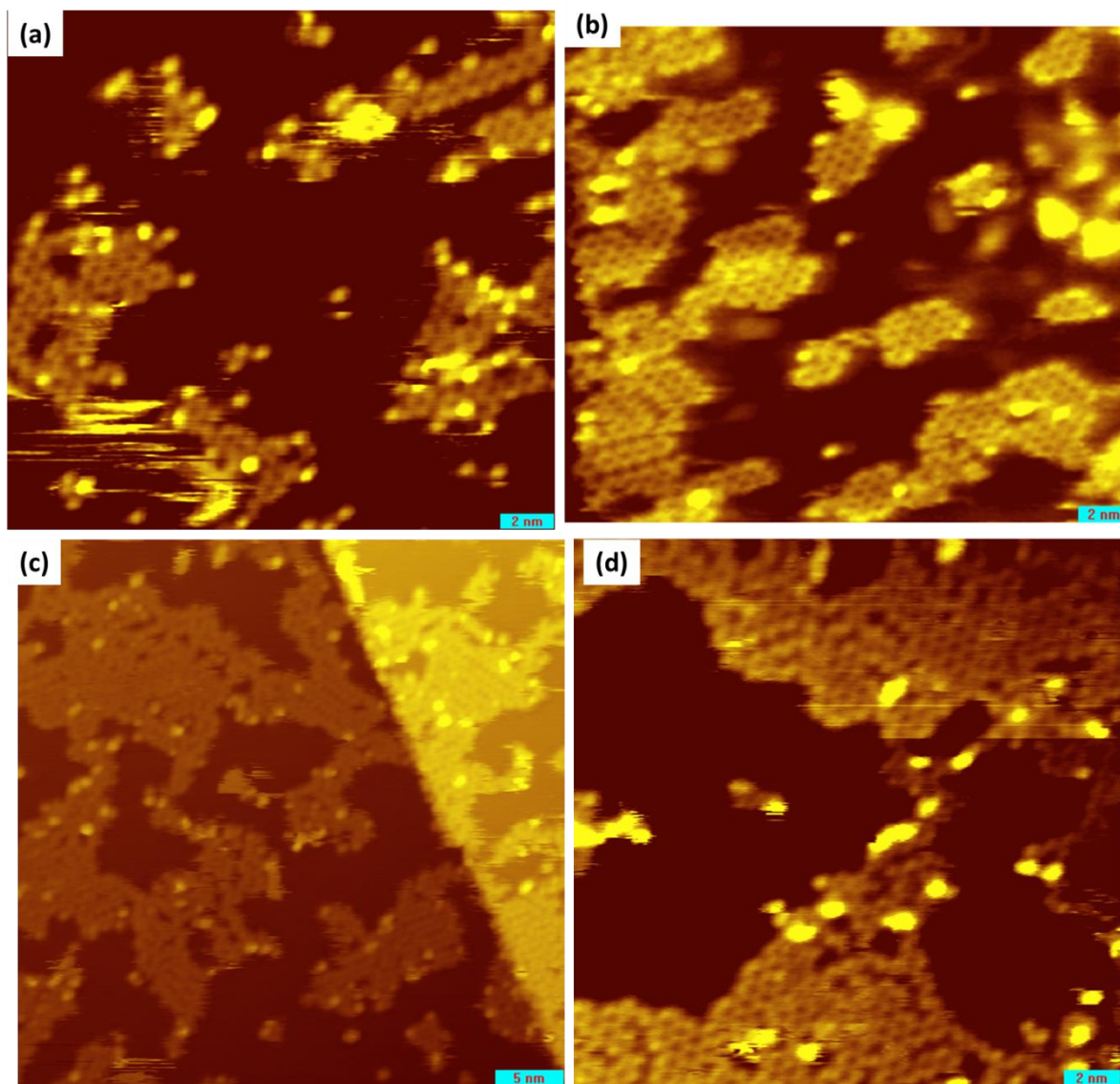
Figure 9-5 Large scale STM images of L-aspartic acid on Pd(111) dosed and imaged at 120 K. In Figure 9-5 (a) to (c) the surface coverage is gradually increased. Figure 9-5 (d) shows a zoomed in image for the same surface as imaged in image 9-5 (c). (V_b = 0.8 V, I_t=200 pA).

Finally Figure 9-6 shows a high-resolution image for a smaller scan area which clearly shows the periodicity within the honeycomb islands.A line profile measurement (indicated by a white line) shows a ~1.12 nm periodicity in a honeycomb island.
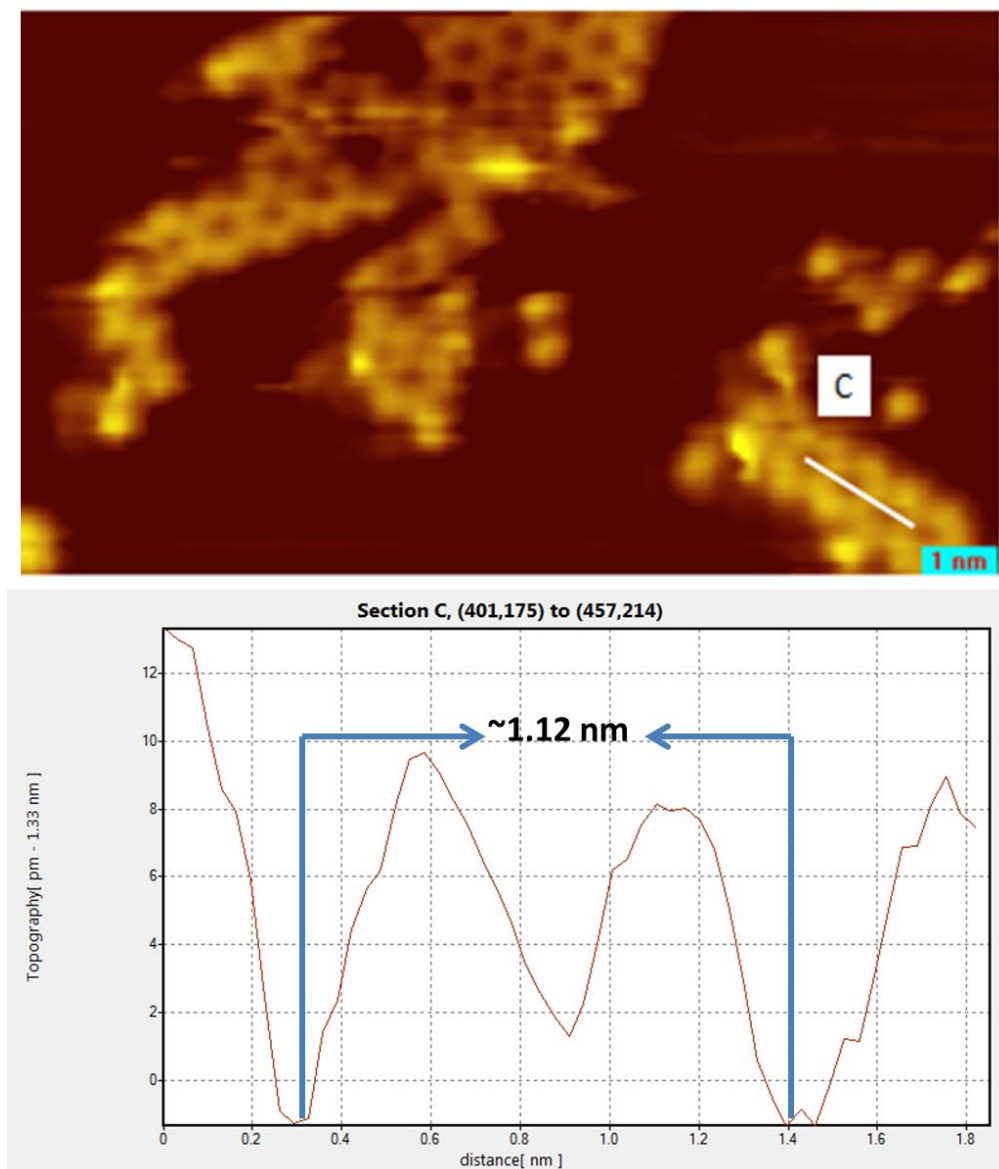
Figure 9-6 Smaller scan area STM image of a low coverage of L-aspartic acid on Pd(111): dosed and imaged at a sample temperature of ~120 K.

Occasionally, the commonly observed honeycomb motifs are observed with a different image contrast where they are imaged as linear rows running parallel to each other. Figure 9-7 shows an example, where a change in image contrasts is observed in four consecutive images. Figure 9-7 (a) shows the regular honeycomb motif, (b) and (c) show some line structures, which are oriented along one of the crystallographic directions of growth of the honeycomb islands, and in (d) the original honeycomb motif is restored.

Here the images are collected with slight variation in the tip bias, so the change in image contrast might be a result of applying different biases.
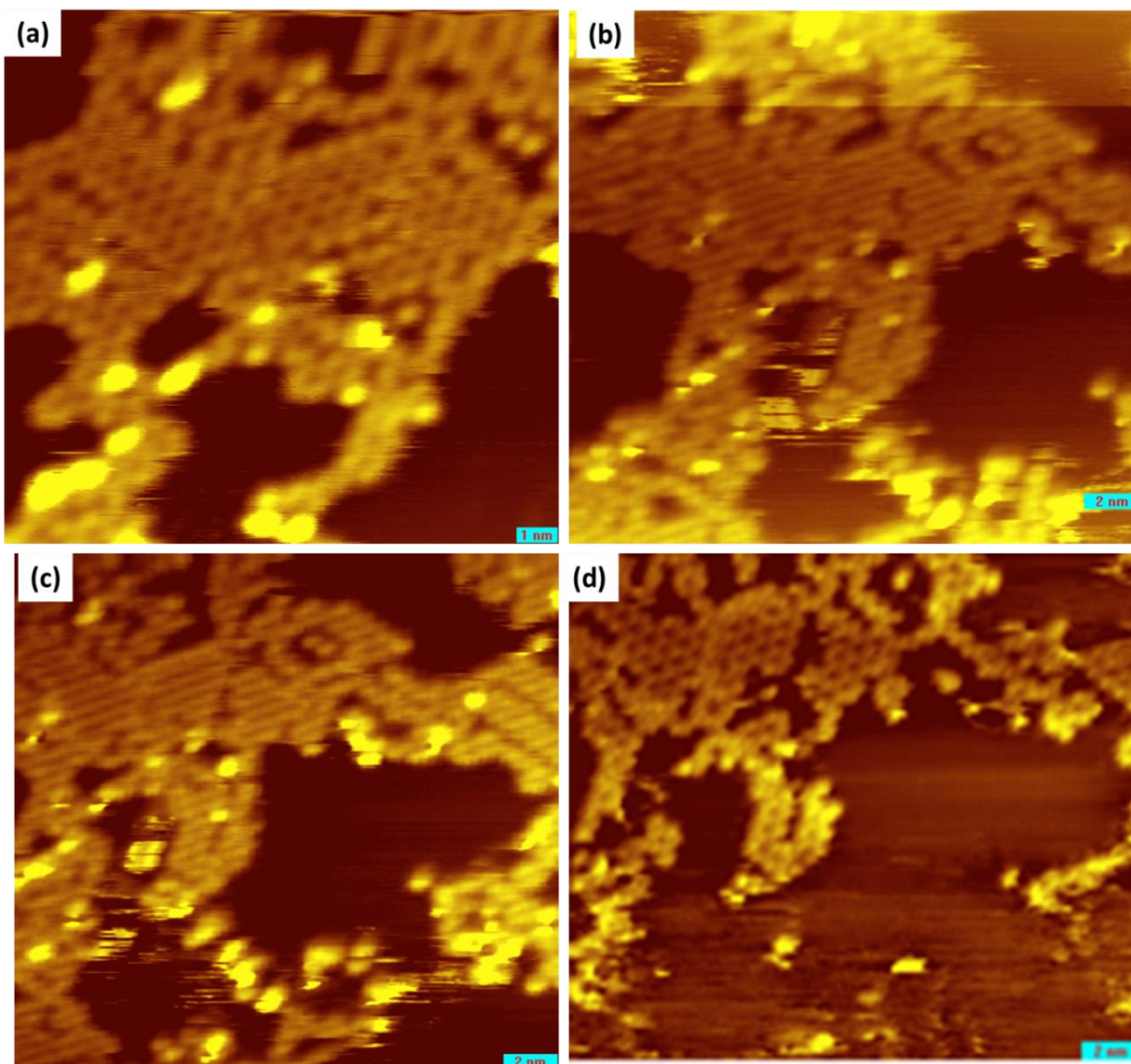
Figure 9-7 (a) to (d) show four consecutive STM images collected for the same scanning area, which show switching between two different image contrasts. (a) shows the original honeycomb motif (1 V, 200 pA), (b) and (c) shows parallel line structures (0.8 V, 200 pA) (d) the original honeycomb motif is restored (0.47 V, 180pA)

However, it has been also noticed that the image contrast changes during scanning with the same bias (data not shown here). Therefore the change is attributed to the adsorption dynamics where the molecules slightly rearrange over the period of scanning

by changing the direction of the hydrogen bonding interaction. By closely examining the images at a smaller scale (Figure 9-7 (d)), it appears that the honeycomb motif consists of two zigzag rows running parallel to each other. The origin of those features will be explained in greater details in the discussion section.
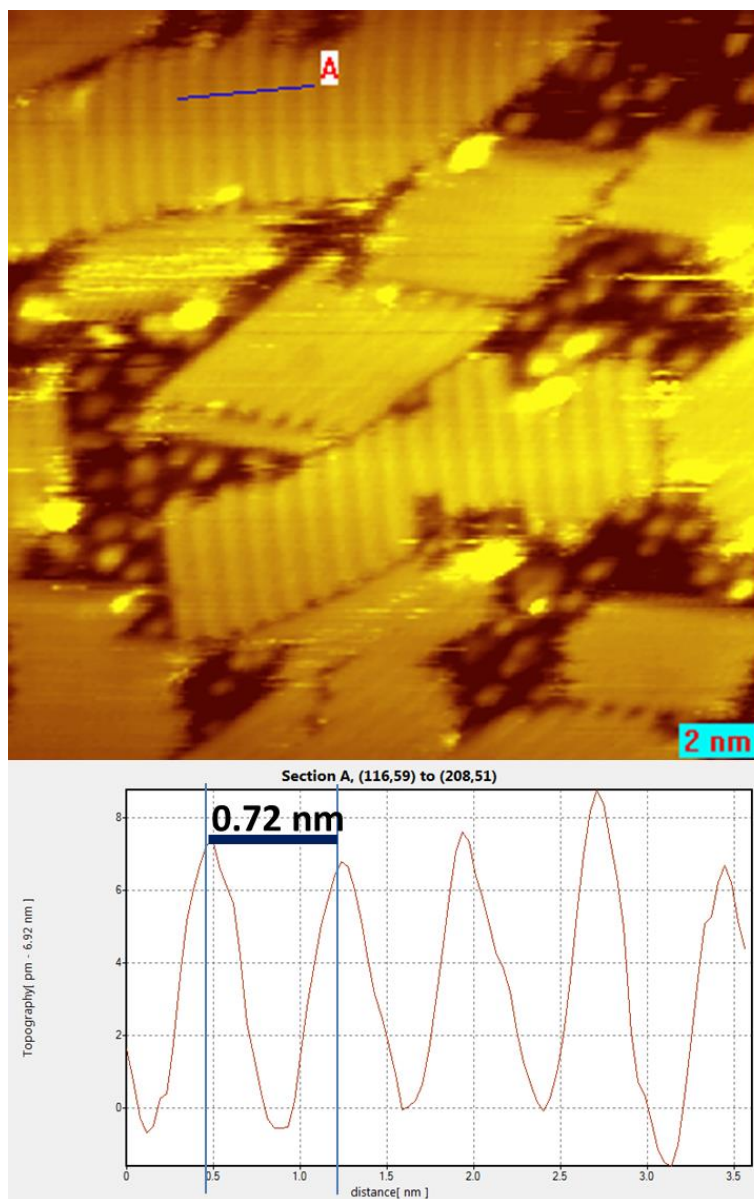
Figure 9-8 STM image of L-aspartic acid on a Pd(111) surface showing the patches of parallel rows. Image is collected when the surface is both dosed and imaged at ~120 K. (1V, 300 pA)

In addition to the commonly observed honeycomb motifs, another striking feature

is observed which consists of patches of parallel rows as shown in Figure 9-8. The domains run at an angle of ~30° or 13° to the surface close-packed crystallographic direction. The spacing between the rows is ~0.72 nm, which is indicated by the line profile measurement in Figure 9-8. In between the domains, some individual isolated aspartate species are observed. Those domains grow with repeated scanning on the same surface as shown in time-lapse images (Figure 9-9).
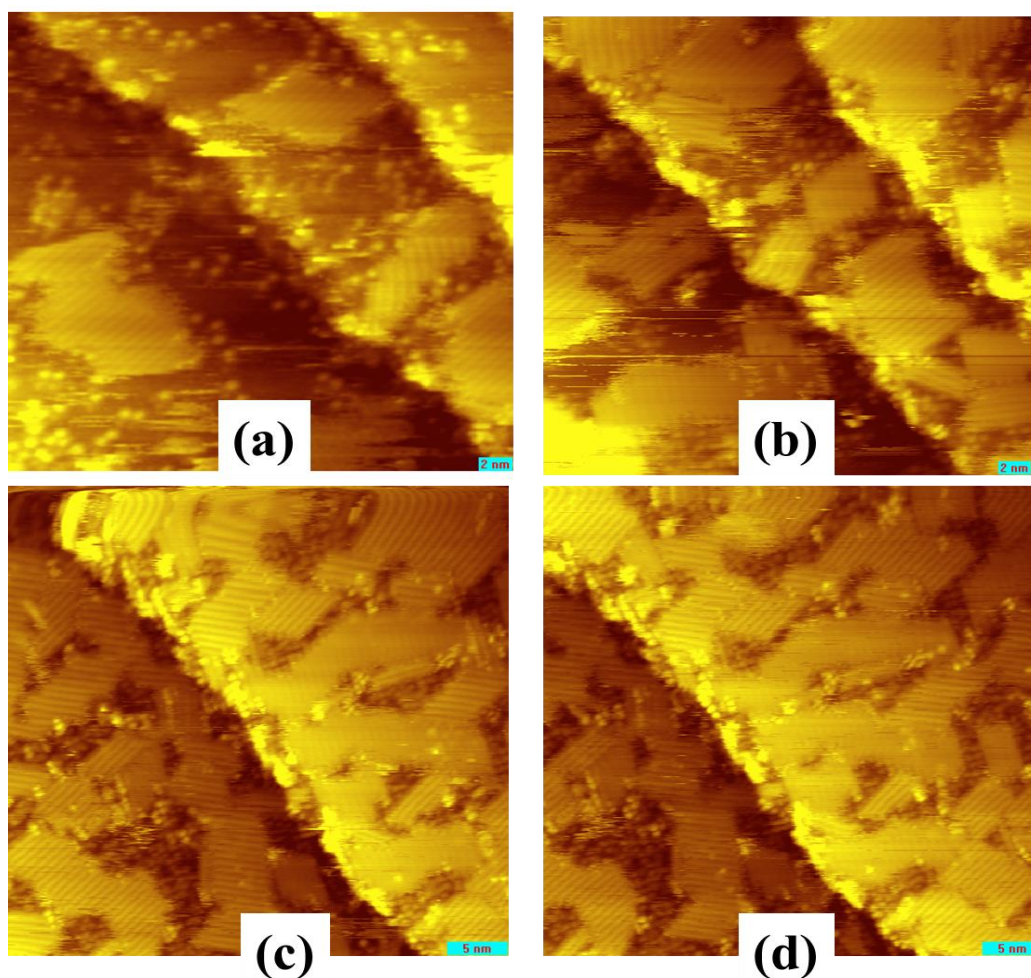
Figure 9-9 (a) to (d) show four time lapse images collected for the same scanning surface. The growth of the ordered domains increase as a function of time

Figure 9-9 (a) shows the presence of individual aspartate species and some ordered domains, which consist of linear rows. Streaky lines appear near the domain

boundary as well near the individual species, which suggests molecular motion. With consecutive scans the number of domains increases and fewer individual species are observed. However, there are still some individual species present which are confined in between the domains. This structure allows the molecules to be more tightly packed on the surface in comparison to the honeycomb pattern. The formation of those domains increased under positive tip bias condition and increased with scanning time. Therefore the possibility of tip induced structure cannot be eliminated.

9.3.4   STM Study Following L-aspartic acid Adsorption at 300 K

Finally STM images are collected after dosing the Pd(111) surface at room temperature and then cooling to 120 K for imaging. Figure 9-10 (a) to (c) show the surface structures formed at 300 K as a function of coverage. At low coverages, the molecules decorate the step edge (Figure 9-10 (a)). In addition, some individual molecules and small clusters are also observed on the terraces. With a slight increase in coverage, (Figure 9-10 (b)), the surface mostly consists of clusters, but individual molecules are also observed. At higher coverages, as shown in Figure 9-10(c), the molecules form complex network-like structures and pores of different sizes are observed. The formation of this network structure originates from the step edge and grows towards the terraces. Figure 9-10 (d) shows a higher-magnification image of the same surface as Figure 9-10 (c), which clearly shows the presence of a number of different surface structures. At the bottom of the image, individual molecules are present, while the top portion consists of complex network structure; the middle portion shows the presence of two-dimensional row structures. It is also noted that the same network structure is obtained when a surface is dosed at 80 K and annealed to ~300 K (data not

shown). The surface structure obtained by dosing at ~300 K is complex and consists of a number of different surface species as observed by IR spectroscopy.
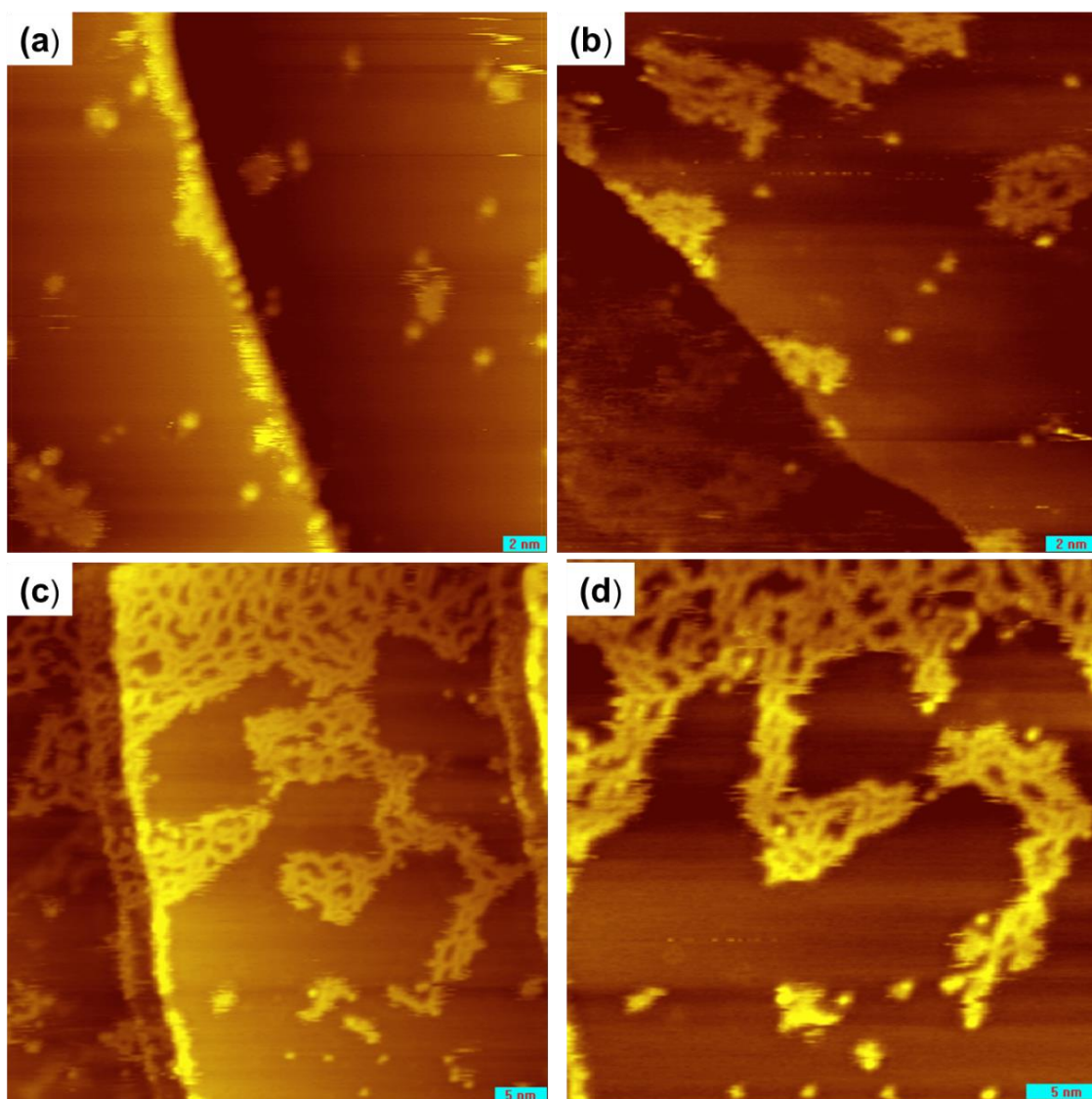
Figure 9-10 STM images of L-aspartic acid on a Pd(111) surface dosed at ~300 K and then cooled to ~120 K for imaging. (a) to (c) show the surface structure as a function of increase in coverage. (d) Zoomed in image for the same surface as (c). Imaging condition for (a) and (b): 0.4 V, 100 pA and for (c) and (d) 1 V, 120 pA

9.4   Discussion

The chemical nature of the adsorbed species is directly identified from the RAIRS study. RAIRS spectra collected by dosing the surface at 100 K for various coverages

show that the surface predominantly consists of monoaspartate species. At low temperatures, monoaspartate species mostly bond to the surface in an η^2 geometry, where it binds to the surface by one of the carboxylate oxygens and the amine group and a smaller proportion accounts for adsorbates with an η^3 adsorption geometry. Similar η^2 adsorption geometry is observed for alanine on Pd and Cu surfaces, where bonding to the surface occurs through one of the oxygen atoms of the carboxylate and the amine group. The other oxygen atom moves away from the surface to hydrogen bond to the neighboring alanine.

However, there are two different kinds of monoaspartate species, which can be expected depending on which carboxylic acid group deprotonates on the surface. DFT calculations were performed for isolated monoaspartate species on a 6×6 Pd(111) slab with a co-adsorbed hydrogen atom on a three-fold hollow site. Two different initial monoaspartrate adsorption geometries were considered and the resulting relaxed structures are shown in Figure 9-11. In Figure 9-11 (a), the β-carboxylic acid deprotonates and bonding to the surface occurs through the oxygen atoms of the β-carboxylate and nitrogen atom of the amine group. The oxygen and the nitrogen atoms bond to palladium atop sites and the C-C molecular backbone is close to parallel to the surface. The α-carboxylic acid group slightly tilts towards the surface which allows internal hydrogen bonding to occur between the oxygen atom of the carboxylic acid group and the hydrogen atom of the amine. This structure yields an adsorption energy of -74 kJ/mol.

In Figure 9-13 (b) the α-carboxylic acid deprotonates and bonds to the surface *via* the oxygen atoms of the α-carboxylate and nitrogen atom of the amine group. In this case

the C-C molecular backbone is perpendicular to the surface and the β-carboxylic acid group slightly tilts towards the surface so that internal hydrogen bonding can occur in a similar manner as in structure (a). The calculated adsorption energy for structure (b) is -64 kJ/mol. The DFT calculations are consistent with the observation of both α and β-carboxylate species in the IR spectra (Table 9-1).
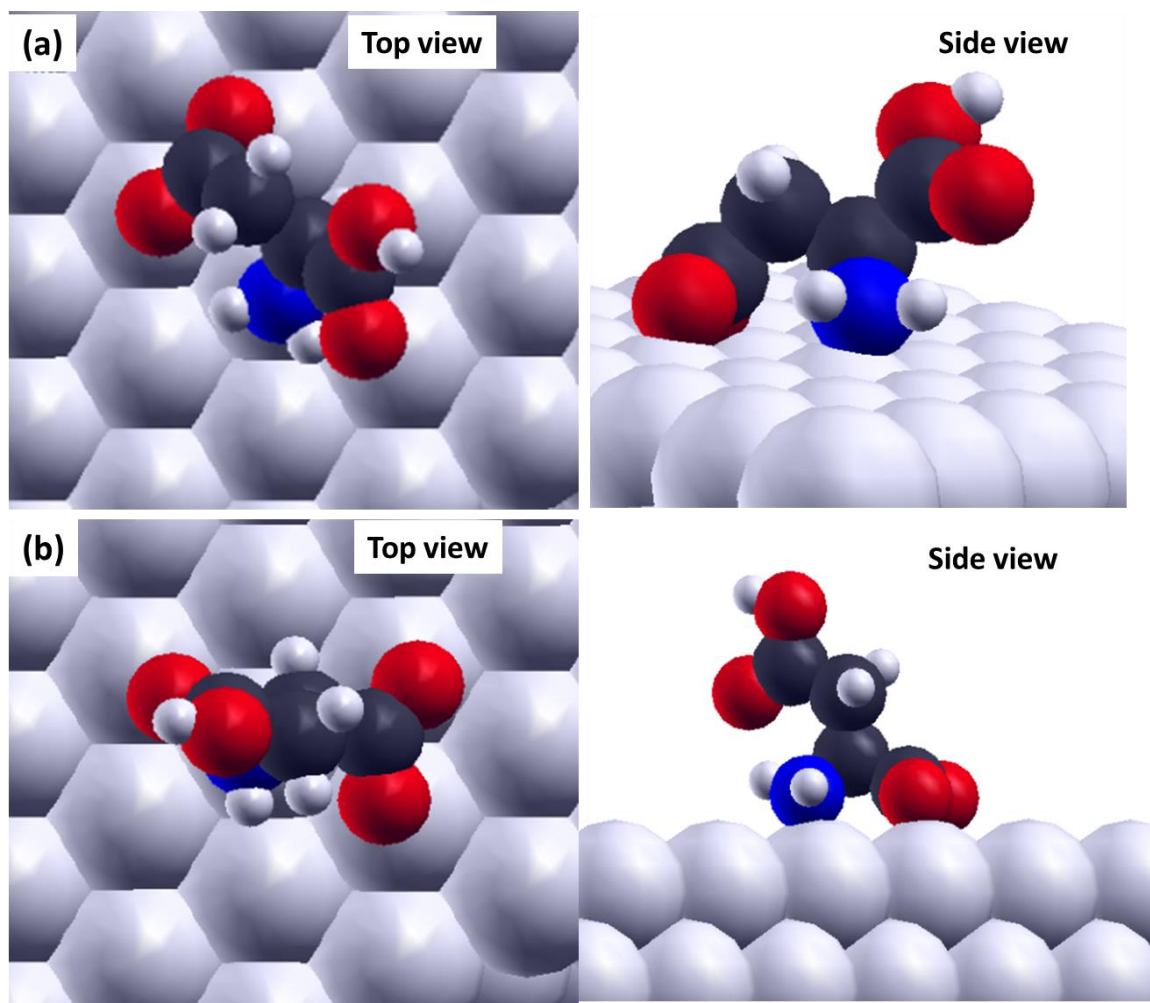
Figure 9-11 Depiction of the two most stable structures of aspartate species on Pd(111) surface calculated by DFT, showing the top and side views for (a) β-carboxylate (b) α-carboxylate

The IR spectra show the proportion of monoaspartate species in which β-carboxylic acid group has deprotonated is higher compared with the deprotonation of the

α-carboxylic acid groups on the surface as indicated by the presence of intense IR modes at 1730 and 1612 cm^{-1} (β-carboxylate) and two shoulders at 1710 and 1590 cm^{-1} (α-carboxylate).

The STM studies carried out following low-temperature adsorption show the presence of honeycomb islands. The origin of the honeycomb motif is most likely due to the self-assembly through hydrogen-bonding interactions between the carboxylate groups with the amine group. A plausible model for the observed honeycomb structure is shown in Figure 9-12. From a chemical point of view, the honeycomb motifs, requires the presence of three functional groups which are capable of forming hydrogen bonds. Aspartic acid has two carboxylic acid groups and an amine group. The structural model is proposed based on the most stable aspartate monomer species calculated by DFT (Figure 9-11(a)). The N and O atoms bond to palladium atop sites and the C-C backbone remains parallel to the surface. The hydrogen-bonding interaction between the β-carboxylate oxygen with the –NH$_2$ group facilitate the formation of zigzag-row structures. Two zigzag rows run parallel to each other and come closer to each other every other molecule due to the hexagonal symmetry of the surface, which allows additional hydrogen bonding interactions to occur through the α-carboxylic acid group of one row with the carboxylate oxygen atom of the adjacent row. In STM, those structures appear as hexagonal features forming honeycomb patterns. The spacing and orientation of the proposed structure match well with the experimentally observed STM images.
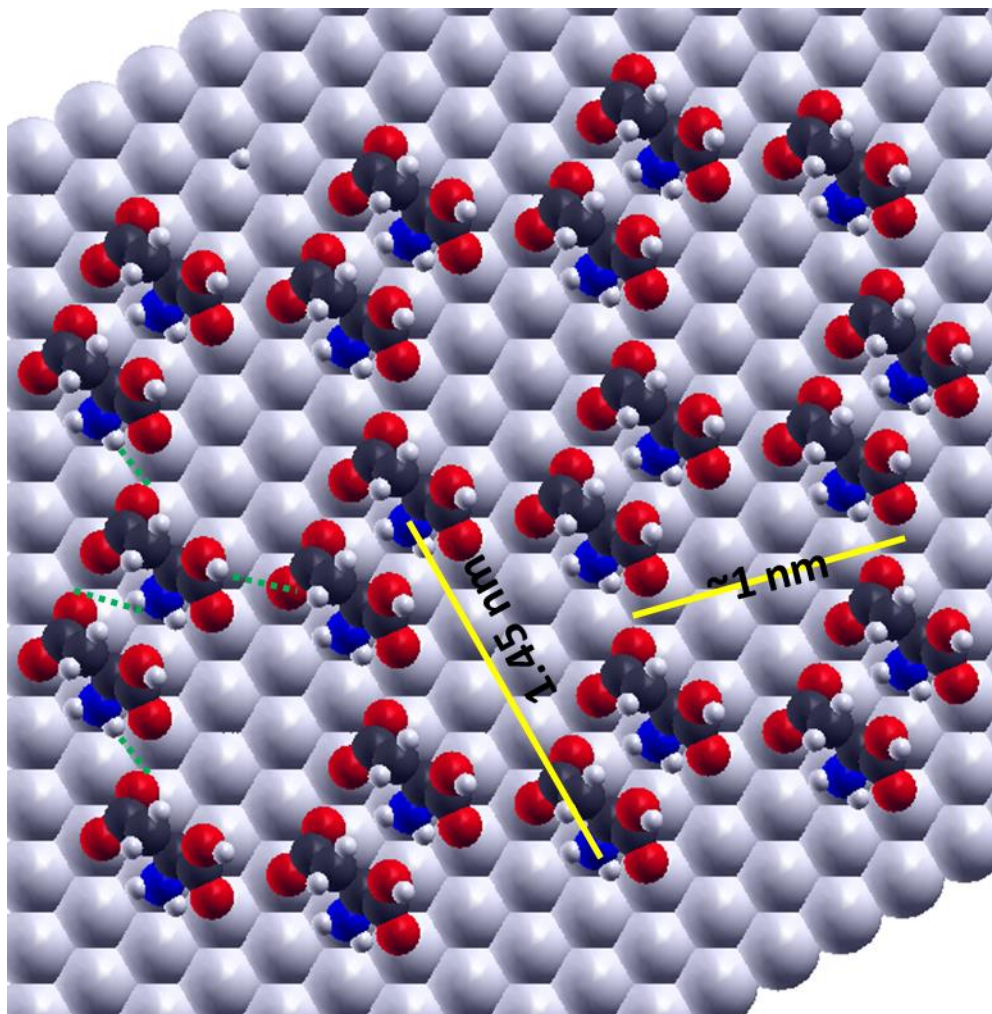
Figure 9-12 A proposed model for the experimentally observed honeycomb motif following aspartic acid adsorption at low temperatures, the hydrogen bonding interactions are shown in green dotted lines

The other type of observed ordered overlayer consists of domains of linear rows, (Figure 9-9) is also proposed to occur due to similar $OCO\cdots H_2N$ hydrogen-bonding interactions. Taking into account the line spacing and orientation of the domains with respect to the substrate crystallographic direction, a model is proposed for the formation of the linear-row structures and is shown in Figure 9-13. The aspartate species self-organize on the surface in linear rows to optimize the hydrogen-bonding interaction between the carboxylate group and the amine group. The individual rows hydrogen bond

to each other through the carboxylic acid group of one row with the carboxylate oxygen

of the adjacent row (as shown in Figure 9-13 in green dotted lines).
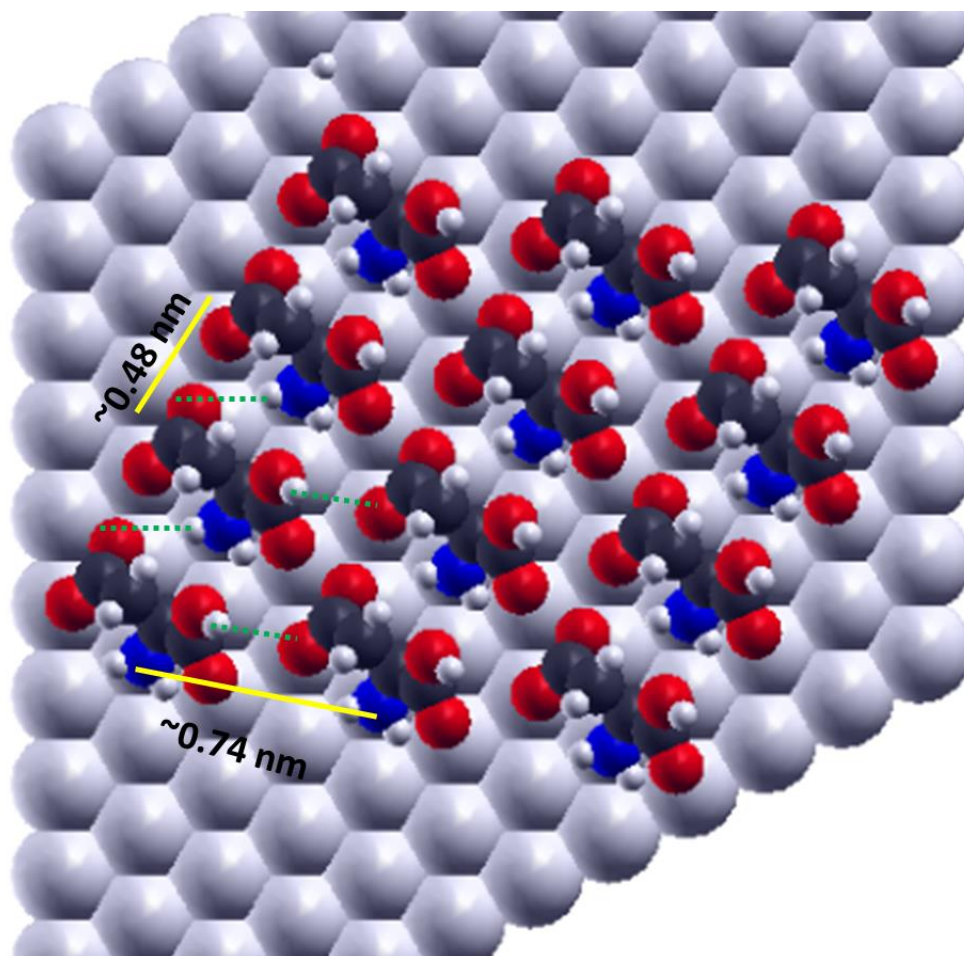
Figure 9-13 A proposed model for the experimentally observed linear row domain

Nevertheless, both types of observed ordered domains are formed due to the

hydrogen-bonding interactions between the monoaspartate species. The honeycomb motif

consists of aspartate zig zag rows and the linear row domains comprise aspartate linear

rows running parallel to each other. In both the cases, within the rows, hydrogen-bonding

interactions occur between the β-carboxylate and the –NH$_2$ group of two neighboring

aspartate species, while the α-carboxylic acid group remains protonated, which hydrogen

bond weakly with the carboxylate oxygen atom of the neighboring row, thus driving the

assembly.

The RAIRS spectra obtained by dosing at room temperature also show the presence of monoaspartate species. In addition to features due to monoaspartate species, two shoulders are observed at a higher frequencies (1761 and ~1743 cm^{-1}), which are assigned to the C=O stretching vibration of the cyclic imide structure, which was not present in the low-temperature spectra. STM images collected following dosing at ~300 K shows different surface structures than those collected at 120 K. The formation of a network structure, which contains pores of different sizes, might indicate the formation of oligosuccinimide rings. The 1600 cm^{-1} peak was much broader at low temperature due to the contribution from the δ_{as} NH$_3^+$ mode, which is usually observed at 1650 cm^{-1}. At room temperature, the 1650 cm^{-1} peak is only present at higher exposures and is very weak in comparison with the spectra collected at 100 K. This strongly indicates that the ratio of zwitterion to anion is very low at room temperature in comparison to low temperatures. Thus, it is likely that the presence of zwitterionic aspartate species is the key driving force for the formation of ordered domains observed in the low temperature STM images. A thorough investigation by XPS is needed to understand the chemical nature of the aspartic acid on a Pd(111) surface which is yet to be explored. DFT calculations are ongoing to characterize different surface structures observed at 120 K and 300 K.

Broadly speaking, the aspartic acid adsorption geometry on Pd(111) resembles that of alanine, where the adsorption to the surface is dominated by the carboxylate and amine groups while in the case of tartaric acid, the absence of amine group forces adsorption to occur either through one or two carboxylate groups. At low temperatures,

the aspartic acid monolayer consists of aspartate species which self-assemble to form hexamers which order in a honeycomb pattern. The pores of the hexamers may provide chiral templates for the adsorption of a suitable chiral-probe molecule. However, the size of the pore (~1 nm) is too large to use propylene oxide or glycidol as chiral probe molecules. DFT modelling is ongoing to help identify a suitable probe molecule. At room temperature the aspartate monolayer forms a complex network by forming pores of different size possibly due to the formation of oligosuccinimide rings.

9.5   Conclusions

Aspartic acid predominantly forms monoaspartate species at low temperatures, which self-organize through hydrogen-bonding interactions, to form ordered honeycomb islands or linear-row structures. At 300 K, the surface consists of both monoaspartate species and oligosuccinimide clusters. DFT calculations predict that the monoaspartate species bonds to the Pd(111) surface through carboxylate oxygen and nitrogen atoms, similar to the adsorption geometry of alanine on Pd(111). Different adlayers form by the self-assembly of aspartic-acid-derived structures will provide different docking sites for an incoming chiral probe molecule. The pores formed in the honeycomb motif are ideal candidates for chiral templating

9.6   References

1.   Mahapatra, M.; Burkholder, L.; Devarajan, S. P.; Boscoboinik, A.; Garvey, M.; Bai, Y.; Tysoe, W. T., Formation of Induced-Fit Chiral Templates by Amino Acid-Functionalized Pd (111) Surfaces. *The Journal of Physical Chemistry C* **2015,** *119* (7), 3556-3563.

2.   Mahapatra, M.; Burkholder, L.; Bai, Y.; Garvey, M.; Boscoboinik, J. A.; Hirschmugl, C.; Tysoe, W. T., Formation of Chiral Self-Assembled Structures of Amino

Acids on Transition-Metal Surfaces: Alanine on Pd (111). *The Journal of Physical Chemistry C* **2014,** *118* (13), 6856-6865.

3.   Mahapatra, M.; Tysoe, W., Chemisorptive Enantioselectivity of Chiral Epoxides on Tartaric-acid Modified Pd (111); Three-Point Bonding. *Physical Chemistry Chemical Physics* **2015**.

4.   Izumi, Y., Modified raney nickel (MRNi) catalyst: Heterogeneous enantio-differentiating (asymmetric) catalyst. *Advances in catalysis* **1983,** *32*, 215-271.

5.   Webb, G.; Wells, P., Asymmetric hydrogenation. *Catalysis today* **1992,** *12* (2), 319-337.

6.   Wilson, K. E.; Baddeley, C. J., Understanding the Surface Chemistry of Enantioselective Heterogeneous Reactions: Influence of Modification Variables on the Interaction of Methylacetoacetate with (S)-Aspartic Acid Modified Ni {111}. *The Journal of Physical Chemistry C* **2009,** *113* (24), 10706-10711.

7.   Jonsson, C. M.; Jonsson, C. L.; Estrada, C.; Sverjensky, D. A.; Cleaves, H. J.; Hazen, R. M., Adsorption of L-aspartate to rutile (α-TiO 2): experimental and theoretical surface complexation studies. *Geochimica et Cosmochimica Acta* **2010,** *74* (8), 2356-2367.

8.   Trant, A. G.; Baddeley, C. J., Surface Chemistry Underpinning Enantioselective Heterogeneous Catalysis: Supramolecular Self-Assembly of Chiral Modifiers and Pro-Chiral Reagents on Ni {111}†. *The Journal of Physical Chemistry C* **2010,** *115* (4), 1025-1030.

9.   Baddeley, C. J.; Jones, T. E.; Trant, A. G.; Wilson, K. E., Fundamental investigations of enantioselective heterogeneous catalysis. *Topics in catalysis* **2011,** *54* (19-20), 1348-1356.

10.   Wilson, K.; Trant, A.; Baddeley, C., Interaction of the Pro-Chiral Molecule, Methylacetoacetate, with (S)-Aspartic Acid Modified Ni {111}. *The Journal of Physical Chemistry C* **2011,** *116* (1), 1092-1098.

11.   Guo, Y.-n.; Lu, X.; Zhang, H.-p.; Weng, J.; Watari, F.; Leng, Y., DFT Study of the Adsorption of Aspartic Acid on Pure, N-Doped, and Ca-Doped Rutile (110) Surfaces. *The Journal of Physical Chemistry C* **2011,** *115* (38), 18572-18581.

12.   Greiner, E.; Kumar, K.; Sumit, M.; Giuffre, A.; Zhao, W.; Pedersen, J.; Sahai, N.,

Adsorption of l-glutamic acid and l-aspartic acid to γ-Al 2 O 3. *Geochimica et Cosmochimica Acta* **2014,** *133*, 142-155.

13.   James, J.; Saldin, D. K.; Zheng, T.; Tysoe, W.; Sholl, D. S., Structure and binding site of acetate on Pd (111) determined using density functional theory and low energy electron diffraction. *Catalysis today* **2005,** *105* (1), 74-77.

14.   Zheng, T.; Stacchiola, D.; Saldin, D.; James, J.; Sholl, D.; Tysoe, W., The structure of formate species on Pd (111) calculated by density functional theory and determined using low energy electron diffraction. *Surface science* **2005,** *574* (2), 166-174.

15.   Williams, J.; Haq, S.; Raval, R., The bonding and orientation of the amino acid L-alanine on Cu {110} determined by RAIRS. *Surface science* **1996,** *368* (1), 303-309.

Chapter 10

Enhanced Hydrogenation Activity and Diastereomeric Interactions of Methyl Pyruvate Co-adsorbed with R-1-(1-Naphthylethylamine) on Pd(111)

10.1 Introduction

One of the most successful examples in heterogeneous enantioselective catalysis is hydrogenation of α-ketoesters, for example, hydrogenation of methyl pyruvate (MP) to methyl lactate on cinchona-modified platinum catalysts.[1-14] While conceptually simple, there are significant challenges associated with modifying an extended surface: it is straightforward to chirally modify all of the reaction centers of an organometallic compound, but it is difficult to precisely adjust the chiral modifier coverage in the heterogeneous phase to modify all of the reaction centers. However, it has been found that hydrogenation rates are substantially increased on chirally modified catalysts compared to their unmodified counterparts[6, 12, 14-16] thereby enhancing the effect of the diastereomeric interaction to produce enantiomeric excesses approaching 100%. This effect provides a potential solution to a central problem in designing heterogeneous chiral catalysts, but the origin of this rate enhancement is not well understood.

In order to understand the diastereomeric interactions of MP with chiral modifiers and to investigate the origins of the enhanced hydrogenation activity, experiments are performed on a model Pd(111) single crystal catalyst surface using R-1-(1-naphthyl)ethylamine (NEA) as a chiral modifier since the cinchona alkaloids are difficult to introduce into vacuum. NEA shares the key functional aspects of cinchonidine and has

been used as a model chiral modifier,[17-21] where both *endo* and *exo* conformers have been identified.[20] NEA has been found to be randomly distributed on both Pd and Pt surfaces implying that NEA molecules act individually to provide a chiral reaction site.[19-20] The chemistry of the simplest α-ketoester, methyl pyruvate (MP) has been explored on several transition-metal surfaces [22-27]where it exists as both the *enol* and *keto* tautomer.[25, 27] MP tends to agglomerate on platinum, the most commonly used catalyst for the enantioselective hydrogenation of MP,[28] making it difficult to identify docking complexes between MP and NEA on this surface. MP interacts to a lesser extent on Pd(111), thereby optimizing the possibility of observing interactions between MP and NEA.

The nature of the docking complexes formed between prochiral MP and the chiral modifier NEA is explored using scanning tunneling microscopy (STM) complemented by first-principles density functional theory (DFT) calculations and image simulations, similar to previous approaches to understand chirality transfer on platinum substrates.[24, 28-31] Temperature-programmed desorption (TPD) experiments of MP+NEA on Pd(111) performed by another member of the Tysoe group reveal that co-adsorbed NEA enhances the MP hydrogenation rate. Since C=C double bond hydrogenation is significantly more facile than C=O hydrogenation,[32] the docking complex formed between the enol form of methyl pyruvate and NEA provides a plausible explanation for the enhanced hydrogenation rate found on chirally modified catalysts which will be described in this chapter.

10.2 Experimental and Theoretical Methods

The Pd(111) substrate was cleaned using a standard procedure consisting of cycles of argon ion sputtering and annealing in 3×10^{-8} Torr of oxygen at 1000 K. STM images were acquired at a sample temperature of ~120 K using an electrochemically etched tip made from recrystallized tungsten wire. This was conditioned by a controlled interaction with a clean Au(111) single crystal surface, likely resulting in a gold-terminated tip.[33] Experiments were performed using a scanning tunneling microscope housed in an ultrahigh vacuum (UHV) chamber.[34] TPD data were collected in another chamber operating at a base pressure of 8×10^{-11} Torr, using a linear heating rate of 2.5 K/s, where desorbing species were monitored using a Dycore quadrupole mass spectrometer placed close to and in line of site of the sample.

(*S*)-(-)-α-(1-naphthyl)ethylamine (Acros Organics, 99% purity) was dosed from a home-built Knudsen source.[35] Because of the high vapor pressure of NEA, the Knudsen source was cooled to ~200 K for at least 60 min before dosing. Methyl pyruvate (Alfa Aesar, 98% purity) was purified by several freeze-pump-thaw cycles. After dosing NEA, the sample was cooled to ~120 K and held at that temperature for all imaging. Methyl pyruvate was dosed onto the Pd(111) surface through a variable leak valve while maintaining a sample temperature of ~120 K.

Density functional theory (DFT) calculations were performed with the projector augmented wave (PAW) method [36-37] as implemented in VASP.[38-40] The exchange-correlation potential was described using the generalized gradient approximation (GGA) of Perdew, Burke and Ernzerhof [41] and hydrogen bonding interactions are reasonably well reproduced (within ~ 4 kJ/mol) using this functional, although the accuracy

deteriorates as the hydrogen bonds deviate from linear.[42] A cutoff of 400 eV was used for the planewave basis set, and the wavefunctions and electron density were converged to within 1×10^{-5} eV. The first Brillouin zone was sampled with a 3×3×1 Γ-centered k-point mesh. Geometric relaxations were considered to be converged when the force was less than 0.02 eV/Å on all unrestricted atoms. Van der Waals corrections were included by using the method of Tkatchenko and Scheffler (TS).[43]

STM topography simulations were performed with the Tersoff-Hamman [44-45] approach as implemented in bSKAN 3.7, which has been found to reproduce the shapes of STM images for methyl pyruvate on Pd(111) [27] as well as the more rigorous Bardeen approach.[46-47].

10.3 Results

The current STM study of coadsorbed MP and NEA is motivated by the background experiments performed by Luke Burkholder [59] to explore the effect of NEA on the hydrogenation activity of MP on palladium which is shown in Figure 10-1. A Pd(111) surface was dosed with various coverages of NEA, following which [48] the surface was dosed with hydrogen (3 L (1L (Langmuir) = 1×10^{-6} Torr s) exposure), and then saturated with methyl pyruvate and TPD experiments were carried out. The resulting 45 amu signals, the most intense fragment of methyl lactate, the hydrogenation product (assigned to the CH_3–CH–OH^+ mass spectrometer ionizer fragment), as a function of sample temperature are displayed in Figure 10-1, for various NEA coverages. 43 amu is the most intense mass spectrometer fragment of MP (from the CH_3–C=O^+ fragment), with a small signal at 45 amu (~2% of the 43 amu signal). This fragment produces a

signal centered at ~170 K due to the desorption of a small amount of condensed MP, confirming that the surface has been saturated.[26]
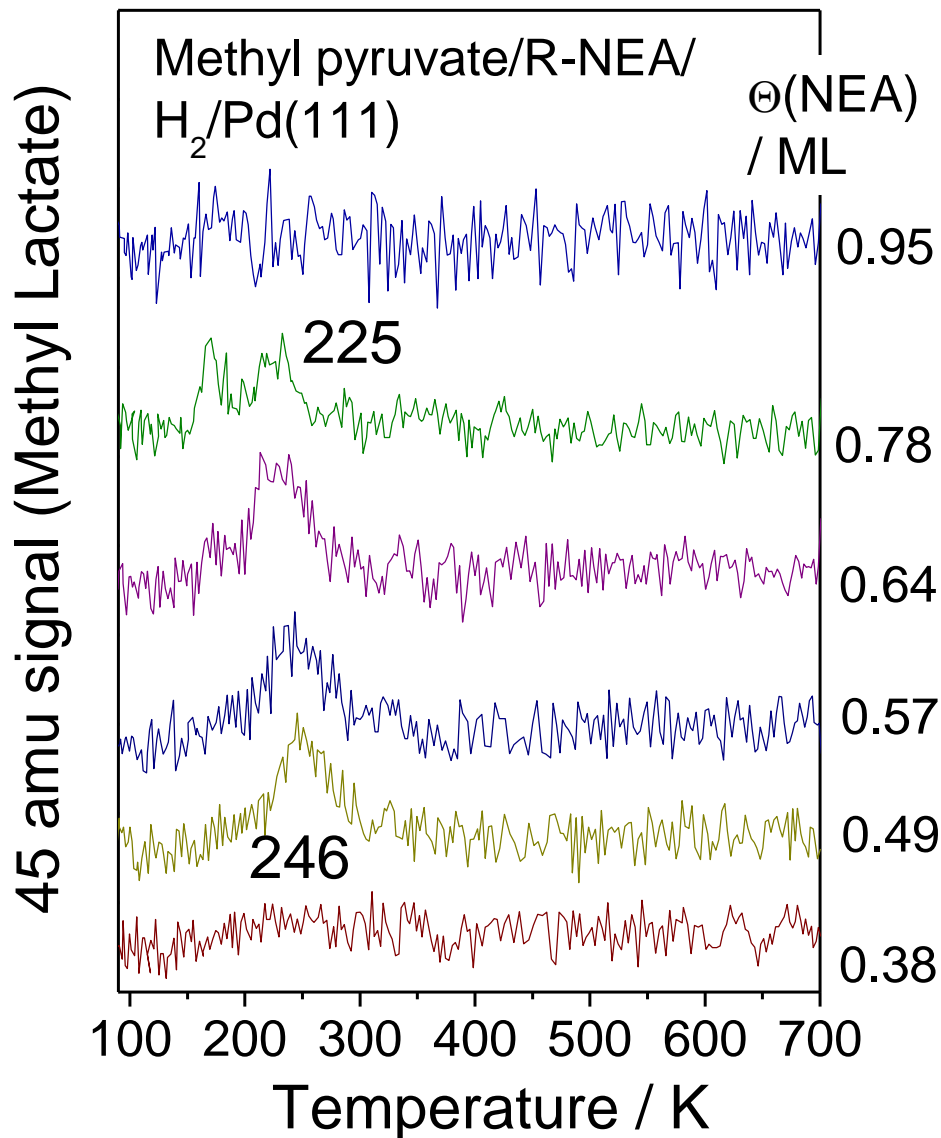
Figure 10-1 45 amu (methyl lactate) TPD profiles collected following the adsorption of 3 L of methyl pyruvate on a Pd(111) surface precovered with NEA and saturated with hydrogen as a function of NEA coverage. (Image reproduced with permission from Luke Burkholder's PhD Thesis 2009 ©) [59]

However, a clear methyl lactate desorption peak is evident, centered at ~246 K for a R-NEA coverage of 0.45 ML, decreasing to ~225 K at higher R-NEA coverages. No

methyl lactate is detected for NEA coverages of 0.38 ML and lower (data not shown), but the methyl lactate yield increases with increasing R-NEA coverage demonstrating that rapid hydrogenation occurs for R-NEA coverages between ~0.6 and 0.8 ML. The hydrogenation yield decreases to zero once again at the highest NEA coverage as MP adsorption is blocked (data not shown). This result indicates that the presence of NEA on the surface enhances the hydrogenation activity of the Pd(111) surface, analogous to the effects seen under catalytic conditions. As mentioned before both keto and enol forms of methyl pyruvate are observed on the Pd(111) surface. To understand the hydrogenation mechanism and nature of the species which hydrogenates, additional experiments are carried out by adsorbing ethylene and hydrogen onto a Pd(111) surface and the results are summarized in Figure 10-2.

In Figure 10-2 (a) 2 L of ethylene is dosed to a Pd(111) surface precovered with hydrogen. A small amount of ethane is produced due to hydrogenation of ethylene which is evidenced by a peak observed at ~250 K for (30 amu). In Figure 10-2 (b) deuterium was used instead of hydrogen and the TPD profiles indicate that ethylene has undergone substantial hydrogen-deuterium exchange. The extent of deuterated ethane formation, as indicated by the 33 amu profile (d_3-ethane) is very small. The proportion of H-D exchange is indicated in Table 10-1 using standard mass spectrometer fragmentation patterns
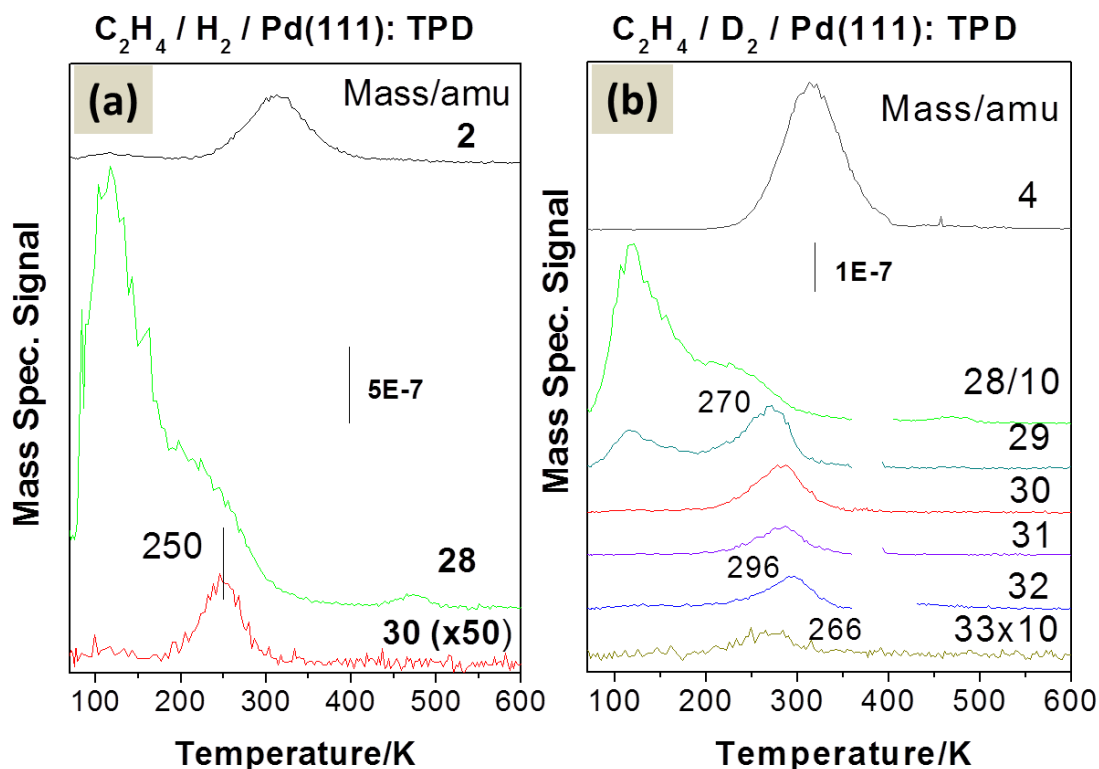
Figure 10-2 Temperature-programmed desorption of ethylene on (a) hydrogen- and (b) deuterium-covered Pd(111). Spectra were collected after dosing of 2 L of C_2H_4 adsorbed onto a (a) hydrogen (2 L) or (b) deuterium (2 L) pre-covered Pd(111) surface at 80 K collected using a heating rate of 3 K/s, monitoring various masses, indicated adjacent to the corresponding spectrum

Deuterated ethylene	Proportion %
C_2H_3D	35
$C_2H_2D_2$	16
C_2HD_3	24
C_2D_4	25

Table 10-1 Proportion of deuterated ethylene isotopomers from reaction of C_2H_4 on deuterium-covered Pd(111)

The similarity between the methyl lactate formation temperature (between ~225 and 246 K) and that for ethylene hydrogenation on Pd(111) (~250 K,[49-50] Figure 10-2) is

consistent with methyl lactate being formed by hydrogenation of a C=C double bond.

The presence of a C=C double bond implies that MP has undergone a *keto-enol*

tautomerization. In order to explore this in greater detail, since H/D exchange is rapid for

ethylene on group VIII transition metals [51] including Pd(111) (Figure 10-2 (b)), TPD

experiments were carried out for MP co-adsorbed with deuterium on NEA-precovered

Pd(111).
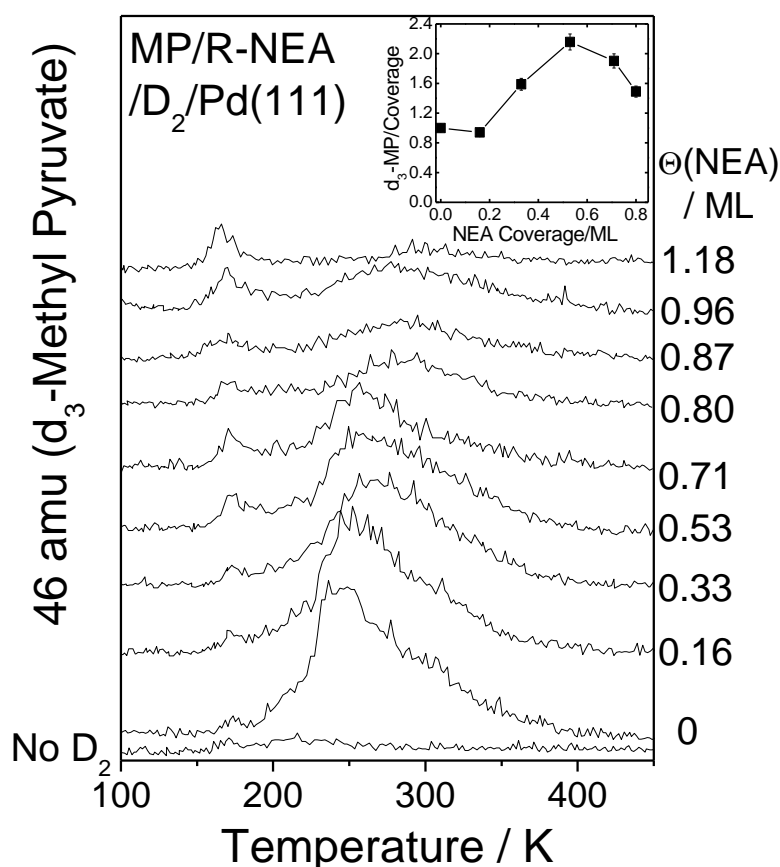
Figure 10-3 46 amu (d_3-methyl pyruvate) TPD profiles collected following the adsorption of 3 L of methyl lactate on a Pd(111) surface precovered with NEA and saturated with deuterium as a function of NEA coverage. (Image reproduced with permission of Luke Burkholder's PhD Thesis 2009 ©) [59]

The resulting 46 amu (d_3-MP) desorption profiles are shown in Figure 10-3 for

various NEA coverages. The presence of deuterated MP indicates that it has undergone

substantial H/D exchange, providing clear evidence for the participation of the *enol* form of MP in the reaction. No 46 amu signal is detected in the absence of deuterium (Bottom profile, Figure 10-3), but H/D exchange occurs even in the absence of NEA (Θ(NEA)=0), consistent with the detection of the *enol* tautomer on clean Pd(111).[27] The inset to Figure 10-3 plots the integrated areas of the 46 amu (d_3-MP) signals ratioed to the MP coverages, measured from the 43 amu TPD profiles collected in the same experiment. This ratio increases over the same NEA coverage range as which enhanced MP hydrogenation is observed.

STM images of co-adsorbed NEA and MP on Pd(111) were collected at a sample temperature of ~120 K by first exposing the surface to *R*-NEA followed by MP. Figure 10-4 shows a typical STM image of a 7×10 nm scan area where the close-packed $< 1\bar{1}0 >$ directions of the underlying Pd(111) lattice, obtained by scanning the clean surface, are shown. While there is some clustering of the NEA on the surface, isolated docking complexes can be discerned, and are circled in Figure 10-4. The docking complexes, once formed are stable and can be imaged for multiple scans. Statistical analyses were performed for multiple images for over 100 distinct and clearly identifiable complexes. Other complexes could have been identified on more crowded regions of the surface, but were not included in the statistical analysis because of the difficulty in unequivocally distinguishing a MP pyruvate molecule from an adjacent naphthyl ring.
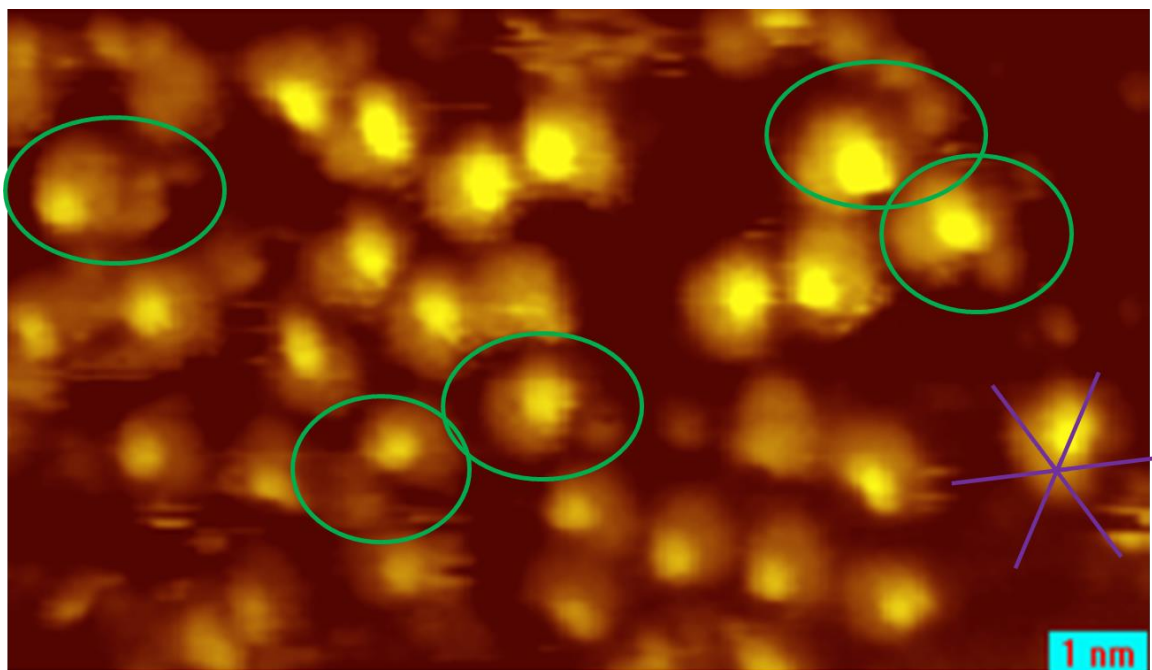
Figure 10-4 A typical STM image of a 7×10 nm scan area of co-adsorbed S-NEA and MP on Pd(111) at 120 K. The close-packed $< 1\bar{1}0 >$ directions of the underlying Pd(111) lattice obtained by scanning the clean surface are shown. Isolated docking complexes are identified and highlighted by ovals.

Two types of clearly discernible docking complexes could be identified. An image of the first, is shown in Figure 10-5A. Here the NEA is clearly visible showing a bright protrusion due to the chiral ethylamine group, and a more diffuse region due to the naphthyl ring. A MP molecule is shown located adjacent to the chiral center on NEA where, in this example, the angle between the long axes of the naphthyl ring on NEA and MP is ~12°. The uncertainly in accurately defining vectors along the parts of the images due to the naphthyl group of NEA and the MP molecule leads to a reasonably large range of angles between 5 and 20° for this complex. A second complex is shown in Figure 10-5B. This again exhibits bright regions due to the ethylamine group and naphthyl ring with an adjacent MP molecule. In this example of the docking complex, the angle between the long axis of the napthyl group and the MP molecule is ~63°. Again difficulties in precisely defining vectors along the naphthyl group and MP molecules leads to a range of

angle between 45 and 65° for this docking complex. In both cases, docking occurred

exclusively with the *exo* isomer of NEA. Statistical analyses showed that structure A

comprised ~44% of the complexes and structure B ~50%. In a very few cases (~6%), two

MP molecules were found adjacent to the NEA as shown in Figure 10-5 C. Majority of

the experimentally observed docking complexes are formed with the *exo* rotamer of

NEA, while only 9 % accounts for *endo* NEA.
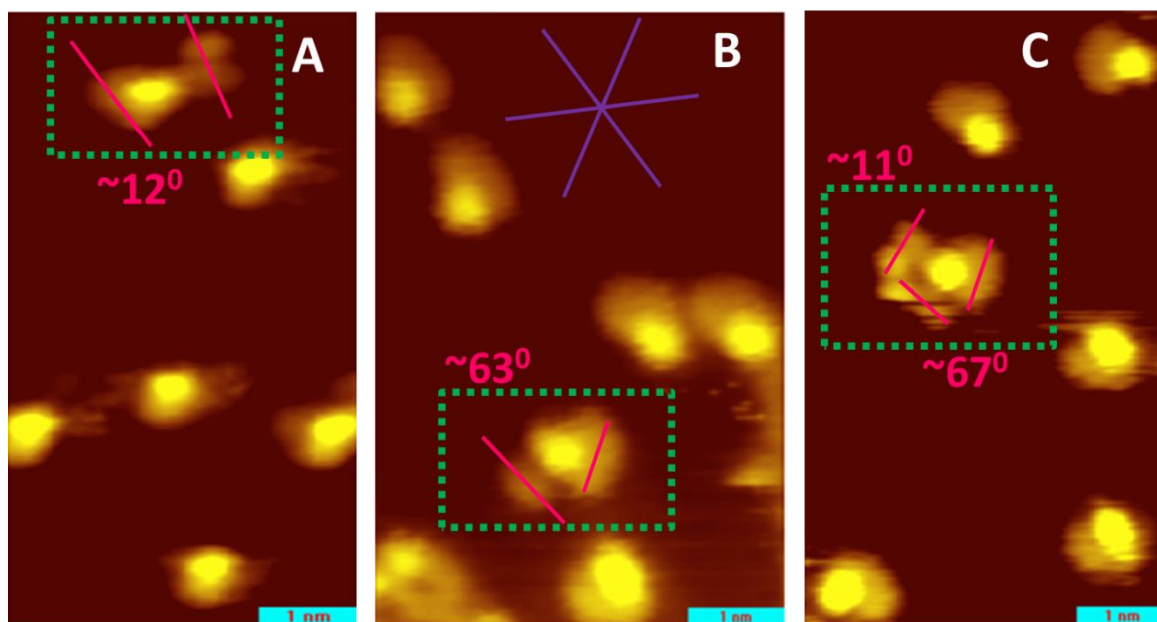
Figure 10-5 High resolution images of the docking complexes identified from co-adsorbed S-NEA and MP on Pd(111) at 120 K of with structures A and B , and an example of an S-NEA molecule with two methyl pyruvate molecules is shown in C. The measured angles between the methyl pyruvate and the naphthyl ring of the *S*-NEA are indicated

The STM results are limited by the coverage of both NEA and methyl pyruvate.

Enhanced hydrogenation reaction was observed when NEA coverage was in the range of

0.5 to 0.8 ML. However, STM experiments are carried out at lower coverages so that the

docking complexes can be identified clearly. When experiments are carried out by dosing

high coverages of methyl pyruvate, it formed clusters and identification of docking

complex inside the clusters was not possible. An example is shown in Figure 10-6.
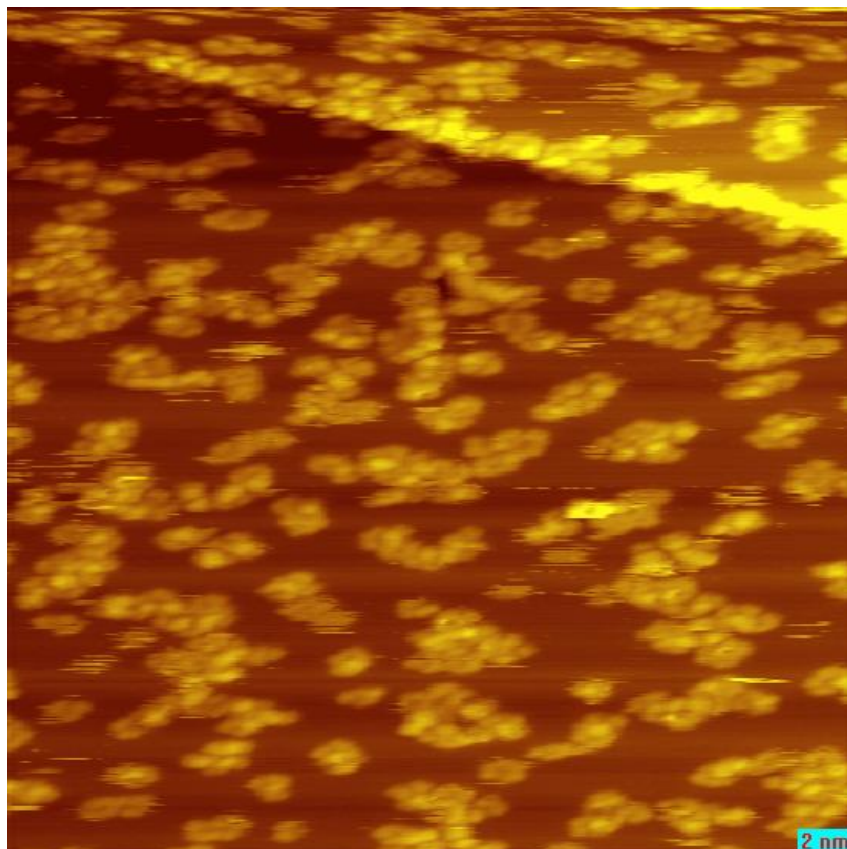
Figure 10-6 A STM image of co-adsorbed MP and NEA; at higher coverages, methyl pyruvate form clusters and identification of docking complexes inside the cluster was not possible

10.4 Discussion

The results indicate that MP forms one-to-one docking complexes with NEA and

that the MP can hydrogenate more easily to methyl lactate on NEA-modified than clean

Pd(111). The enhanced hydrogenation rate correlates with a larger extent of H/D

exchange. This suggests that the more easily hydrogenated *enol* tautomer preferentially

forms one-to-one docking complexes with NEA. In order to understand this behavior, the

docking of the *enol* and *keto* tautomers of MP with *R*-NEA was investigated using DFT

for both the *endo* and *exo* configurations by constructing isolated 1:1 complexes of all four combinations, with MP adsorption constrained to be proximate to the chiral ethylamine center on *R*-NEA. Previous DFT calculations found that NEA adsorbs with the naphthyl ring located on the dibridge[7] adsorption site on Pd(111) with almost isoenergetic *exo* and *endo* rotamers.[21] However, NEA was found to adsorb on the dibridge[6] site on Pt(111).[28] Calculations for NEA on the dibridge[6] site on Pd(111) reveal that the *exo* form is ~20 kJ/mol more stable on dibridge[6] than on the dibridge[7] site, and that the *endo* conformer is ~11 kJ/mol more stable. Thus, the *exo* form of NEA is more stable than the *endo* form on the Pd(111) dibridge[6] site. Similar energetic differences were found for the dibridge[6] site on Pt(111).[28] However, STM images of NEA on Pd(111) reveal that the *exo* conformer occurs only slightly more often than the *endo* conformer (with a ratio of 6:4), with a corresponding ratio of 7:3 on Pt(111). LEED experiments are ongoing to identify the adsorption site of NEA on a Pd(111) surface.

Initial DFT calculations were performed using NEA on dibridge[7] adsorption sites on Pd(111), without including van der Waals' interaction and the results are summarized in the appendix. The DFT results reveal that all complexes involving *keto* methyl pyruvate are repulsive, while only those containing both the *R-exo* rotamer of NEA and the *enol* tautomer of MP have stable configurations. Including van der Waals' interactions for the two most stable structures increased the interaction energy by ~10 kJ/mol, but did not influence the relative energies. The most stable docking complexes are shown in Figure 10-7, where structure **A**, with an interaction energy of 16 kJ/mol, , and structure **B**, with an interaction energy of 17.3 kJ/mol. Interestingly the interaction energies on Pd(111) are lower than for calculations for complexes between fluorinated

MP and NEA on Pt(111).[52] This is reflected in the temperatures at which the experiments were carried out where docking complexes were imaged at ~300 K on Pt(111), while on Pd(111), cooling to ~120 K was required to stabilize the complexes.
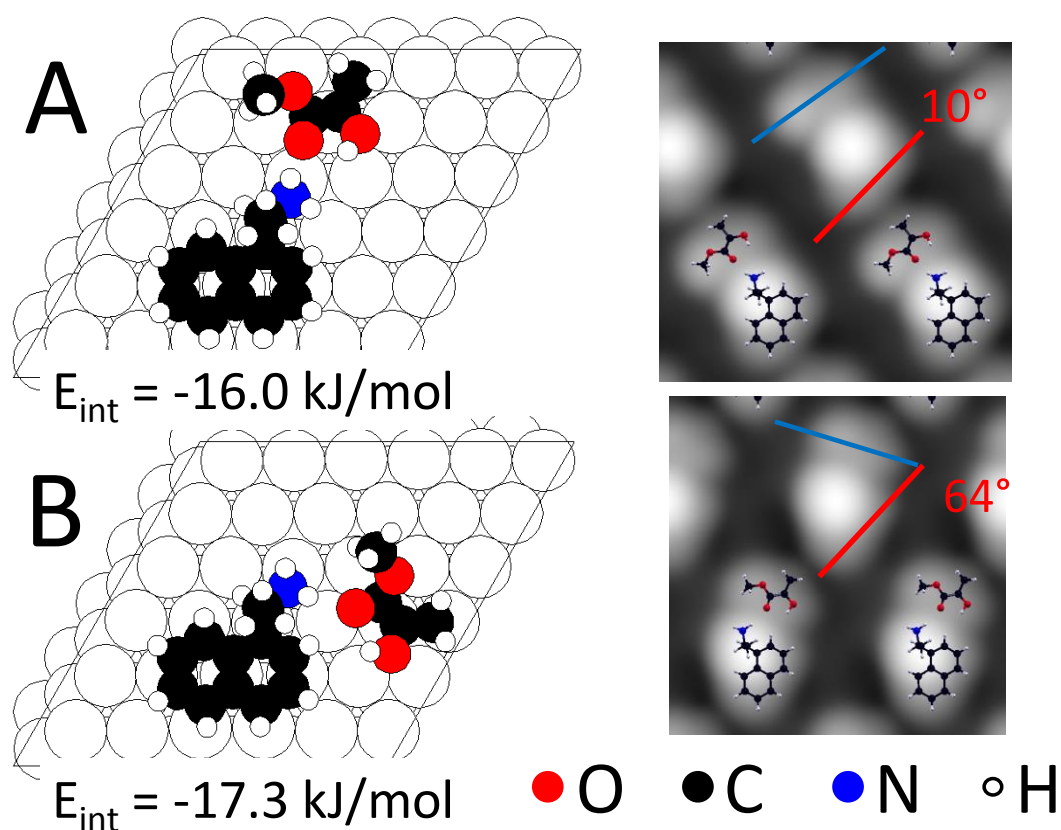
Figure 10-7 Structures of the two most stable docking complexes formed from NEA adsorbed on the dibridge[7] site, indicated as A (top structure) and B (bottom structure). The interaction energies calculated including van der Waals' interactions are shown below each structure. The STM images simulated by the Tersoff-Hamman method are shown adjacent to each structure. The angles between the axis in the simulated images of the *enol* tautomer of MP, indicated by a blue line, and the long axis of the naphthyl group of *R*-NEA, indicated by a red line, are also indicated.

DFT calculations for NEA adsorbed on the dibridge[6] site is currently under investigation and some initial results are also shown in the appendix. Figure 10-7 also displays the simulated STM images obtained using the Tersoff-Hamman approach, which has been shown to accurately reproduce both the experimental images and the

simulations obtained using the Bardeen method for MP on Pd(111).[27] The simulations are in good agreement with the experimental images of the docking complexes; the simulated image in Figure 10-7A is in good agreement with the experimental image in Figure 10-5A, and the simulation in Figure 10-7B agrees well with the experimental image in Figure 10-5B. The calculated relative proportions, assuming a Boltzmann distribution show that complex **A** should comprise ~21%, and complex **B**, ~79% of the structures, whereas experimentally observed percentage are 44% and 50% respectively. But as mentioned before, the statistical analysis of docking complexes may have suffered from not being able to identify a large proportion of the docking complexes present within the MP clusters. A very small portion of the observed docking complex consists of endo conformer of NEA which agrees with the small interaction energy calculated by DFT (Appendix).

Both docking complex involve the *exo* form of *R*-NEA interacting with the *enol* tautomer of MP, consistent with the H/D exchange and hydrogenation experiments. *Enol*-MP is constrained to be in the *cis* form in both complexes as found previously on Pd(111),[27] with the C=C double bond located at Pd–Pd bridge sites. The methylene hydrogens are distorted from a planar geometry in both structures due to rehybridization of the double bond as found for ethylene on Pd(111).[53] The docking between *R*-NEA and MP is dominated by C=O$\cdots$H$_2$N hydrogen-bonding interactions, where the two stable structures interact with an amino hydrogen, and the amine group is bound to palladium through the nitrogen lone pair. The docking complexes form by optimizing the amine-carbonyl–hydrogen-bonding interaction while simultaneously allowing binding of the vinyl group to the most stable palladium bridge sites.

It has been shown previously that NEA is disordered on transition-metal surfaces [19-20] consistent with it forming one-to-one docking complexes. A combination of STM imaging and DFT calculations show preferential diastereomeric docking between the *enol* tautomer of methyl pyruvate with *R-exo* NEA, with interaction energies of ~16 to 17 kJ/mol, while the interaction with the *keto* tautomer is found to be repulsive. The binding of the *enol* in the stable complexes allow simultaneous binding of the vinyl group to the most stable palladium bridge sites, as found for di-σ bonded ethylene, along with stabilizing hydrogen-bonding interactions between the carbonyl and amine groups in the *exo* rotamer of NEA that is not available in the *endo* structure (Appendix). Both are pro-*R* structures on *R*-NEA-functionalized surfaces.

Interestingly, the fluorinated *keto* analog of MP, methyl 3,3,3-trifluoropyruvate (MTFP), where *enol* formation is suppressed to avoid chain formation,[25, 54] interacts strongly (with energies between -52 to -62 kJ/mol) with NEA on Pt(111),[52] emphasizing the importance of the substrate in controlling complexation, where complexes are measured at ~300 K on platinum, but at lower temperatures on palladium.

The stabilization of the *enol* tautomer results in the formation of a C=C double bond that hydrogenates more easily than does a carbonyl group, resulting in enhanced hydrogenation on NEA-modified Pd(111) (Figure 10-1). The participation of *enol-keto* tautomerization is corroborated by the enhancement of H-D exchange on Pd(111) in the presence of NEA (Figure 10-3). This process also occurs on Pd(111) in the absence of co-adsorbed NEA, but the proportion of MP undergoing complete methyl group exchange increases on NEA-modified Pd(111). Thus, while sufficient *enol* is present on Pd(111) at low NEA coverages to undergo extensive H/D exchange, it does not hydrogenate to

methyl lactate. Ethylene hydrogenates on transition-metal surfaces, including palladium, by a sequential addition of atomic hydrogen, the Horiuti-Polanyi mechanism.[55] H/D exchange occurs through the half-hydrogenated ethyl intermediate, which repeatedly undergoes β-hydride elimination to incorporate deuterium. Ethane is formed by hydrogenation of the ethyl species. The enhancement of H/D exchange in MP can be ascribed to its stabilization by interacting with NEA, but the enhanced methyl lactate formation indicates that the half-hydrogenated MP is also stabilized. Hydrogenation of the methylene group would form a half-hydrogenated species that maintains the $C=O\cdots H_2N$ hydrogen-bonding interaction that could stabilize this state.

The proposed binding motif obeys the three-point bonding rule obeyed in biological system such as enzymes.[56-57] Here, three-point binding occurs between the vinyl group carbons that preferentially bind to atop sites on Pd(111), and the $C=O\cdots H_2N$ hydrogen-bonding interaction between the *enol* MP tautomer and the nitrogen on the chiral center. Three-point binding has also been observed between *R*-glycidol and *S,S*-bitartrate on Pd(111),[58] which were found to interact by a simultaneous hydrogen donation from the CH_2-OH group to the carboxylate, and a hydrogen acceptor interaction between the CH_2-OH group and a hydroxyl group of the bitartrate. Thus, in the NEA-MP interaction, two of the three bonds are to the surface and one with the modifier, while in the glycidol-bitatrtate system, glycidol binds to the surface through the epoxide oxygen to an atop palladium sites, with two stereodirecting interactions with the modifier. Chemisorption energies to surfaces are typically stronger than hydrogen-bonding interactions, and thus surface bonding dictates the most stable locations of both the chiral modifier and chiral species or prochiral reactants. The most energetically stable

interactions between a chiral modifier with a chiral probe (as in the case of glycidol) or a prochiral reactant (in the case of methyl pyruvate) appear to be predominantly influenced by the way in which their binding location on the surface controls the stereochemistry of the weaker hydrogen-bonding interactions between them. Such a molecular-level understanding of the chiral and diastereomeric interactions with chiral modifiers will eventually lead to the rational design of heterogeneous chiral catalysts.

10.5 Conclusion

Two stable docking complexes are found to form between the *enol* tautomer of MP and the *R-exo* rotamer of NEA, predicted both by first-principles DFT calculations and also confirmed by comparing experimental STM images with Tersoff-Hamman simulations of the calculated structures. The formation of the complexes is dictated by the surface ensemble requirements of the binding of the carbon-carbon double bond to the surface with $C=O\cdots H_2N$ hydrogen-bonding interactions that stabilize the *enol* tautomer in a pro-*R* configuration on an *R*-NEA-modified surface. The stabilization of the *enol* tautomer results in enhanced hydrogenation of the *enol* MP to methyl lactate. The combination of chiral-NEA driven diastereomeric docking with a tautomeric preference causes an enhancement in the hydrogenation activity that will lead to increase enantiomeric excesses in the catalytic reaction for chirally modified surface, as found experimentally. While this model structure provides a rationale for the catalytic observations, although care must be taken in directly transferring observations made for model systems in ultrahigh vacuum to supported catalysts operating in more severe environments.

10.6 References

1.   Orito, Y.; Imai, S.; Niwa, S., Asymmetric hydrogenation of a-keto esters using a platinum-alumina catalyst modified with cinchona alkaloid. *J. Chem. Soc. Jpn.* **1980,** (4), 670-2.

2.   Meheux, P. A.; Ibbotson, A.; Wells, P. B., Enantioselective hydrogenation. II. Variation of activity and optical yield with experimental variables in methyl pyruvate hydrogenation catalyzed by cinchona-modified platinum/silica (EUROPT-1). *J. Catal.* **1991,** *128* (2), 387-96.

3.   Blaser, H. U.; Jalett, H. P.; Muller, M.; Studer, M., Enantioselective hydrogenation of alpha-ketoesters using cinchona modified platinum catalysts and related systems: A review. *Catalysis Today* **1997,** *37* (4), 441-463.

4.   Pfaltz, A.; Heinz, T., Enantioselective Hydrogenation of Ethyl Pyruvate over Pt/Alumina - Systematic Variation of the Modifier Structure. *Topics in Catalysis* **1997,** *4* (3), 229-239.

5.   LeBlond, C.; Wang, J.; Andrews, A. T.; Sun, Y.-K., Establishment and maintenance of an optimal chiral surface in cinchona-modified 1% Pt/Al_2O_3 for enantioselective hydrogenation of □-keto esters. *Top. Catal.* **2000,** *13* (3), 169-174.

6.   Blaser, H. U.; Jalett, H. P.; Lottenbach, W.; Studer, M., Heterogeneous Enantioselective Hydrogenation of Ethyl Pyruvate Catalyzed by Cinchona-Modified Pt Catalysts: Effect of Modifier Structure. *J. Am. Chem. Soc.* **2000,** *122* (51), 12675-12682.

7.   Kacprzak, K.; Gawroński, J., Cinchona Alkaloids and Their Derivatives: Versatile Catalysts and Ligands in Asymmetric Synthesis. *Synthesis* **2001,** (07), 0961-0998.

8.   Vayner, G.; Houk, K. N.; Sun, Y.-K., Origins of enantioselectivity in reductions of ketones on cinchona alkaloid modified platinum. *J. Am. Chem. Soc.* **2004,** *126*, 199-203.

9.   Bürgi, T.; Baiker, A., Heterogeneous enantioselective hydrogenation over cinchona alkaloid modified platinum: mechanistic insights into a complex reaction. *Accounts of chemical research* **2004,** *37* (11), 909-917.

10.   Bürgi, T.; Baiker, A., Heterogeneous Enantioselective Hydrogenation over Cinchona Alkaloid Modified Platinum: Mechanistic Insights into a Complex Reaction. *Accounts of chemical research* **2004,** *37* (11), 909-917.

11.   Diezi, S.; Hess, M.; Orglmeister, E.; Mallat, T.; Baiker, A., Chemo and enantioselective hydrogenation of fluorinated ketones on platinum modified with (R)-1-(1-naphthyl)ethylamine derivatives. *J. Mol. Catal. A-Chem.* **2005,** *239* (1-2), 49-56.

12.   Blaser, H.-U.; Studer, M., Cinchona-Modified Platinum Catalysts: From Ligand Acceleration to Technical Processes. *Accounts of chemical research* **2007,** *40* (12), 1348-1356.

13.   Mink, L.; Ma, Z.; Olsen, R.; James, J.; Sholl, D.; Mueller, L.; Zaera, F., The Physico-chemical Properties of Cinchona Alkaloids Responsible for their Unique Performance in Chiral Catalysis. *Topics in Catalysis* **2008,** *48* (1), 120-127.

14.   Talas, E.; Margitfalvi, J. L.; Egyed, O., Additional data to the origin of rate enhancement in the enantioselective hydrogenation of activated ketones over cinchonidine modified platinum catalyst. *Journal of Catalysis* **2009,** *266* (2), 191-198.

15.   Garland, M.; Blaser, H. U., A heterogeneous ligand-accelerated reaction: enantioselective hydrogenation of ethyl pyruvate catalyzed by cinchona-modified platinum/aluminum oxide catalysts. *J. Am. Chem. Soc.* **1990,** *112* (19), 7048-7050.

16.   Vermeer, W. A. H.; Fulford, A.; Johnston, P.; Wells, P. B., New Enantioselective Reactions catalysed by cinchonidine-modified platinum. *Journal of the Chemical Society, Chemical Communications* **1993,** (13), 1053-1054.

17.   Heinz, T.; Wang, G. Z.; Pfaltz, A.; Minder, B.; Schurch, M.; Mallat, T.; Baiker, A., 1-(1-Naphthyl)Ethylamine and Derivatives Thereof as Chiral Modifiers in the Enantioselective Hydrogenation of Ethyl Pyruvate over Pt-Alumina. *Journal of the Chemical Society-Chemical Communications* **1995,** (14), 1421-1422.

18.   Minder, B.; Schuerch, M.; Mallat, T.; Baiker, A.; Heinz, T.; Pfaltz, A., Enantioselective hydrogenation of ethyl pyruvate over Pt/alumina modified by (R)-1-(1-naphthyl)ethylamine derivatives. *Journal of Catalysis* **1996,** *160* (2), 261-268.

19.   Bonello, J. M.; Williams, F. J.; Lambert, R. M., Aspects of enantioselective heterogeneous catalysis: Structure and reactivity of (S)-(-)-1-(1-naphthyl)ethylamine on Pt{111}. *J. Am. Chem. Soc.* **2003,** *125* (9), 2723-2729.

20.   Boscoboinik, J. A.; Bai, Y.; Burkholder, L.; Tysoe, W. T., Structure and Distribution of S-alpha-(1-Naphthyl)-ethylamine on Pd(111). *Journal of Physical Chemistry C* **2011,** *115* (33), 16488-16494.

21.   Burkholder, L.; Garvey, M.; Weinert, M.; Tysoe, W. T., Structure of Methyl Pyruvate and alpha-(1-Naphthyl)ethylamine on Pd(111). *Journal of Physical Chemistry C* **2011,** *115* (17), 8790-8797.

22.   Sholl, D. S., Adsorption of chiral hydrocarbons on chiral platinum surfaces. *Langmuir* **1998,** *14* (4), 862-867.

23.   Baddeley, C. J., Fundamental investigations of enantioselective heterogeneous catalysis. *Topics in Catalysis* **2003,** *25* (1-4), 17-28.

24.   Lavoie, S.; Laliberte, M. A.; McBreen, P. H., Adsorption states and modifier-substrate interactions on Pt(111) relevant to the enantioselective hydrogenation of alkyl pyruvates in the Orito reaction. *J. Am. Chem. Soc.* **2003,** *125* (51), 15756-15757.

25.   Lavoie, S.; Laliberté, M.-A.; Mahieu, G.; Demers-Carpentier, V.; McBreen, P., Keto-Enol Driven Assembly of Methyl Pyruvate on Pt(111). *J. Am. Chem. Soc.* **2007,** *129* (38), 11668-11669.

26.   Burkholder, L.; Tysoe, W. T., Structure and Reaction Pathways of Methyl Pyruvate on Pd(111). *Journal of Physical Chemistry C* **2009,** *113* (34), 15298-15306.

27.   Garvey, M.; Bai, Y.; Boscoboinik, J. A.; Burkholder, L.; Sorensen, T. E.; Tysoe, W. T., Identifying Molecular Species on Surfaces by Scanning Tunneling Microscopy: Methyl Pyruvate on Pd(111). *The Journal of Physical Chemistry C* **2013,** *117* (9), 4505-4514.

28.   Demers-Carpentier, V.; Goubert, G.; Masini, F.; Lafleur-Lambert, R.; Dong, Y.; Lavoie, S.; Mahieu, G.; Boukouvalas, J.; Gao, H.; Rasmussen, A. M. H.; Ferrighi, L.; Pan, Y.; Hammer, B.; McBreen, P. H., Direct Observation of Molecular Preorganization for Chirality Transfer on a Catalyst Surface. *Science* **2011,** *334* (6057), 776-780.

29.   Lavoie, S.; McBreen, P. H., Evidence for C-H center dot center dot center dot O=C bonding in coadsorbed aromatic - Carbonyl systems on Pt(111). *Journal of Physical Chemistry B* **2005,** *109* (24), 11986-11990.

30.   Lavoie, S.; Laliberte, M. A.; Temprano, I.; McBreen, P. H., A generalized two-point H-bonding model for catalytic stereoselective hydrogenation of activated ketones on chirally modified platinum. *J. Am. Chem. Soc.* **2006,** *128* (23), 7588-7593.

31.   Laliberté, M.-A.; Lavoie, S.; Hammer, B.; Mahieu, G.; McBreen, P. H., Activation in Prochiral Reaction Assemblies on Pt(111). *J. Am. Chem. Soc.* **2008,** *130*

(16), 5386-5387.

32.   Claus, P., Selective hydrogenation of ά,β-unsaturated aldehydes and other C=O and C=C bonds containing compounds. *Topics in Catalysis* **1998,** *5* (1-4), 51-62.

33.   Landman, U.; Luedtke, W. D.; Burnham, N. A.; Colton, R. J., Atomistic Mechanisms and Dynamics of Adhesion, Nanoindentation, and Fracture. *Science* **1990,** *248* (4954), 454-461.

34.   Burkholder, L.; Stacchiola, D. o.; Boscoboinik, J. A.; Tysoe, W. T., Enantioselective Chemisorption on Model Chirally Modified Surfaces: 2-Butanol on α-(1-Naphthyl)ethylamine/Pd(111). *The Journal of Physical Chemistry C* **2009,** *113* (31), 13877-13885.

35.   Boscoboinik, J. A. Small Organic Molecules on Transition Metal Surfaces and Monte Carlo Simulations of Bimetallic Surface Alloys. Ph.D. Dissertation, University of Wisconsin-Milwaukee, Milwaukee, WI, 2010.

36.   Blöchl, P. E., Projector augmented-wave method. *Physical Review B* **1994,** *50* (24), 17953-17979.

37.   Kresse, G.; Joubert, D., From ultrasoft pseudopotentials to the projector augmented-wave method. *Physical Review B* **1999,** *59* (3), 1758-1775.

38.   Kresse, G.; Furthmüller, J., Efficient iterative schemes for ab initio total-energy calculations using a plane-wave basis set. *Physical Review B* **1996,** *54* (16), 11169-11186.

39.   Kresse, G.; Furthmüller, J., Efficiency of ab-initio total energy calculations for metals and semiconductors using a plane-wave basis set. *Computational Materials Science* **1996,** *6* (1), 15-50.

40.   Kresse, G.; Hafner, J., Ab initio molecular dynamics for liquid metals. *Physical Review B* **1993,** *47* (1), 558-561.

41.   Perdew, J. P.; Burke, K.; Ernzerhof, M., Generalized Gradient Approximation Made Simple. *Physical Review Letters* **1996,** *77* (18), 3865-3868.

42.   Ireta, J.; Neugebauer, J.; Scheffler, M., On the Accuracy of DFT for Describing Hydrogen Bonds: Dependence on the Bond Directionality. *The Journal of Physical Chemistry A* **2004,** *108* (26), 5692-5698.

43.   Tkatchenko, A.; Scheffler, M., Accurate Molecular Van Der Waals Interactions

from Ground-State Electron Density and Free-Atom Reference Data. *Physical Review Letters* **2009,** *102* (7), 073005.

44.   Tersoff, J.; Hamann, D. R., Theory and Application for the Scanning Tunneling Microscope. *Physical Review Letters* **1983,** *50* (25), 1998-2001.

45.   Tersoff, J.; Hamann, D. R., Theory of the scanning tunneling microscope. *Physical Review B* **1985,** *31* (2), 805-813.

46.   Bardeen, J., Tunnelling from a Many-Particle Point of View. *Physical Review Letters* **1961,** *6* (2), 57-59.

47.   Krisztián, P.; Werner, A. H., Multiple scattering in a vacuum barrier obtained from real-space wavefunctions. *Journal of Physics: Condensed Matter* **2005,** *17* (17), 2705.

48.   Burkholder, L.; Stacchiola, D.; Boscoboinik, J. A.; Tysoe, W. T., Enantioselective Chemisorption on Model Chirally Modified Surfaces: 2-Butanol on alpha-(1-Naphthyl)ethylamine/Pd(111). *Journal of Physical Chemistry C* **2009,** *113* (31), 13877-13885.

49.   BURKHOLDER, L.; STACCHIOLA, D.; TYSOE, W. T., KINETIC AND REACTIVE PROPERTIES OF ETHYLENE ON CLEAN AND HYDROGEN-COVERED Pd(111). *Surface Review and Letters* **2003,** *10* (06), 909-916.

50.   Stacchiola, D.; Azad, S.; Burkholder, L.; Tysoe, W. T., An Investigation of the Reaction Pathway for Ethylene Hydrogenation on Pd(111). *The Journal of Physical Chemistry B* **2001,** *105* (45), 11233-11239.

51.   Zaera, F., Mechanisms for ethylene hydrogenation and hydrogen-deuterium exchange over platinum(111). *The Journal of Physical Chemistry* **1990,** *94* (12), 5090-5095.

52.   Demers-Carpentier, V.; Rasmussen, A. M. H.; Goubert, G.; Ferrighi, L.; Dong, Y.; Lemay, J.-C.; Masini, F.; Zeng, Y.; Hammer, B.; McBreen, P. H., Stereodirection of an α-Ketoester at Sub-molecular Sites on Chirally Modified Pt(111): Heterogeneous Asymmetric Catalysis. *J. Am. Chem. Soc.* **2013,** *135* (27), 9999-10002.

53.   Zheng, T.; Stacchiola, D.; Poon, H. C.; Saldin, D. K.; Tysoe, W. T., Determination of the structure of disordered overlayers of ethylene on clean and hydrogen-covered Pd(111) by low-energy electron diffraction. *Surface Science* **2004,** *564*

(1-3), 71-78.

54.   Demers-Carpentier, V.; Laliberté, M.-A.; Lavoie, S. p.; Mahieu, G.; McBreen, P. H., Two-Dimensional Self-Assembly and Catalytic Function: Conversion of Chiral Alcohols into Self-Assembled Enols on Pt(111)†. *The Journal of Physical Chemistry C* **2009,** *114* (16), 7291-7298.

55.   Horiuti, I.; Polanyi, M., Exchange reactions of hydrogen on metallic catalysts. *Transactions of the Faraday Society* **1934,** *30* (0), 1164-1172.

56.   Easson, L. H.; Stedman, E., Studies on the relationship between chemical constitution and physiological action: Molecular dissymmetry and physiological activity. *Biochem. J.* **1933,** *27* (4), 1257-1266.

57.   Ogston, A. G., Interpretation of experiments on metabolic processes, using isotopic tracer elements. *Nature* **1948,** *162* (4129), 963.

58.   Mahapatra, M.; Tysoe, W., ChemisorptiveEnantioselectivity of Chiral Epoxides on Tartaric-acid Modified Pd(111); Three-Point Bonding *Physical Chemistry Chemical Physics* **2015,** *In press*.

59.   Burkholder, L.; The Surface Chemistry of Enantioselectively Modified Palladium (111) Systems. **2009**, Ph.D. dissertation, University of Wisconsin-Milwaukee

Chapter 11

STM Study of C_3 Epoxides and Olefins on Pd(111) Surface

11.1 Introduction

This chapter presents a STM study of four different C_3 hydrocarbons on a Pd(111) surface. The first part of the chapter consists of characterization of two C_3 epoxide compounds: propylene oxide (PO) and glycidol by STM and DFT and the second part focuses on the STM study of two C_3 olefins: propene and trifluoropropene. The principal idea behind this study is to characterize the surface structure of the compounds on Pd(111).

Propylene oxide has been used extensively as a chiral probe molecule to measure the enantioselectivity of chirally modified surfaces on both palladium and platinum. The general aspects of adsorption of propylene oxide has been studied previously on both Pd(111)[1] and Pt(111)[2] single crystal surfaces, where it was observed that molecular adsorption occurs at low temperature. The molecules desorbs intact in two different states upon heating: the monolayer desorbs at ~175 K and the multilayer desorbs at ~ 150 K.

Two enantiomers of a chiral compound have identical physical and chemical properties in an achiral environment. However, when the two enantiomers interact with each other, their difference in relative handedness can lead to difference in physical and chemical properties. For example the normal melting point of pure D- or L-menthol is 316 K, whereas DL-menthol mixture has a melting point of 307 K.[3] This is because racemic menthol forms 1:1 racemic compound in the solid phase. When two enantiomers

of any chiral compounds are intermixed, there are three most common types of interaction. First, the opposite enantiomers interact with each other strongly to form 1:1 racemic mixture (racemate). In fact, 90 to 95 % of the chiral compounds crystallize by forming racemates.[4-5] The second most common possibility is the formation of solid conglomerates, where the same enantiomers interact strongly to form homochiral domains.[5] Therefore opposite enantiomers condense separately to produce mixtures of enantiomerically pure crystals. The third possibility is the formation of a random solution which is quite rare (~1%). It is a solid solution containing equal numbers of both enantiomers but the distribution is random because of equal affinity for pairing with a homo or a hetero enantiomer. Nevertheless, the choice of formation of racemate, solid conglomerate or solid solution depends on the strength of the interaction between the enantiomers of the same *versus* opposite handedness.[6]

However, propylene oxide adsorption on Pt(111) surface contradicts this observation where racemic mixtures and pure enantiomers exhibit different physical properties despite the strong intermolecular interaction between the enantiomers.[6] The STM images of propylene oxide on Pt(111) surface did not show any racemate formation or long-range order. The saturation monolayer of a racemic mixture of propylene oxide on a Pt(111) surface was found to be ~20 % less dense than that from enantiomerically pure propylene oxide and that difference is attributed to adsorbate-assisted adsorption kinetics with different probabilities for homo *versus* hetero enantiomeric pairs. However, similar experiments on Pd(111) using propylene oxide reveal no difference in absolute coverage for single enantiomer and racemic mixture.

The STM study of propylene oxide on Pd(111) surface is motivated to compare

the adsorbate structures to rationalize the difference between the adsorption of propylene oxide on Pd and Pt.

Another chiral molecule, glycidol which is structurally similar to propylene oxide but has a $-CH_2OH$ group instead of a $-CH_3$ group in propylene oxide is also investigated by STM and DFT, and the results are compared with that of propylene oxide.

The selective hydrogenation of olefins is required for numerous chemical processes including petrochemical hydrotreating, chemical and pharmaceutical synthesis, and the treatment of fats in the food industry.[7] The general reaction mechanism for hydrogenation is first proposed by Horiuti and Polayni which proceeds by (a) hydrogen dissociation (b) alkene adsorption (c) sequential hydrogen addition to alkenes (d) desorption of the product (alkane).[8] More recently, the interaction of the alkenes with transition-metal surfaces has been studied on model catalyst systems to gain mechanistic insights into the reaction pathway. [9-12]

Among unsaturated hydrocarbons, ethylene is the most studied compound. The reaction of ethylene on both Pd(111) [13] and Pt(111) [14] has been thoroughly investigated and it was observed that ethylene binds to both the surfaces in di-σ form, and on hydrogen pre-covered surfaces it adopts a π-bonding form. There has been substantially fewer investigation of propylene than ethylene on transition-metal surfaces with the most complete investigation being carried out on platinum. The adsorption of propylene on Pd(111) and Pt(111) surfaces at ~ 80 K show two distinct di-σ bonded species in the monolayer as well as the formation of a π-bonded species in the second layer.[9, 11] Both ethylene and propylene can form several dehydrogenated species on Pd(111) and Pt(111) surfaces, when dosed at room temperature. Most of the surface science studies of olefins

on transition-metal surfaces are largely focused on spectroscopy. In this chapter, we report an STM study of intermediate coverage of propene adsorption on Pd(111) surface at ~ 120 K to observe the topological aspects and to see if there is any ordering on the surface. The second reason for characterizing propene is for chirality related phenomena, which is induced by adsorption of achiral molecules on metal surfaces. On a metal surface, symmetry elements perpendicular to the surface plane are possible. Such lower dimensionality often cause mirror symmetry breaking upon adsorption. There are many examples of achiral molecules that become chiral when adsorbed on a metal surface. Propene on Cu(211) surface [15-18] is one of the examples, where propene forms two adsorbate enantiomers . Finally STM images are collected for trifluoro propene on Pd(111) surface to observe if replacing the –CH_3 group by a –CF_3 group has any effect on the surface ordering and surface structure.

11.2 Experimental Section

Propylene oxide, glycidol, propene and 3,3,3-trifluoro propene were purchased from Aldrich Co. chemicals and introduced into the UHV chamber *via* gas-handling manifolds attached to the respective UHV chambers. Propylene oxide and glycidol are transferred to glass vials and further purified by several freeze-pump-thaw cycles before dosing onto the sample surface. Propene and 3,3,3 trifluoropropene are dosed directly from the gas cylinders which were attached to the gas line. All the reactants are dosed by leak valves with a dosing tube mounted to it to enhance the dosing rate.

TPD experiments are carried out in the TPD chamber as described in Chapter 2. The desorbing species are detected by using a Dycor quadrupole mass spectrometer placed in line of sight of the crystal.

Scanning Tunneling Microscopy experiments were performed using a scanning tunneling microscope (RHK UHV350) housed in an ultrahigh vacuum (UHV) chamber operating at a base pressure below 2×10^{-10} Torr following bakeout, as described in Chapter 2. STM images were acquired using an electrochemically etched tip made from recrystallized tungsten wire. This was conditioned by a controlled interaction with a clean Au(111) single crystal. This is expected to result in a gold-terminated tip.

The Pd(111) sample was cleaned using a standard procedure that consisted of cycles of Ar ion bombardment followed by heating at 800 K in ~4×10^{-8} Torr of oxygen and then annealing at ~1100 K in *vacuo* to remove any remaining oxygen.

11.3 Results

11.3.1 Adsorption of Propylene Oxide (PO) on Pd(111)

A temperature-programmed desorption uptake study has been performed by dosing various amounts of S-PO at ~120 K by using a linear heating rate of ~2 K/s and monitoring 58 amu which corresponds to molecular propylene oxide desorption and is shown in Figure 11-1. For small doses, PO desorbs in one state at ~175 K, which correspond to desorption from the monolayer. With increase in exposure the monolayer peak saturates, and another peak grows at ~140 K, which is due to desorption of PO from the multilayer. The peaks observed at 120 K is desorption form the sample mount (post peak). The results are consistent with the previous PO TPD [1] results on Pd(111), which were acquired by using a higher heating rate. Here the experiments are carried out at a low heating rate, so that the monolayer and multilayer peaks are well separated.
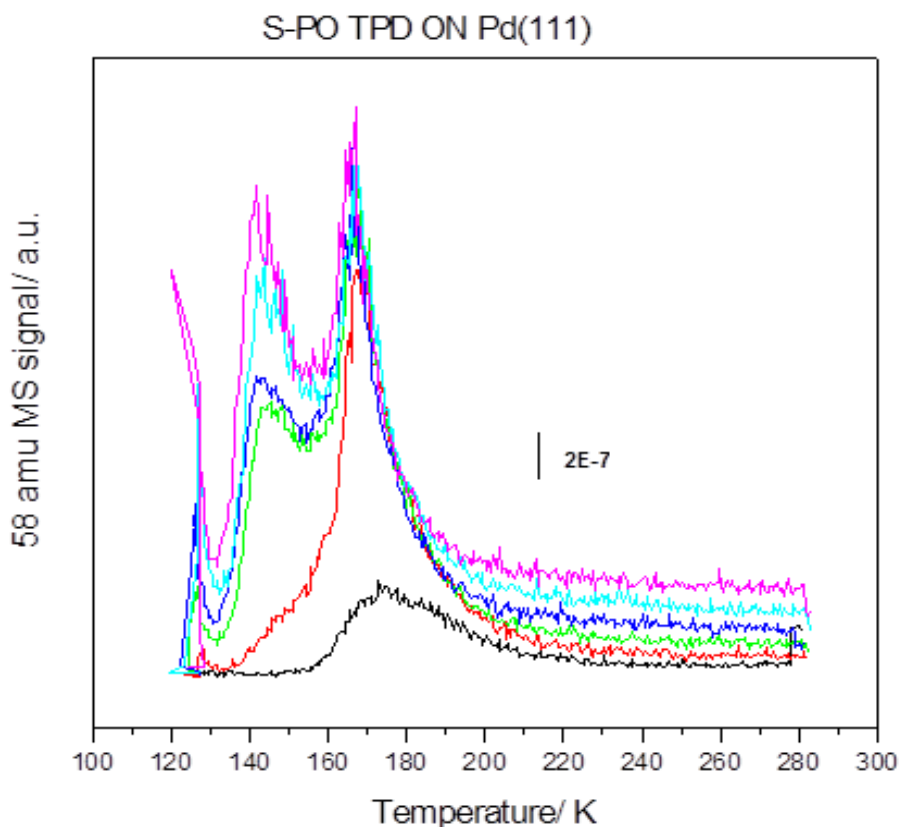
Figure 11-1 TPD uptake profile following S-propylene oxide (PO) adsorption on a Pd(111) surface at ~125 K. The spectra were collected at 58 amu by using a linear heating rate of ~2 K/s

Further experiments were carried out to measure the monolayer coverage of enantiopure *versus* racemic PO on a Pd(111) surface. As mentioned above, on Pt(111) surface, the saturation coverage of a racemic mixture of PO was found to be 20% less than a similar saturated coverage of enantiopure PO.[6] Figure 11-2 shows the desorption profiles for a saturated monolayers of R-PO and racemic PO (color coded by red and green respectively). These experiments were carried out by using a heating rate of ~6 K/s. PO is dosed at a sample temperature of ~140 K to avoid populating the multilayer.
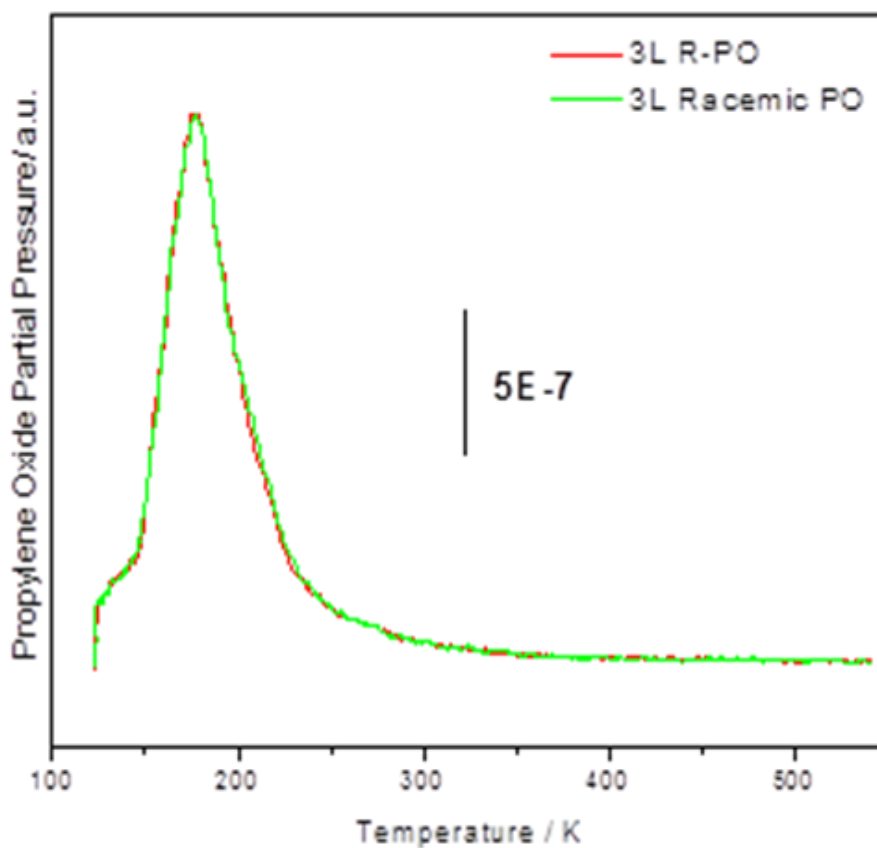
Figure 11-2 TPD profiles following a saturated dose of R-propylene oxide (PO) and racemic propylene oxide on a Pd(111) surface at ~140 K. The spectra were collected for 58 amu by using a linear heating rate of ~6 K/s.

As expected, PO monolayer desorbs at ~175 K and no multilayer desorption is observed. Interestingly, the desorption profiles for R-PO and racemic PO overlap with each other, and there is no difference in either the desorption temperature or coverage, which is different to what was observed on Pt(111) surface. STM experiments were carried out to examine the structure of PO on Pd(111) as a basis for understanding the differences.

11.3.1.1 STM of Propylene Oxide on a Pd(111) Surface

STM images were acquired following PO adsorption on a Pd(111) surface at ~120 K and the results are shown in Figure 11-3. It is observed that PO forms one-dimensional linear chain structures as observed in Figure 11-3. The linear chains grow at an angle of 30° to the close-packed direction on the (111) face. The spacing between the rows is 9.6 Å and along the rows is 4.8 Å. Previous DFT calculations showed that PO adsorbs on a Pd atop site with the –CH_3 group oriented away from the surface. Based on the observed STM image, a proposed model for the observed linear chain structure is presented in Figure 11-4. The chains run diagonally at an angle of 30° to the close-packed directions and the spacing and angle match with the experimentally observed STM image.
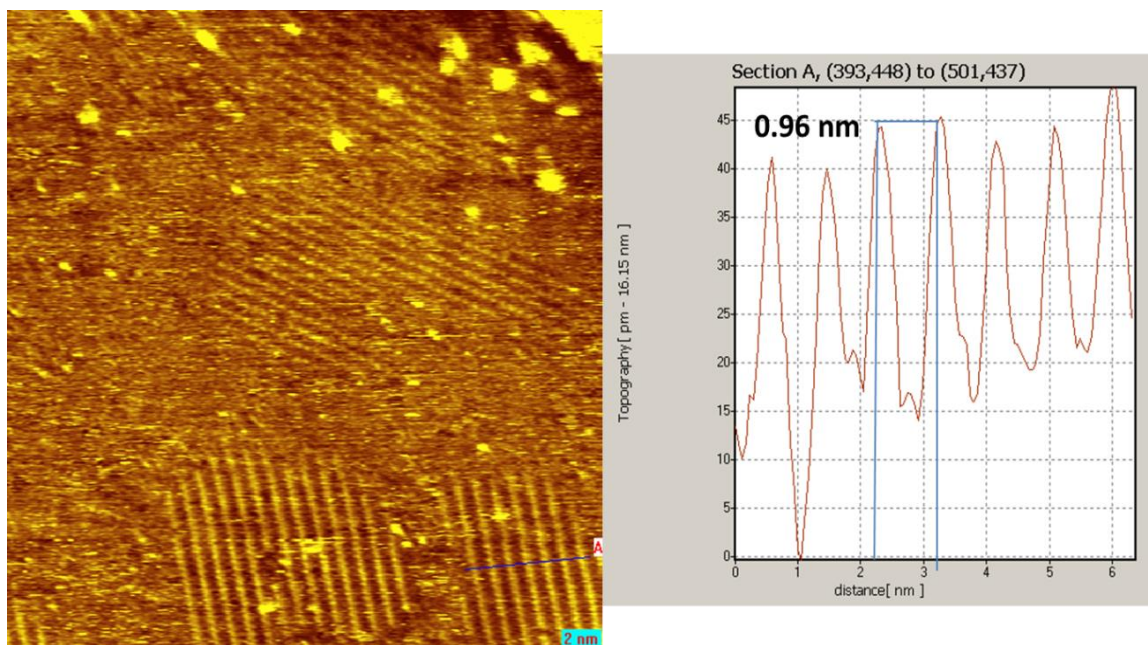
Figure 11-3 STM image for an intermediate coverage of propylene oxide adsorbed on a Pd(111) surface at 120 K. The line profile measurement is shown in the right. (V_b= -0.2 mv, I_t=30pA)
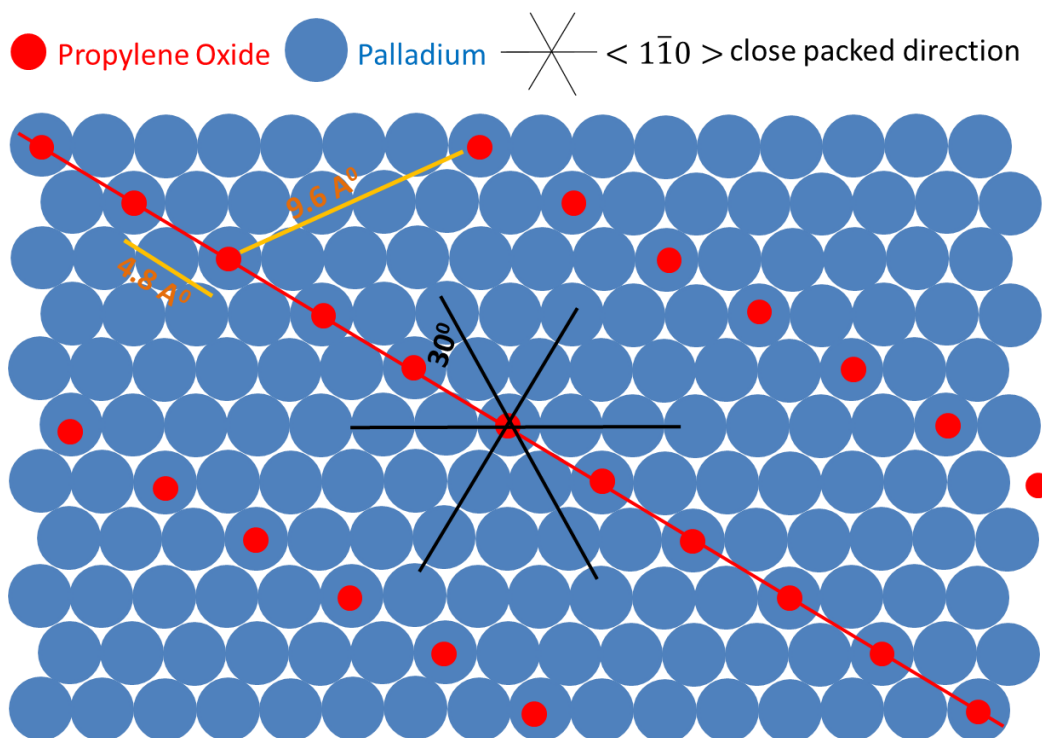
Figure 11-4 A plausible model for the observed propylene oxide one dimensional chain structure. The chains grow at an angle of 30° to the close packed direction. The line spacing between two rows is 9.6 Å and along the row is 4.8 Å, which match with the experimentally observed STM images.

11.3.1.2 Tip Induced Polymerization of Propylene Oxide on Pd(111)

PO forms one dimensional linear chain structures on Pd(111) surface as shown in Figure 11-3. However, it was very difficult to image PO and upon scanning the same surface repeatedly the molecules polymerize and show the presence of a number of different species as shown in Figure 11-5. In Figure 11-5(a), linear structures are observed due to PO. In addition, there are some fuzzy lines that appear in between the PO row structures. With continuous scanning on the same area, now the surface only consists of closely spaced lines which line up in one of the close packed direction as shown in Figure 11-5 (b). These linear structures order in lamellae. The spacing between the closely spaced lines is ~0.54 nm. The average length of the linear structures is about ~ 3 to 4 nm.
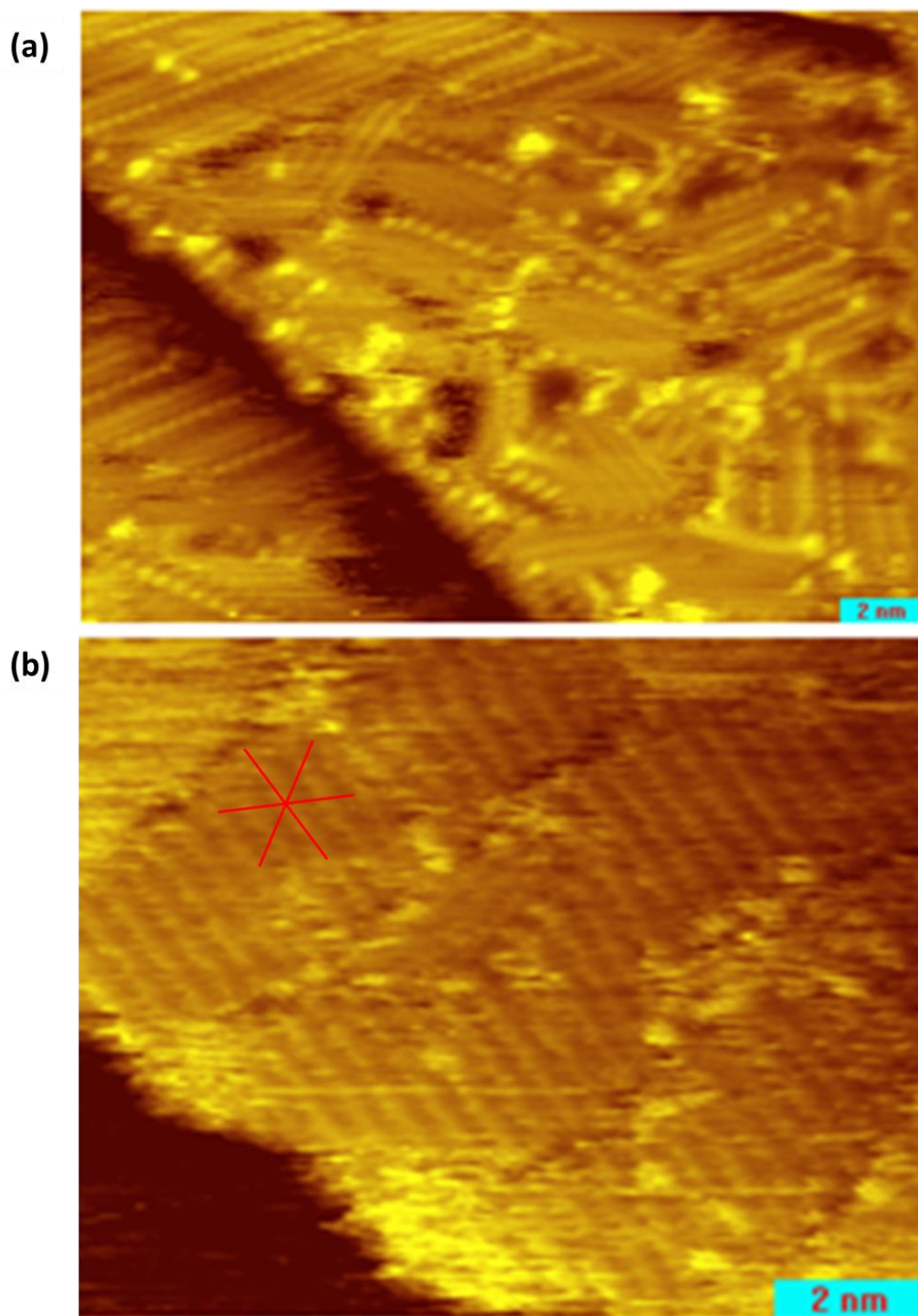
Figure 11-5 Tip induced polymerized structures of propylene oxide on Pd(111). (a) Shows the presence of commonly observed propylene oxide linear chains and some polymerized structures (- 0.8 V, 83 pA) (b) The surface only consists of polymerized propylene oxide which order on the surface in lamellae (- 0.16 V, 80 pA). The orientation of the close packed $< 1\bar{1}0 >$ direction of the underlying lattice are provided in red lines

In addition, there is another striking feature was observed when the surface was scanned at a higher bias voltage. Figure 11-6 shows an STM image, where the top half of the scan area consists of domains of linear rows running in different orientations and the bottom half consists of hexagonal features, which are ordered in hexagonal pattern on the surface. We propose that the linear patch domains are the same structure as those observed previously in the Figure 11-5 (b). However, the hexagonal features are different to the linear structures and are oriented at an angle of 30° to the surface crystallographic directions.

2 nm
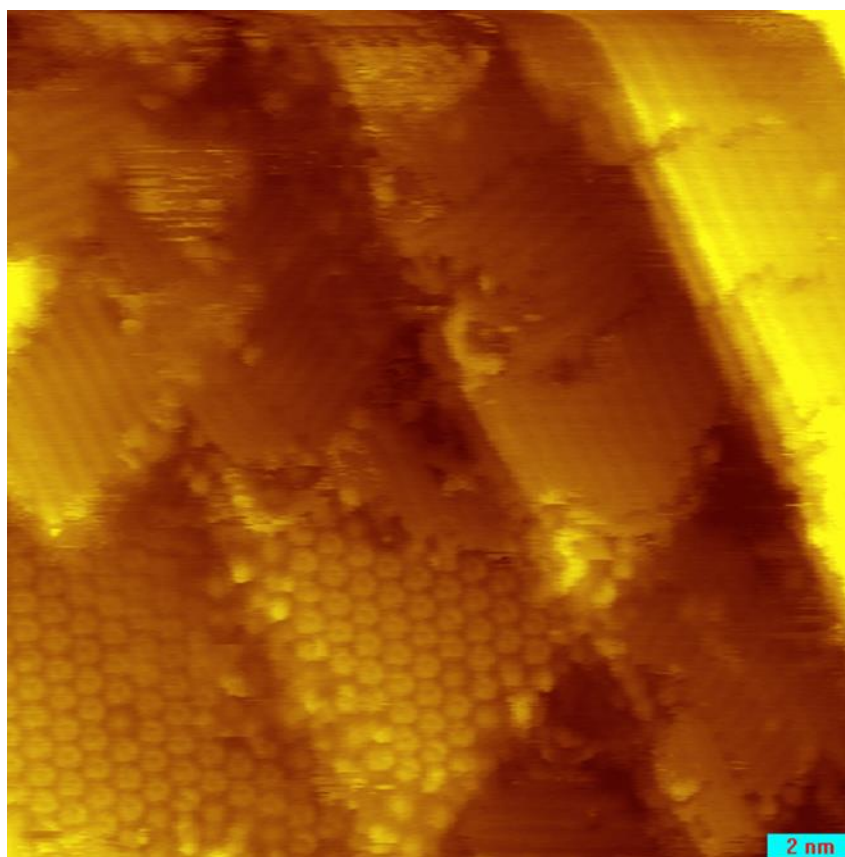
Figure 11-6 Tip induced propylene oxide polymerized structures. The top portion of the image consists of ordered domains which consist of patches of linear rows and the bottom of the image consists of hexagonal features ordered in hexagonal pattern. (-1 V, 179 pA)

Figure 11-7 shows a zoomed in image for the same scanning area as in Figure 11-6. The line profile measurements (indicated as C and D in the STM image) are shown in

the right side of the image. The spacing between two hexagonal features is 0.74 nm and the pore size is ~0.3 nm.
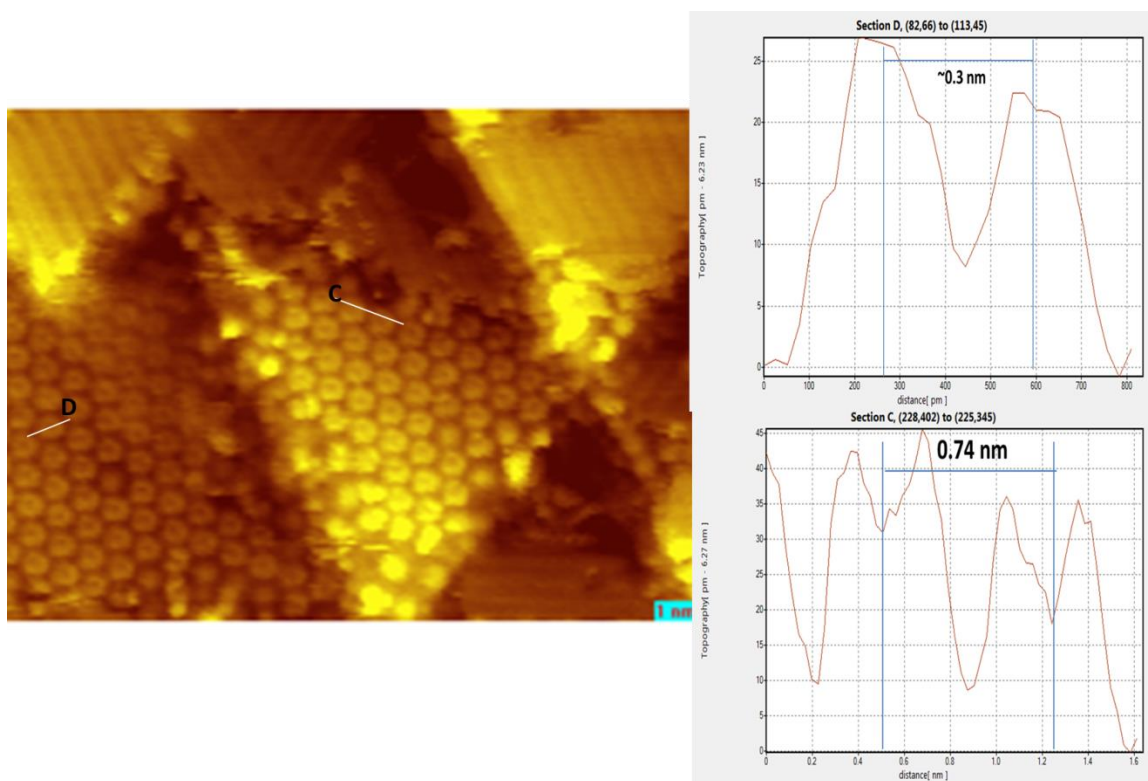
Figure 11-7 A smaller scan area STM image showing the presence of two different ordered domains resulting from the tip induced polymerization of propylene oxide on a Pd(111) surface. Line profile measurements are shown in the right. (-1 V, 179 pA)

The origin of the tip induced features is not fully understood. One plausible model for the formation of these structures is given in Figure 11-8. As a result of tip bias, PO undergoes a ring-opening reaction to form oxametallacycle structures, which is a very common decomposition pathway of the epoxy compound on transition- metal surfaces.[19-21] The oxametallacycle compounds polymerize to produce linear structures of various lengths and/or two oxametallacycle compounds produce crown ethers, which appear as hexagonal features in the STM images. The pore size of the hexagonal features observed in STM is ~ 0.32 nm, which is close to the pore size of the crown ether (dimethyl 6-crown 2). Those structures were found to be very stable on the surface and, once formed,

can be imaged over a very long period of time. The polymerized linear structures

possibly bind to the palladium surface by oxygen atoms and the methyl groups protrude

from the surface and are imaged in the STM. The length of the linear structures in each

domain are about the same size and have an average length of 3 to ~4 nm, which suggests

that they consists of 9 to 12 PO units. It is not clear why PO polymerizes to produce

oligomers of equal length.
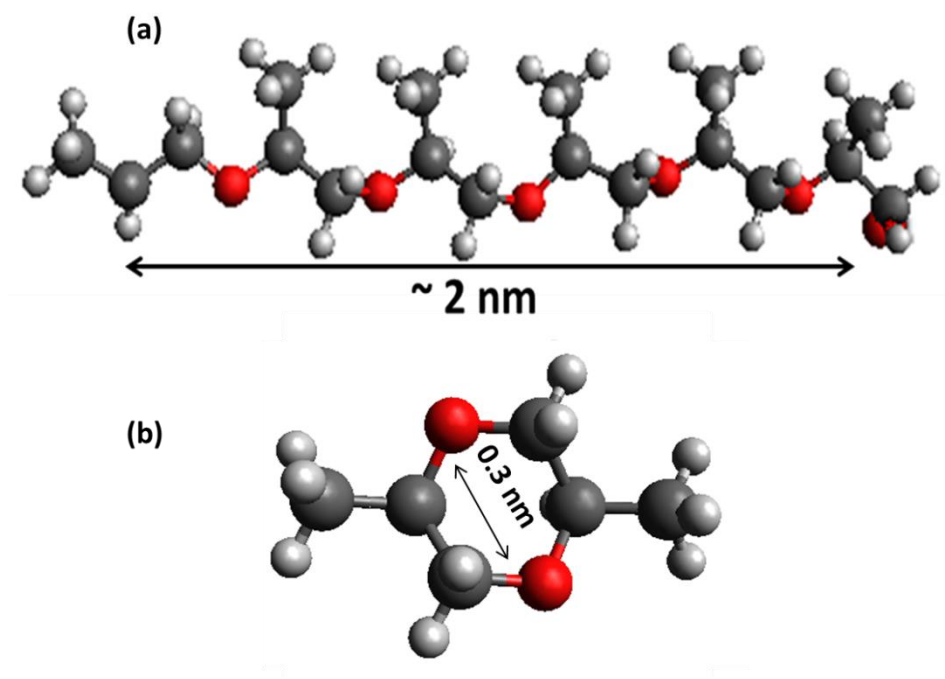
Figure 11-8 Plausible structural models for the observed tip induced polymerized structure of propylene oxide on Pd(111): (a) linear structures are composed of a number of oxametallacycle (b) hexagonal features are proposed to be crown ether (dimethyl 6-crown-2)

11.3.2 STM of Glycidol

Glycidol was dosed onto a Pd(111) surface at ~150 K and the surface was cooled

to 120 K for imaging. At low coverages, glycidol molecules self-organize to form

hexamers in which the molecules are less densely packed (Figure 11-9). The line profile

measurement shows that the spacing between two glycidol molecules within the hexamer

is 0.756 nm and 0.46 nm as shown in the inset in Figure 11-9. Noisy streaks appear

adjacent to the hexamers, indicating that they exhibit mobility during the time scale of

one scan.
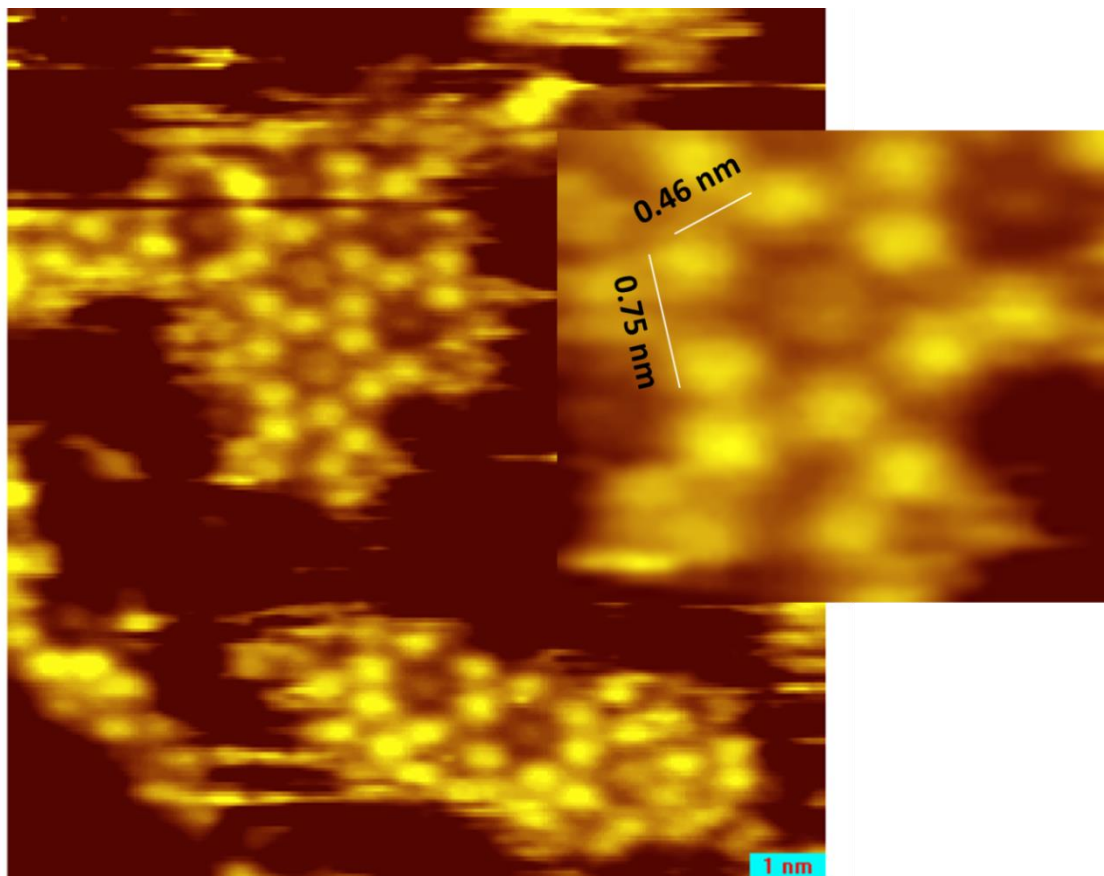
Figure 11-9 Low coverage STM image of glycidol on a Pd(111) surface collected at ~120 K, which shows the formation of hexamers, the inset shows the spacing between the glycidol molecules in a hexamer (-254 mv, 40 pA)

Figures 11-10 (a) to (c) shows three consecutive time-lapse images which clearly

show the diffusion of molecules on the surface. The area highlighted in white dotted

squares show the growth of hexamers with time.
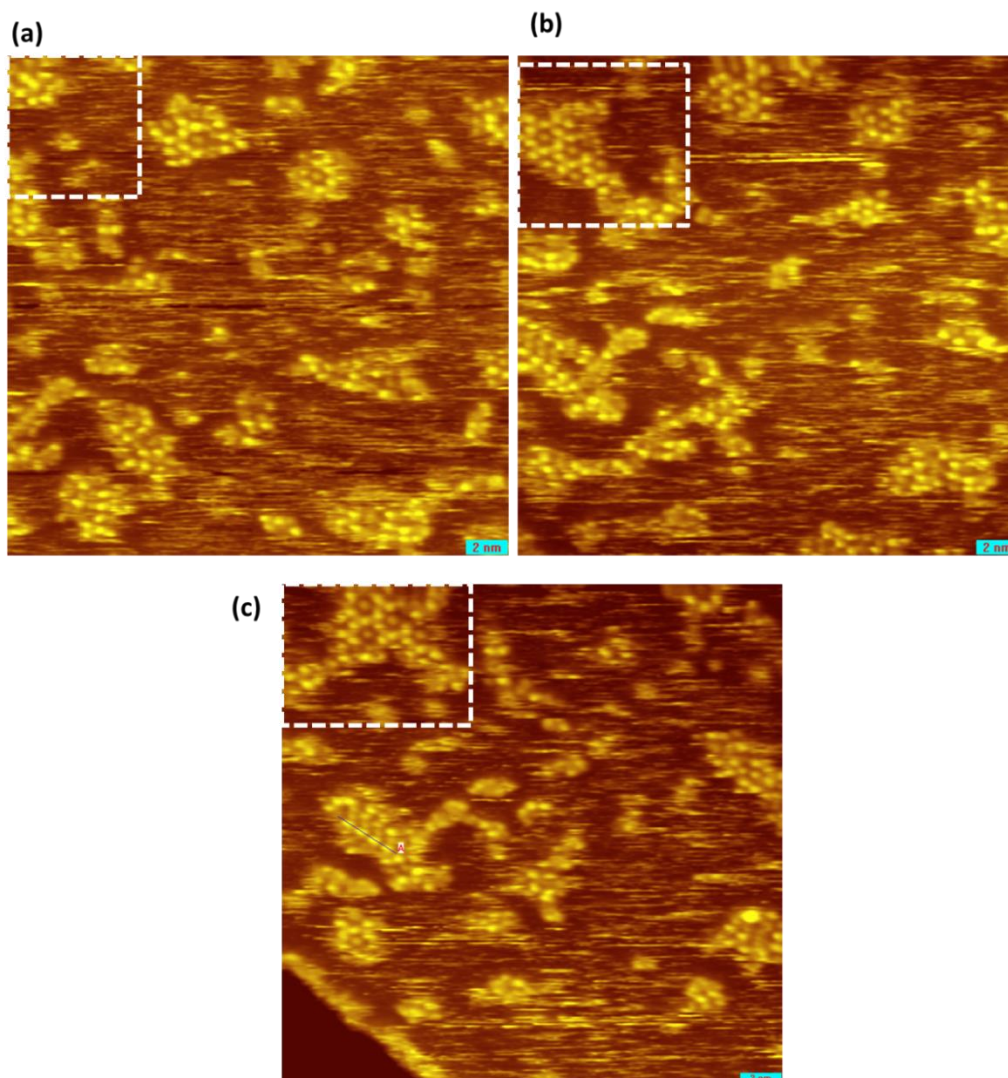
Figure 11-10 Three sequential STM images of glycidol on Pd(111), which shows the mobility of the molecules. The images are collected in 8 minute interval. The area highlighted in white dotted squares shows the growth of hexamers with time. (-254 mv, 40 pA)

Figure 11-11 shows an STM image of a high coverage of glycidol on Pd(111).

Unlike propylene oxide, glycidol forms extended hydrogen-bonded network on the

surface due to the presence of –OH group. The surface is densely packed and consists of

a mixture of glycidol monomers, dimers, tetramers, hexamers and longer monomer and

dimer rows. The dimers and dimer rows interact with each other to form extended

hydrogen-bonded over layer.
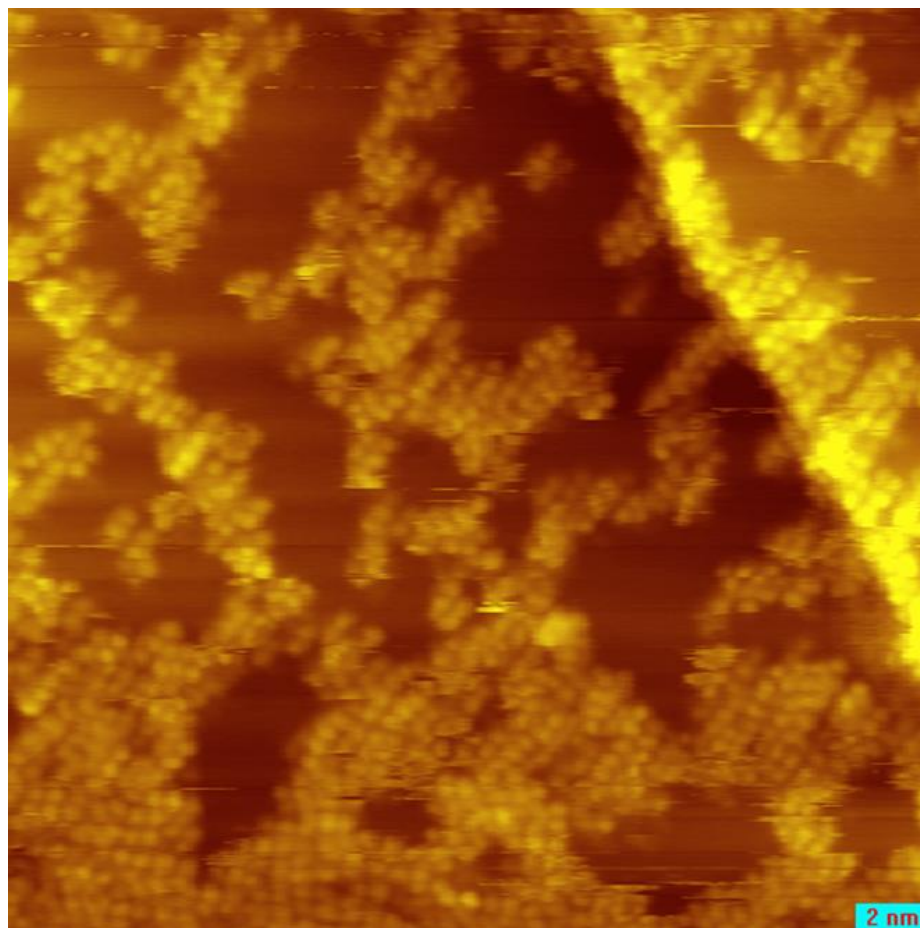
Figure 11-11 STM image of a high coverage of glycidol on a Pd(111) surface. The surface is densely packed due to extended hydrogen bonding interactions. (-250 mv, 50 pA)

11.3.2.1 DFT Calculations

In order to characterize the observed hexamer structure in STM, DFT calculations were performed for different glycidol dimer structures. Dimer structures consist of the most stable glycidol monomeric species as depicted in Chapter 4. DFT calculations showed that glycidol monomer [22-23] bonds to a palladium atop site through the epoxy oxygen and the adsorption energy of the most stable structure was found to be -22 kJ/mol.
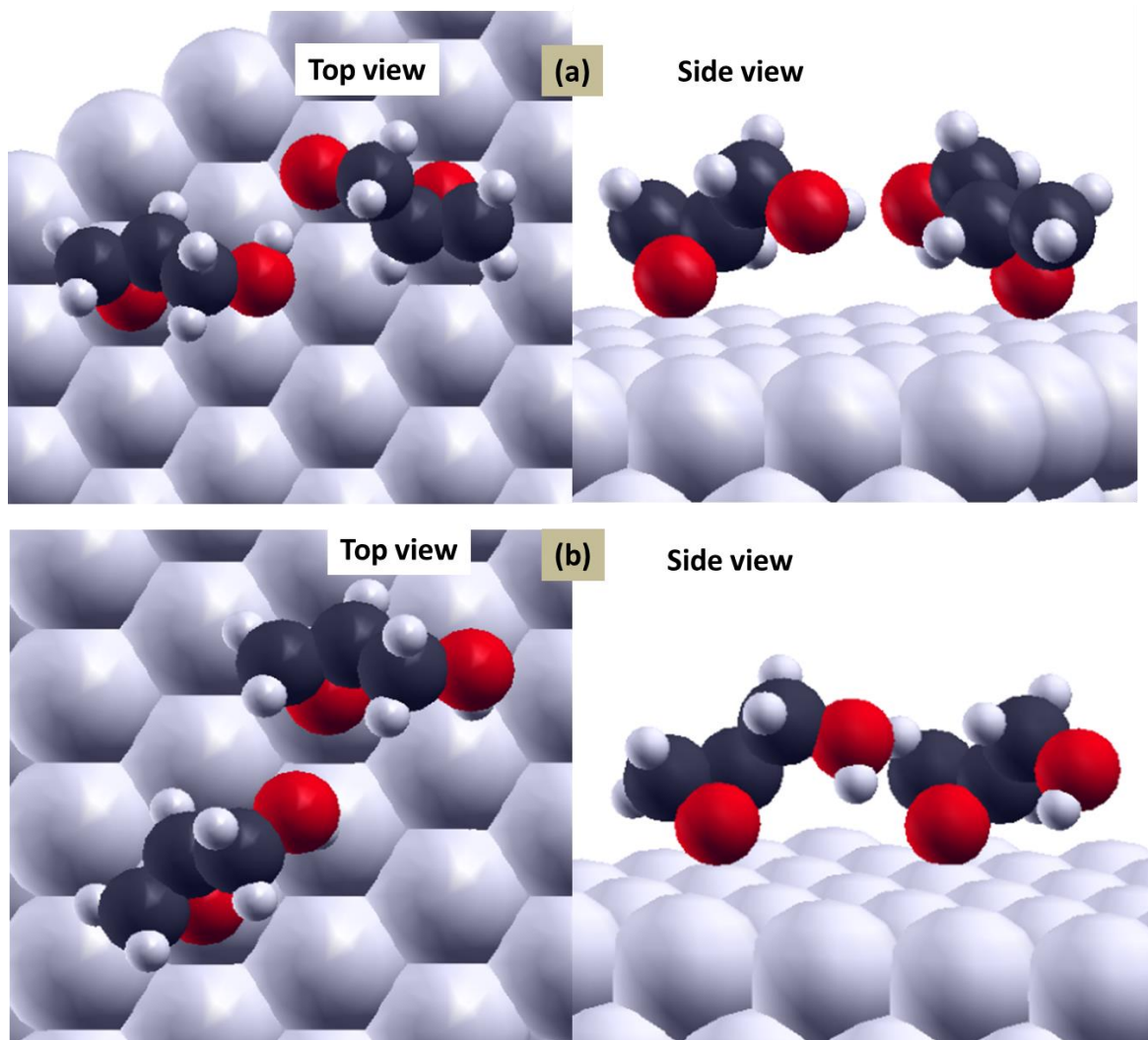
Figure 11-12 DFT optimized glycidol dimer structures. The dimer adsorption geometry allows hydrogen bonding interaction between (a) the –OH groups (b) the –OH group of one glycidol with the epoxy oxygen of the other

   DFT calculations were performed by placing two glycidol molecules on a Pd(111)

slab for a number of different geometries, which allows either hydrogen bonding

interactions between two –OH groups or the epoxy oxygen of one glycidol with the –OH

group of other, and the two most stable dimer structures are shown in Figure 11-12.

Figure 11-12 (a) shows a dimer structure which facilitate OH····OH hydrogen bonding

interactions and, as expected, this structure was found to be very stable and yielded an

interaction energy of – 17 kJ/mol. Figure 11-12 (b) shows the other relaxed dimer

structure, where hydrogen bonding interactions occur between the epoxide oxygen of one

glycidol with the –OH group of other. The molecular axis of one glycidol is rotated ~30°

with respect to the other which allows the -OH group to interact with the epoxy oxygen.

The interaction energy was found to be -3 kJ/mol. Therefore from energetic point of

view, it is expected that the glycidol dimer pairs form due to OH····OH interactions. On

the basis of the above DFT calculations we propose a model for the origin of the hexamer

structures observed in STM and is shown in Figure 11-13.
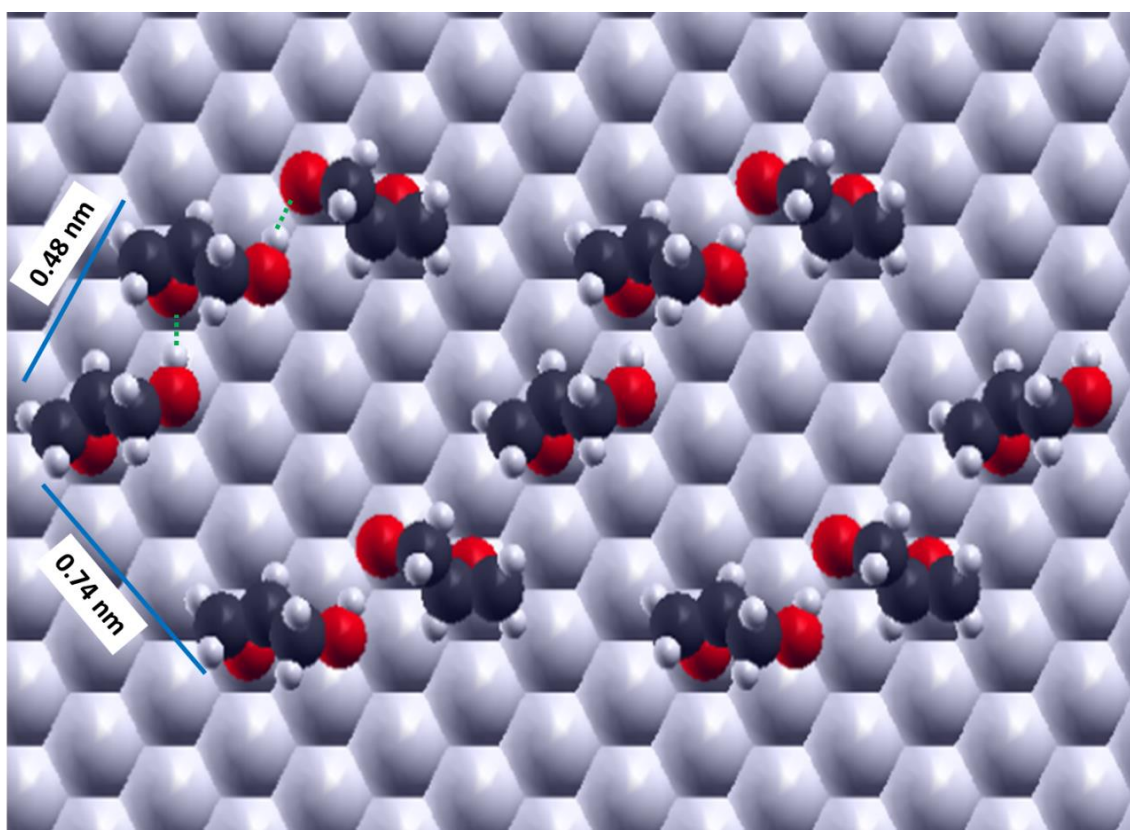
Figure 11-13 A proposed model for the glycidol hexamer structure observed in STM. The hydrogen bonding interactions are indicated in green dotted lines. The spacing between the glycidol molecules in the proposed hexamer match with the experimentally observed STM images

The hexamers are proposed to consist of glycidol dimer pairs, which are coupled

by glycidol monomers. The glycidol dimer pairs, where hydrogen bonding occurs

between the two –OH groups (as shown in Figure11-12(a)) were placed parallel to each other. The glycidol monomers, whose molecular backbone is at an angle of ~30° to the glycidol dimer pairs fit in between the dimer pairs, which facilitate weak hydrogen bonding interactions between the epoxy oxygen atoms and the –OH groups, in a similar manner as shown in Figure 11-12(b) and leads to the formation of hexamer structures.

11.3.3 STM of Propene on Pd(111)

STM images are collected following propene adsorption on a Pd(111) surface at ~120 K and is shown in Figure 11-14.
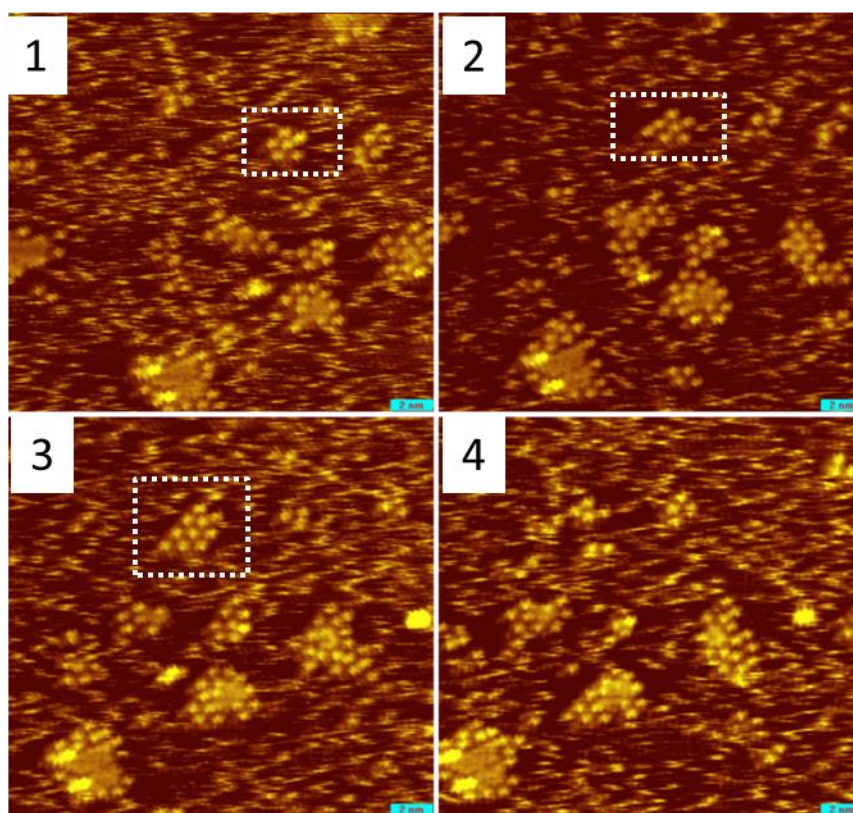
Figure 11-14 Four sequential STM images of propene on a Pd(111) surface showing mobility. Propene was dosed and imaged at a sample temperature of ~120 K (-1 V, 49 pA). The white dotted squares show the growth of a propene ensemble (1 to 3), which disappears in image 4

Figure 11-14 shows 4 time-lapse images collected immediately after dosing

propene onto the surface, which clearly shows the adsorption dynamics. The molecules self-organize to form clusters of different sizes and orientations. Next to the clusters, streaky lines appear in the scanning direction indicating that the individual molecules are diffusing on the surface. The size and orientation of the clusters varies in the sequential images. The individual molecules are observed to freely attach and detach from a cluster. An example is highlighted by white dotted boxes. Scan 1 to 3 shows the growth of a propene ensemble which disappears in scan 4. It has also been observed that the local coverage of the molecules increase on step edges over time (data not shown).

Figure 11-15 shows an STM image which was collected after a long time interval of dosing, which shows the presence of larger propylene ensembles and step edge decoration. No molecular motion was observed, which indicates that once propylene molecules coalesce into an ensemble, they become quite stable. Within the cluster, propene molecules are oriented in different directions.
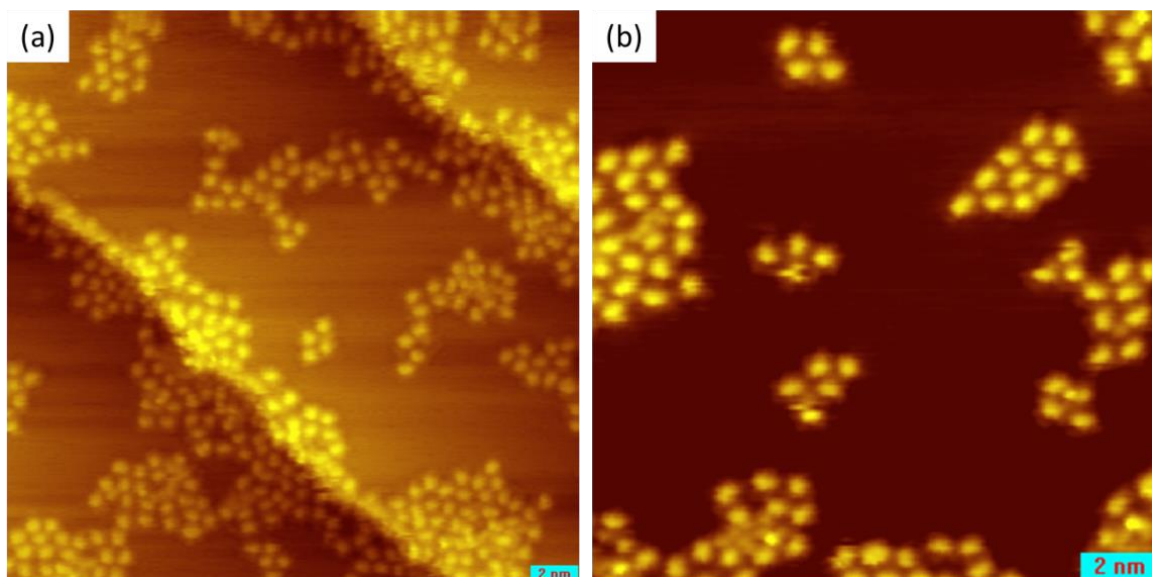
Figure 11-15 (a) STM image of propene on Pd(111) collected at ~120 K after a long interval of dosing. Propene molecules decorate the step edge and form clusters of different size (b) A zoomed in image which clearly show the molecular resolution within the cluster (0.5 V, 80 pA).

Figure 11-16 shows an STM image which was collected after annealing the surface to 140 K. Annealing the surface did not allow any additional ordering but the surface ensembles are slightly larger in size than those collected at 120 K. There are some molecules observed on the step edges and the terraces mostly consist of larger surface ensembles and fewer individual molecules.
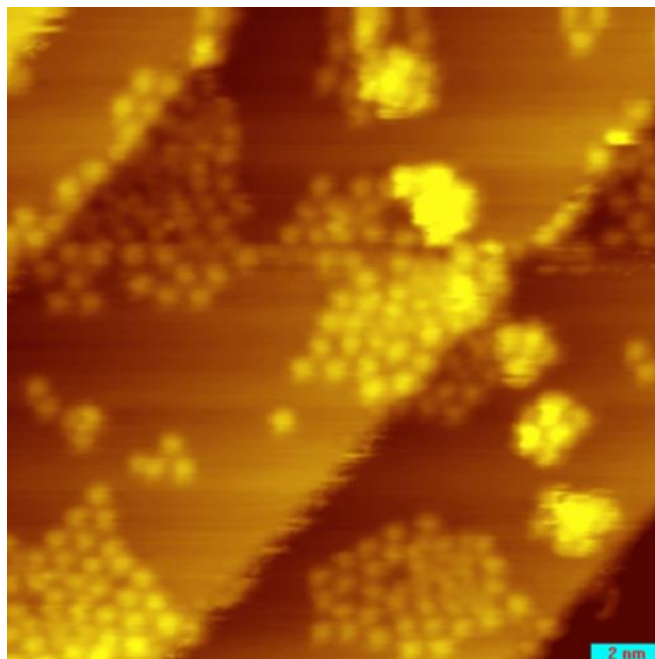
Figure 11-16 STM image of propene on Pd(111) collected at ~140 K after a long interval of dosing. Propene molecules form larger surface ensembles (0.55 V, 95 pA)

Figure 11-17 (a) and (c) show images collected over two different surface areas which show the presence of large surface ensembles. Figure 11-17 (a) shows some smaller clusters and a larger ensemble. By closely examining the smaller clusters, which consist of four propene molecules (highlighted in white and green dotted squares), it was observed that one of them is oriented along the surface close-packed direction, as highlighted in white square, and other is oriented at an angle of 30° to it, as highlighted by green square. Within the cluster, molecules are oriented in different directions which make it difficult to assign any unit cell unambiguously.

However, the approximate spacing between the propene molecules in those two different clusters is ~0.8 nm, which is close to three Pd lattice spacing (0.825 nm) and suggests the formation of a 3×3 unit cell.
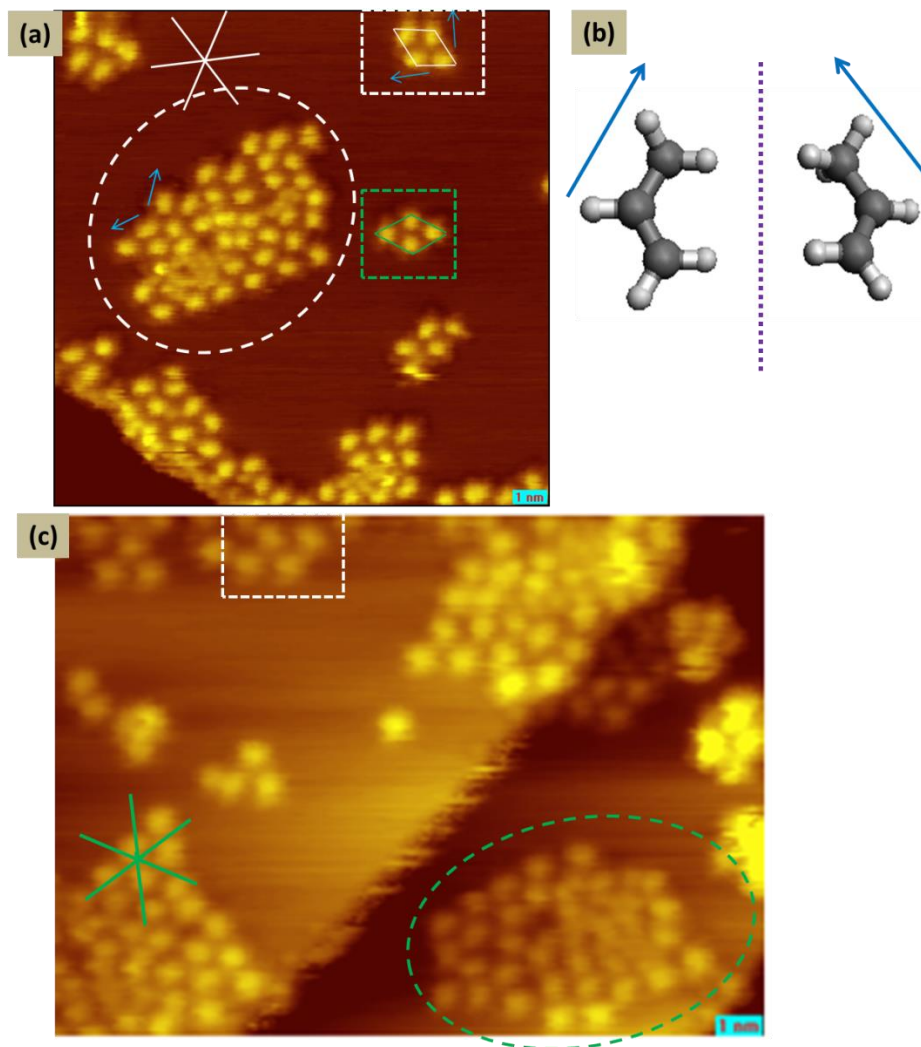
Figure 11-17 (a) 14×14 nm scan area STM image of propene on Pd(111), which shows the presence of two different unit cells as highlighted by white and green square boxes. The larger ensemble consists of unit cell as highlighted by white square box. The surface close-packed direction is shown in white lines. Two adsorbate enantiomers of propene are observed, which are highlighted in blue arrows. (b) Schematic showing mirror breaking on the surface: depending on which side turn towards the surface propene from two different adsorbed enantiomers. (c) The ensembles consists of unit cells as highlighted by green dotted square (figure 11-17(a)), where the molecules are rotated 30° to the surface close-packed direction (shown in green lines). (0.55 V, 95 pA)

By examining a number of the larger ensembles, it was observed that the smaller clusters, shown in white and green dotted squares, are the repeat units for the larger ensembles. The larger cluster shown in Figure 11-17 (a) (white dotted circle) consists of the unit cell as shown in white dotted square, where the molecules are aligned in the crystallographic direction. Figure 11-17 (c) shows an example where the larger surface ensemble (highlighted in green dotted circle) consists of the unit cell as highlighted in green dotted square box, where the molecules are oriented at an angle of 30° to the close-packed direction.

When propene is adsorbed on the surface, depending on which side of the molecule adsorb on the surface, it can form two adsorbate enantiomers (as shown in Figure 11-17 (b)). The two resulting static adsorption configurations are enantiomers because rotation and translation does not allow their superposition. Only rolling or flipping the adsorbed species could can cause an inversion of enantiomers, which is energetically not favorable on the surface. Some examples of propene molecules with different enantiomeric form induced by adsorption are shown in Figure 12-17(a) and highlighted by blue arrows.

11.3.4 STM of 3,3,3-Trifluoro Propene on Pd(111)

STM images are collected following trifluoro propene adsorption on Pd(111) at ~120 K to explore whether replacing the $-CH_3$ group by $-CF_3$ group has any influence on the surface structure. The same clustering of molecules was observed with triflouro propene, but no additional ordering was found. Within the clusters some fuzzy background was observed, which is probably due to some trapped water molecule adsorbed from the background.
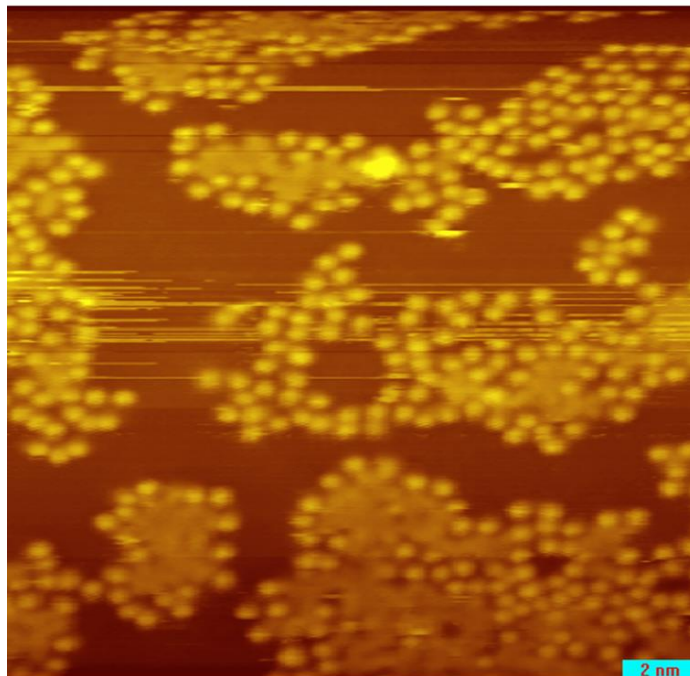
Figure 11-18 STM image of trifluoropropene on Pd(111) when the surface was dosed and imaged at ~120 K. (-0.5 V, 75 pA)

11.4 Discussion

From the previous DFT calculations, it was observed that PO [24] bonds to a Pd atop site through the lone pair electrons of the epoxy oxygen. PO forms equally spaced, one-dimensional linear chain structures on Pd(111) surface, which is completely different from what was observed on a Pt(111) surface, where propylene oxide forms disordered overlayer. On Pt(111) surface,[6] the saturated layer of enantiopure PO is 20 % more dense than the racemic PO, in spite of the absence of any long range ordering on the surface. However, on Pd(111) surface the desorption yield of both enantiopure and racemic PO are identical, which is different to what has been observed on Pt(111). The difference in these experimental findings between Pd and Pt is surprising because based on spectroscopic evidences, PO follows similar chemistry on both the metal surfaces. The difference could be attributed to slightly different reactivity of the two metals which leads

to one dimensional ordering of PO on Pd(111) and a disordered overlayer on Pt(111). On Pt(111), the difference in desorption yield of enantiopure versus racemic PO is attributed to adsorbate assisted kinetic effect, where adsorption of a PO molecule assist the adsorption of other PO molecules with different probabilities for homo *versus* hetero enantiomeric pair. It is possible that on Pd(111), this kinetics is very fast at 140 K and thus not observed under the experimental conditions.

Glycidol molecules adopt an adsorption geometry which is similar to PO and bonds to a palladium atop site.[22] Rather than forming one-dimensional linear chain structures like PO, glycidol forms hexamers which consists of glycidol dimers. DFT calculations suggest that there are two different possibility of hydrogen-bonding interactions between glycidol molecules; one in which the interaction is through the –OH group of one glycidol and the epoxy oxygen of the other, and the other is through –OH – OH interactions while the latter being energetically more favorable. The hexamer structures are proposed to consist of glycidol dimer pairs which are connected by glycidol monomers through weak hydrogen-bonding interactions between the –OH group of glycidol monomers with the epoxy oxygen of the glycidol dimer pairs. At high coverages the glycidol molecules are densely packed and form a crowded over layer structure due to extended hydrogen-bonding interactions.

Previous spectroscopic study shows that propene monolayer adopts a di-σ bonding structure on both Pd(111) and Pt(111) surfaces, while the multilayer adsorption is through π bonding. DFT calculations for propene adsorption on a Pt(111) surface further supports this findings. DFT calculation has been performed for both di-σ bonded and π bonded propene on a Pt(111) surface,[25] which shows that the di-σ bonded species is

energetically more favorable. Based on the above study, it is expected that on Pd(111), the observed propene molecules in STM adopt di-σ bonding adsorption geometry. Individual propene molecules are very mobile on the surface at ~120 K. Over a very long period of time, propene molecules form larger ensembles on the surface in which the individual propene molecules are very stable, which indicates that there are lateral interactions between the propene molecules on Pd(111). The size and orientation of the clusters vary and within the cluster, different adsorbate enantiomers of propene were observed. Gas-phase propene has a small dipole moment of ~0.33 D and it is less likely that the formation of clusters is due to dipole-dipole interaction between the molecules. Therefore, the driving force for the formation of these stable ensembles is van der Waal's interactions between the adjacent molecules, which lead to the formation of clusters, but not structures with long-range order.

When a trifluoro methyl group is substituted, a large structural change is expected since fluorine is the most electronegative element. 3,3,3 trifluoro propene has a dipole moment of ~2.5 D. STM images of 3,3,3 trifluoro propene on Pd(111) surface shows clustering of the molecules like propene, with no long range-ordering. This also confirms that both propene and trifluoro propene form ensembles on the surface due to van der Waal's interactions.

11.5 Conclusions

In contrast to PO adsorption on Pt(111), no difference in the saturation coverages of enantiopure propylene oxide *versus* racemic propylene oxide is obtained on a Pd(111) surface. The complete different results obtained on both the metals is ascribed to the surface ordering: PO forms a disordered overlayer on Pt(111) surface, while it order in

one dimensional linear chain structures on Pd(111). Thus, it indicates that the lateral interaction between the propylene oxide molecules on Pt surface is weaker than that observed on Pd(111) surface. Glycidol self-assemble to form hexamer structures at low coverage and at higher coverages the surface consists of dimer rows. This explains the role of hydrogen bonding interactions for the formation of overlayer structures. The absence of any hydrogen bonding group in propylene oxide leads to the formation of one-dimensional chain while the presence of a –OH group in glycidol allows the formation of different two dimensional structures. Propene form larger ensembles on Pd(111) surface, in which different adsorbate enantiomers can be identified. Replacing the –CH$_3$ group in propene by a more electronegative group –CF$_3$ did not change the surface structure, which indicates that both propene and trifluoropropene from ensembles on the surface due to van der Waal's interaction.

11.6 References

1.   Stacchiola, D.; Burkholder, L.; Tysoe, W. T., Enantioselective chemisorption on a chirally modified surface in ultrahigh vacuum: Adsorption of propylene oxide on 2-butoxide-covered palladium (111). *Journal of the American Chemical Society* **2002,** *124* (30), 8984-8989.

2.   Lee, I.; Zaera, F., Enantioselectivity of adsorption sites created by chiral 2-butanol adsorbed on Pt (111) single-crystal surfaces. *The Journal of Physical Chemistry B* **2005,** *109* (26), 12920-12926.

3.   Corvis, Y.; Négrier, P.; Massip, S.; Leger, J.-M.; Espeau, P., Insights into the crystal structure, polymorphism and thermal behavior of menthol optical isomers and racemates. *CrystEngComm* **2012,** *14* (20), 7055-7064.

4.   Collet, A., Separation and purification of enantiomers by crystallisation methods. *Enantiomer* **1999,** *4* (3-4), 157-172.

5.   Srisanga, S.; ter Horst, J. H., Racemic compound, conglomerate, or solid solution: phase diagram screening of chiral compounds. *Crystal Growth & Design* **2010,** *10* (4), 1808-1812.

6.   Karakalos, S.; Lawton, T. J.; Lucci, F. R.; Sykes, E. C. H.; Zaera, F., Enantiospecific Kinetics in Surface Adsorption: Propylene Oxide on Pt (111) Surfaces. *The Journal of Physical Chemistry C* **2013,** *117* (36), 18588-18594.

7.   Ponec, V.; Bond, G. C., *Catalysis by metals and alloys*. Elsevier: 1995; Vol. 95.

8.   Horiuti, I.; Polanyi, M., Exchange reactions of hydrogen on metallic catalysts. *Transactions of the Faraday Society* **1934,** *30*, 1164-1172.

9.   Zaera, F.; Chrysostomou, D., Propylene on Pt (111) I. Characterization of surface species by infra-red spectroscopy. *Surface science* **2000,** *457*, 71-88.

10.   Stacchiola, D.; Burkholder, L.; Tysoe, W., Structure and reactivity of propylene on clean and hydrogen-covered Pd (111). *Surface science* **2003,** *542* (1), 129-141.

11.   Zaera, F.; Chrysostomou, D., Propylene on Pt (111). *Surface science* **2000,** *457* (1), 89-108.

12.   Zaera, F., Probing catalytic reactions at surfaces. *Progress in surface science* **2001,** *69* (1), 1-98.

13.   Stacchiola, D.; Burkholder, L.; Tysoe, W., Ethylene adsorption on Pd (111) studied using infrared reflection–absorption spectroscopy. *Surface science* **2002,** *511* (1), 215-228.

14.   Zaera, F., On the mechanism for the hydrogenation of olefins on transition-metal surfaces: The chemistry of ethylene on Pt (111). *Langmuir* **1996,** *12* (1), 88-94.

15.   Ernst, K.-H., Molecular chirality in surface science. *Surface science* **2013,** *613*, 1-5.

16.   Ernst, K. H., Molecular chirality at surfaces. *physica status solidi (b)* **2012,** *249* (11), 2057-2088.

17.   Parschau, M.; Hug, H. J.; Rieder, K. H.; Ernst, K. H., Hopping, turning and flipping of single molecules during lateral manipulation with a scanning tunneling microscope. *Surface and Interface Analysis* **2010,** *42* (10-11), 1629-1633.

18.   Parschau, M.; Passerone, D.; Rieder, K. H.; Hug, H. J.; Ernst, K. H., Switching the chirality of single adsorbate complexes. *Angewandte Chemie International Edition*

2009, *48* (22), 4065-4068.

19.   Brown, N. F.; Barteau, M. A., Epoxides as probes of oxametallacycle chemistry on Rh (111). *Surface science* **1993,** *298* (1), 6-17.

20.   Lambert, R.; Ormerod, R.; Tysoe, W., Thermal decomposition of ethylene oxide on Pd (111): comparison of the pathways for the selective oxidation of ethylene and olefin metathesis. *Langmuir* **1994,** *10* (3), 730-733.

21.   Shekhar, R.; Barteau, M. A., Ring-opening reactions of ethylene oxide on Pd (110) surfaces. *Surface science* **1996,** *348* (1), 55-66.

22.   Mahapatra, M.; Tysoe, W., Chemisorptive Enantioselectivity of Chiral Epoxides on Tartaric-acid Modified Pd (111); Three-Point Bonding. *Physical Chemistry Chemical Physics* **2015**.

23.   Mahapatra, M.; Tysoe, W. T., Adsorption and reaction pathways of a chiral probe molecule, S-glycidol on a Pd (111) surface. *Catalysis Science & Technology* **2015**.

24.   Bustos, V.; Linares, D.; Rebaza, A. G.; Tysoe, W.; Stacchiola, D.; Burkholder, L.; Zgrablich, G., Monte Carlo Theory Analysis of Thermal Programmed Desorption of Chiral Propylene Oxide from Pd (111) Surfaces. *The Journal of Physical Chemistry C* **2009,** *113* (8), 3254-3258.

25.   Nykänen, L.; Honkala, K., Density functional theory study on propane and propene adsorption on Pt (111) and PtSn alloy surfaces. *The Journal of Physical Chemistry C* **2011,** *115* (19), 9578-9586.

Chapter 12
Conclusions

In this dissertation some of the fundamental aspects of chiral modification of a metal (Pd(111)) surface have been studied. These investigations were motivated by the increasing demand of performing heterogeneous enantioselective catalysis on chirally modified surfaces. We have investigated the chirality bestowed by adsorption of small organic molecules to an active metal surface. The complex metal/modifier interfaces are characterized by powerful surface-science techniques performed in UHV and the experimental results are complemented by first principle DFT calculations. The enantioselectivity of the chirally modified surfaces is measured in UHV by using chiral probe molecules to help explain the nature of interaction of a chirally modified surface with another chiral molecule. These model studies combined with theoretical calculations are a promising strategy for the fundamental investigation of asymmetric catalysis.

Four different organic molecules: D-alanine, D-tartaric acid, L-aspartic acid and *R*-1-(1-naphthyl) ethylamine (NEA) are used as chiral modifiers on Pd(111) surface and the way the modifiers impart chirality is investigated.

Alanine has been studied in detailed by various methods, including TPD, RAIRS, XPS, STM and DFT. The results indicated that alanine is present both as zwitterions and anions on the surface. Alanine self-assembles on the surface *via* hydrogen-bonding interactions between the zwitterionic and anionic species to form dimeric pairs and tetramers. The pocket of the amino acid tetramers allow enantiospecific adsorption of the chiral probe molecule propylene oxide and glycidol which is measured by TPD. DFT

calculations indicate that the chiral pocket is provided by the metastable tetramer, while the most stable tetramer is too small to accommodate the chiral probes. However, the energy barrier between the two isomers of alanine tetramer is very small so that interconversion between the two tetrameric forms is possible at 300 K, which allows the adsorption of the probe in the chiral pocket. These amino acid tetrameric templates are reminiscent of the induced-fit model for enzymes in which fluctuations enable the reactant–substrate binding. Overall it has been concluded that amino acids provide organizational chirality to the Pd(111) surface by forming discrete chiral templates in the form of tetramers, and enantioselectivity is induced by fitting the chiral probe into the pocket defined by the tetramers. The results are shown in Chapters 3, 4 and 5.

D-(-)-tartaric acid spectroscopic results and STM images showed that the adsorption of tartaric acid results in various adsorbate structures where the nature of the adsorbed species is highly dependent on coverage and dosing temperature. The thermodynamically most stable bitartrate species only form at low coverages while monotartrate species form at higher coverages. At low coverages, isolated bitartrate species provide the chiral motifs and the hydrogen-bonding interaction between two bitartrate species is not favorable due surface stress induced by the bitartrate adsorption. On the other hand the monotartrate species undergo extensive mutual hydrogen-bonding interactions and form oligomeric species. Two different tartaric acid derived ordered structures are formed on the Pd(111) surface, the formation of which are kinetically limited. One of the observed ordered domains consists of rows of bitartrate dimers with empty channels between the dimer rows. The evolution of this phase is ascribed to surface stress energy; when two or more bitartrate species are placed adjacent to each

other, the surface stress energy increases and can be relieved by redistribution of the adsorbed species to larger separations. Thus, the ordered domains formed from the bitartrate species is proposed to occur to minimize the surface stress energy. The second type of ordered domain is formed due to mutual hydrogen bonding interaction between the monotartrate species. The results indicate that the interaction between the bitartrate species is through substrate whereas the interaction between the monotartrate species is largely due to hydrogen-bonding interactions. DFT calculations yield excellent agreement with the experimentally observed results.

Among all the surface structures observed from tartaric acid derived species, only the bitartrate species is enantioselective. Propylene oxide did not show any enantioselectivity while glycidol provides a modest enantioselectivity at low tartaric acid coverages, ascribed to its ability to hydrogen bond to the isolated bitartrate species. In this case enantioselectivity is achieved due to a one-to-one interaction between the modifier and the probe. DFT calculations model the enantiospecific interaction between the modifier and the probe, where, an energy difference of 6 kJ/mol is calculated for the homo *versus* hetero-chiral pairing. The enantioselectivity obeys a traditional three-point rule which is dominated by the strongest binding of the chiral probe (glycidol) to the surface and the ability of a group (or groups) in the probe to be correctly positioned to simultaneously undergo two distinct bonding interactions with the chiral center. In the case of glycidol, these are hydrogen-bonding interactions. These results are discussed in Chapters 6, 7 and 8.

Thus alanine and tartaric acid modified Pd(111) surface provides enantioselectivity by completely different mechanisms; alanine provides a templated

surface while tartaric acid provides one-to-one chiral modifier. The study of aspartic acid was motivated by its functional groups that are similar to both alanine and tartaric acid. The experimental results indicate that aspartic acid resembles the bonding and orientation of alanine on Pd(111), where bonding to the surface occurs through the amine group and one carboxylate group. Aspartic acid self-assembles on the surface due to hydrogen-bonding interactions and forms honeycomb islands which are completely different from the structural motifs observed when alanine and tartaric acid were used as modifiers on Pd(111). However, the honeycomb motif exposes chiral pores which are ideal candidates for chiral templating. The size of the pore is too large to use propylene oxide or glycidol as chiral probe molecules. DFT modeling is continuing to explore the nature of the self-assembly mechanism and to assist in selecting an ideal chiral probe. The results are summarized in Chapter 9.

R-1-(1-naphthyl) ethylamine (NEA), a chiral modifier, forms a disordered overlayer which provided a 1:1 docking interaction with the prochiral reactant methyl pyruvate (MP). The interaction between NEA and MP is dominated by $C=O\cdots H_2N$ hydrogen-bonding interaction which stabilizes the enol tautomer of MP. The combination of chiral-NEA driven diastereomeric docking with a tautomeric preference causes an enhancement in the hydrogenation activity that will lead to increase enantiomeric excesses in the catalytic reaction for the chirally modified surface, as found experimentally. In this case also, the binding motifs obey the three-point bonding rule. The vinyl group carbons bond to the Pd atop sites and hydrogen bonding occurs between the $C=O\cdots H_2N$ group of enol MP tautomer and the N on the chiral center of NEA. Chemisorption energies to surfaces are typically stronger than hydrogen-bonding

interactions, and thus surface bonding dictates the most stable locations of both the chiral modifier and chiral species or prochiral reactants. The most energetically stable interactions between a chiral modifier with a chiral probe (as in the case of glycidol) or a prochiral reactant (in the case of methyl pyruvate) appear to be predominantly influenced by the way in which their binding location on the surface controls the stereochemistry of the weaker hydrogen-bonding interactions between them. Such a molecular-level understanding of the chiral and diastereomeric interactions with chiral modifiers will eventually lead to the rational design of heterogeneous chiral catalysts. The results are shown in Chapter 10

Finally, in Chapter 11, four different C_3 hydrocarbons have been investigated by STM. Propylene oxide shows one dimensional chain structures while glycidol molecules self-organize to from hexamers due to hydrogen-bonding interactions. The comparative study performed for propylene oxide on Pd and Pt surfaces show that the chemistry is different on both the metals, which is attributed to a strong lateral interaction between the propylene oxide molecules on Pd than Pt. Propene and 3,3,3- trifluropropene form clusters on Pd(111) surface due to van der Waal's interactions. Individual propene and 3,3,3- trifluoropropene molecules were found to be highly mobile on the surface as observed in STM, However, once they form ensembles they were trapped and no molecular motion was observed.

Overall, the results of this dissertation highlight some major aspects of the chiral interactions on surfaces. An understanding of the nature of the interactions between the modifier and the surface is critical for probing the enantioselectivity of modified surfaces. This has been achieved in our model studies by performing experiments at various

coverages and temperatures to identify the nature of the active sites. The importance of hydrogen bonding for supramolecular self-assembly and in the interaction between the modifier and the probe is also observed.

Appendix

Density Functional Theory (DFT) Calculations of NEA/Methyl Pyruvate Docking Complexes

Previous DFT calculations of methyl pyruvate on Pd(111) have shown that it is present both in the *keto* form [2,3] with the C-C bond between the carbonyl carbons located over an atop site and rotated 30° from the $<1\overline{1}0>$ directions, and a flat-lying syn *enol* form [3] with the alcohol oxygen located at an atop site and the carbonyl oxygen located at a bridge site in the initial configuration. Previous work suggested that NEA adsorbs with the bicyclic ring on the dibridge[7] adsorption site on Pd(111).[2] Rotation of the ethylamine group gives rise to two conformers defined as *endo* and *exo* for Pd(111),[2] where the *exo* conformer was found to be very slightly more stable than the *endo* conformer on the dibridge[7] site, by ~2 kJ/mol without van der Waals interactions, increasing to ~3 kJ/mol when they are included. However, the dibridge[6] NEA adsorption site was found to be the most stable on Pt(111) [4] with the *exo* conformer being ~13 kJ/mol more stable than the *endo* conformer. The most-stable NEA structure was therefore recalculated on the dibridge[6] site on Pd(111) and found to be slightly more stable than on the dibridge[7] site. In particular, the *exo* conformer was more stable by ~20 kJ/mol and the *endo* by 11 kJ/mol, indicating that the *exo* conformer is calculated to be ~11 kJ/mol more stable than the *endo* conformer on the dibridge[6] site. However, STM images of NEA on Pd(111) reveal that the *exo* conformer occurs only slightly more often than the *endo* conformer (with a ratio of 6:4) [5] and with a ratio of 7:3 on Pt(111).[4]

This implies that the adsorption of the *endo* and *exo* conformers should be almost isoenergetic.

Based on these results, initial DFT calculations were performed for combinations of the two most stable forms of methyl pyruvate with the two forms of NEA adsorbed on dibridge[7] sites by Garvey *et al.*,[7] initially without including van der Waals interactions. In this appendix van der Waal's corrections are added to the most stable docking complexes observed for NEA adsorbed on dibridge[7] site. In addition, some of the results for the docking complex calculations carried out for NEA adsorption on dibridge[6] sites are also included. For each combination of NEA and methyl pyruvate species, calculations were performed with the methyl pyruvate molecule located at a range of sites around the ethylamine group of the NEA molecule. The carbonyl and alcohol oxygen atoms of the methyl pyruvate species were oriented towards the amine group on the NEA molecule. All the docking complex calculations are carried out for pro-R conformer of methyl pyruvate. The docking complex calculations using the pro-S conformer of methyl pyruvate are currently under investigation.

1. Docking Complexes for NEA Adsorbed on Dibridge[7] Sites.

The docking complex for NEA adsorbed on dibridge[7] sites are reproduced with permission from Garvey *et al.*[7] Eight reasonable starting geometries were identified for methyl pyruvate adjacent to the chiral ethylamine group of *endo* NEA. The converged geometries are displayed in Figure A1. Adsorption energies are calculated from:

$$E_{ads} = E_{tot} - E_{Pd} - E_{MP} - E_{NEA} \qquad \text{(A 1)}$$

where E_{tot} is the total energy of combined methyl pyruvate and NEA on Pd(111), and E_{Pd},

E_{MP}, and E_{NEA} are the total energies the Pd(111) substrate, gas-phase methyl pyruvate, and gas-phase NEA, respectively. Interaction energies are defined as follows:

$$E_{int} = E_{ads} - E_{ads,NEA} - E_{ads,MP} \qquad (A\ 2)$$

where E_{ads} is the adsorption energy of the system as defined above and $E_{ads,NEA}$ and $E_{ads,MP}$ are the adsorption energies of the NEA and methyl pyruvate species, respectively, calculated separately on Pd(111). Adsorption and interaction energies for the eight geometries shown in Figure A-1 are listed in Table A-1.

Eight reasonable starting geometries were then identified for *keto* methyl pyruvate near the ethylamine group of *exo* NEA. The converged geometries of those calculations are shown in Figure A-2 and the adsorption and interaction energies were calculated as described above and are listed in Table A-2. For the combination of *enol* methyl pyruvate and *endo* NEA, seven reasonable starting geometries were considered and the converged geometries are displayed in Figure A-3 and the energies are listed in Table A-3. Finally, seven reasonable starting geometries were identified for *enol* methyl pyruvate near the ethylamine group of *exo* NEA. The converged geometries of those calculations are shown in Figure A-4 and the energies are summarized in Table A-4. The initial calculations without van der Waals' interaction were used to exclude energetically unfavorable docking complexes and these corrections were included for the most stable geometries as the last step.

Figure A-1 Converged geometries for the eight combinations of R-endo NEA and keto methyl pyruvate on Pd(111) calculated with DFT. They are identified as: (a) Geo01, (b) Geo02, (c) Geo03, (d) Geo04, (e) Geo05, (f) Geo06, (g) Geo07, and (h) Geo08.[7]

System	E_{ads} (kJ/mol)	E_{int} (kJ/mol)
R-endo NEA + MP keto A30		
Geo01	-252.2	+18.5
Geo02	-267.6	+3.1
Geo03	-238.5	+32.2
Geo04	-268.9	+1.9
Geo05	-267.0	+3.8
Geo06	-243.8	+26.9
Geo07	-257.2	+13.6
Geo08	-259.7	+11.0

Table A-1 Adsorption and interaction energies of R-endo NEA and keto methyl pyruvate on Pd(111) calculated using DFT for the geometries shown in Figure A-1.

Figure A-2 Converged geometries for the eight combinations of R-exo NEA and keto methyl pyruvate on Pd(111) calculated with DFT. They are identified as: (a) Geo01, (b) Geo02, (c) Geo03, (d) Geo04, (e) Geo05, (f) Geo06, (g) Geo07, and (h) Geo08.[7]

System	E_{ads} (kJ/mol)	E_{int} (kJ/mol)
R-exo NEA + MP keto A30		
Geo01	-263.1	+9.2
Geo02	-271.9	+0.5
Geo03	-258.1	+14.3
Geo04	-251.2	+21.1
Geo05	-262.5	+9.8
Geo06	-260.8	+11.5
Geo07	-257.3	+15.0
Geo08	-235.1	+37.3

Table A-2 Adsorption and interaction energies of R-exo NEA and keto methyl pyruvate on Pd(111) calculated using DFT for the geometries shown in Figure A2. [7]
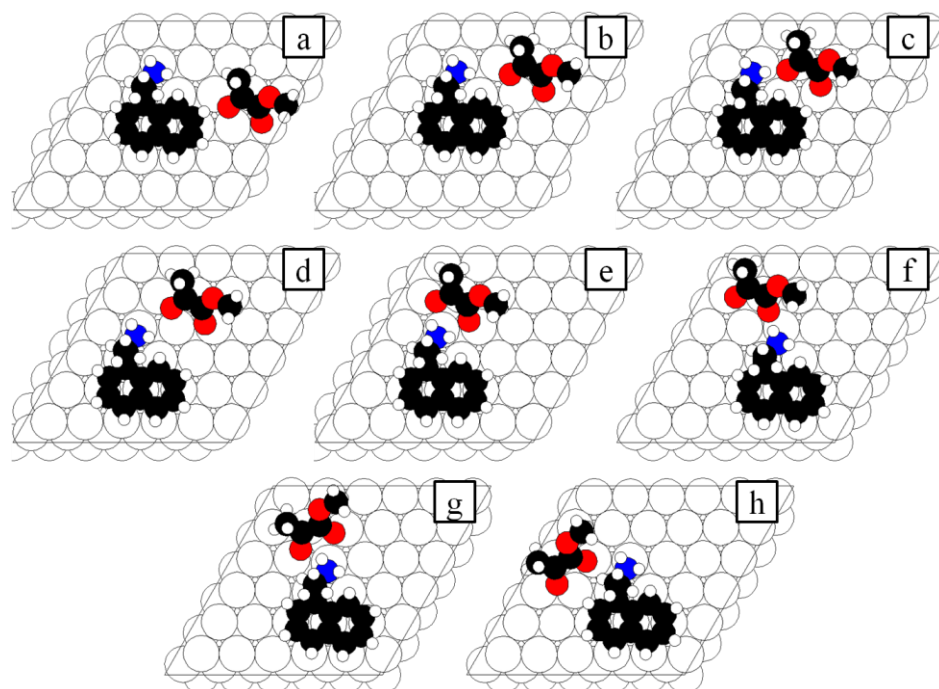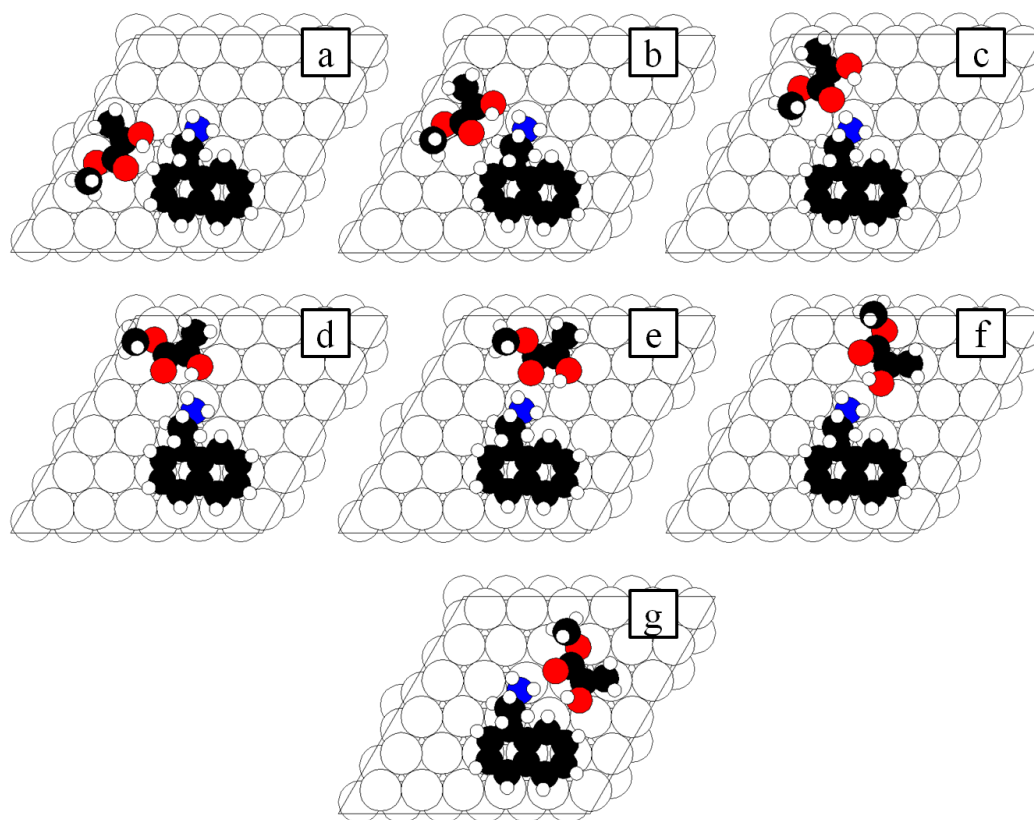
Figure A-3 Converged geometries for the seven combinations of R-endo NEA and enol methyl pyruvate on Pd(111) calculated with DFT. They are identified as: (a) Geo01, (b) Geo02, (c) Geo03, (d) Geo04, (e) Geo05, (f) Geo06, and (g) Geo07. [7]

System	E_{ads} (kJ/mol)	E_{int} (kJ/mol)
R-endo NEA + MP enol syn AB		
Geo01	-229.7	+55.9
Geo02	-246.4	+39.2
Geo03	-286.3	-0.7
Geo04	-265.8	+19.8
Geo05	-286.5	-0.9
Geo06	-272.8	+12.7
Geo07	-272.7	+12.9

Table A-3 Adsorption and interaction energies of R-endo NEA and enol methyl pyruvate on Pd(111) calculated using DFT for the geometries shown in Figure A3.[7]
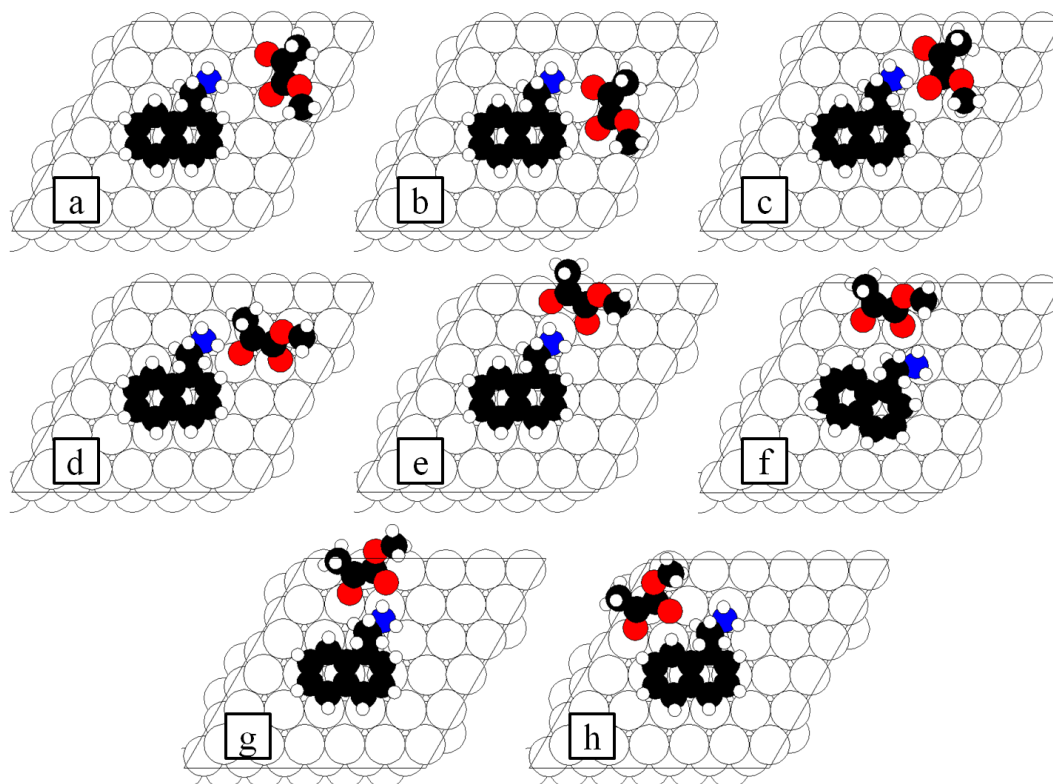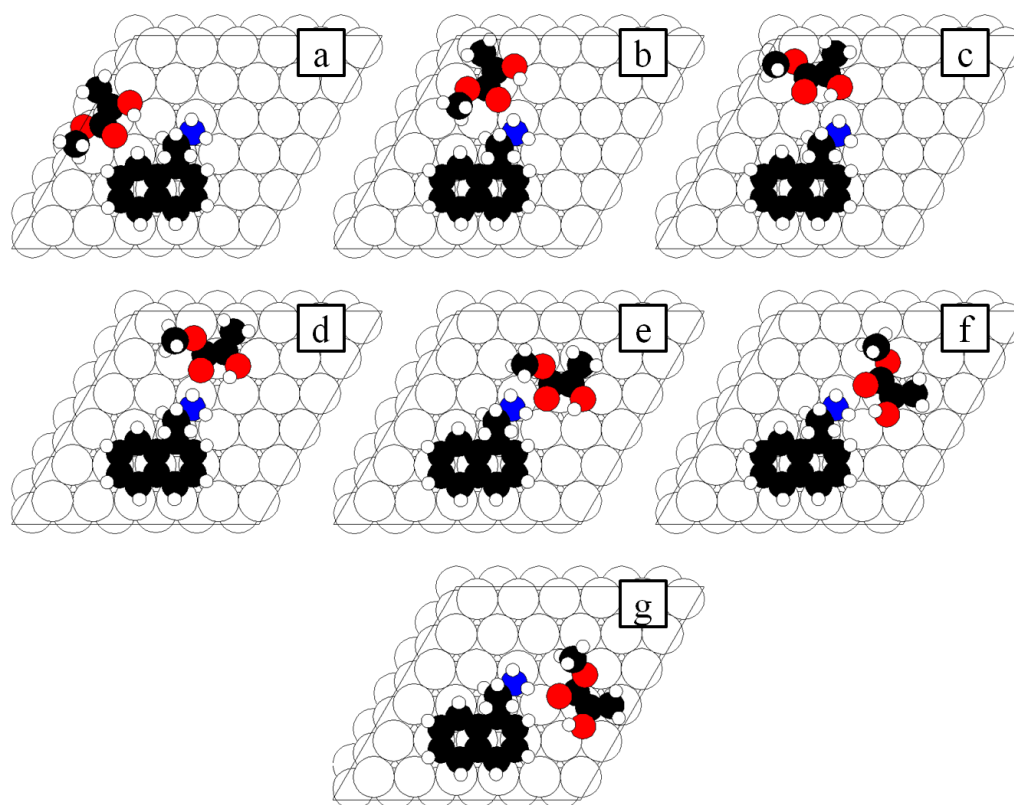
Figure A-4 Converged geometries for the seven combinations of R-exo NEA and enol methyl pyruvate on Pd(111) calculated with DFT. They are identified as: (a) Geo01, (b) Geo02, (c) Geo03, (d) Geo04, (e) Geo05, (f) Geo06, and (g) Geo07.[7]

System	E_{ads} (kJ/mol)	E_{int} (kJ/mol)
R-exo NEA + MP enol syn AB		
Geo01	-273.9	+13.3
Geo02	-288.1	-0.9
Geo03	-269.8	+17.4
Geo04	-292.5	-5.2
Geo05	-265.1	+22.1
Geo06	-277.3	+10.0
Geo07	-292.7	-5.5

Table A-4 Adsorption and interaction energies of R-exo NEA and enol methyl pyruvate on Pd(111) calculated using DFT for the geometries shown in Figure A-4.[7]

The adsorption energies for the NEA+methyl pyruvate docking complexes range from ~-230 kJ/mol to ~-293 kJ/mol indicating that all complexes are relatively strongly bound to the surface. However, the majority of the interactions are repulsive; in particular, the interactions of all the geometries for *keto* methyl pyruvate with both *endo*- and *exo*-NEA are higher than for the separated species. There are only two geometries (Geo03 and Geo05 in Figure A-3, Table A-3) for *endo* NEA with *enol* methyl pyruvate that gain energy relative to the separated species, but the gain is small.

Finally, the effect of including van der Waals interactions on the energies of the two most stable complexes (Geo04 and Geo07 Figure A-4 Table A-4) were then included.[6] This increased the interaction energy for structure Geo04 from -5.2 to -16.0 kJ/ml, and for structure Geo07 from -5.5 to -17.3 kJ/mol.

2. Docking Complexes for NEA Adsorbed on Dibridge[6] Sites.

Nine reasonable starting geometries were identified for *keto* methyl pyruvate in the A0 configuration [3] adjacent to the chiral ethylamine group of *endo* NEA. The converged geometries are displayed in Figure A-5 where the adsorption and interaction energies are defined as in Section 1 of Appendix. Adsorption and interaction energies for the eight geometries shown in Figure A-5 are listed in Table A-5.

Twelve reasonable starting geometries were then identified for *keto* methyl pyruvate in the A30 configuration near the ethylamine group of *endo* NEA. The converged geometries of those calculations are shown in Figure A-6. Adsorption and interaction energies were calculated as described above and are listed in Table A-6. For the combination of *keto* methyl pyruvate in the A0 configuration and *exo* NEA, six reasonable starting geometries were considered and the converged geometries are

displayed in Figure A-7 and the energies are listed in Table A-7. Eight reasonable

starting geometries were identified for *keto* methyl pyruvate in the A30 configuration

near the ethylamine group of *exo* NEA. The converged geometries of those calculations

are shown in Figure A-8 and the energies are summarized in Table A-8.

The following combinations of *enol* methyl pyruvate and NEA were also

considered. Seven reasonable starting geometries were then identified for *enol* methyl

pyruvate in the AB configuration near the ethylamine group of *endo* NEA. The

converged geometries of those calculations are shown in Figure A-9 and the adsorption

and interaction energies were calculated as described above and are listed in Table A-9.

For the combination of *enol* methyl pyruvate in the HH configuration and *endo* NEA,

seven reasonable starting geometries were considered and the converged geometries are

displayed in Figure A-10 and the energies are listed in Table A-10. Eleven reasonable

starting geometries were identified for *enol* methyl pyruvate in the AB configuration near

the ethylamine group of *exo* NEA. The converged geometries are displayed in Figure A-

11 and the energies are listed in Table A-11. Finally, eleven reasonable starting

geometries were identified for *enol* methyl pyruvate in the HH configuration near the

ethylamine group of *exo* NEA. The converged geometries of those calculations are

shown in Figure A-12 and the energies are summarized in Table A-12.

The initial calculations without van der Waals' interaction were used to exclude

energetically unfavorable docking complexes and these corrections were included for the

most stable geometries as the last step.

Figure A-5 Converged geometries for the nine combinations of R-endo NEA and keto methyl pyruvate A0 on Pd(111) calculated with DFT. They are identified as: (a) Geo01, (b) Geo02, (c) Geo03, (d) Geo04, (e) Geo05, (f) Geo06, (g) Geo07, (h) Geo08, and (i) Geo09.

System	E_{ads} (kJ/mol)	E_{int} (kJ/mol)
R-endo NEA + MP keto A0		
Geo01	-296.0	-15.1
Geo02	-287.1	-6.2
Geo03	-292.0	-11.1
Geo04	-299.3	-18.4
Geo05	-285.0	-4.1
Geo06	-283.0	-2.1
Geo07	-299.2	-18.3
Geo08	-294.2	-13.3
Geo09	-258.7	22.2

Table A- 5 Adsorption and interaction energies of R-endo NEA and keto methyl pyruvate A0 on Pd(111) calculated using DFT for the geometries shown in Figure A-5.
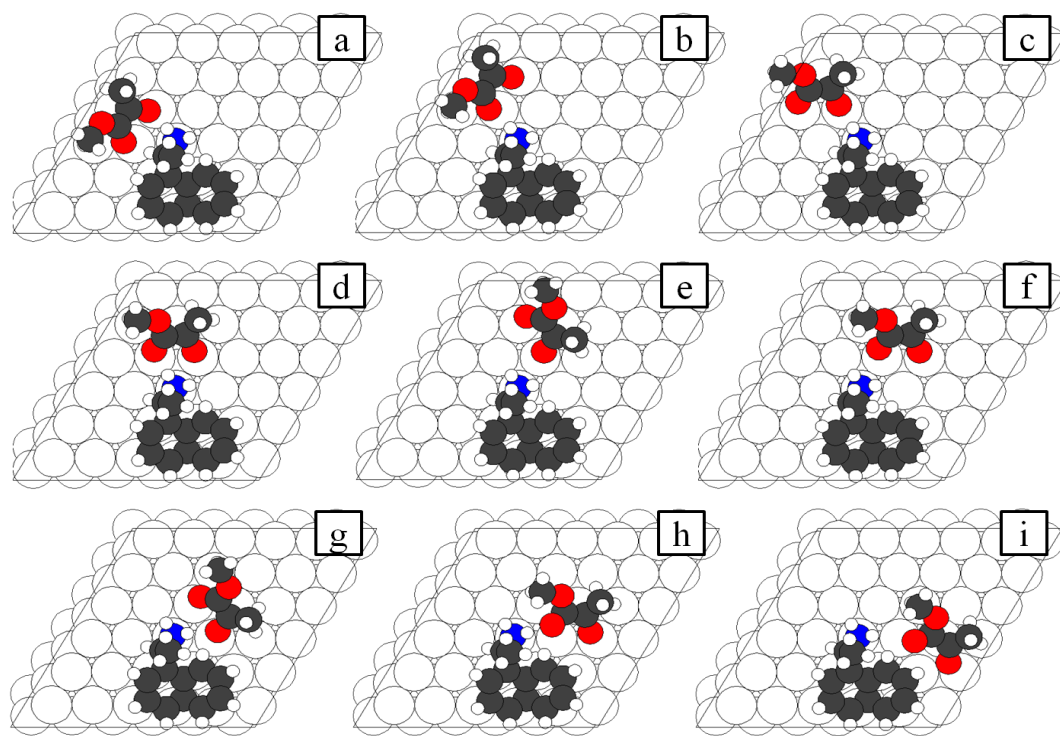
Figure A-6 Converged geometries for the twelve combinations of R-endo NEA and keto methyl pyruvate A30 on Pd(111) calculated with DFT. They are identified as: (a) Geo01, (b) Geo02, (c) Geo03, (d) Geo04, (e) Geo05, (f) Geo06, (g) Geo07, (h) Geo08, (i) Geo09, (j) Geo10, (k) Geo11, and (l) Geo12.

System	E_{ads} (kJ/mol)	E_{int} (kJ/mol)
R-endo NEA + MP keto A30		
Geo01	-272.3	9.4
Geo02	-283.7	-2.0
Geo03	-281.4	0.2
Geo04	-293.6	-11.9
Geo05	-301.0	-19.3
Geo06	-292.3	-10.6
Geo07	-282.5	-0.8
Geo08	-278.0	3.7
Geo09	-276.4	5.3
Geo10	-288.6	-7.0
Geo11	-283.4	-1.7
Geo12	-255.1	26.6

Table A-6 Adsorption and interaction energies of R-endo NEA and keto methyl pyruvate A30 on Pd(111) calculated using DFT for the geometries shown in Figure A-6

.

Figure A-7 Converged geometries for the six combinations of R-exo NEA and keto methyl pyruvate A0 on Pd(111) calculated with DFT. They are identified as: (a) Geo01, (b) Geo02, (c) Geo03, (d) Geo04, (e) Geo05, and (h) Geo06.

System	E_{ads} (kJ/mol)	E_{int} (kJ/mol)
R-exo NEA + MP keto A0		
Geo01	-297.2	-5.7
Geo02	-303.3	-11.8
Geo03	-308.7	-17.2
Geo04	-295.4	-3.9
Geo05	-311.6	-20.1
Geo06	-302.5	-10.9

Table A-7 Adsorption and interaction energies of R-exo NEA and keto methyl pyruvate A0 on Pd(111) calculated using DFT for the geometries shown in Figure A-7.
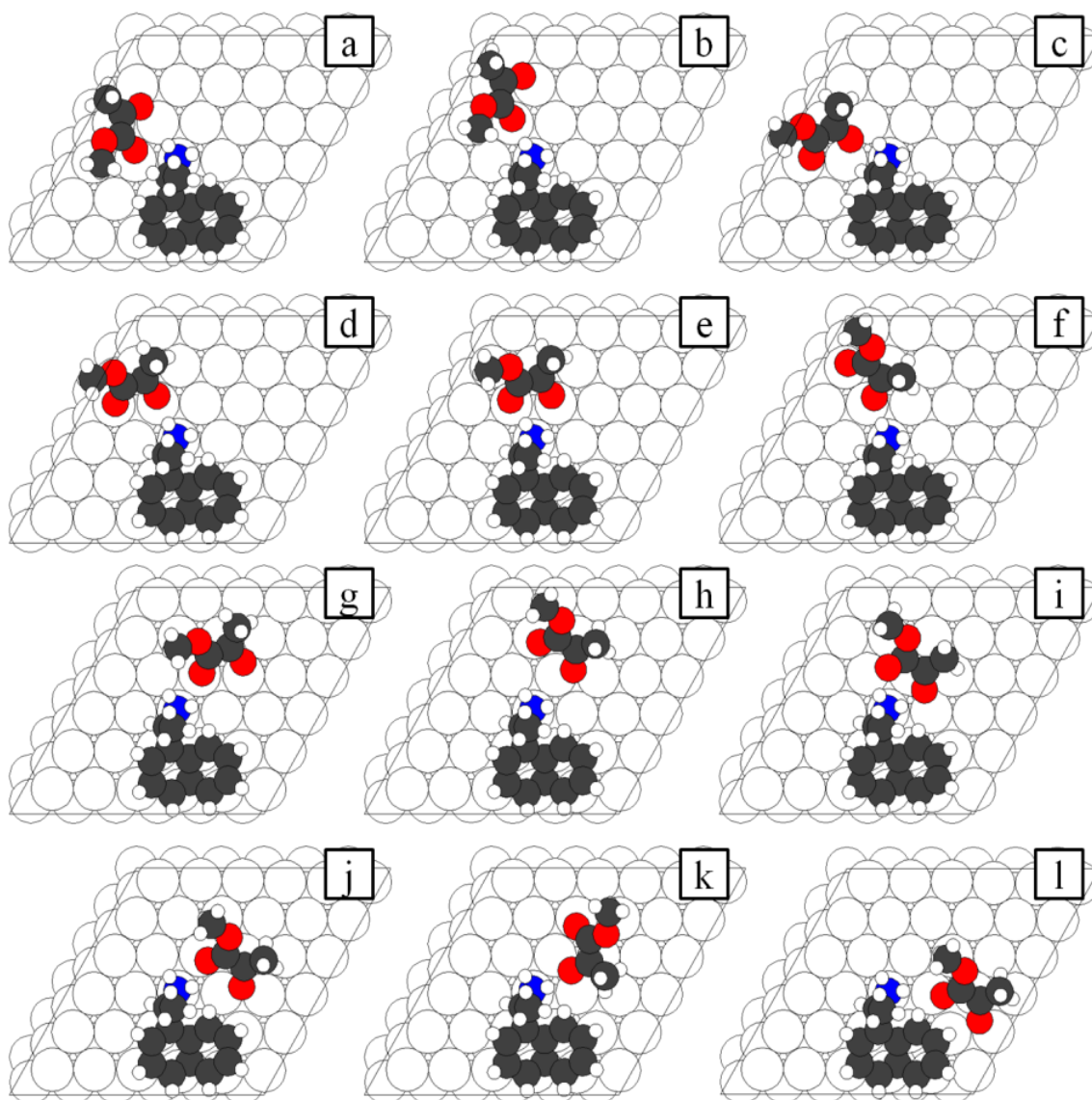
Figure A-8 Converged geometries for the eight combinations of R-exo NEA and keto methyl pyruvate A30 on Pd(111) calculated with DFT. They are identified as: (a) Geo01, (b) Geo02, (c) Geo03, (d) Geo04, (e) Geo05, (f) Geo06, (g) Geo07, and (h) Geo08.

System	E_{ads} (kJ/mol)	E_{int} (kJ/mol)
R-exo NEA + MP keto A30		
Geo01	-288.6	3.7
Geo02	-299.0	-6.7
Geo03	-296.3	-4.0
Geo04	-295.0	-2.7
Geo05	-294.1	-1.8
Geo06	-288.3	4.0
Geo07	-299.7	-7.4
Geo08	-283.0	9.3

Table A-8 Adsorption and interaction energies of R-exo NEA and keto methyl pyruvate A30 on Pd(111) calculated using DFT for the geometries shown in Figure A-8.
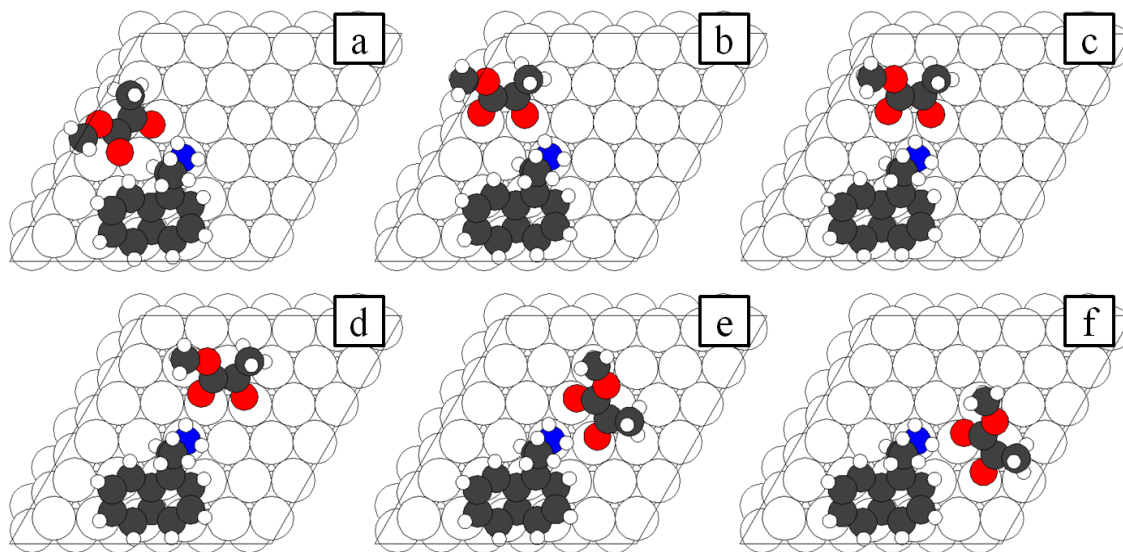
Figure A-9 Converged geometries for the seven combinations of R-endo NEA and enol methyl pyruvate AB on Pd(111) calculated with DFT. They are identified as: (a) Geo01, (b) Geo02, (c) Geo03, (d) Geo04, (e) Geo05, (f) Geo06, and (g) Geo07.

System	E_{ads} (kJ/mol)	E_{int} (kJ/mol)
R-endo NEA + MP enol syn AB		
Geo01	-297.9	-1.3
Geo02	-293.7	2.9
Geo03	-285.4	11.2
Geo04	-300.5	-4.0
Geo05	-272.5	24.0
Geo06	-298.1	-1.5
Geo07	-281.6	14.9

Table A- 9 Adsorption and interaction energies of R-endo NEA and enol methyl pyruvate AB on Pd(111) calculated using DFT for the geometries shown in Figure A-9.
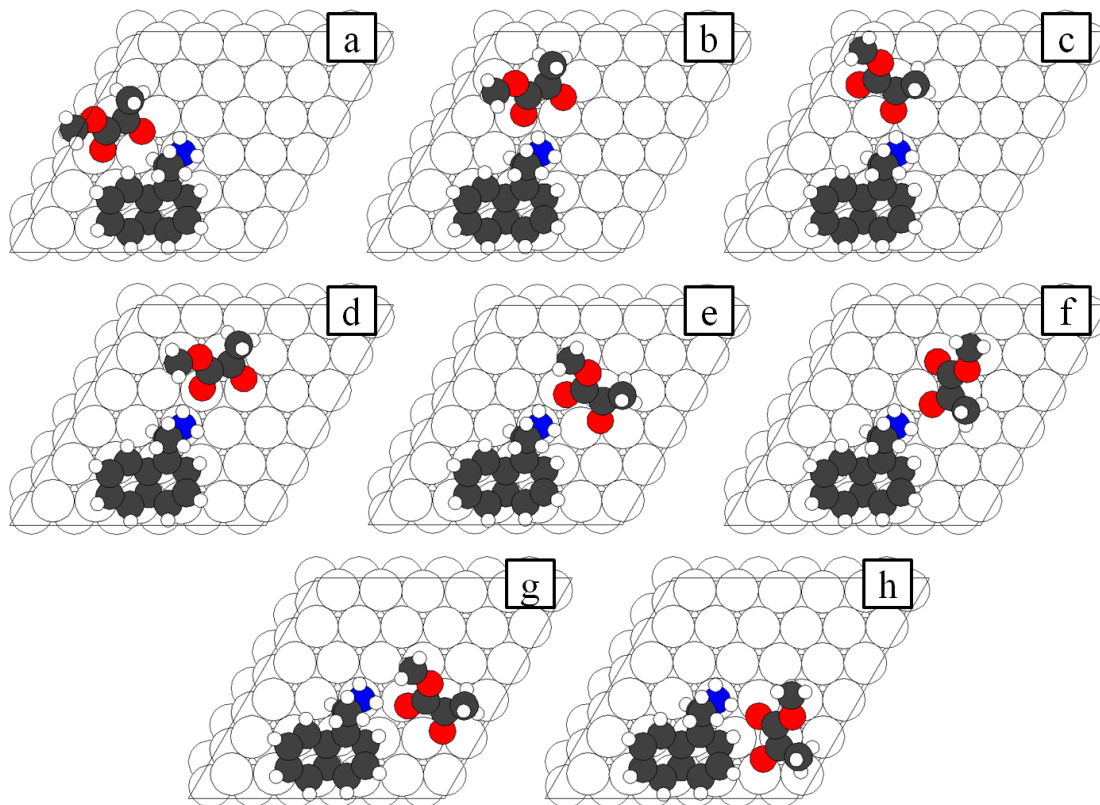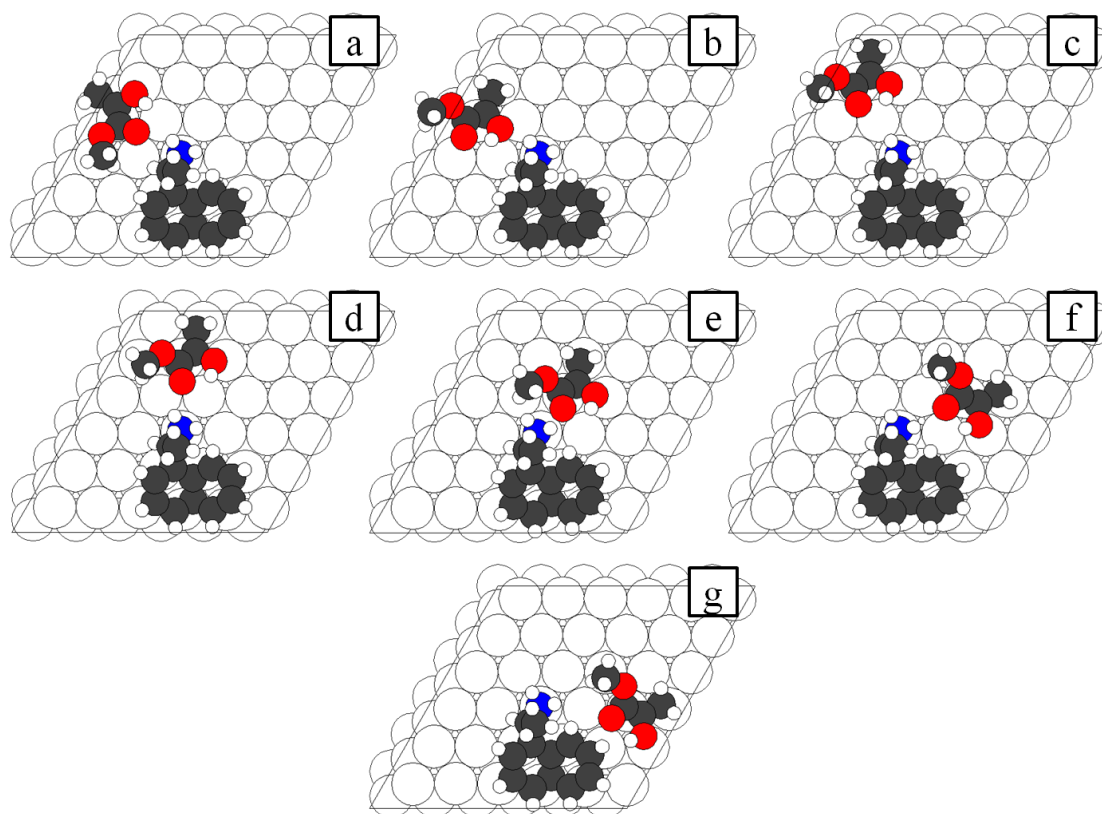
Figure A-10 Converged geometries for the seven combinations of R-endo NEA and enol methyl pyruvate HH on Pd(111) calculated with DFT. They are identified as: (a) Geo01, (b) Geo02, (c) Geo03, (d) Geo04, (e) Geo05, (f) Geo06, and (g) Geo07.

System	E_{ads} (kJ/mol)	E_{int} (kJ/mol)
R-endo NEA + MP enol syn HH		
Geo01	-269.6	27.0
Geo02	-299.3	-2.8
Geo03	-285.8	10.8
Geo04	-273.9	22.7
Geo05	-288.9	7.6
Geo06	-300.2	-3.6
Geo07	-278.6	18.0

Table A-10 Adsorption and interaction energies of R-endo NEA and enol methyl pyruvate HH on Pd(111) calculated using DFT for the geometries shown in Figure A-10.

Figure A-11 Converged geometries for the eleven combinations of R-exo NEA and enol methyl pyruvate AB on Pd(111) calculated with DFT. They are identified as: (a) Geo01, (b) Geo02, (c) Geo03, (d) Geo04, (e) Geo05, (f) Geo06, (g) Geo07, (h) Geo08, (i) Geo09, (j) Geo10, and (k) Geo11.

System	E_{ads} (kJ/mol)	E_{int} (kJ/mol)
R-exo NEA + MP enol syn AB		
Geo01	-300.8	6.4
Geo02	-300.9	6.3
Geo03	-299.7	7.5
Geo04	-311.9	-4.7
Geo05	-298.5	8.6
Geo06	-288.8	18.4
Geo07	-294.3	12.9
Geo08	-307.6	-0.4
Geo09	-303.3	3.9
Geo10	-299.2	8.0
Geo11	-288.5	18.6

Table A-11 Adsorption and interaction energies of R-exo NEA and enol methyl pyruvate on Pd(111) calculated using DFT for the geometries shown in Figure A-11.
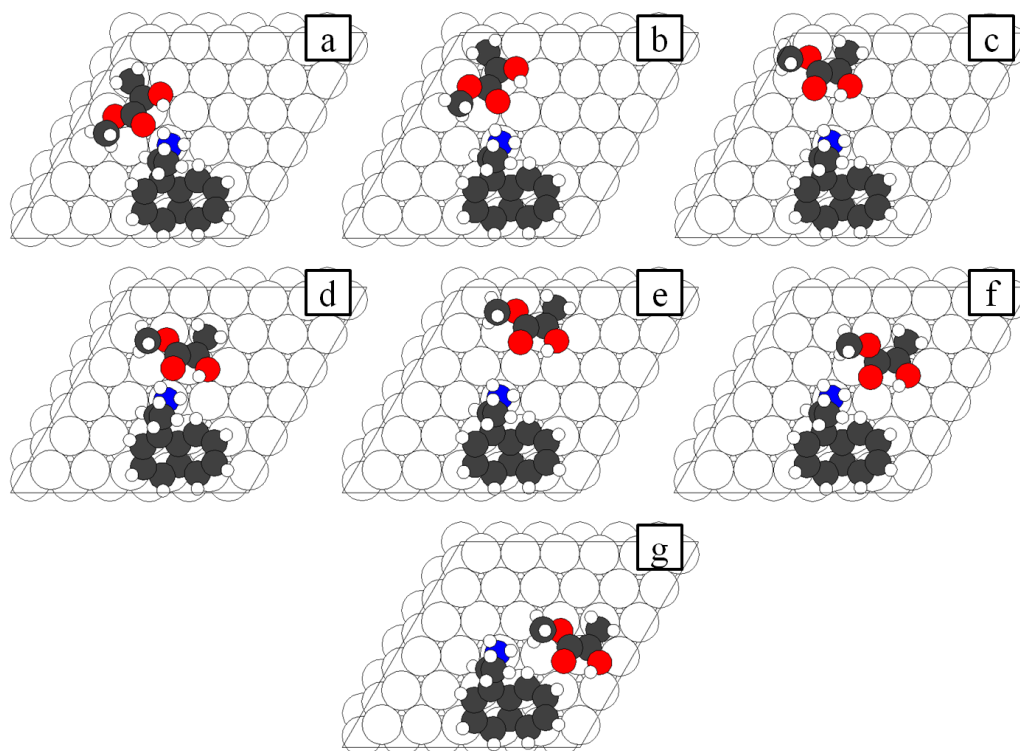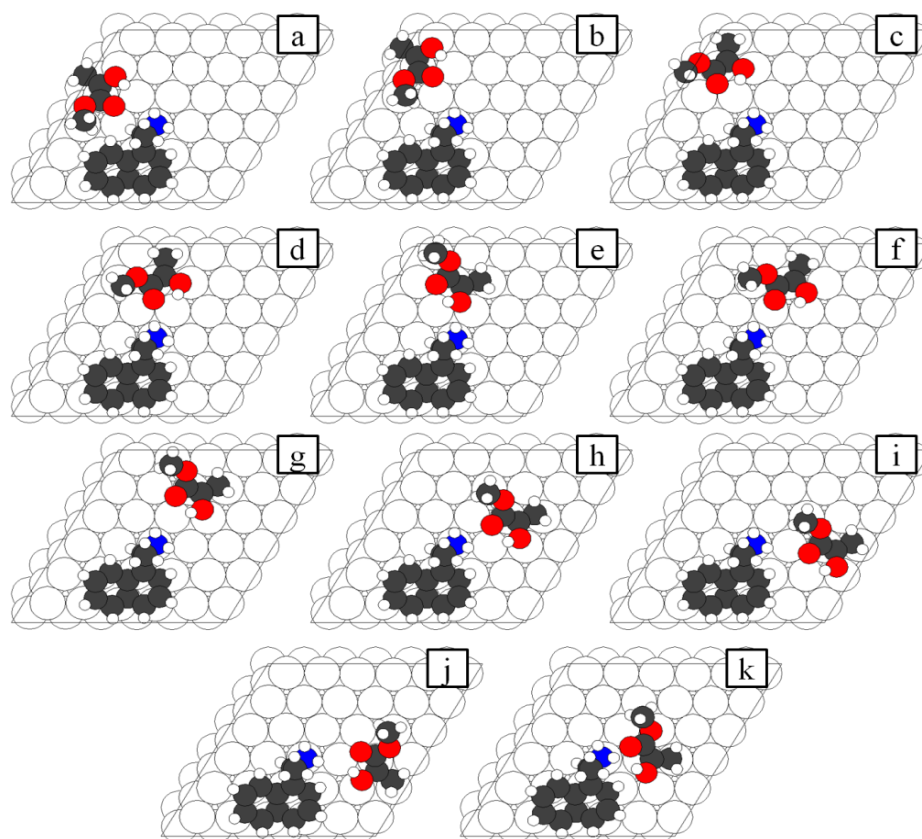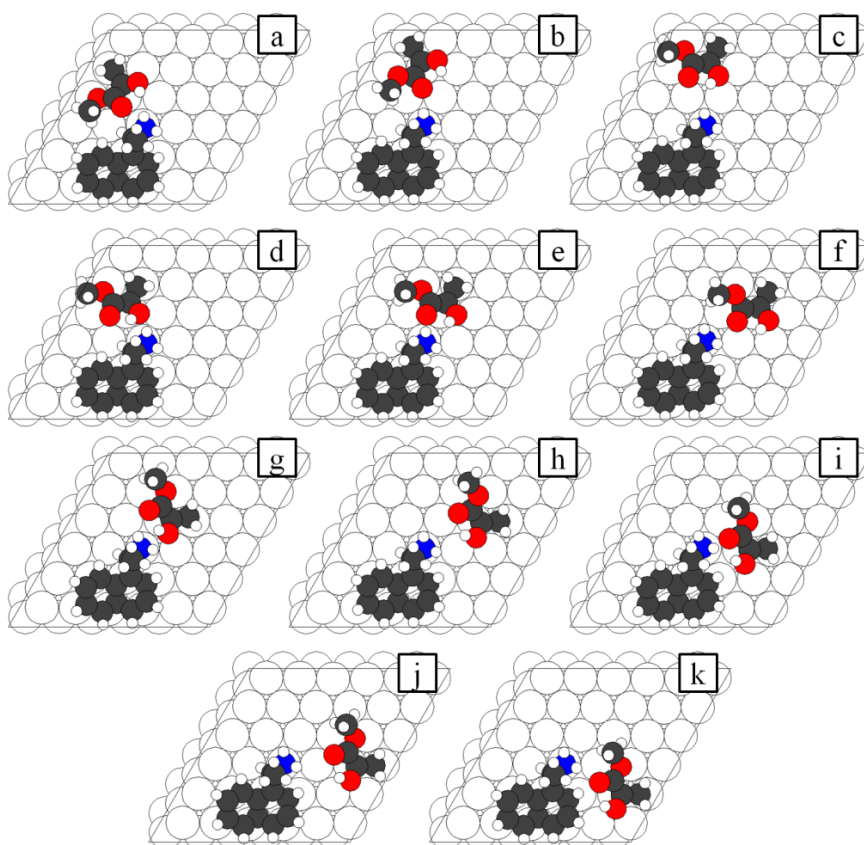
Figure A-12 Converged geometries for the eleven combinations of R-exo NEA and enol methyl pyruvate HH on Pd(111) calculated with DFT. They are identified as: (a) Geo01, (b) Geo02, (c) Geo03, (d) Geo04, (e) Geo05, (f) Geo06, (g) Geo07, (h) Geo08, (i) Geo09, (j) Geo11

System	E_{ads} (kJ/mol)	E_{int} (kJ/mol)
R-exo NEA + MP enol syn HH		
Geo01	-274.9	32.3
Geo02	-312.0	-4.8
Geo03	-295.5	11.6
Geo04	-285.2	21.9
Geo05	-294.9	12.3
Geo06	-305.6	1.6
Geo07	-275.3	31.8
Geo08	-295.6	11.5
Geo09	-288.6	18.5
Geo10	-300.6	6.6
Geo11	-306.4	0.8

Table A-12 Adsorption and interaction energies of R-exo NEA and enol methyl pyruvate HH on Pd(111) calculated using DFT for the geometries shown in Figure A-12.

The adsorption energies for the NEA+methyl pyruvate docking complexes range from ~-255 kJ/mol to ~-312 kJ/mol indicating that all complexes are relatively strongly bound to the surface. Experimental results showed that majority of the docking complexes are formed between the *exo* conformer of NEA and methyl pyruvate. Therefore further calculations to include van der Waals interaction are considered only for the docking complexes with *exo* NEA.
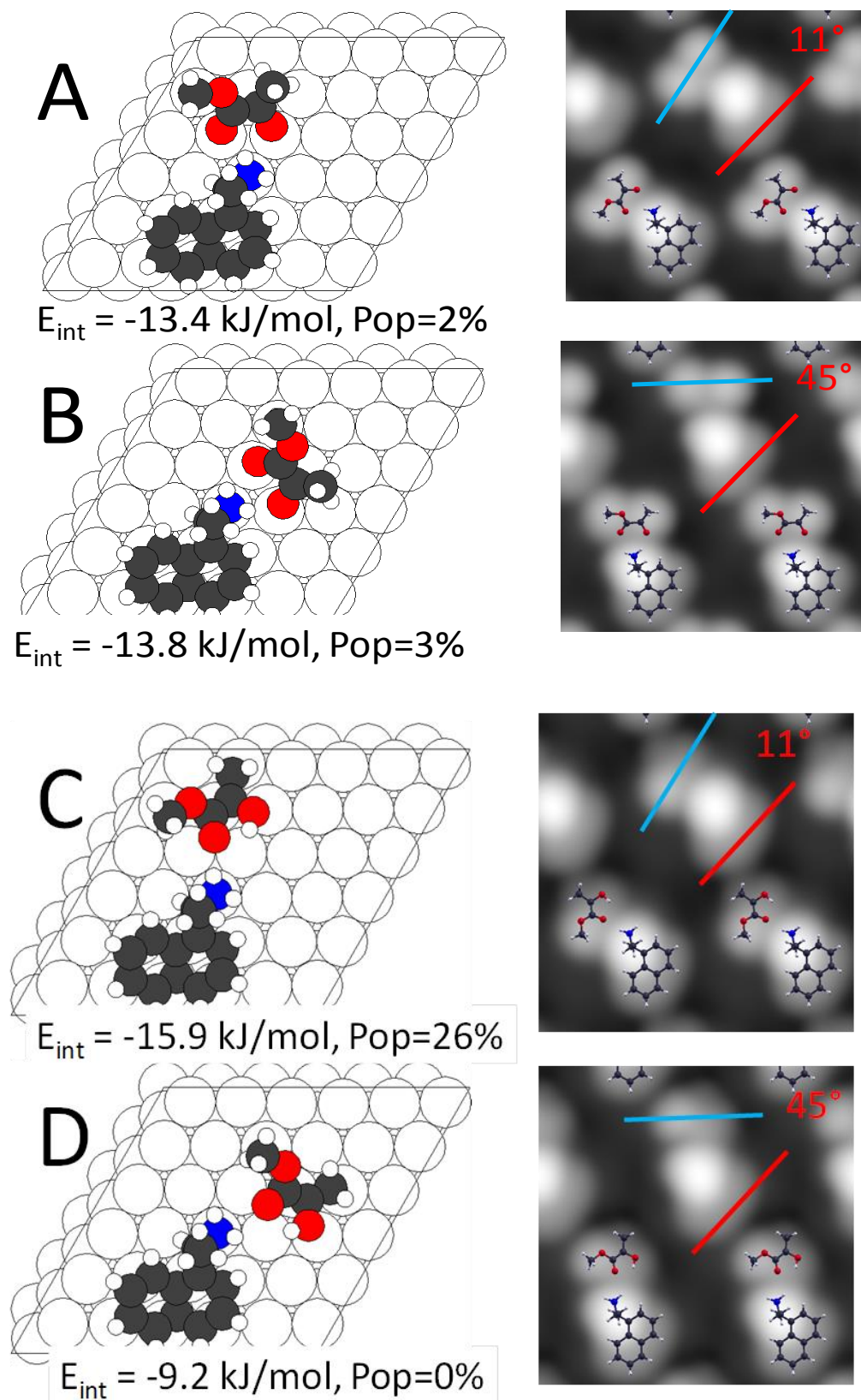
All complexes with an adsorption energy magnitude greater than 305 kJ/mol were calculated by including van der Waals interactions. This included the following complexes all with *exo* NEA: *keto* methyl pyruvate A0, Geo03 and Geo05; *enol* methyl pyruvate AB, Geo04 and Geo08; *enol* methyl pyruvate HH, Geo02, Geo06, and Geo11. The adsorption and interaction energies were calculated as described above (all reference calculations were performed with the inclusion of van der Waals interactions) and are listed in Table A-13.

System	E_{ads} (kJ/mol)	E_{int} (kJ/mol)
R-exo NEA + MP keto A0		
Geo03	-572.5	-13.4
Geo05	-572.9	-13.8
R-exo NEA + MP enol syn AB		
Geo04	-575.0	-15.9
Geo08	-568.4	-9.2
R-exo NEA + MP enol syn HH		
Geo02	-575.9	-16.8
Geo06	-567.3	-8.2
Geo11	-573.5	-14.4

Table A- 13 Adsorption and interaction energies of the most stable complexes between exo NEA and methyl pyruvate with van der Waals interactions included.

The final structures are summarized in Figure A-13 (A-G), which also shows the

simulated images and their relative Boltzmann populations.
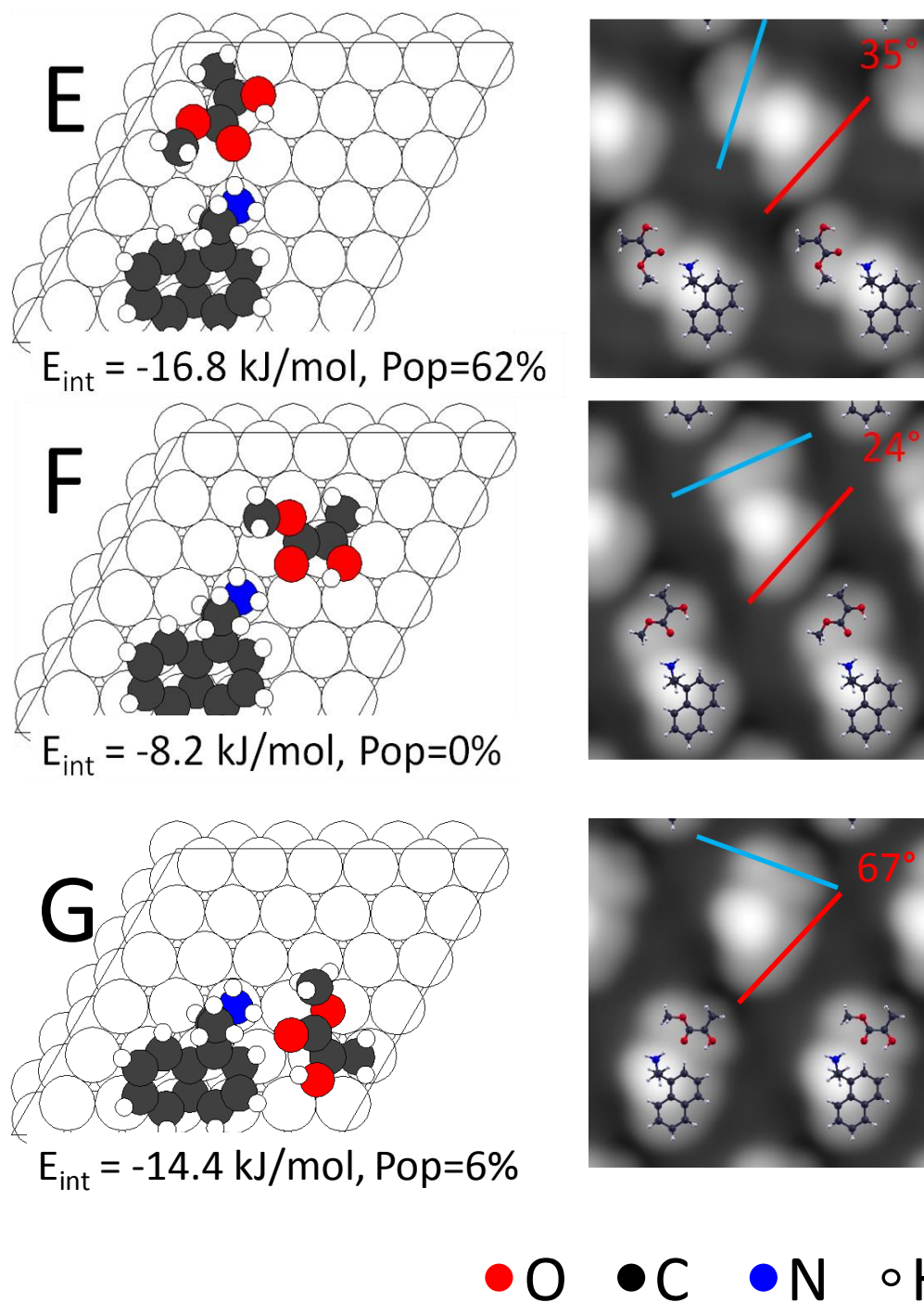
A E_{int} = -13.4 kJ/mol, Pop=2%

B E_{int} = -13.8 kJ/mol, Pop=3%

C E_{int} = -15.9 kJ/mol, Pop=26%

D E_{int} = -9.2 kJ/mol, Pop=0%

Figure A-13 Structures of the most stable docking complexes from the keto tautomer of MP (A and B) and from the enol tautomer (C through G). The interaction energies calculated including van der Waals' interactions are shown below each structure, as well as the expected equilibrium proportions. The STM images simulated by the Tersoff-Hamman method are shown adjacent to each structure. The angles between the axis in the simulated images of the *enol* tautomer of MP, indicated by a blue line, and the long

axis of the naphthyl group of R-NEA, indicated by a red line, are also indicated.

References

1.	Lenz, D. H.; Conner Jr, W. C. *Analytica Chimica Acta* **1985**, *173*, 227.

2.	Burkholder, L.; Garvey, M.; Weinert, M.; Tysoe, W. T. *Journal of Physical Chemistry C* **2011**, *115*, 8790.

3.	Garvey, M.; Bai, Y.; Boscoboinik, J. A.; Burkholder, L.; Sorensen, T. E.; Tysoe, W. T. *The Journal of Physical Chemistry C* **2013**, *117*, 4505.

4.	emers-Carpentier, V.; Goubert, G.; Masini, F.; Lafleur-Lambert, R.; Dong, Y.; Lavoie, S.; Mahieu, G.; Boukouvalas, J.; Gao, H.; Rasmussen, A. M. H.; Ferrighi, L.; Pan, Y.; Hammer, B.; McBreen, P. H. *Science* **2011**, *334*, 776.

5.	Boscoboinik, J. A.; Bai, Y.; Burkholder, L.; Tysoe, W. T. *Journal of Physical Chemistry C* **2011**, *115*, 16488.

6.	Tkatchenko, A.; Scheffler, M. *Physical Review Letters* **2009**, *102*, 073005.

7.	Garvey, T. Michael; Applying Computational Methods to Interprete Experimntal Results in Tribology and Enantioselctive catalysis **2013**. Ph.D. dissertation, University of Wisconsin-Milwaukee

CURRICULUM VITAE

Mausumi Mahapatra

Place of Birth: Rabara, Odisha, India

Education

B.Sc	Nayagarh Autonomous College, Nayagarh, Odisha, India	2004
MS	Ravenshaw College, Cuttack, Odisha, India	2006
B.Ed	Nalini Devi Women's College of Teacher Education, Bhubaneswar, Odisha, India	2008

Dissertation Title: Chiral Modification of the Pd(111) Surface by Small Organic Molecules   2015

Employment   University of Wisconsin-Milwaukee, Department of Chemistry and Biochemistry Milwaukee, WI

                        Teaching Assistant   August 2009 - May 2011
                        Research Assistant   June 2011 - May 2015

Fellowship   Chancellor's Fellowship UW-Milwaukee   Aug 2009, Aug 2010

Publications

1. **Mahapatra, M.;** Tysoe, W. T., Adsorption and reaction pathways of a chiral probe molecule, S-glycidol on a Pd (111) surface. *Catalysis Science & Technology* **2015**.

2. **Mahapatra, M.;** Tysoe, W., Chemisorptive Enantioselectivity of Chiral Epoxides on Tartaric-acid Modified Pd (111); Three-Point Bonding. *Physical Chemistry Chemical Physics* **2015**.

3. **Mahapatra, M.;** Burkholder, L.; Devarajan, S. P.; Boscoboinik, A.; Garvey, M.; Bai, Y.; Tysoe, W. T., Formation of Induced-Fit Chiral Templates by Amino Acid-Functionalized Pd (111) Surfaces. *The Journal of Physical Chemistry C* **2015,** *119* (7), 3556-3563.

4. **Mahapatra, M**.; Burkholder, L.; Bai, Y.; Garvey, M.; Boscoboinik, J. A.; Hirschmugl, C.; Tysoe, W. T., Formation of Chiral Self-Assembled Structures of

Amino Acids on Transition-Metal Surfaces: Alanine on Pd (111). *The Journal of Physical Chemistry C* **2014,** *118* (13), 6856-6865.

5. Calaza, F.; **Mahapatra, M**.; Neurock, M.; Tysoe, W. T., Disentangling ensemble, electronic and coverage effects on alloy catalysts: Vinyl acetate synthesis on Au/Pd (111). *Journal of Catalysis* **2014,** *312*, 37-45.

6. **Mahapatra, M.;** Tysoe, W. T., Structure and decomposition pathways of D-(−)-tartaric acid on Pd (111). *Surface science* **2014,** *629*, 132-138.

7. **Mahapatra, M**.; Burkholder, L.; Calaza, F.; Stacchiola, D.; Tysoe, W. T., An Infrared Spectroscopic and Temperature-programmed Desorption Study of 1, 1-Difluoroethylene on Clean and Hydrogen-covered Pd (111). *Adsorption Science & Technology* **2011,** *29* (6), 595-602

Poster Presentations   Annual day poster presentation**,** University of Wisconsin-Milwaukee, Department of Chemistry & Biochemistry, Milwaukee, WI

April 2013	Probing Enantioselectivity on Chirally Modified Pd(111) Systems
April 2011	The Coverage and Chemical State of α-Amino Acids Under Enantioselective Conditions on Pd(111)
May 2010	Hydrogenation and H-D Exchange of Ethylene on Clean and Ethylidyne-Covered Pd(111)

Oral Presentation

June 25th, 2014	"Observation of Enantioselectivity on Chirally Modified Surface in Ultrahigh Vacuum: Identifying 1:1 Docking Complex between 1-Naphthylethylamine and Methyl Pyruvate"
	Physical Electronics Conference, La Cross, WI
June 6th, 2013	"Probing Enantioselectivity on Chirally Modified Pd(111) Systems"
	2013 Great Lakes Regional Meeting of the American Chemical Society, La Crosse, WI